Energy, water and carbon fluxes in the suburban environment

Ward, Helen

Awarding institution:
King's College London

ENERGY, WATER AND CARBON FLUXES IN THE SUBURBAN ENVIRONMENT

Helen Claire Ward

Department of Geography
King's College London

Submitted to the University of London for the degree of Doctor of Philosophy

July 2013

Abstract

To better understand boundary layer processes and improve hydro-meteorological models it is essential to quantify contributions from different land surface types to the total energy exchange. The effects of urban areas must be represented not only within densely populated towns and cities, but also at the regional scale. A multi-scale field campaign designed to investigate the exchange of energy and mass over suburban land surfaces was undertaken in Swindon, UK. Observations of heat, water vapour and carbon dioxide fluxes suggest Swindon behaves much like a natural landscape during summer, whereas anthropogenic activities dominate in winter. Eddy covariance data collected exhibit broad trends that are in accordance with studies in other locations, whilst marked seasonal contrasts build a more complete picture of the suburban environment.

Scintillometry, a ground-based remote sensing technique, estimates turbulent heat fluxes at larger scales (0.1-10 km), comparable to model grids. The conventional single-wavelength method provides the sensible heat flux. Additionally, use of a unique millimetre-wave scintillometer in conjunction with an infrared scintillometer enabled both sensible and latent heat fluxes to be determined. These results represent the first observations of large-scale evaporation over urban areas using scintillometry. The technique is shown to perform reasonably well and recommendations are made for future research. Advantages include spatially integrated fluxes, particularly useful over heterogeneous surfaces where a mosaic of different land cover characteristics can lead to contrasts in surface-atmosphere exchanges.

These observations are used to investigate the controls on evaporation and the behaviour of fluxes at different scales. Particular attention is given to seasonal variability, land cover and the availability of surface moisture and energy. Rapid evaporation directly after rainfall and dew are also explored. With improved understanding of the suburban climate, more accurate predictions can be made regarding the impact of land use development, environmental management schemes and climate change.

Declaration of originality

I confirm that the contents of this thesis are my own work except where otherwise acknowledged.

Table of Contents

Table of Figures

Table of Tables

Notation

A_q structure parameter coefficient for specific humidity [-]

A_T structure parameter coefficient for temperature [-]

C_n^2 structure parameter of the refractive index [$m^{-2/3}$]

C_q^2 structure parameter of humidity [$kg^2\ kg^{-2}\ m^{-2/3}$]

C_{Tq} temperature-humidity cross-structure parameter [$K\ kg\ kg^{-1}\ m^{-2/3}$]

C_T^2 structure parameter of temperature [$K^2\ m^{-2/3}$]

c_p specific heat capacity of air at constant pressure [$J\ K^{-1}\ kg^{-1}$]

$c_{T1\text{-}3}$ similarity function constants [-]

D aperture diameter [m]

D_{qq} structure function of humidity [$kg^2\ kg^{-2}$]

D_{TT} structure function of temperature [K^2]

d lateral displacement of apertures [m]

E evaporation [$kg\ m^{-2}\ s^{-1}$]

e vapour pressure [Pa]

F first Fresnel zone [m]

F_C carbon flux [$\mu mol\ m^{-2}\ s^{-1}$]

f frequency [s^{-1}]

f_{MO} similarity function [-]

g acceleration due to gravity [$m\ s^{-2}$]

g_s surface conductance [$m\ s^{-1}$]

K eddy wavenumber [m^{-1}]

$K_\downarrow$ incoming shortwave radiation [$W\ m^{-2}$]

$K_\uparrow$ outgoing shortwave radiation [$W\ m^{-2}$]

k optical wavenumber [m^{-1}]

L path length [m]

L_{Ob} Obukhov length [m]

L_v latent heat of vaporisation [$J\ kg^{-1}$]

$L_\downarrow$ incoming longwave radiation [$W\ m^{-2}$]

$L_\uparrow$ outgoing longwave radiation [$W\ m^{-2}$]

L_0 outer scale of turbulence [m]

l eddy size [m]

l_0 inner scale of turbulence [m]

n refractive index [-]

p atmospheric pressure [Pa]

Q absolute humidity [kg m^{-3}]

Q_B component of anthropogenic heat flux due to building energy use [W m^{-2}]

Q_E latent heat flux [W m^{-2}] (L_vE in Chapter 6)

Q_{Eq} equilibrium evaporation [W m^{-2}]

Q_F anthropogenic heat flux [W m^{-2}]

Q_G soil heat flux [W m^{-2}]

Q_H sensible heat flux [W m^{-2}] (H in Chapter 6)

Q_M component of anthropogenic heat flux due to metabolism [W m^{-2}]

ΔQ_S storage heat flux [W m^{-2}]

Q_V component of anthropogenic heat flux due to vehicle use [W m^{-2}]

Q^* net all-wave radiation [W m^{-2}]

$Q_{\downarrow}$ incoming radiation [W m^{-2}]

q specific humidity [kg kg^{-1}]

q_* specific humidity scaling variable [kg kg^{-1}]

R_d specific gas constant for dry air [J K^{-1} kg^{-1}]

R_v specific gas constant for water vapour [J K^{-1} kg^{-1}]

r mass mixing ratio of water vapour [kg kg^{-1}]

r_a aerodynamic resistance [s m^{-1}]

r_s surface resistance [s m^{-1}]

r_{Tq} temperature-humidity correlation coefficient [-]

s slope of saturation vapour pressure-temperature curve [Pa K^{-1}]

T temperature [K]

T_* temperature scaling variable [K]

U horizontal wind speed [m s^{-1}]

u longitudinal component of wind speed [m s^{-1}]

u_* friction velocity [m s^{-1}]

v lateral component of wind speed, crosswind speed [m s^{-1}]

w vertical component of wind speed [m s^{-1}]

z_d zero plane displacement height [m]

z_{ef} effective height [m]

z_m measurement height [m]

z_0, z_{0m} roughness length for momentum [m]

z_{0v} roughness length for water vapour [m]

α	albedo [-]
α_{PT}	Priestley-Taylor aridity parameter [-]
β	Bowen ratio [-]
δ	spatial separation [m]
γ	psychrometric constant [Pa K^{-1}]; R/R_d in Chapter 6 [-]
ζ	stability parameter [-]
κ_v	von Kármán's constant (0.4) [-]
λ	wavelength [m]
λ_B	built fraction [-]
λ_I	impervious fraction [-]
λ_V	vegetation fraction [-]
ν	molecular viscosity of air [m^2 s^{-1}]
ρ	density of (moist) air [kg m^{-3}]
ρ_d	density of dry air [kg m^{-3}]
σ_χ^2	log-amplitude variance [-]
τ	temporal separation, time lag [s]
χ	log-amplitude [-]
Ψ	stability function [-]

BLS	Boundary layer scintillometer (Scintec's BLS900 model)
LAS	Large aperture scintillometer (Kipp and Zonen's LAS 150 model)
MWS	Millimetre-wave scintillometer
OHM	Objective hysteresis model
PAR	Photosynthetically active radiation [µmol m^{-2} s^{-1}]
PE	Potential evaporation [W m^{-2}]
PSD	Power spectral density [Hz^{-1}]
PWF	Path weighting function
RES	Residual of the energy balance [W m^{-2}]
RH	Relative humidity [%]
VPD	Vapour pressure deficit [Pa]

Acknowledgements

I would like to thank my supervisors Sue Grimmond and Jonathan Evans, first of all for giving me the opportunity to undertake this research and also for their guidance, insight and inspiration. I am grateful for their support and encouragement. Special thanks are due to the co-authors of the papers contained in this thesis. I have been very privileged to work with, and learn from, some of the most knowledgeable and skilled scientists in micrometeorological research. In particular, discussions with Oscar Hartogensis and Arnold Moene have been both enjoyable and enlightening, and Henk De Bruin kindly took the time to teach and engage with me on many discussions of the fundamentals of scintillometry, from which I learnt a great deal.

In terms of the experimental campaign, I am indebted to John Bradford at Rutherford Appleton Laboratory. Firstly for the original build of the millimetre-wave scintillometer which made a big part of this research possible, and secondly for his expertise in pinning down the cause of the noise problem and his generosity in finding the time to carry out efficient repairs. The support of the Science and Technology Facilities Council staff at Chilbolton Observatory is greatly appreciated. I would especially like to say thank you to Alan Warwick, Cyril Barrett, Geoff Wicks, Ned Hewitt, Dave McNeil and others at CEH for their skilled assistance and moral support. James Blake kindly provided geological maps of the study area. Mike Wilson set up the Swindon Observatory website and the CEH Computer Services team have been very helpful.

The enthusiasm and hospitality of Swindon residents made site visits a pleasure. I would particularly like to thank Mr and Mrs Fuller for their kind permission to install equipment in their garden and interest in this work. It would not have been possible to carry out the range and duration of measurements made without the support of Evelyn and Walter Ineson, whose generosity, interest and insights into local history are very much appreciated. The co-operation of staff at Polaris House in allowing the rooftop meteorological station to be installed on the property is gratefully acknowledged.

Finally I must say a huge thank you to colleagues, close friends and family. Whilst studying at King's College I was lucky enough to work alongside some wonderful people. I especially thank Simone Kotthaus for her inspiring example, encouragement and friendship. Thank you to old friends for not giving up on me, especially over the last few months, and to my family for their patience and support.

This work was funded by the Natural Environment Research Council, UK, through a CEH algorithm studentship.

Chapter 1 Introduction

1.1 Motivation

Urban areas are characterised by a dense mixture of land cover types often with contrasting properties. As a result this environment is complex and challenging to study. However, knowledge of its meteorology is critical – not only for the safety and wellbeing of the inhabitants but also for its influence on the weather and climate at larger scales (Collier, 2006).

Unquestionably, human modifications to the landscape and atmosphere impact the environment. Compared to rural areas, typically much of the urban surface is impervious, so water infiltration and storage are greatly reduced. Thus the urban water cycle is accelerated: run-off rates are high, quickly followed by limited water availability once it has been removed via drainage systems (Oke, 1982; Rodriguez et al., 2003). Evapotranspiration is limited by the amount of vegetation (Grimmond and Oke, 1999c; Grimmond and Oke, 2002; Christen and Vogt, 2004), yet can be enhanced by additional water supplied through irrigation or leaking pipes, and by energy from anthropogenic activities or advected from warm, dry surroundings (Oke, 1979; Spronken-Smith et al., 2000; Moriwaki and Kanda, 2004).

Evaporation, or latent heat flux, thus depends on the availability of energy and water. Understanding this variable has the potential to offer considerable environmental, economic and health benefits in terms of developing intelligently designed cities and effective strategies to manage the environment. Building architecture, material properties and anthropogenic heat release combine to give elevated temperatures in cities compared to similar rural locations (Oke, 1982). This urban heat island effect can bring increased risks to human health and wellbeing associated with heat stress (Eliasson et al., 2007; Lindberg and Grimmond, 2011a). Control measures include use of vegetation or open water to promote evapotranspiration and maintain lower surface and air temperatures; the influence of humidity on thermal comfort must also be considered. Studies have investigated the most suitable species (Peters et al., 2011), location (McPherson and Simpson, 2003) and arrangement of plants (Spronken-Smith and Oke, 1998; Lindberg and Grimmond, 2011b), and effective distributions of water bodies (Theeuwes et al., 2013).

Decisions on urban design and policy rely heavily on numerical modelling, as do routine weather prediction and flood forecasting. Future climate scenarios predict a higher frequency of extreme weather events. For example, increased frequency and intensity of heat waves

(Beniston, 2004; Meehl and Tebaldi, 2004), and occurrences of both flooding and drought are expected to become more common (Fowler and Hennessy, 1995; Schreider et al., 2000; Suarez et al., 2005). Provision of sustainable water supplies and managing flood risk will inevitably become even more pressing challenges as the world's population increases (Xiao et al., 2007; Mitchell et al., 2008). Globally, more than half the world's population now live in urbanised areas and this continues to rise (United Nations, 2011). Accurate and representative input data, robust parameterisation of atmospheric processes and evaluation of model performance are all crucial.

Two main issues confronting current meteorological research and its applications are (1) the spatial heterogeneity of the landscape at the relevant scales, and (2) variability of the ecosystem in time. In many regions the Earth's surface is heterogeneous at the 'sub-grid' scale, i.e. of the order of a few kilometres or less. These patches of different land cover, surface properties or sub-surface properties lead to different surface-atmosphere exchanges of energy, water, carbon dioxide and other trace gases (Beyrich and Mengelkamp, 2006; Blyth et al., 2006; Evans et al., 2012). The most widely used technique to measure fluxes, namely eddy covariance (Section 1.2), is representative of the local-scale that approximates to a single field or a few neighbourhoods. The majority of observational datasets are therefore representative of a single land cover type, or alternatively a time-dependent mixture that varies with atmospheric conditions controlling the instrument footprint. How to 'up-scale' these measurements to larger areas remains an unresolved question (Hasager and Jensen, 1999; Gockede et al., 2003; Kustas et al., 2006; Xiao et al., 2011). In urban areas direct inputs of heat, carbon dioxide and other pollutants from anthropogenic activities often originate from highly concentrated localised sources (Ichinose et al., 1999; Sparks and Toumi, 2010; Sailor, 2011; Kotthaus and Grimmond, 2012), which can further complicate interpretation and up-scaling of measurements. Urban land use is responsible for well over half of anthropogenic carbon emissions (Grimmond et al., 2010b) and forms a non-negligible proportion of the land surface (around 14% in the UK (Home, 2009)).

With regard to variability of the ecosystem in time, there is a shortage of urban observational datasets lasting longer than one season; to date most have been collected in summer. The few multi-seasonal campaigns that do exist document significant changes in the energy partitioning across the year (Christen and Vogt, 2004; Offerle et al., 2005a; Coutts et al., 2007b; Weber and Kordowski, 2010). The implications of this seasonality for models, many of which have been parameterised using summertime observations, are discussed by Loridan and Grimmond (2012) and Best and Grimmond (2013). Longer-term studies in urban areas have focused on carbon fluxes (Crawford et al., 2011; Järvi et al., 2012; Liu et al., 2012). The

inter-annual variability revealed by these studies makes a strong case for more long-term measurements.

Despite its central role in urban climates, the latent heat flux has received relatively little attention in the literature. Much of our current understanding originates from studies of North American cities, mainly from summertime observations (Grimmond and Oke, 1995; Grimmond and Oke, 1999c) accompanied by model development (Grimmond and Oke, 1991; Grimmond and Oke, 2002). Results of an extensive comparison of urban energy balance models (Grimmond et al., 2010a) revealed the latent heat flux to be the least well modelled of the energy fluxes. Recent improvements to the representation of evaporative processes in energy and water balance models have been made by Mitchell et al. (2008) and Järvi et al. (2011). Both studies conclude that accurate parameterisation of the surface conductance is crucial, and underline the wide applicability of such knowledge to assessing urban design options, water conservation schemes and climate mitigation strategies.

Technological advances over recent years have dramatically increased both instrumental and model capability. Combining simulations and observations is necessary in order to make the best use of available tools. However data from each must be compatible, of suitably high quality and properly representative of reality. A key consideration is spatial scale: how to link local observations (e.g. individual plots or neighbourhoods) or small-scale simulations (e.g. single street canyons), to the larger scale of numerical weather prediction and hydrological models. Before outlining the specific project objectives, it is necessary to introduce micrometeorological measurement techniques for determining fluxes across a range of scales.

1.2 Measurement techniques

Turbulent flux measurements can be attributed to a source area upwind of the instrumentation, typically extending out to distances of the order of hundreds of metres. The exact siting of instruments is critical, both to ensure that the measurement position is typical of the study area and that the assumptions of micrometeorological theory can be satisfied. These include steady-state conditions (addressed through selection of suitable averaging intervals) and horizontal homogeneity (related to site selection). Over urban environments measurements should be made above the roughness sub-layer – the lowest portion of the atmosphere extending to approximately twice the average building height and including the complex spaces in which we live, i.e. along streets, around buildings, within gardens and parks (Oke, 1987). Within the roughness sub-layer, individual roughness elements (such as buildings and trees) influence the flow. The atmosphere is not well understood here; there have been a few experimental studies revealing complex flow patterns along street canyons (Rotach et al.,

2005; Eliasson et al., 2006), at an intersection (Balogun et al., 2010) and around buildings (Christen et al., 2007). For the purposes of this study, it is the intention that such micro-scale effects are averaged out below the height of the instruments so that the measurements are representative of the local-scale (10^2-10^4 m), i.e. a few neighbourhoods. When selecting a site the representativeness of these neighbourhoods compared to the surrounding area is an important consideration.

The eddy covariance (EC) method is currently the most established technique for measuring surface energy and mass exchange. The sensible and latent heat fluxes and the carbon dioxide flux are obtained from the covariance between the appropriate quantities (temperature, water vapour concentration and CO_2 concentration) and the vertical wind speed (see e.g. Stull (1988) or Foken (2008b)). Typically, a sonic anemometer makes fast-response measurements of temperature and the three components of wind speed *u*, *v* and *w*, and a fast-response infra-red gas analyser (IRGA) measures carbon dioxide and water vapour concentrations. If the optical path of the gas analyser is 'open' to the atmosphere, measurements are taken *in situ* and data cannot be used when the instrument windows are wet, i.e. during and following rainfall or heavy dew. For closed-path systems an intake tube draws the air from the sampling location into an enclosed measurement chamber, which resolves the issue of obstruction of the path by water but can introduce lag time and tube adsorption issues, and the required pump system takes more power.

Although widely used, EC is not without drawbacks. Data processing is intensive and complex, requiring many corrections and adjustments, some of which are still the subject of debate (Lee et al., 2004; Mauder et al., 2008). Typical under-closure of the energy balance of about 10-20% (Wilson et al., 2002; Foken, 2008a) suggests that the measured turbulent fluxes may be underestimated. In combination with factors such as not fully accounting for energy storage, proposed explanations for this underestimation include the presence of large secondary circulations not measured by the EC system, particularly over heterogeneous surfaces (Foken, 2008a), phase lags between energy fluxes (Leuning et al., 2012), flux divergence (Katul et al., 2006), incomplete corrections (e.g. not accounting for the full range of contributing frequencies) and violation of the required assumptions for the EC technique (see e.g. Kaimal and Finnigan (1994), Foken (2008b)). Identification of the cause(s) is a non-trivial task, even in the simplest environments, as it requires the combined assessment of all energy components, each with their own uncertainties, measurement limitations and sampling volumes.

The scintillometry technique offers an alternative method for monitoring heat fluxes. A scintillometer consists of a source of electromagnetic radiation and a detector separated by a

distance of between 50 m and 10 km (Figure 1-1). Changes in the intensity of the electromagnetic beam propagating between transmitter and receiver are the result of changes in the turbulent atmosphere along the length of the path, so that the measurements are spatially averaged over an area of typically 0.1-10 km^2. The scintillometer receiver detects fluctuations in the beam strength. These scintillations are essentially the same phenomenon as 'heat haze' – the shimmering effect that can often be seen when looking at a distant object close to the ground on a hot day – and are caused by changes in the refractive index of the atmosphere as a result of density differences due to variations in temperature and humidity. These are expressed as structure parameters and, in turn, can be related to the surface fluxes using similarity theory (see Chapters 5 and 6 for details). An electromagnetic beam of optical or near-infrared wavelength is primarily sensitive to temperature fluctuations, whereas longer wavelengths (e.g. microwaves or radio-waves) are also scattered significantly by changes in humidity.

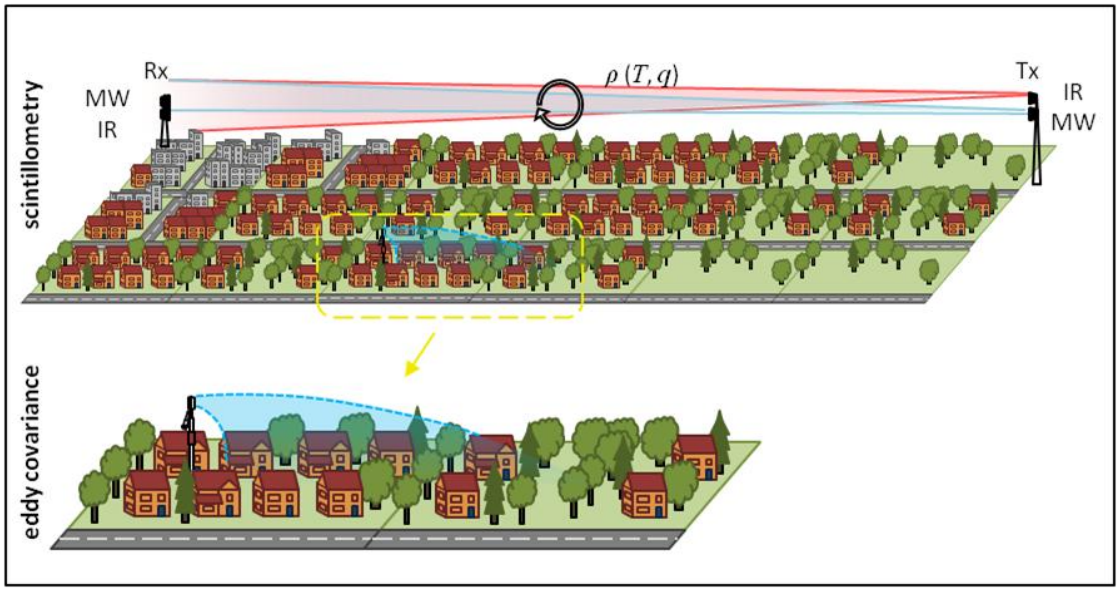

Figure 1-1 A schematic representation (not to scale) of the scintillometry technique: infrared (IR) and millimetre-wave (MW) beams propagate from transmitter (Tx) to receiver (Rx) refracted by turbulent eddies of density ρ at temperature T and humidity q; and the eddy covariance technique.

A single optical scintillometer enables the sensible heat flux to be determined; if the necessary additional measurements are made, the latent heat flux may also be estimated from the energy balance. Over heterogeneous surfaces several point measurements of net radiation and storage heat flux may be required to adequately capture the spatial variability of these

terms. In urban areas the appreciable size, associated observational difficulties and spatial complexity of the storage flux lead to large uncertainties in this term.

With two scintillometers of different wavelengths aligned along the same path, both the sensible and latent heat fluxes can be estimated directly. The 'two-wavelength' method (Hill et al., 1988; Andreas, 1991; Meijninger et al., 2002a; Evans, 2009), assumes a constant value for the correlation coefficient between temperature and humidity, r_{Tq}. Alternatively the 'bichromatic correlation' method (Lüdi et al., 2005) exploits the covariance between signals from each scintillometer with a view to obtaining a more representative value of r_{Tq}. This third quantity completes the third simultaneous equation in a system with three unknowns, in theory giving an unambiguous and more accurate solution, and therefore improved fluxes. A three-wavelength method has also been proposed but is less practicable as it requires a third instrument (Andreas, 1990).

Compared to EC, scintillometry offers a number of advantages. Spatially integrated quantities inherently average surface heterogeneity and facilitate comparison with other methods. The larger-scale measurements are also more representative as they are sampled over a greater area. The spatial integration leads to more statistically robust measurements over a shorter period of time (e.g. 5-10 min compared to 30 min for EC). From a practical perspective scintillometers demand little maintenance beyond alignment. Since they are effectively remote sensing instruments installation can be facilitated particularly in areas of steep topography where impractically tall masts would be required for EC instrumentation, and over urban surfaces where gaining permissions to install even unobtrusive instrumentation can be problematic. The scintillometer is most sensitive at the centre of the path, which means the locations of the mountings are less crucial than for EC instruments, where the mast itself can affect turbulence close to the point of measurement. A limitation of scintillometry is that there must be line-of-sight between transmitter and receiver which means that rain, fog or other beam obscuration precludes high quality measurements. Calculation of heat fluxes from scintillometry requires the use of similarity theory, whereas EC is more a direct measurement.

Large aperture infrared scintillometry is now a fairly well established technique. Recent studies indicating considerable variability between instruments (Kleissl et al., 2008; Van Kesteren and Hartogensis, 2011) calls for a method of inter-instrument calibration; currently the best option seems to be comparison prior to the main field campaign (e.g. Lagouarde et al. (2006)). Lack of a commercially available system of longer wavelength means the two-wavelength and bichromatic methods have been little tested despite the considerable advantages that they potentially offer. Over the past few years the scintillometry technique

has been successfully employed in increasingly complicated environments including over heterogeneous cropland (Chehbouni et al., 2000a; Meijninger et al., 2002b), complex topography (Poggio et al., 2000; Evans, 2009) and cities (Kanda et al., 2002; Lagouarde et al., 2006). The general consensus is that scintillometer beams should be above or close to the blending height to best satisfy the requirements of similarity theory scaling needed for the estimation of fluxes. The blending height represents the height above the surface at which spatial heterogeneity in the flow is averaged out by turbulent mixing.

Additional instrumentation that can be used to estimate evaporation includes lysimeters and sap-flow gauges, both micro-scale measurements. A lysimeter consists of a container installed in the ground, with a weighing device underneath to monitor the quantity of water contained within the soil-plant volume. Evaporation is deduced from the change in mass after accounting for precipitation and infiltration. Lysimeters are labour intensive to install and this must often be done several months in advance to give the soil time to settle back into an undisturbed state. Edge effects and advection can compromise data quality but replicates can capture spatial variability and are reasonably simple to scale up to a larger area. Examples of the use of lysimetry in urban settings include measurement of evaporation from grass lawns (Feldhake et al., 1983), run-off from asphalt (Ramier et al., 2004) and dewfall (Richards, 2005).

Sap-flow gauges monitor the flow of water through trees using heat as a tracer. The result is a measure of the transpiration rate from a particular tree, but gauges are fairly difficult to install and are invasive, requiring holes to be drilled into the trunk. The main drawback with this method, however, is the difficulty of selecting representative trees. In theory, tree cover and a species survey can be used to scale the measurements from individual trees to represent a garden or neighbourhood but multiple factors will influence the health of each tree, such as sunlight, water availability, soil and air temperature, nutrient availability, proximity to other vegetation, disease and age. This technique is thus best-suited to uniform areas or studies of individual trees. The diversity of species, gardening practices and tree position in urban areas demand large sample numbers and make appropriate sample selection very difficult. Peters et al. (2011) sampled a mixture of evergreen and deciduous trees over four sites in a suburban area of Minnesota (37 trees in total).

1.3 Objectives

The overall objective of this research is to further the understanding of energy and mass exchange within suburban environments, with a particular focus on evaporative processes. As there were no existing datasets for suburban areas in the UK, the first goal of the project was to gather suitable observational data. The town of Swindon in southern England was the site

selected for study. Other work in the UK has focused on city centres: London (Helfter et al., 2011; Kotthaus and Grimmond, 2012) and Edinburgh (Nemitz et al., 2002). Given different climate, water use trends and town architecture it might not be appropriate to apply results from other countries to the UK, and findings from city centre studies are unlikely to be transferrable to the more vegetated, lower density suburbs.

To capture temporal variability in the behaviour of the surface it was important for the measurement campaign to extend across multiple seasons. Long-term flux datasets covering a diversity of urban landscapes are very much in demand (Grimmond, 2010). Although the number of study sites is increasing, their typically short duration and favouring of summertime conditions limit current understanding and model evaluation (Best and Grimmond, 2013).

To assess spatial variability a combination of eddy covariance and scintillometry was used. An eddy covariance station was installed in a residential garden and provided local-scale energy, water and carbon fluxes representative of the surrounding neighbourhoods. Three scintillometers were also deployed. A large aperture scintillometer was installed on a 2.8 km path over newly-built residential areas to provide the sensible heat flux at a larger scale. A 5.5 km path from the rural outskirts to the town centre traverses the whole study area and comprises a second infrared scintillometer plus a unique millimetre-wave scintillometer (MWS) built by the Centre for Ecology and Hydrology and Rutherford Appleton Laboratory (Evans, 2009; Evans et al., 2010). The longer path setup constitutes the first use of a two-wavelength scintillometer system in the urban environment and enabled determination of large-area sensible and latent heat fluxes via the two-wavelength method. The performance of the scintillometers and the applicability of the different measurement techniques are examined.

The Swindon dataset is considered relative to other studies around the world and similarities and differences between sites are discussed. Analysis of the observations covers a range of temporal scales. These include short-term (sub-hourly) variation of energy fluxes in response to incoming radiation and following rainfall; typical patterns of diurnal evolution; changes over several days to a few weeks resulting from changing surface and synoptic conditions such as decreasing water availability; seasonal patterns; and inter-annual variations. The main focus of the analysis is on evaporative processes within the wider topic of the suburban energy balance. Analysis of the carbon flux is complementary to the goals of this study through the link with vegetative activity. Moreover, as the first long-term measurements of UK suburban carbon fluxes these are also important data in their own right.

Further analysis is directed towards improvements to suburban energy and water balance modelling. Surface conductance is used to parameterise many of the evaporative controls in

the Penman-Monteith equation (Monteith, 1965). The Penman-Monteith equation was inverted to yield 'measured' values of the surface conductance using the Swindon observations. The behaviour of these measured values is explored.

1.4 Overview of the thesis

Chapter 2 describes the Swindon study site and measurement campaign. Full details of the instrumentation are also provided.

Chapter 3 presents the meteorological conditions for the two-year period discussed in this thesis (i.e. 2011-12). This chapter gives some background information for the analyses to follow, describes the observational period in comparison to the average UK climate and provides some context for global comparisons.

Chapters 4, 5, 7 and 8 describe the experimental results. Analysis of the first twelve months of eddy covariance data is discussed in Chapter 4 and offers insight into the climatology of a UK suburban area. The scintillometry results are presented in Chapters 5, 7 and 8. First, sensible heat fluxes at three scales are discussed (Chapter 5). This chapter features the longest time-series presented in the thesis – two years of sensible heat flux data for 2011-12. Results from the two-wavelength scintillometer system are separated into two parts. Part 1 (Chapter 7) includes description of the measurement techniques and observations of structure parameters and temperature-humidity correlation. Part 2 (Chapter 8) is concerned with the fluxes, their derivation using similarity theory and interpretation. In both parts scintillometry results are analysed alongside structure parameters and fluxes calculated from eddy covariance.

Discussion of the scintillometry work includes critical assessment of the techniques used. To successfully deploy new observational techniques in complex environments requires careful consideration. Prior to installation of equipment in Swindon, the effect of a variable wind field along a scintillometer path was considered. This work is presented in Appendix A. The pairing of scintillometers at two wavelengths offers many advantages but has not been widely used. A critical re-evaluation of the methodology revealed a necessary adjustment – that the variable used to represent the effect of water vapour should be the specific humidity. This work is presented in Chapter 6.

Finally, in Chapter 9, the conclusions of the project are summarised and recommendations are made for future work.

Chapter 4, Chapter 6 and Appendix A have been published in peer-reviewed journals. Chapters 5, 7 and 8 are in preparation for submission.

Chapter 2 Site description and experimental details

An overview of the experimental campaign is given in this chapter. First, a description of the study site is presented, followed by details of the instrumentation. The following chapters focus on subsets of the data for specific analyses and the relevant experimental details for each chapter are also provided therein (Chapters 4, 5, 7 and 8). This chapter serves as a reference point for the Swindon dataset.

2.1 Site Description

Swindon, Wiltshire (51.57°N 1.77°W, see Figure 2-1) is located in southern England, approximately 120 km west of London. Swindon has a population of around 175,000 and in recent years has been one of the fastest growing towns in Europe. Dating from the time of the Saxons, the settlement existed as a small market town (with population 1200 in 1801) until the arrival of the Great Western railway works in 1840, which initiated rapid development of north Swindon. By 1900, the new town to the north of the railway merged with the old town to the south. The rate of urbanisation increased during the 20th century as new housing developments and estates were built to house the overspill population from London. The railway works closed in 1986 but Swindon continued to develop to the north and west. The study area (Figure 2-2) covers the northern portion of the town, from the town centre out to the rural fringe, where expansion is ongoing. As well as being an important location in its own right, this region is very typical of suburban areas in the UK (e.g. Figure 2-3). There is a mixture of land uses but the study area is predominantly residential, with some commercial and institutional buildings and recreational green space.

The elevation of the study area varies between 80 and 150 m above mean sea level (Figure 2-4a). The oldest part of the town is built on high ground at the south of the study area. At the northern edge of the settlement the elevation increases and the land is generally higher in the east than the west. The underlying geology is predominantly mudstone with some siltstone, sandstone and limestone at the edges of the study area[1]. A mixture of soil types are found across Swindon - mainly clay loams with some sandy areas[2]. The River Ray runs along the western edge of northern Swindon and has some small tributaries running approximately east

[1] Based on data from British Geological Survey
[2] www.bgs.ac.uk

to west through the study area (Figure 2-1). Swindon has suffered from problems with flooding and water shortages, making it a very relevant location for this study.

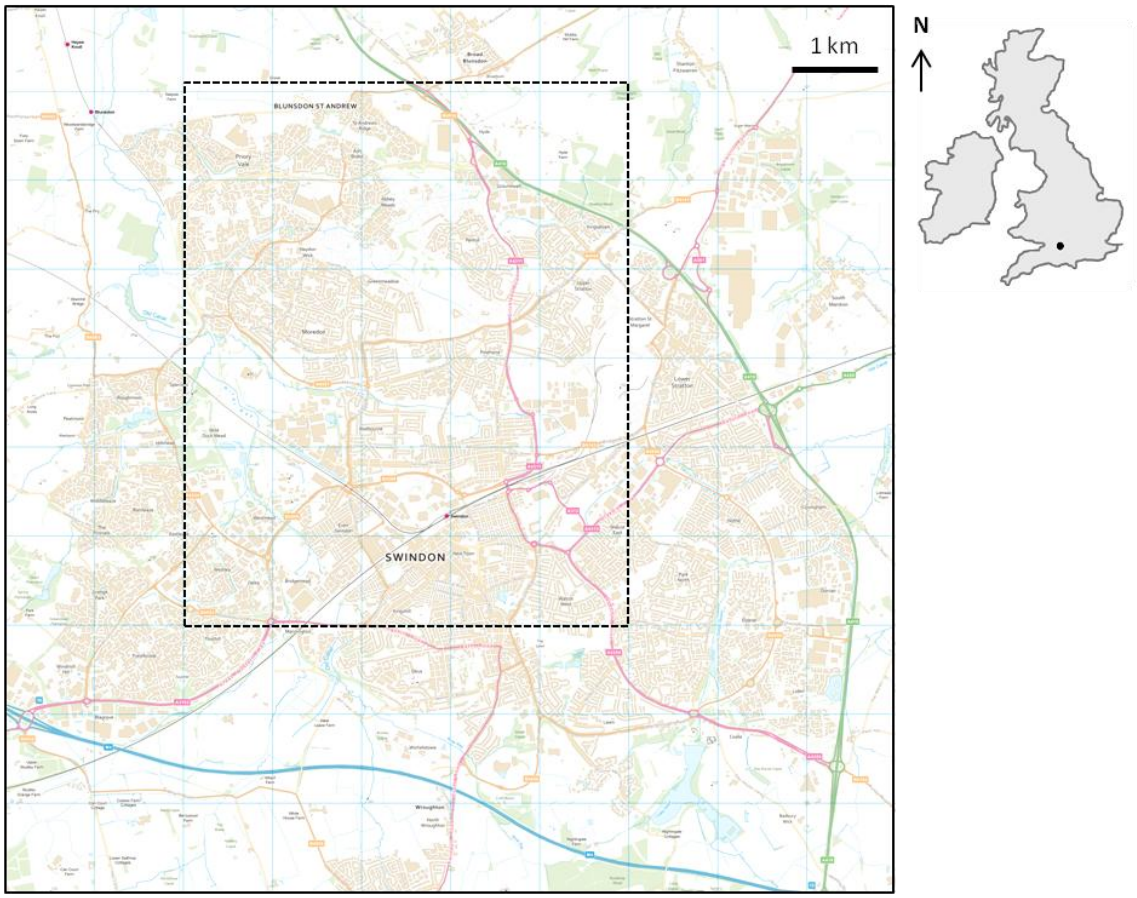

Figure 2-1 OS map of the town of Swindon (Ordnance Survey data © Crown copyright and database right 2013) and its location within the British Isles. Dashed lines indicate the study area.

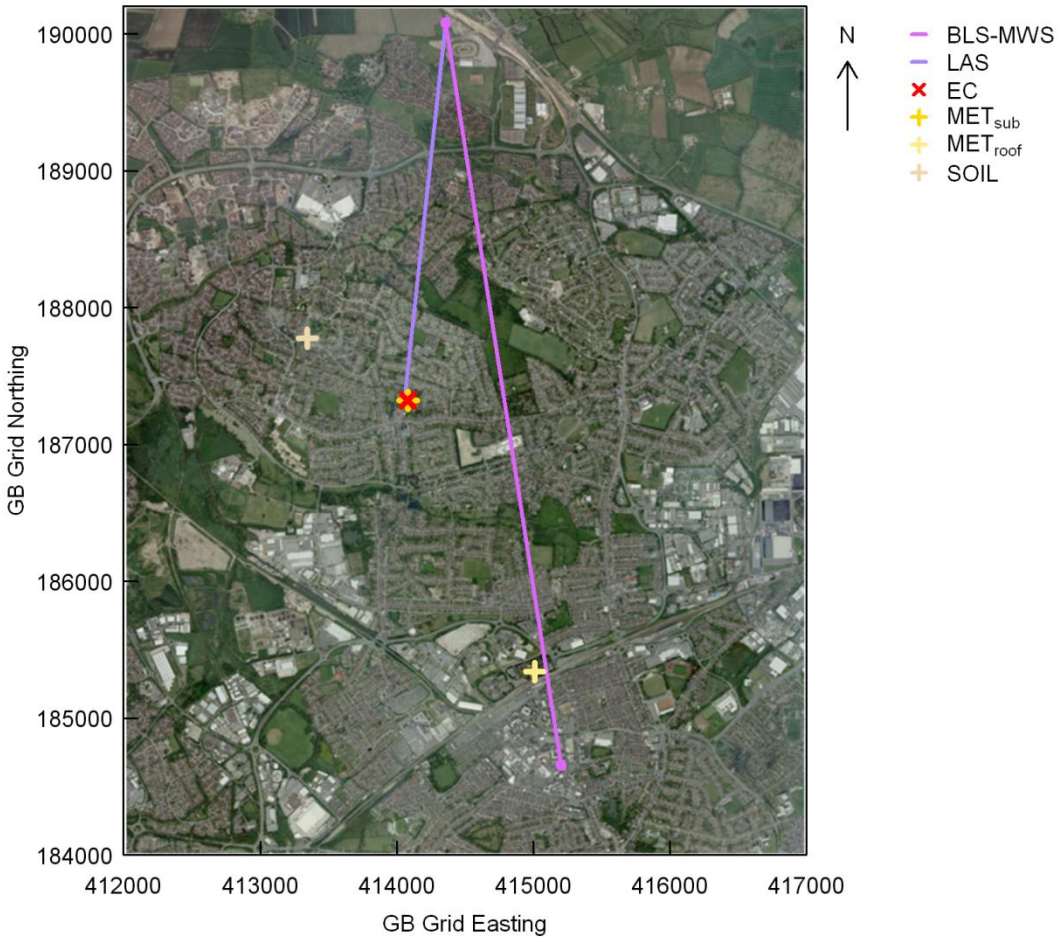

Figure 2-2 Aerial photograph (2009, ©GeoPerspectives) of the study area (bounded by dashed lines in Figure 2-1) with locations of the two-wavelength scintillometer path (BLS-MWS), large aperture scintillometer path (LAS), eddy covariance station (EC), two meteorological stations (MET_{sub}, MET_{roof}) and soil station (SOIL), see Section 2.2 for details.

Figure 2-3 View over part of the study area. Photograph taken on 30 July 2012 from the north of the study area looking south-southwest.

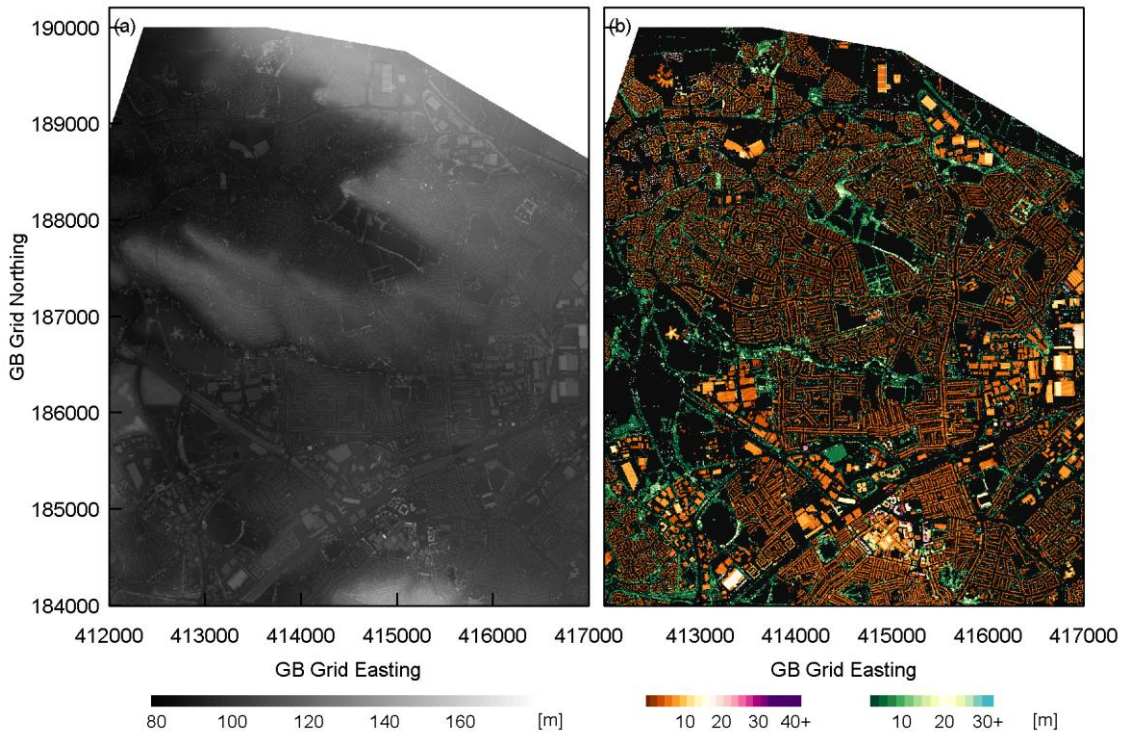

Figure 2-4 (a) Digital surface model from lidar data (2007 ©Infoterra Ltd) and (b) extracted building (orange-purple) and tree (green-blue) heights for the study area (5 m horizontal resolution).

Across most of the suburban area, variation in building height is generally small (Figure 2-4b). Residential buildings are mostly 2-3 storey houses or bungalows, with some small blocks of flats (Figure 2-5s-t) and a few taller blocks to the east (Figure 2-5u). Institutional buildings, small supermarkets and parades of shops are found amongst the residential areas, often accompanied by small car parks, playgrounds or green spaces (Figure 2-5d-f, o). Buildings are mostly brick with tiled roofs (Figure 2-5a-c, l-n) and most houses have at least a small garden. Larger scale variation in land use includes retail outlets and industrial areas (Figure 2-5j-k, p), consisting of large low-rise buildings constructed from metal sheeting, extensive impervious areas and little or no vegetation. In the town centre buildings are taller, more variable in height and shape, and constructed from a wider range of materials (more concrete, glass and metal, Figure 2-5q, w-x). Here, buildings are mostly offices and commercial properties. There is less vegetation and more paved areas (e.g. Figure 2-5r). The age of housing decreases moving away from the town centre; towards the north, much of the development has occurred in the last 20-30 years and consists of densely packed new-build homes interspersed with recreational areas and 'village centres' – groups of shops and facilities such as health care provision and community centres. The M4 motorway runs about 3 km south of Swindon centre (Figure 2-1).

There is a considerable proportion of vegetation across the study area as a whole (53%). A large nature reserve lies close to the centre of the study area. There are also green corridors intentionally left undeveloped between neighbourhoods, as well as smaller parks, playing fields, allotments and grass verges alongside roads (Figure 2-5g). Although the area fraction of vegetation is predominantly grass (44%), trees form a significant part of the urban canopy and are of similar height to the buildings. There is a variety of tree species and more deciduous than evergreen. Siting ranges from small wooded areas and green corridors (Figure 2-4b, Figure 2-5e-f) to lone trees in gardens or surrounded by paved areas (Figure 2-5a, p, r). Impervious surfaces cover 31% of the study area (13% roads; 18% other impervious areas). The built fraction is 14% and there is very little open water (< 1%).

Figure 2-5 Land cover variation across the study area.

2.2 Instrumental setup

Figure 2-2 illustrates the instrument locations for the Swindon measurement campaign. A 5.5 km scintillometer path provides turbulent heat fluxes for the study area. A shorter scintillometer path (2.8 km) is located over more recent development towards the north. Near the centre of the study area local-scale energy and carbon fluxes are obtained from an eddy covariance station. There are two meteorological stations, one co-located with the EC station (MET_{sub}) and the other closer to the town centre (MET_{roof}). Soil measurements are made at the EC site and at a second site further west (SOIL). The setup of each site is described below and a summary of the instrumentation is given in Table 2-1.

2.2.1 Long scintillometer path

The long scintillometer path traverses the study area from the edge of the suburbs to the town centre and is orientated approximately north-south. Two instruments were installed on this 5492 m path: a dual beam Scintec boundary layer scintillometer (BLS900) – a large aperture scintillometer which operates at a wavelength of 880 nm, and a unique millimetre-wave scintillometer (MWS) built by the Centre for Ecology and Hydrology and Rutherford Appleton Laboratory (Evans, 2009) with a wavelength of 3.2 mm (94 GHz). This combination enables estimation of large-area sensible and latent heat fluxes via the two-wavelength or bichromatic method. Mounting brackets were designed and built in-house at CEH Wallingford to (a) position the BLS and MWS beams as close together as possible and (b) minimise vibrations which can contribute unwanted variance to the signal (Von Randow et al., 2008; Beyrich et al., 2012). The transmitters were mounted at 28 m above ground level (a.g.l.) on a telecommunications mast (51°36'33.9" N, 1°47'38.6" W) and the receivers at 26 m a.g.l. on the rooftop of the telephone exchange in central Swindon (51°33'38.1" N, 1°46'55.3" W). In combination with the local topography, this provided an average beam height of 44 m. The relative positions of the BLS and MWS were swapped at each end so that their beams crossed close to the centre of the path. The setup is shown in Figure 2-6a-c.

The two-wavelength scintillometer system was installed in late December 2010. Instrumental faults reduced the availability of data from the MWS during spring in both 2011 and 2012 (Figure 2-11) but the BLS ran almost continuously throughout 2011-12. Results from the BLS (but not MWS) are discussed in Chapter 5. Chapters 7 and 8 present findings from the operational two-wavelength scintillometer system (BLS and MWS together).

2.2.2 Shorter scintillometer path

A shorter scintillometer path of 2761 m was set up in June 2011. A Kipp and Zonen LAS 150, which also operates at 880 nm, was installed over newly built residential areas. The LAS transmitter was mounted on the same mast as the BLS and MWS transmitters at a height of 27 m (Figure 2-6a-b) and the receiver installed on a 1.7 m post in the garden of a residential property (51°35'4.9" N, 1°47'53.0" W, Figure 2-6d). The topography helps to provide sufficient beam height away from the ends of the path. The average height of the beam above the surface is 32 m. This single-wavelength setup is able to provide the sensible heat flux at an intermediate scale between the 5.5 km path and the EC measurements.

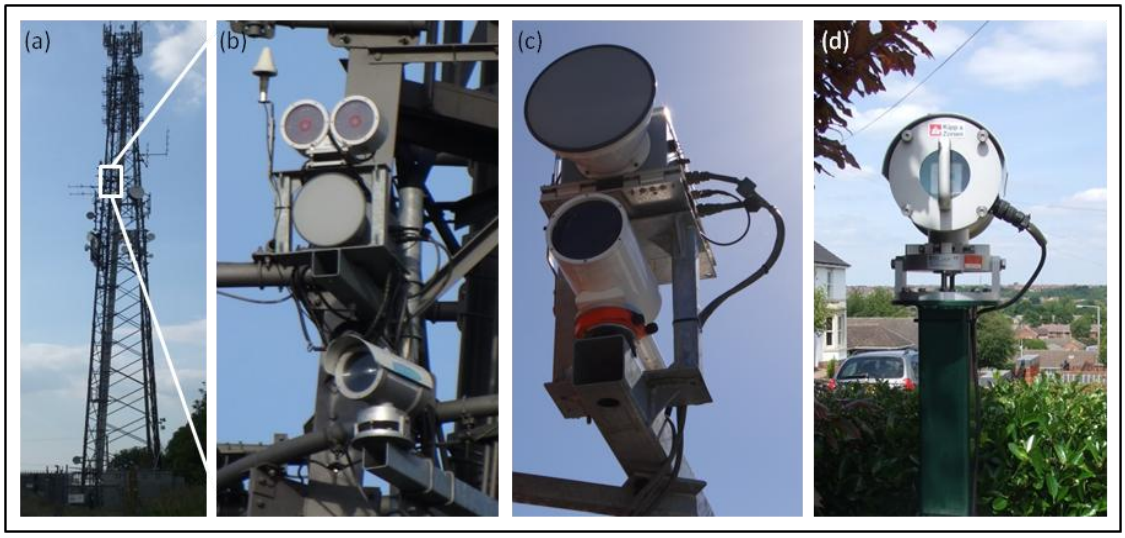

Figure 2-6 (a, b) Scintillometer transmitters; (c) MWS and BLS receivers and (d) LAS receiver.

2.2.3 EC station and co-located meteorological station (MET_{sub})

A pneumatic mast was installed in a residential garden approximately 3 km north of Swindon town centre (51°35’4.6’’ N, 1°47’53.2’’ W, Figure 2-7) on 9 May 2011. A sonic anemometer and open-path infrared gas analyser were positioned at the top of the mast at a height of 12.5 m, 2-3 times the mean height of the surrounding buildings and trees. The eddy covariance station provides turbulent sensible and latent heat fluxes and the carbon dioxide flux at the local-scale, representative of the surrounding neighbourhoods. The surrounding area is predominantly residential but there are some institutional (schools) and light commercial buildings nearby.

A four-component radiometer, net radiometer and weather station were installed on the same mast, and a temperature profile from ground level up to 9 m height. Additional

measurements in the surrounding garden include soil temperature, moisture and heat flux, surface temperature, surface wetness and rainfall using a tipping bucket rain gauge. Since 16 September 2011 a camera photographed the garden at 15 min intervals to supply useful information about the conditions on site, such as snow cover or vegetation phenology.

The first twelve months of EC data from this site are presented in Chapter 4. Results are further analysed and discussed both in comparison with scintillometry and in their own right in Chapters 5, 7 and 8. The meteorological data collected at this site (MET_{sub}) are used as the main dataset for the study area.

Figure 2-7 Eddy covariance station and meteorological measurements situated in the garden of a residential property.

2.2.4 Rooftop meteorological station (MET_{roof})

A second meteorological station was installed on the rooftop of an office building (51°34'0.29" N, 1°47'5.34" W, Figure 2-8) near Swindon town centre on 21 September 2010. The height of the roof surface is 13 m a.g.l. In addition to temperature, pressure, relative humidity and rainfall, the four components of radiation were measured, along with surface temperatures and surface wetness. A heat flux plate provided an estimate of the energy stored and released through the roof. Wind speed and direction were recorded by a 2-D sonic anemometer (WXT automatic weather station, see Table 2-1 for details), but at a height of only 2 m above the roof surface and with the presence of a nearby building turret, these are influenced by the surrounding building form.

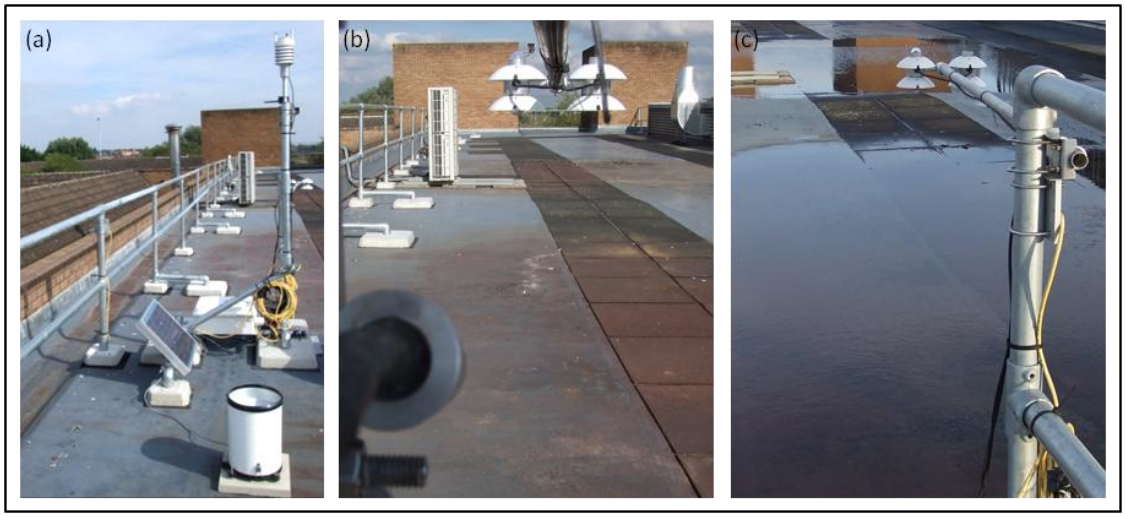

Figure 2-8 (a) Rooftop meteorological station with four-component radiometer in (b) dry and (c) wet conditions.

2.2.5 Soil station (SOIL)

Additional soil measurements were made at a second site (51°35'19.30" N, 1°48'31.54" W) in a small garden from 6 May 2011 (Figure 2-9). The soil here contains a higher proportion of clay compared to the EC site. Soil temperature, moisture and heat flux were measured at three different depths: 0.10, 0.30 and 0.45 m, and another heat flux plate was installed just below the surface at 0.05 m. These data are not explicitly used in the remainder of this thesis.

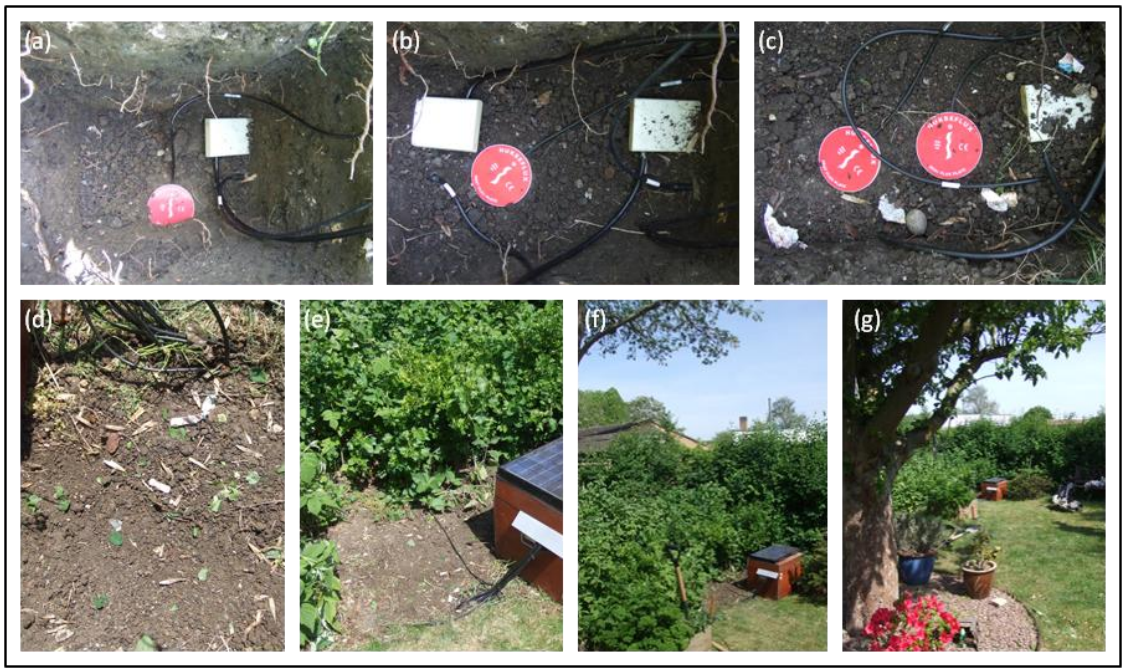

Figure 2-9 Installation of soil sensors at (a) 0.45 m, (b) 0.3 m and (c) 0.10 m depth, (d) recovered soil surface and (e-g) location of soil station within the garden. The soil moisture probes were inserted horizontally in the vertical soil wall (a-c).

Site	Equipment	Model, manufacturer	Details Height, depth [m]	Dates of operation
5.5 km path	Infrared scintillometer	BLS900, Scintec	45.0	01 Jan 2011 – 31 Dec 2012
	Millimetre-wave scintillometer	CEH-RAL MWS	42.8	10 Jun 2011 – 13 Jan 2012, 16 Apr 2012 – 31 Dec 2012
2.8 km path	Infrared scintillometer	LAS 150, Kipp and Zonen	35.9	26 Jun 2011 – 31 Dec 2012
EC	Sonic anemometer	R3, Gill Instruments	12.5	09 May 2011 – 31 Dec 2012
	Infrared gas analyser	LI-7500, LI-COR Biosciences	12.2	09 May 2011 – 31 Dec 2012
MET_{sub}	Four-component radiometer	NR01, Hukseflux	10.1	09 May 2011 – 31 Dec 2012
	Net radiometer	NRLite, Kipp and Zonen	8.7	09 May 2011 – 31 Dec 2012
	Automatic weather station	WXT 510/520, Vaisala	10.6	09 May 2011 – 15 May 2012 / 15 May 2012 – 31 Dec 2012
	Tipping bucket rain gauge	0.2 mm tip, Casella CEL	Ground level	09 May 2011 – 31 Dec 2012
	Infrared temperature sensors x 3	IRT, Apogee Instruments	Various surfaces	09 May 2011 – 31 Dec 2012
	Thermocouple profile (x 10)	Type T, Omega Engineering	0.05-9.1 m a.g.l.	19 May 2011 – 31 Dec 2012
	Heat flux plate x 3	HFP01, Hukseflux	0.03-0.05 m in clay loam flowerbed / in slightly sandier soil / under broken concrete	09 May 2011 – 31 Dec 2012
	Soil moisture probe x 2	CS616, Campbell Scientific Ltd.	0.03-0.05 m in flowerbed / below grass lawn	09 May 2011 – 31 Dec 2012
	Soil temperature probe x 2	107, Campbell Scientific Ltd.	0.05 m in flowerbed / below grass lawn	09 May 2011 – 31 Dec 2012
	Wetness sensor	237, Campbell Scientific Ltd.	Soil surface of flowerbed	09 May 2011 – 31 Dec 2012
	Camera	CC5MPX, Campbell Scientific Ltd.	1.45	16 Sep 2011 – 31 Dec 2012
MET_{roof}	Four-component radiometer	NR01, Hukseflux	1.11	01 Jan 2011 – 31 Dec 2012
	Automatic weather station	WXT 510, Vaisala	2.00	01 Jan 2011 – 31 Dec 2012
	Tipping bucket rain gauge	0.2 mm tip, Casella CEL	Roof level	01 Jan 2011 – 31 Dec 2012
	Infrared temperature sensors x 2	IRT, Apogee Instruments	0.91 south-facing tiles / 0.96 roof surface	01 Jan 2011 – 31 Dec 2012
	Thermocouples (x 6)	Type T, Omega Engineering	Various surfaces	01 Jan 2011 – 31 Dec 2012
	Heat flux plate	HFP01, Hukseflux	Roof surface, under rubber mat	01 Jan 2011 – 31 Dec 2012

	Wetness sensor	237, Campbell Scientific Ltd.	Roof surface	01 Jan 2011 – 31 Dec 2012
SOIL	Heat flux plate x 5	HFP01, Hukseflux	0.10-0.45 m profile and 0.05 m	06 May 2011 – 31 Dec 2012
	Soil moisture probe x 4	CS616, Campbell Scientific Ltd.	0.10-0.45 m profile	06 May 2011 – 31 Dec 2012
	Soil temperature probe x 4	107, Campbell Scientific Ltd.	0.10-0.45 m profile	06 May 2011 – 31 Dec 2012

Table 2-1 Summary of instrumentation deployed in Swindon during the period 01 January 2011 – 31 December 2012. The effective heights of the scintillometers are given (see Chapters 5 and 7), for MET_{roof} the heights above the roof surface are given.

2.2.6 Data Collection

Table 2-2 and Figure 2-10 summarise data collection by a series of loggers at the different sites. Automated data collection via GPRS (General Packet Radio Service) modems connected to on-site computers or directly to loggers enabled near real-time monitoring and rapid identification of instrument or power failures. A graphical summary of measurements was uploaded to a project webpage (swindonobservatory.ceh.ac.uk) allowing the data to be checked daily. Being able to diagnose instrument issues remotely facilitated prompt field repairs and helped to maintain a high data capture rate.

		Logging system details		Post-processing resolution
Site	**Logger**	**Sampling frequency**	**Output resolution**	
5.5 km path	CR5000	100 Hz raw data	100 Hz raw data, 1 min statistics	1, 10 min
	BLS SPU	500 Hz raw data	500 Hz raw data, 30 s statistics	1 min
2.8 km path	CR5000	500 Hz raw data, 1 Hz statistics	500 Hz raw data, 1 min statistics	1, 10 min
EC	CR3000	20 Hz raw data	20 Hz raw data, 30 min statistics	30 min
MET_{sub}	CR1000	2 s	1 min	1, 10, 30 min
MET_{roof}	CR1000	2 s	1 min	1, 10, 30 min
SOIL	CR1000	10 s	1 min	1, 10, 30 min

Table 2-2 Specification of the data collection, logging frequency and resolution of data after processing. The signal processing unit (SPU) is supplied with the BLS by Scintec; Campbell Scientific Ltd. supplied all other loggers used.

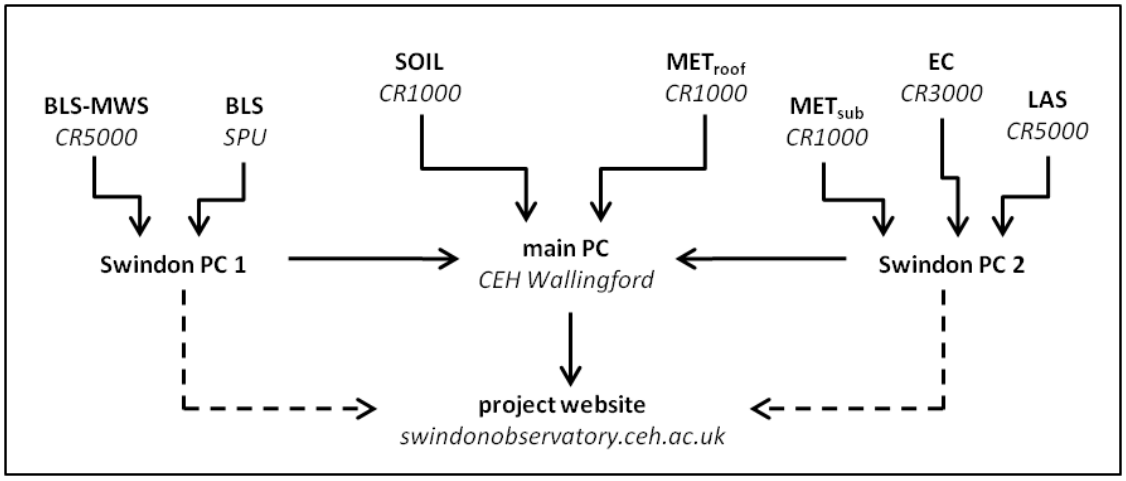

Figure 2-10 Overview of the data flow from sites in Swindon to a central PC at CEH Wallingford and daily uploads to the project website.

The data discussed in this thesis were collected during the main two-year study period 1 January 2011 – 31 December 2012 (Figure 2-11). Additional meteorological data are available from installation of the MET_{roof} site (21 September 2010), and all sites are expected to continue running until spring-summer 2013, although these data are not discussed as part of this thesis.

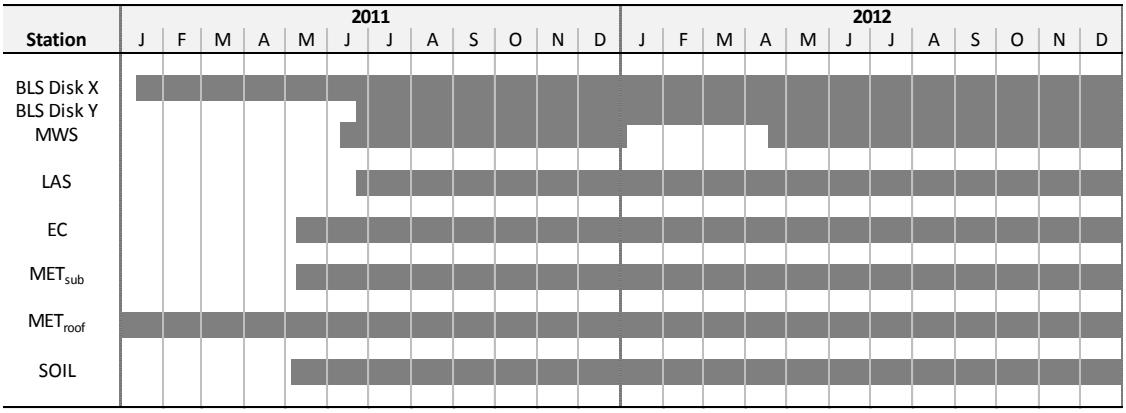

Figure 2-11 Timeline of sites and operational measurements in 2011-12.

2.3 Use of the meteorological datasets

To provide a continuous meteorological dataset for the 2011-12 study period, data from the two stations (MET_{sub} and MET_{roof}) were combined. Data from MET_{sub} were used when available as they are expected to be most representative of the study area in terms of location and surrounding land cover, and instruments are sited above or just inside the roughness sub-layer. The MET_{sub} data were then gap-filled with adjusted MET_{roof} data based on linear regression of concurrent data (9 May 2011 – 31 December 2012). The resulting combined

dataset therefore consists of adjusted MET_{roof} data before installation of MET_{sub} on 9th May 2011. This combined dataset is used for the overview of meteorological conditions during the study period (Chapter 3) and for processing the scintillometry data; MET_{sub} data are presented alongside the EC results in Chapter 4.

Chapter 3 Meteorological conditions during the study period

This chapter describes the meteorological conditions measured in Swindon for 1 January 2011 – 31 December 2012. This provides context for in-depth analyses in the following chapters. The climate of the study area and deviations from the average climatic conditions encountered during the study period are presented. The influence of natural variability in weather conditions on the collected dataset is relevant for interpretation of the results and when drawing comparisons with other sites. This chapter also acts as a reference for future use of the dataset, such as for land-surface modelling applications.

Unless otherwise stated, data shown here are from the combined meteorological dataset (i.e. MET_{sub} gap-filled with adjusted MET_{roof}) described in Section 2.3.

The UK generally experiences warm summers and cool wet winters. The influence of the Gulf Stream brings relatively warm temperatures given the latitude. The climate is temperate-marine: the Atlantic has a moderating effect and gives rise to relatively mild winters compared to mainland Europe, but the continental influence can bring periods of hotter weather in summer and colder in winter, particularly in the south of the UK. The combination of these different influences adds to the variability of UK weather. Atlantic low-pressure systems bring frequent rain, winds and cloudy conditions. The prevailing wind direction is from the southwest. Average annual rainfall for southern England is ~780 mm and the mean minimum and maximum temperatures are 1.2 °C in February and 21.3 °C in July[1].

For the two year study period, the most dramatic variation was in the rainfall (Section 3.2). For most of 2011 rainfall was below average with the threat of drought conditions by early spring 2012. From April 2012 rainfall was well above average and many regions experienced flooding. However, both summers were fairly wet and cooler and cloudier than average with warm, dry and sunny periods more common in spring or autumn of both years (Section 3.3). Winter 2012 was warmer than average.

3.1 Temperature, humidity and pressure

Figure 3-1 summarises the atmospheric conditions during the study period. Times of warm, usually fair, weather can be picked out from the temperature time-series. In 2011 these were

[1] Met Office climate averages (1971-2000), http://www.metoffice.gov.uk/climate

spring, late September to early October; in 2012, late March, late May to early June, several days in July and the first half of September. The generally mild 2011-12 winter contrasts with cold spells in February 2012 (with snowfall). Other cold periods lasted a few days in January 2011 and December 2012. The times of relatively warm and sunny conditions are seen clearly against the background of the generally cool, cloudy and frequently wet two-year period in the vapour pressure deficit (VPD). The change from high to low pressure in spring 2012 marks the shift between warm and dry conditions in early spring to heavy rains in April.

The following chapters explore some of these changes in more detail. The limited water availability in early spring 2012 is examined in Chapter 4. The warm, clear-sky days at the end of May 2012 are investigated in Chapter 8. Seasonal trends and contrasts between the two years are discussed throughout.

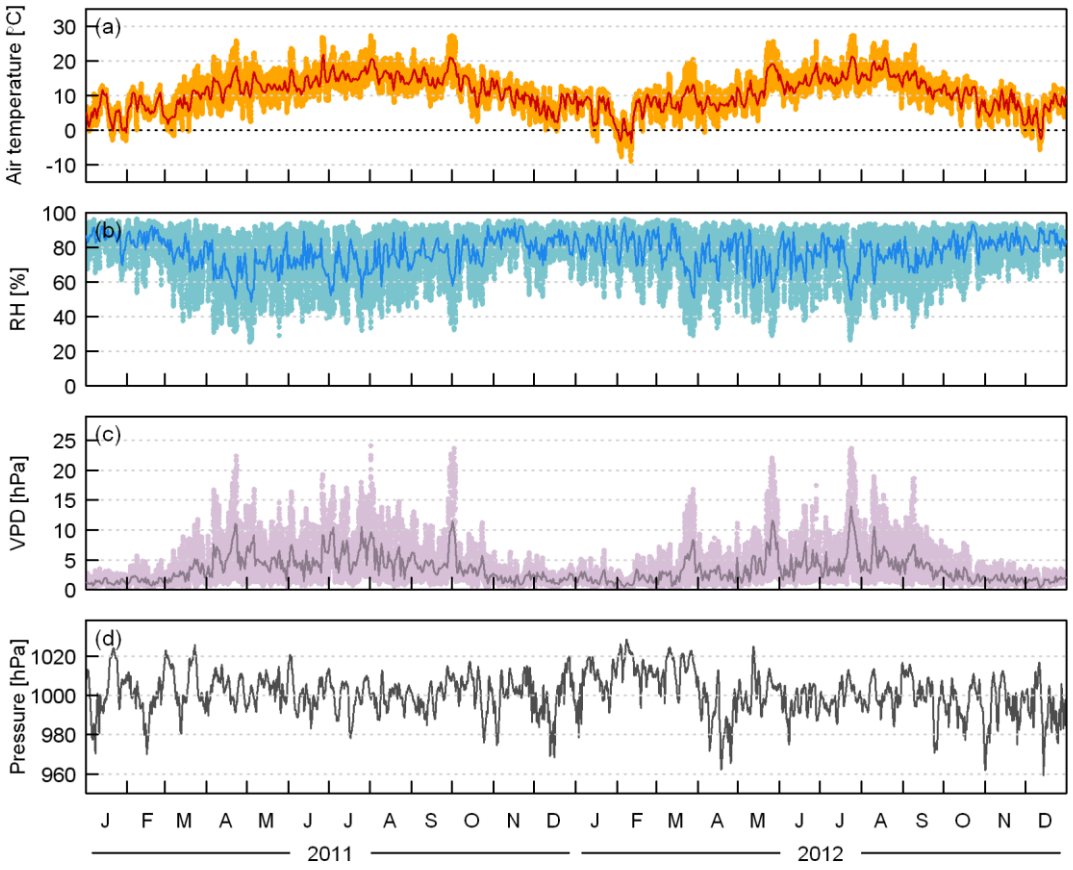

Figure 3-1 Time-series (30 min values and daily means) of temperature, relative humidity (RH), vapour pressure deficit (VPD) and atmospheric pressure.

3.2 Rainfall

The two years studied had contrasting rainfall patterns (Figure 3-2). Almost twice as much rain fell in 2012 as in 2011, the annual totals measured were 1019 mm and 531 mm respectively. The average annual rainfall for the UK is 1126 mm, but lower in southern England at 782 mm. The nearest Met Office station at Lyneham (about 15 km southwest of Swindon) has an average of 719 mm for the period 1971-2000[1]. In both 2011 and 2012, spring was dry with below average rainfall. March and April 2011 were exceptionally dry and rainfall in February and March 2012 was well below average. The dry period continued to early April 2012, after which followed a very wet summer with monthly rainfall considerably higher than average, particularly in April and June 2012. By late 2012 the continued rainfall meant many areas of the UK suffered from flooding, contrary to the start of the year when there had been concerns of drought. Although rainfall in 2011 was below average, summer 2011 was wet and fairly cloudy, but less so than 2012.

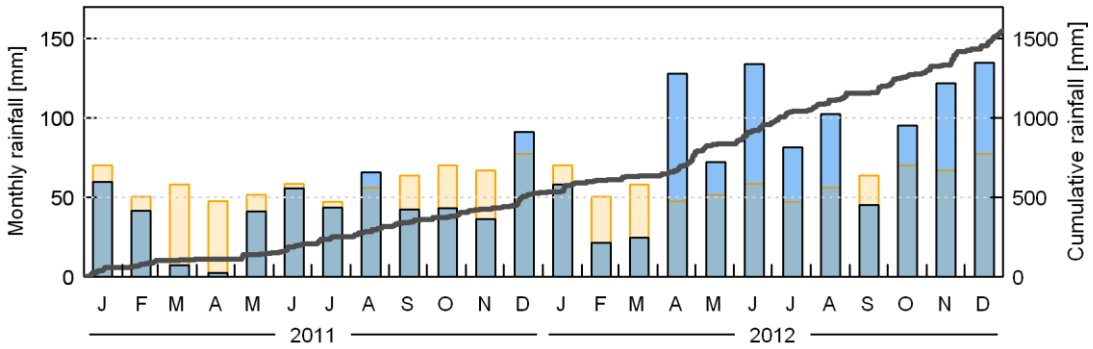

Figure 3-2 Monthly total rainfall measured in Swindon (blue bars) with the 1971-2000 averages for nearby Met Office station at Lyneham (orange bars) and cumulative rainfall for Swindon (right-hand axis)

3.3 Radiation Balance

3.3.1 Cloud cover

Figure 3-3 gives an indication of cloud cover using a clearness index which expresses the proportion of incoming shortwave radiation ($K_{\downarrow}$) measured relative to an estimate of $K_{\downarrow}$ under clear-sky conditions. The prolonged sunny weather in spring 2011 can be seen, whereas the clear-sky periods in 2012 tended to be of shorter duration (≤ 10 days) and are spread over the year (March, May, July, September). These periods are evident in Figure 3-3 and in the time-series of other variables (Figure 3-1a, c; Figure 3-5d, Figure 3-6).

[1] Met Office climate averages (1971-2000), http://www.metoffice.gov.uk/climate

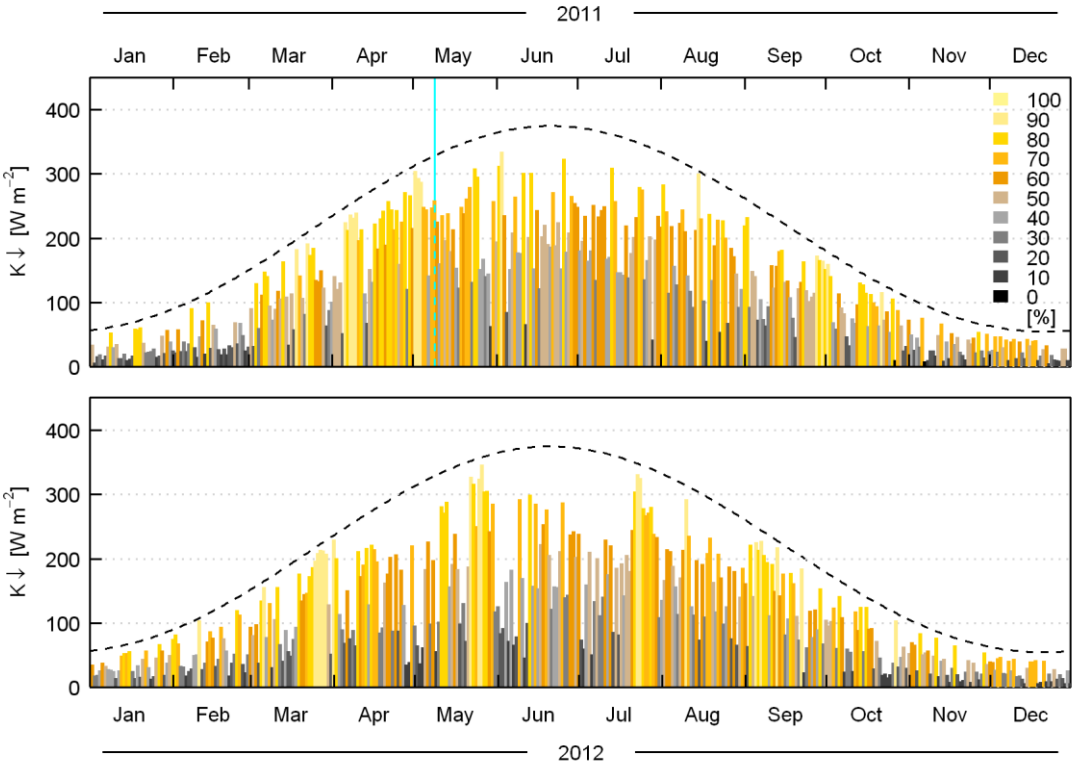

Figure 3-3 Mean daily $K_{\downarrow}$ coloured according to a clearness index expressing the observed $K_{\downarrow}$ relative to $K_{\downarrow}$ under clear-sky conditions (dashed line). Clear-sky $K_{\downarrow}$ approximated using sun-earth geometry from the solaR package (Perpiñán, 2012), the solar constant and a reduction factor of 0.75 to account for atmospheric transmissivity. Observations are from MET_{roof} (undajusted) until 9 May 2011 (blue vertical line) and MET_{sub} after this date.

3.3.2 Radiation characteristics between sites

Each of the meteorological stations was equipped with a four-component radiometer (Chapter 2). Comparison enables an assessment of the spatial variation in the radiation balance due to cloud cover, which primarily dictates the incoming components, and the various properties of materials making up the urban surface, which alter the outgoing components. Overall, the net all-wave radiation (Q^*) looks similar between the two very different sites (Figure 3-4). There are larger differences between the two years studied, e.g. median Q^* peaks at notably smaller values in April, June and October 2012 compared to the same months in 2011. There is a marked change in median Q^* between September and October 2012.

Regression of concurrent data from the MET_{roof} and MET_{sub} yields $Q^*_{roof} = 0.94\ Q^*_{sub} + 4.07$ W m^{-2}. Considering the very different fields of view (MET_{sub} views a mix of suburban surfaces including a large proportion of grass whereas MET_{roof} is almost entirely influenced only by the roof surface) the net radiation balance is quite similar. The correlation is high ($r^2 = 0.94$) but

there is considerable scatter (RMSE = 37.3 W m^{-2}) particularly at high Q* when rapidly changing cloud cover leads to sudden large fluctuations in $K_{\downarrow}$ and spatial differences in $K_{\downarrow}$ between the two stations.

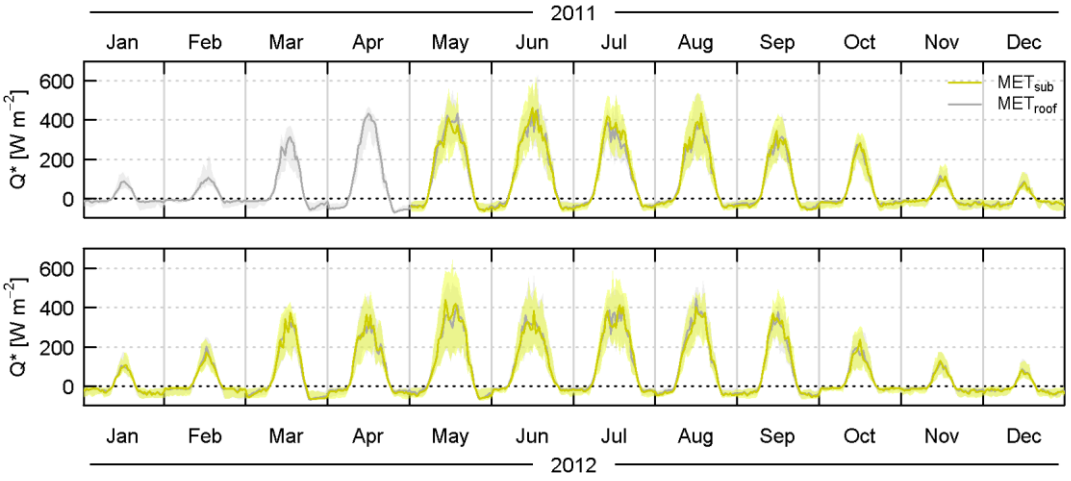

Figure 3-4 Monthly median diurnal cycles and inter-quartile ranges (shaded) of the net all-wave radiation.

Study of the radiation components reveals the influence of the different characteristics of the surfaces. Incoming shortwave and longwave ($L_{\downarrow}$) components are almost the same between sites. Linear regression slopes are 0.98 ($K_{\downarrow}$) and 1.00 ($L_{\downarrow}$) with much more scatter in $K_{\downarrow}$ (RMSE = 40.1 W m^{-2}) than $L_{\downarrow}$ (6.2 W m^{-2}). However, the outgoing shortwave component ($K_{\uparrow}$) is much smaller at the rooftop site, due to the lower albedo of the surface, whilst outgoing longwave ($L_{\uparrow}$) is considerably larger. These two opposing effects tend to compensate in the total radiation balance, hence the overall similarity in Q*. These findings corroborate previous work. For example, Schmid et al. (1991) state that the spatial variability of Q* is small in suburban environments due to the compensating effects of albedo and radiative temperature on the shortwave and longwave components.

The smaller $K_{\uparrow}$ and larger $L_{\uparrow}$ at MET$_{roof}$ can also be seen in the time-series (Figure 3-5b, d). The effect of snow cover on $K_{\uparrow}$ is evident in February 2012 and increases the average albedo (α) from 0.1-0.2 to 0.4 (Figure 3-6). There were two brief snow coverings, the first on 5 February, when the snow melted after one day, and the second on 10-12 February, which was heavier and lasted three days.

Periods of increased $L_{\uparrow}$ correspond to dry, sunny spells and include the few clear-sky days in the two-year period (Figure 3-3). Patterns in $L_{\uparrow}$ are replicated at both sites, though to a much larger extent by MET$_{roof}$. Surface water was often observed at MET$_{roof}$. The impervious roof

surface and lack of drainage means rain water collects and remains until there is sufficient energy for it to evaporate (Figure 2-8). At MET_{sub} pervious surfaces (grass, gravel, soils) and drainage pathways from impervious surfaces (roads, pavements, roofs) ensure that water is quickly removed from the surface following rainfall, through run-off and infiltration which are prevented at MET_{roof}. These differences in the local water balance of each site clearly impact the energy exchange of the surface. The gradual drying out of the gardens and mixture of suburban surfaces at MET_{sub} is expected to exhibit different behaviour to the wet/dry transition at MET_{roof}. In addition, many surfaces respond differently to direct and diffuse radiation. As well as differences in material properties (Grimmond and Oke, 1999c), shadow patterns can alter the radiation balance (e.g. Lindberg et al. (2008)).

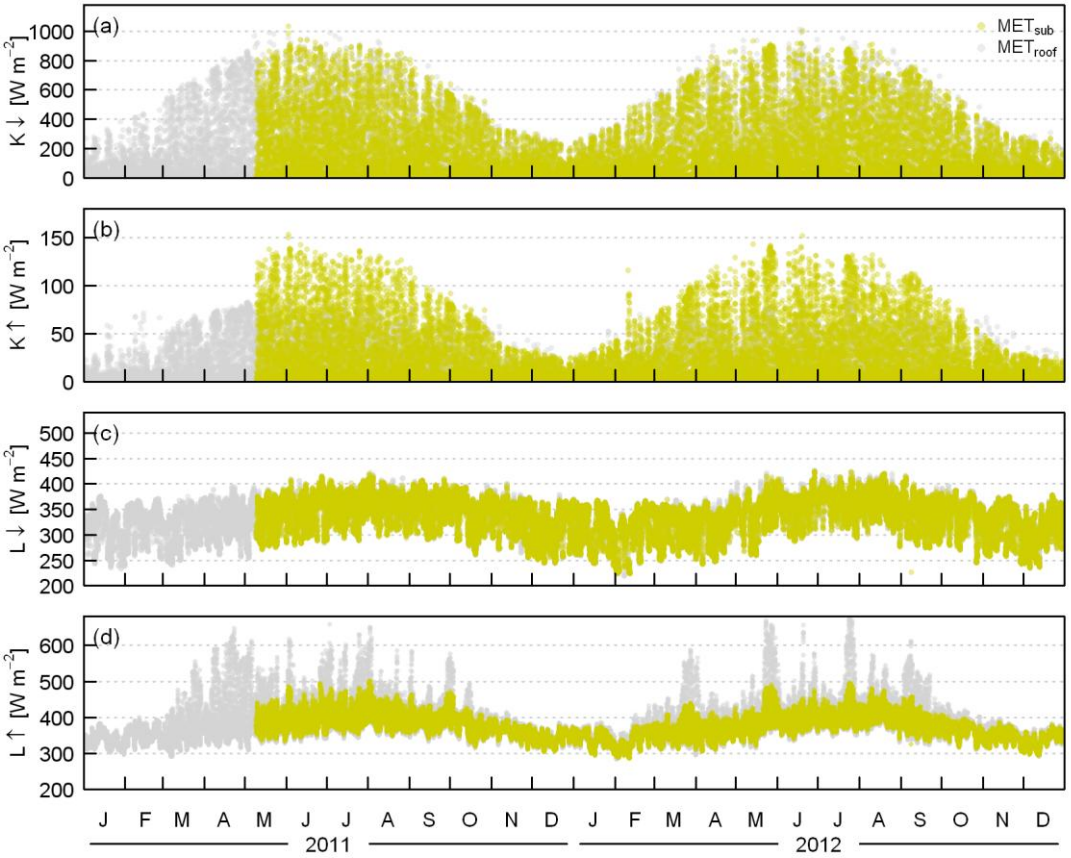

Figure 3-5 Time-series (30 min values) of the four components of radiation as recorded at the MET_{sub} and MET_{roof} sites.

The albedo at MET_{roof} shows a marked change between wet/cloudy (0.07-0.08) and dry/clear (0.10) conditions (Figure 3-6); the increases are much smaller and subtler at MET_{sub}. There is a clear seasonal cycle to the albedo of vegetation within the field of view of the radiometer at MET_{sub} and during summer α is about 0.02 higher than when vegetation is dormant. In winter there is a clear increase in the spread of α. Because the albedo plays a

major role in determining the energy available at the surface, it is crucial to correctly parameterise this variable in models.

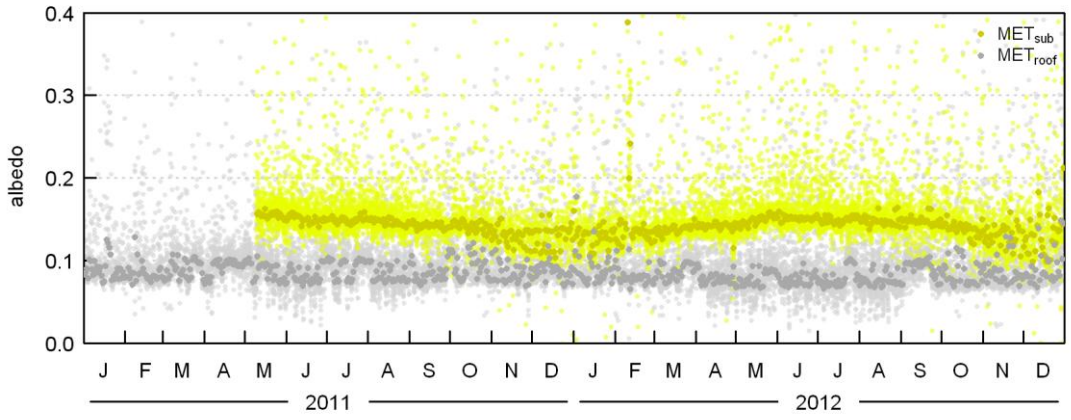

Figure 3-6 Time-series (30 min values and daily daytime medians) of the albedo at MET_{sub} and MET_{roof}.

3.4 Characteristics of the wind field

In this section data from the sonic anemometer at the EC site were used as these represent the longest time-series available (a logging fault meant that no wind direction data were available for the WXTs until 30 June 2011). The wind speeds in Figure 3-7 are therefore representative of a height of 12.5 m (Table 2-1). The largest 30 min mean wind speeds recorded were around 10 m s^{-1} and the mean value is 3.1 m s^{-1}. The predominant measured wind direction was southwesterly, followed by northeasterly, as is typical for the UK. The monthly distributions (Figure 3-8) reveal northeasterlies were more common in spring 2012 (MAM), but otherwise the remaining months are fairly similar.

The roughness of urban surfaces gives rise to larger friction velocities (u_*, Figure 3-9) than over smoother sites (e.g. Crawford et al. (2011)). The mean u_* for the study period is 0.50 m s^{-1} (0.43 m s^{-1} at night). Cases of very low u_* were rare: values of $u_* < 0.1$ m s^{-1} were observed for 3% of the dataset (6% at night). As is typical, wind speeds and friction velocities were weaker at night. Nocturnal wind speeds were largest in autumn-winter, and particularly December, of both years.

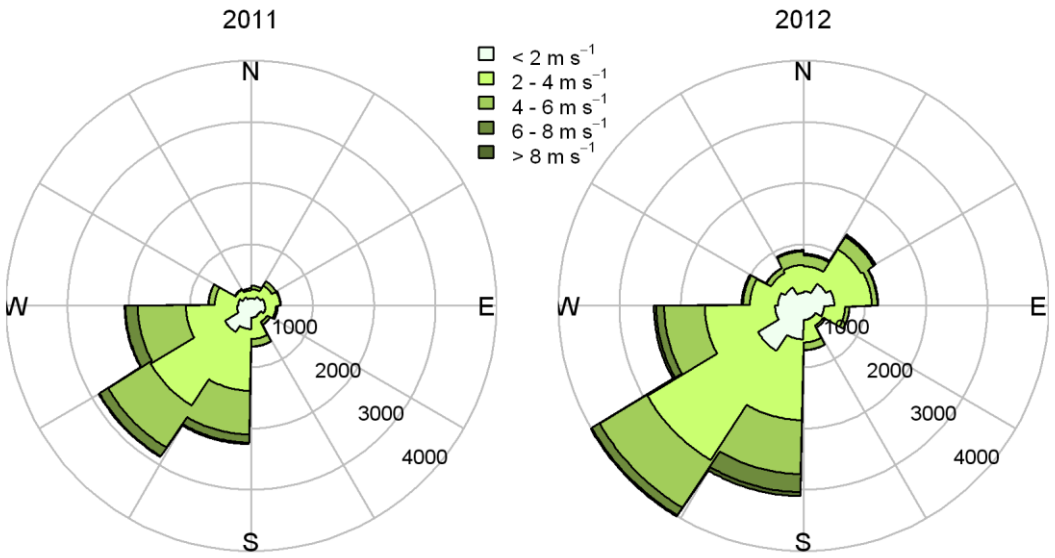

Figure 3-7 Wind direction distribution for 2011 (09 May – 31 December) and 2012 subset by wind speed. Radial lines indicate 30° wind sectors; circles mark the number of samples (30 min periods). Data are from the sonic anemometer at the EC site.

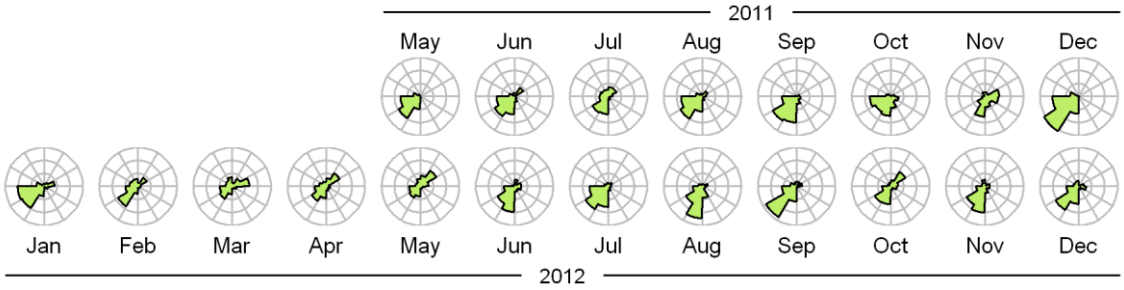

Figure 3-8 Wind direction distribution by month. Radial lines indicate 30° wind sectors; circles mark the number of samples (30 min periods): 200, 400 and 600. Data are from the sonic anemometer at the EC site.

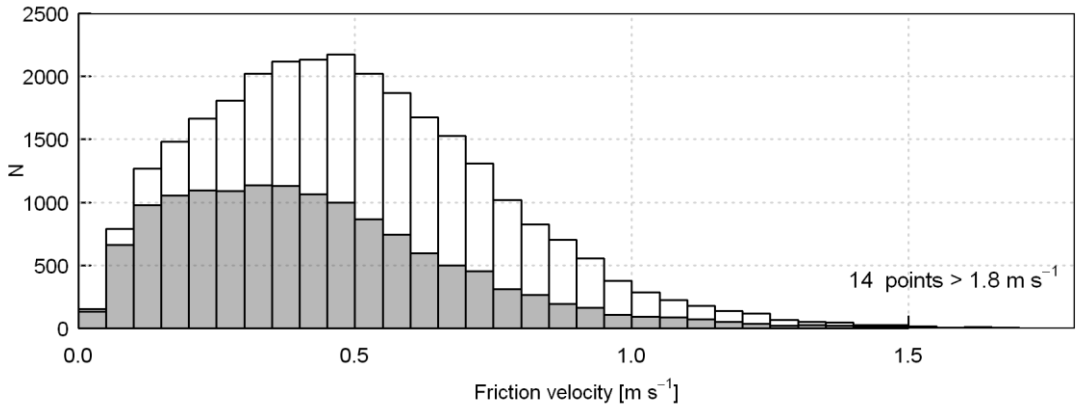

Figure 3-9 Distribution of 30 min friction velocities (09 May 2011 – 31 December 2012). Night time values are shaded. N denotes the number of data points.

3.5 Atmospheric stability

High wind speeds (and cool wet summers) meant conditions were predominantly neutral or near-neutral both on average and for each month separately (Figure 3-10). Using the stability parameter ζ (Chapter 4) and similar thresholds (see Figure 3-10 caption) to Christen and Vogt (2004) or Bergeron and Strachan (2010) classifies 79% of data as near-neutral or neutral. The remainder are fairly equally divided between stable (10%) and unstable (7.6% unstable, 2.4% strongly unstable). There were hardly any occurrences of strongly stable stratification (18 30 min periods in total), which is an important consideration for the scintillometers – that they are rarely outside the surface layer. Neutrally classified conditions are typical of suburban areas, as the sensible heat flux is smaller than for areas of higher population density (which are more built-up and have greater anthropogenic energy release) whilst the zero plane displacement height may still be appreciable due to the height of buildings and trees, so that ζ is usually small. In 2012 spring and early summer were the most unstable. March 2012 was also the month with the greatest frequency of stable periods; wind speeds were generally lower compared to other months. In 2011 most unstable times occurred in summer (out of the data collected May-December).

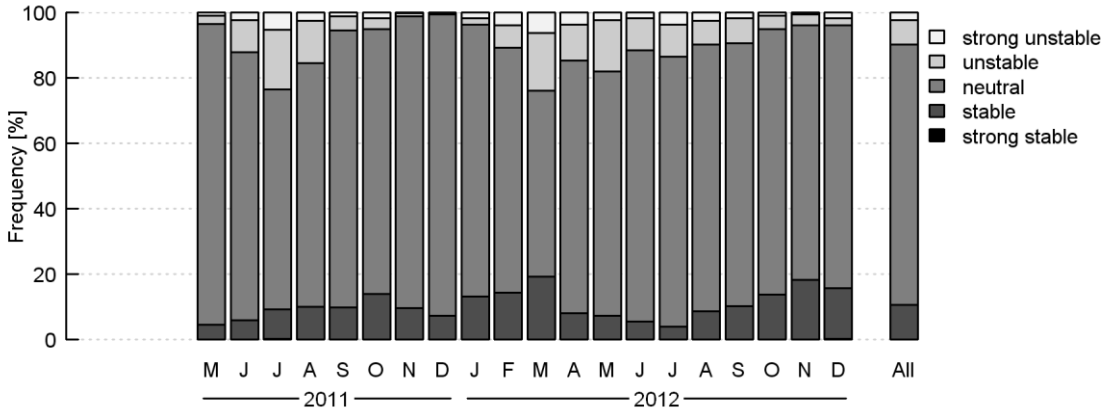

Figure 3-10 Stability regimes as observed at the EC site classified as strongly unstable ($\zeta \leq -0.5$), unstable ($-0.5 < \zeta \leq -0.1$), neutral ($-0.1 < \zeta \leq 0.1$), stable ($0.1 < \zeta \leq 10$) and strongly stable ($\zeta > 10$).

The frequency of the occurrence of positive and negative sensible (Q_H) and latent (Q_E) heat fluxes (see Chapter 4 for details) are presented in Figure 3-11a. Measurement uncertainties are large when the observed fluxes are very small, so these times of weak flux are indicated (-5 to 5 W m^{-2}). It is immediately obvious that Q_H is predominantly negative, i.e. directed towards the surface, for the winter months, and reasonably often negative during summer months (at night). All year round some negative latent heat flux, i.e. dewfall, is recorded. Overall, 14% of the measured Q_E values were negative and 3% below -5 W m^{-2}. Taking into account the

measurement uncertainty it is reasonable to conclude that dewfall occurs fairly frequently (which is in accordance with observations from the wetness sensor and on site visits).

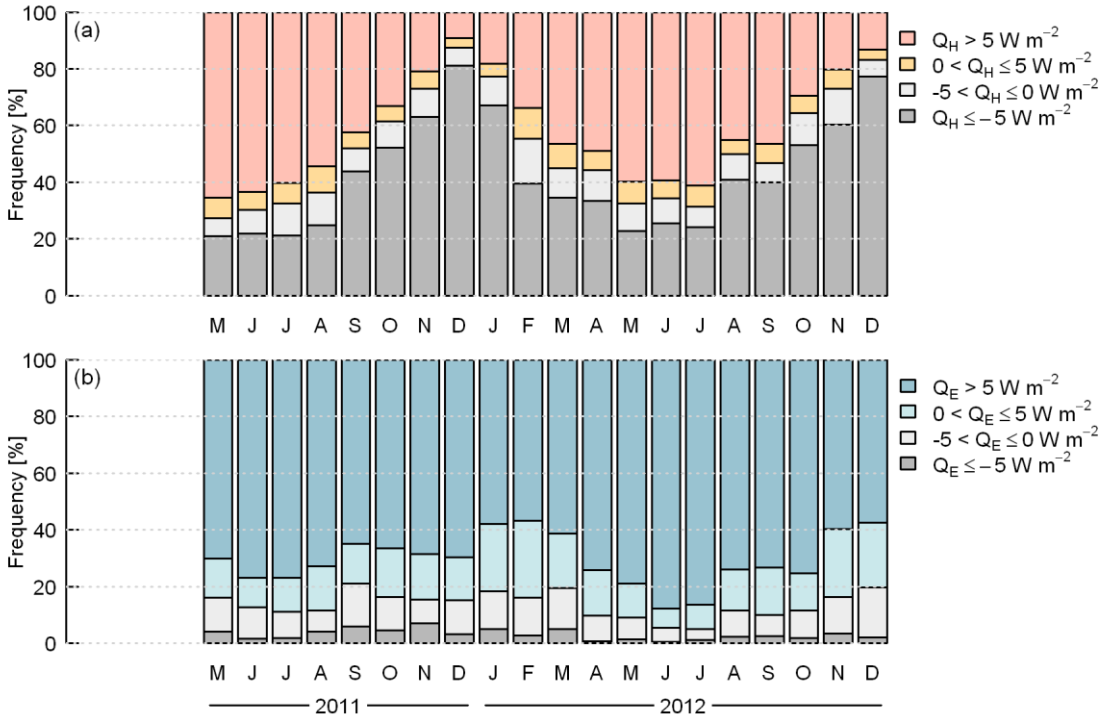

Figure 3-11 Frequency distributions of positive, negative and near-zero (a) sensible and (b) latent heat fluxes observed at the EC site.

Chapter 4 Multi-season eddy covariance observations of energy, water and carbon fluxes over a suburban area in Swindon, UK[1]

4.1 Introduction

Understanding interactions between land surfaces and the atmosphere has an important role in assessing human impact on the environment and improving the predictive capability of models. Underpinning these models are representations of relevant processes governing the transport of heat, water, momentum and pollutants. Besides weather forecasting, simulations are increasingly used in the following ways: to predict the occurrence and impact of extreme events such as flooding or heat waves; to make informed planning decisions, such as identifying suitable sites for wind power generation (Heath et al., 2007) or assessing the effect of building form on pollutant dispersion (Xie et al., 2005; Balogun et al., 2010); and in the optimisation of strategies for sustainable water supplies (Mitchell et al., 2008) or thermal comfort (Lindberg and Grimmond, 2011b). In order to develop and refine our understanding of such processes, observational datasets are required that encompass a range of environments and span sufficient timescales to offer insight into the driving factors.

That human behaviour impacts the environment has been well-documented, particularly for urban areas where modification is most apparent. The construction of buildings, roads and other impervious surfaces, changes in vegetation cover and type and the behavioural patterns of people have been shown to dramatically affect local climatology, within the urban areas themselves and up to regional scales (Oke, 1987; Roth, 2000; Collier, 2006; Grimmond, 2010). Urban temperatures tend to be warmer than for the rural surroundings – the urban heat island effect (Oke, 1982; Arnfield, 2003). A higher proportion of sealed surfaces and reduced plant cover usually means evaporation is lower in cities (Oke et al., 1999; Grimmond et al., 2004), whilst the amount of energy that can be stored in the thermal mass of buildings and anthropogenic materials becomes a major component of the energy balance (Grimmond and Oke, 1999b; Offerle et al., 2005a; Roberts et al., 2006). Direct input of heat released from

[1] Ward, H.C., Evans, J.G. and Grimmond, C.S.B., 2013a. Multi-season eddy covariance observations of energy, water and carbon fluxes over a suburban area in Swindon, UK. Atmos. Chem. Phys., 13(9): 4645-4666.

human activities can also be significant, especially during winter months or in cool climates (Ichinose et al., 1999; Bergeron and Strachan, 2010) or in regions of very high population density (Hamilton et al., 2009). The energy balance for urban areas is thus modified from the rural case (Oke, 1987):

$$Q^* + Q_F = Q_H + Q_E + \Delta Q_S, \quad (4\text{-}1)$$

where Q^* is the net all-wave radiation, Q_F the anthropogenic heat flux, Q_H the turbulent sensible heat flux, Q_E the latent heat flux and ΔQ_S the net storage heat flux. In addition to anthropogenic heat, there are emissions of CO_2 (and other gases) as a result of human metabolism and fuel combustion for transport or other energy use. High emission rates coupled with modification of the wind field by buildings and recirculation of trapped air within street canyons, means air quality can be a major health risk in cities (Mayer, 1999). It is clearly vital to understand the impacts of urbanisation on the environment.

Suburban areas represent a significant, and increasing, proportion of the land surface worldwide. In the UK, urban areas cover 14.4% of the land surface (Home, 2009); most of this is made up of suburbs housing around 80% of the country's population (Gwilliam et al., 1998). The results presented here are the first suburban measurements of energy, water and carbon fluxes in the UK. Previous urban flux campaigns in the UK have taken place in city centres, with work in central London (Helfter et al., 2011; Kotthaus and Grimmond, 2012) and Edinburgh (Nemitz et al., 2002). Annual total emissions of CO_2 for both London and Edinburgh are around 10 kg C m^{-2} y^{-1}, considerably larger than the emissions from other studied cities around the world (Helfter et al., 2011; Järvi et al., 2012).

Other highly urbanised city campaigns (of various durations) have included Mexico City (Oke et al., 1999), Marseille (Grimmond et al., 2004), Tokyo (Moriwaki and Kanda, 2004) and Łódź (Offerle et al., 2005a). Energy balance measurements over lower density sites include the following: winter to spring in Vancouver (Grimmond, 1992); winter to autumn (nine months) in Helsinki (Vesala et al., 2008); the dry season in Ouagadougou (Offerle et al., 2005b); and summertime in Miami (Newton et al., 2007), Tucson, Sacramento, Chicago and Los Angeles (Grimmond and Oke, 1995). The least built-up sites documented in the urban literature include a highly vegetated neighbourhood in Baltimore (Crawford et al., 2011) and a recently developed low density residential area in Kansas City (Balogun et al., 2009). Despite the increase in field studies in recent years, there is still demand for multi-seasonal flux datasets covering the diverse range of urban landscapes (Grimmond et al., 2010b).

There are a few comparisons between multiple areas within the same city. As part of the BUBBLE project, three rural, three urban and one suburban site in Basel, Switzerland were monitored simultaneously for one month in the summer of 2002 (Christen and Vogt, 2004). Offerle et al. (2006) present data from rural, suburban residential, dense urban and industrial areas in Łódź. Four sites of increasing housing density are compared in Melbourne (Coutts et al., 2007b). Weber and Kordowski (2010) compare one year of data for urban residential and suburban (residential bordering parkland) zones in Essen, Germany; and three sites along a rural-urban transect are contrasted during winter in Montreal (Bergeron and Strachan, 2010).

The objective of this paper is to investigate the temporal variability of energy, water and carbon exchange of a typical suburban area within the UK (Section 4.2) using local-scale (10^2-10^4 m) eddy covariance (EC) measurements (Section 4.3). Attention is given to the representativeness of the 12 month study period (Section 4.4) and the role of variability in surface cover on flux measurements (Section 4.5.4). Temporal changes in the observed fluxes are examined and related to the physical processes which govern surface-atmosphere exchange (Section 4.5). In particular the influences of water availability, vegetation and anthropogenic activities are considered. Estimation of the surface conductances under different conditions offers empirical data for comparison with models or model development (Section 4.5.2).

4.2 Site description

The study was conducted within the town of Swindon, 120 km west of London (Figure 4-1), in a residential area very typical of UK suburbia. Swindon has a population of 175,000 and in recent years has been one of the fastest growing towns in Europe. High population density in southern England puts pressure on water supplies and creates demand for land to build on: it is estimated that 10% of new homes built in the UK in 2007 are situated in areas at risk of flooding (Home, 2009). Swindon has previously experienced problems with both flooding and drought.

An eddy covariance mast was installed in a residential garden located approximately 3 km north of Swindon town centre (51°35'4.6" N, 1°47'53.2" W). The area has some institutional buildings (schools) and light commercial buildings (small supermarkets, local shops) along the main road that runs about 150 m south of the mast (Figure 4-1). Southwest of the mast is the area with the largest proportion of built and impervious surface cover and least vegetation (Figure 4-2). However, the study area as a whole has significant vegetation cover (vegetated plan area fraction, λ_V = 0.44 within a 500 m radius of the mast (Table 4-1)), comprising mainly

gardens, some open space (playing fields, parks, intentionally undeveloped green corridors) and verges alongside roads. A large nature reserve lies 0.75-1 km to the northeast.

The trees and shrub, which constitute 9% of the total area (500 m radius), are within gardens, bordering open green spaces, in green corridors and along roadsides (Figure 4-1). The average tree height is around 6 m (defining trees as vegetation > 3.5 m). Species are predominantly deciduous rather than evergreen. The tree canopy is very apparent when looking across the study area and changes in leaf area dominate seasonal variation in the appearance of the landscape. Directly northeast of the mast the properties have relatively large gardens with a large proportion of mature trees (Figure 4-1).

Buildings are mostly 1-2 storeys, with more single storey housing to the north of the mast and a few three storey blocks of flats to the south. The population density is around 4700 inh km^{-2} in this area of Swindon[1]. The average building height is 4.5 m and the proportion of built area, λ_B, is 0.16. The style, density and arrangement of housing vary between neighbourhoods (Figure 4-1) but are typical of today's UK suburban areas. Many houses are packed into the available space with compact new-build homes constructed between older developments. Most houses have small gardens which usually include some paved (or otherwise) impervious area (patios, driveways). The total impervious land cover fraction, λ_I, is 0.33, with almost half attributable each to roads and impervious surfaces within gardens (Table 4-1).

From the mean obstacle height, the displacement height, z_d, is estimated to be 3.5 m and the roughness length for momentum, z_0, to be 0.5 m. Using z_d = 3.5 m, anemometrically-derived z_0 ranges between 0.25 m and 2.00 m for different wind directions, with the larger values attributed to the effect of nearby buildings. Similar variability has been observed at other sites (Grimmond et al., 1998; Pawlak et al., 2010; Nordbo et al., 2013) and z_d will also vary to some extent. The literature suggests a realistic range of z_0 for this site may be about 0.3-1.0 m (Grimmond and Oke, 1999a). The value of 0.5 m is adopted here.

The footprint model of Hsieh et al. (2000) was used to determine the probable source area of the turbulent fluxes. During stable conditions the measurement footprint can extend over many hundreds of metres; under unstable conditions it is much closer to the mast. For the majority (89%) of the data (ζ < 0.1, i.e. unstable to just-stable conditions) the peak contribution to the measured flux is predicted to come from within 100 m of the mast and 80% of the source area lies within 700 m (using z_0 = 0.5 m and z_d = 3.5 m). Although the land cover fractions will vary for different flux footprints, even within the same wind sector, there are

[1] http://www.ons.gov.uk, last access: 21 September 2011

clear differences between the higher vegetation fraction (to the northeast) and more built-up areas (to the southwest).

The land cover classification was based mainly on a geodatabase (OS MasterMap 2010 © Crown Copyright), with a spatial resolution of 1 m, in combination with lidar data (2007, ©Infoterra Ltd) and aerial photography (2009, ©GeoPerspectives). To determine the locations of trees not specifically classified by the database, vegetated areas with an obstacle height greater than 3.5 m were defined as trees. For the wind sector 120-150° a large proportion of vegetation is shown in Figure 4-2, which is partly attributable to the corner of the large grassed area in this sector (Figure 4-1b) that has since been built on (under development in Figure 4-1a). Hence the land cover fractions for 120-150° are least representative of the current land cover and overestimate the contribution from vegetation. Aside from this change, the classification scheme and aerial photograph are judged to be good representations of the surface cover during the measurement period (based on observations when visiting the site). To establish the composition of gardens (classified only as multiple surfaces by the database), 96 randomly selected gardens were subdivided into different surface cover types by visual inspection of aerial photography. Then the average surface cover percentages obtained were used to apportion the area of 'garden' into grass, trees, paved, bare soil, etc. Although significant variation was seen between gardens, the sample was judged to be sufficiently large for clear trends to emerge (running means approached constant values) and consistent results were obtained for the identification of trees using lidar data.

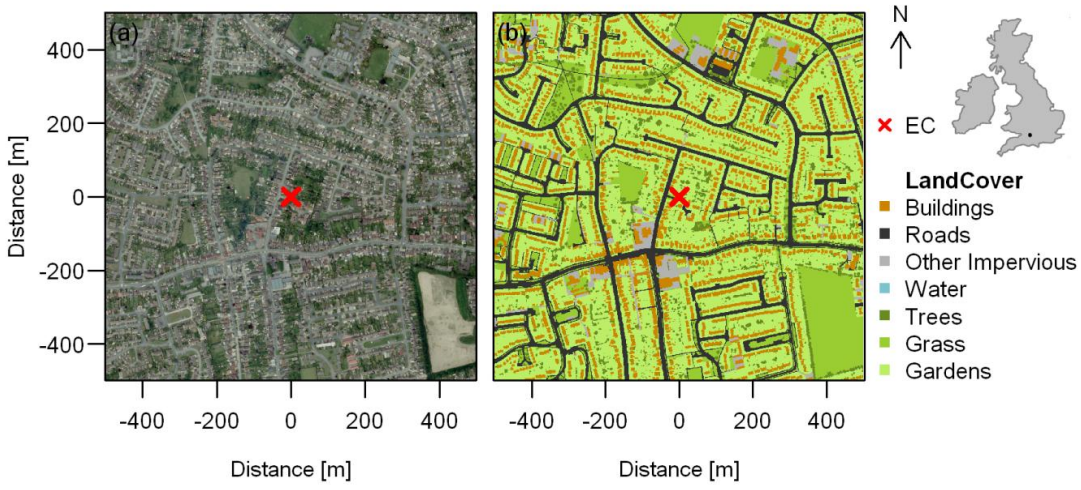

Figure 4-1 (a) Aerial photograph (2009, ©GeoPerspectives) and (b) land cover map for ± 500 m around the flux mast (EC). The large area southeast of the mast classified as grass in (b) has since been built on (it can be seen undergoing development in (a)). The location of Swindon within the British Isles is shown (top right).

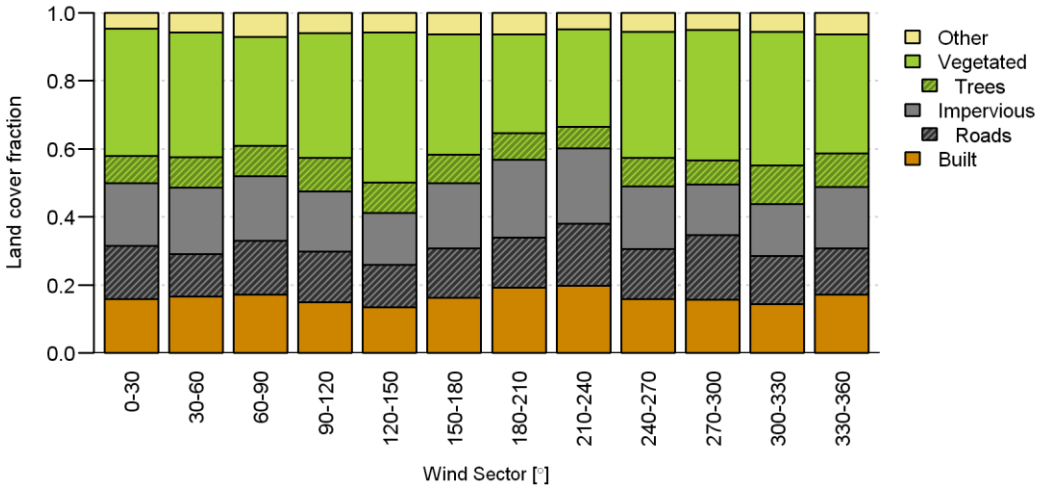

Figure 4-2 Land cover fractions for 30° wind sectors within a radius of 500 m around the flux mast.

Land cover type	Area fraction
Buildings	0.16
Impervious	0.33
- roads	0.15
- within gardens	0.15
Vegetation	0.44
- grass	0.36
- trees	0.09
Water	0.00
Pervious (bare soil, gravel)	0.06

Table 4-1 Land cover within a radius of 500 m around the flux mast. Land cover not classified by these classes comprised less than 0.5% of the total area. 'Trees' includes all vegetation not classified as grass (i.e. includes hedges, shrubs, small bushes).

4.3 Instrumental setup, data collection and data processing

Eddy covariance measurements were made on a pneumatic mast at 12.5 m above ground level (108 m above sea level), providing a measurement height, z_m, of 2-3 times the height of the roughness elements. Fast-response temperature and wind measurements from a sonic anemometer (R3, Gill Instruments, Lymington, UK) combined with water vapour and carbon dioxide from an open-path infrared gas analyser (IRGA) (LI-7500, LI-COR Biosciences, Lincoln, USA) yield turbulent sensible and latent heat fluxes and the carbon flux (F_C). On the same mast a four-component radiometer (NR01, Hukseflux Thermal Sensors, Delft, The Netherlands), at a height of 10.1 m, provides incoming and outgoing longwave ($L_{\downarrow}$ and $L_{\uparrow}$) and shortwave ($K_{\downarrow}$ and $K_{\uparrow}$) radiation and net all-wave radiation. Additional meteorological data are supplied by an automatic weather station (WXT510, Vaisala, Finland) at 10.6 m, also on the same mast. The field of view of the downward-facing radiation sensors encompasses a range of surfaces: gardens, roads, pavements, grass verges, hedges and small trees, bare soil, gravel, roofs of

garages, small sheds and single-storey extensions and brick and painted walls. Following Schmid et al. (1991), 95% of the radiometer source area is calculated to lie within a radius of 44 m from the mast. At the same site, there is a tipping bucket rain gauge (0.2 mm tip, Casella CEL, Bedford, UK) and a digital camera (CC5MPX, Campbell Scientific Ltd., Loughborough, UK) which provides a visual indication of conditions within the garden (changing phenology, snow cover). Soil moisture (CS616, Campbell Scientific Ltd.) and soil temperature (model 107, Campbell Scientific Ltd) sensors were installed around the base of the mast, measuring different surfaces within the garden. Soils are mainly clayey loams with some sandier areas. A wetness sensor (model 237, Campbell Scientific Ltd.) positioned in a nearby flowerbed provides an indication of whether the surface is wet or dry. Soil heat flux plates (HFP01, Hukseflux) were installed within the garden; data used here (Q_G) are from sandy soil at a depth of 0.03 m. No adjustment was made for heat storage in the soil layer above the plate.

The raw flux data were logged at 20 Hz (CR3000, Campbell Scientific Ltd.) and post-processed to 30 min statistics. Meteorological data are available at a resolution of 1 min (CR1000, Campbell Scientific Ltd.), although 30 min block averages are presented here to match the eddy covariance output. Data transfer via a wireless router (Sierra Raven XE, Sierra Wireless, USA) enables daily collection and real-time monitoring of instrumentation. Flux data were processed using EddyPro Advanced (v3.0.0beta, LI-COR) following standard procedures, including despiking of raw data, correction for angle of attack, time-lag compensation by seeking maximum covariance, double co-ordinate rotation, correction of sonic temperature for humidity, high and low frequency spectral corrections (Moncrieff et al., 1997) and the density corrections of Webb et al. (1980). No adjustment was made to account for instrument surface heating of the open-path IRGA, however the relatively mild UK climate means this effect is not expected to be significant (Thomas et al., 2011). Subsequent quality control programs written in R (The R Foundation for Statistical Computing) exclude data collected at times of instrument malfunction and/or bad diagnostic values (LI-7500 output), when rain or moisture could adversely affect readings (particularly from the IRGA), and if data fell outside physically reasonable thresholds.

Data are analysed from installation on 9 May 2011 to 30 April 2012 (so May 2011 data are not complete). Of the potential 17145 30 min periods, 97 are missing due to power failure. After quality control 96% of Q_H, 74% of Q_E and 73% of F_C data are available for analysis. A significant proportion of IRGA data loss was due to the high frequency of wet instrument windows because of rainfall. No friction velocity screening was used here but u_* values < 0.1 m s^{-1} were observed for less than 4% of the dataset, so the impact on the overall results is likely very small. Data failing the stationarity and developed turbulence tests of Foken and

Wichura (1996) were not excluded from analysis as other studies have shown that the integral turbulence characteristics tests in particular may be too restrictive for urban areas (Fortuniak et al., 2013). This decision has a small effect on the fluxes: the magnitude of Q_H and Q_E monthly means would be increased by 0-3 W m^{-2} if these values were excluded. The biggest impact is on the friction velocity: the distribution is shifted to larger values (mean increases by 0.03 m s^{-1}), more so at night (mean increases by 0.05 m s^{-1}).

In the urban environment, the available energy can be supplemented by heat released from anthropogenic activities, such as building heating, traffic and human metabolism. Although difficult to measure directly, the anthropogenic heat flux can be estimated using statistical information and inventories relevant to the study area (Sailor and Lu, 2004; Bergeron and Strachan, 2010). The release of CO_2 from the associated combustion processes can also be estimated via the same method. Details of the methodology used for Swindon are given in Section 4.7.

Given the complexities of direct measurements of the storage heat flux (Offerle et al., 2005a; Roberts et al., 2006) two alternative methods are used here: ΔQ_S is estimated using the objective hysteresis model (OHM) of Grimmond et al. (1991), see Section 4.8; and the residual term (RES = $(Q^* + Q_F) - (Q_H + Q_E)$) is calculated. Using RES as an estimate of the storage flux assumes closure of the energy balance at the time interval of estimation and collects all the errors in the other terms. The lack of energy balance closure in other environments is well documented – measurement under-closure of 10-20% is common (Wilson et al., 2002). This has been partially attributed to ignoring heat storage, especially in forests (Leuning et al., 2012), but also to underestimation of Q_H and Q_E by eddy covariance measurements (Wilson et al. 2002, Foken 2008). Thus if RES is used as a proxy for storage it should be taken as an upper limit (Coutts et al., 2007b; Bergeron and Strachan, 2010).

4.4 Meteorological conditions during the study period

Swindon generally experiences warm summers and cool wet winters. Southern England is drier than the UK as a whole – the Met Office normal annual rainfall for central and southeast England (1971-2000) is 780 mm. Recent summers have been wet and cloudy with more favourable weather in spring and/or autumn. The period May 2011 to April 2012 followed this trend. Spring 2011 was warm and sunny with less than a third of normal rainfall (50 mm in March-May compared to the 1971-2000 normal 160 mm (at nearby Met Office station at Lyneham)). Summer 2011 was slightly cooler than normal with rain events occurring as frequent showers rather than intense downpours. Autumn was warm, with a warm and sunny spell from the end of September to early October (Figure 4-3b). Slightly above normal

temperatures continued through winter; with heavy frost in late January and snow in February 2012 (the longest period of snow cover was 2-3 days). February and March were dry with warm sunny weather from the end of March to early April, after which over three times the normal rain fell in Swindon (Figure 4-3f) accompanied by low temperatures (Figure 4-3b), and April 2012 became the wettest on UK records. The diurnal patterns of temperature, vapour pressure deficit (VPD) and wind speed were typical, with the highest values in the middle of the day and the expected inverse in relative humidity (RH) (data not shown). The prevailing wind is from the southwest quadrant (59% of all data, Figure 4-3e) and the next most common wind directions are from the northeast (16%) and northwest (15%).

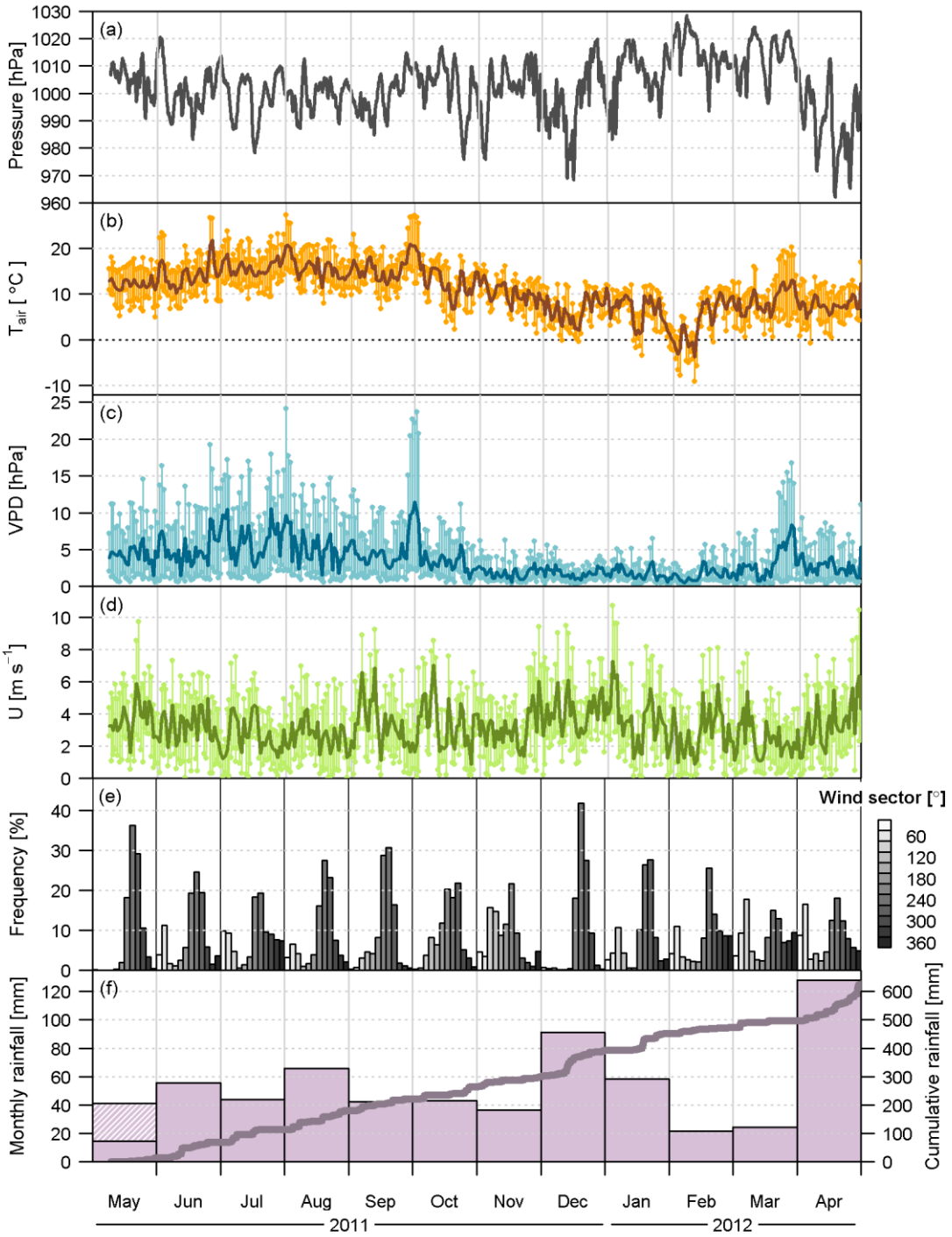

Figure 4-3 Meteorological conditions during the study period: (a) mean station pressure; daily mean, maximum and minimum (b) air temperature, (c) vapour pressure deficit (VPD), (d) wind speed; (e) frequency distribution of 30 min wind direction by month; (f) cumulative and monthly rainfall totals. In (f) the hatched bar represents rainfall during May 2011 before the start of this dataset (measured in central Swindon (51°34'0.3" N, 1°47'5.3" W)).

4.5 Results and discussion

4.5.1 Energy balance

The net all-wave radiation provides energy to the surface that can be transformed into turbulent sensible or latent heat, or stored in the urban fabric. For the data collected here, ΔQ_S constitutes 19% of daily Q^*, whilst Q_H constitutes 45% and Q_E 34% in June 2011. The coloured bars in Figure 4-4 represent monthly averages calculated using all available data, whereas the unfilled bars indicate times when data for all energy fluxes are available concurrently. The main restriction is the availability of Q_E so this flux does not change, but average Q^* and Q_H both increase if the averages are calculated for times when all energy fluxes are available, i.e. mainly excluding times during and following rainfall when there are no Q_E data. Data availability had the biggest impact in April 2012, when frequent rainfall significantly reduced the number of Q_E data points.

Q^* is the largest flux except for November to January (Figure 4-4), when solar radiative input is at a minimum. The peak in median diurnal Q^* is about 470 W m^{-2} in June compared to 80 W m^{-2} in December (Figure 4-5a). Warmer surfaces create a larger nocturnal Q^* loss in summer than winter. The size of Q_F is small but non-negligible, especially in winter when the demand for central heating of buildings is largest and Q^* smallest (Figure 4-4). Monthly mean values of 6-10 W m^{-2} are smaller than estimates from other city-based UK studies: Q_F is estimated at 16-24 W m^{-2} across Greater London (Allen et al., 2011), with typical mean city centre values of 18-150 W m^{-2} (Hamilton et al., 2009), and at 44 W m^{-2} in Edinburgh during October and November 2000 (Nemitz et al., 2002). However, the Swindon values agree reasonably well with suburban studies elsewhere (Christen and Vogt, 2004; Bergeron and Strachan, 2010).

The contribution from building energy use (Q_B) varies according to season whilst human metabolism (Q_M) and vehicle emissions (Q_V) form a fairly constant contribution to Q_F throughout the year (Figure 4-6). The morning rush-hour peak in Q_V coincides with a peak in domestic energy use as people get up and travel to work. A sharp morning peak in Q_F is produced, whereas later in the day a secondary rise in Q_V and then Q_B leads to a more distributed release of Q_F in the evenings. For the residential site in Swindon, road transport is estimated to be the most important contribution to the anthropogenic heat flux. It is not surprising that this differs from Bergeron and Strachan (2010), who found that Q_B formed the largest contribution to Q_F at both their urban and suburban sites in Montreal, given the colder winters in Canada. As for other studies, the contribution of human metabolism is small

(approximately 5% during daytimes and up to 25% during summer nights – less than 1 W m^{-2} in absolute terms).

Physically, the net storage heat flux is expected to be positive during summer and negative during winter so that annually there is minimal net gain or release of energy by the surface (Grimmond et al., 1991). The soil heat flux (Q_G) is one component of the storage flux measured in this study. It shows the expected behaviour at daily and annual timescales, whereas the residual term (RES) remains positive all year round (Figure 4-4). The residual data are biased to when all observed variables are available and most notably by the absence of data during and immediately following precipitation. It seems unlikely that this is the sole explanation here, although Kawai and Kanda (2010) observed enhanced release of stored energy on rainy days. In the summertime RES behaves like the storage flux, rising rapidly in the morning with Q^* and being of similar magnitude to other studies. The residual has been used as an estimate of storage for several suburban locations in the USA (Grimmond and Oke, 1995; Balogun et al., 2009). In winter, however, RES is considerably larger than ΔQ_S during daytime and less negative at night (Figure 4-5d), resulting in a daily total RES that remains positive in winter in contrast to ΔQ_S and Q_G. The use of OHM to estimate ΔQ_S in Vancouver by Grimmond (1992) also suggested no significant annual gain in energy by the surface and a net release of stored heat over 24 h in winter. However, according to Figure 4-5d, OHM suggests a large release of stored energy during winter which does not appear as outgoing radiation, Q_H or Q_E and so is not physically justified. Whilst the energy balance closure is close to 100% in summer, it is over-closed by about 20% in winter. That ΔQ_S changes sign at similar times to Q_G gives some support to the OHM estimates, but there is also a clear decrease in the magnitude of nocturnal Q_G from summer through to winter which is not replicated by OHM. This is mainly due to the negative a_3 term in the ΔQ_S estimation (see Section 4.8) which seems to be too large during winter, although studies are limited. Clearly there is a need for more winter-based evaluations of OHM (Best and Grimmond, 2013) and for more wintertime field campaigns to improve estimates of ΔQ_S.

Of the turbulent heat fluxes, Q_H is largest in May, whilst Q_E peaks in June along with Q^* (Figure 4-4). During the winter when Q^* is negative so is Q_H, whereas mean daily Q_E remains clearly positive throughout the year. The exception is small negative values of Q_E that are sometimes observed at night (around 15% of all data) when the latent heat flux is directed towards the surface, i.e. dewfall. Generally, Q_E remains close to and slightly above zero during night time (mean 5.7 W m^{-2}, median 3.4 W m^{-2}), as also documented in other suburban studies (Grimmond and Oke, 1995; Balogun et al., 2009). Average night time values are largest during winter, peaking in November-December, and are also quite high in July. However, given the

small size of the signal, the relative uncertainty in these data can be significant: the majority of night time values lie between -15 and 15 W m^{-2}, similar in size to the uncertainty (the larger of 15% of Q_E or 15 W m^{-2}, according to Mauder et al. (2006)).

The diurnal course of the sensible heat flux changes considerably with season, from being large and positive during daytime and small and negative at night (May to August), to remaining below zero (around -25 W m^{-2}) and only reaching positive values for a few hours around midday (December) (Figure 4-5b). Such negative Q_H values are seen when the fraction of built-up area is small, but these observations are rare in the literature. Rather the focus has been either for warm periods or more heavily urbanised areas, where there is a larger anthropogenic energy input and release of energy from storage (Nemitz et al., 2002; Offerle et al., 2005a; Loridan and Grimmond, 2012). Recent results from a suburban site in Oberhausen, Germany show similar wintertime behaviour to that observed in Swindon (Goldbach and Kuttler, 2013), supporting the idea that the sensible heat flux becomes more negative in winter and at night with decreasing building density.

Of particular interest is the changing relation between Q_H and Q_E (i.e. the Bowen ratio, β). In summer, when solar radiation provides energy for warming the atmosphere and evaporation, the turbulent heat fluxes are largest with more energy directed into heating the air than evaporation (June median diurnal peaks at 189 and 121 W m^{-2}, respectively, giving a Bowen ratio of 1.6). Both Q_H and Q_E decrease through autumn into winter, Q_E remains positive and begins to dominate the increasingly negative Q_H so that in autumn and winter more energy is partitioned into Q_E than Q_H and β drops below 1. This demonstrates an important difference in behaviour to the bulk of studies of suburban environments and is discussed in more detail in Section 4.5.2.

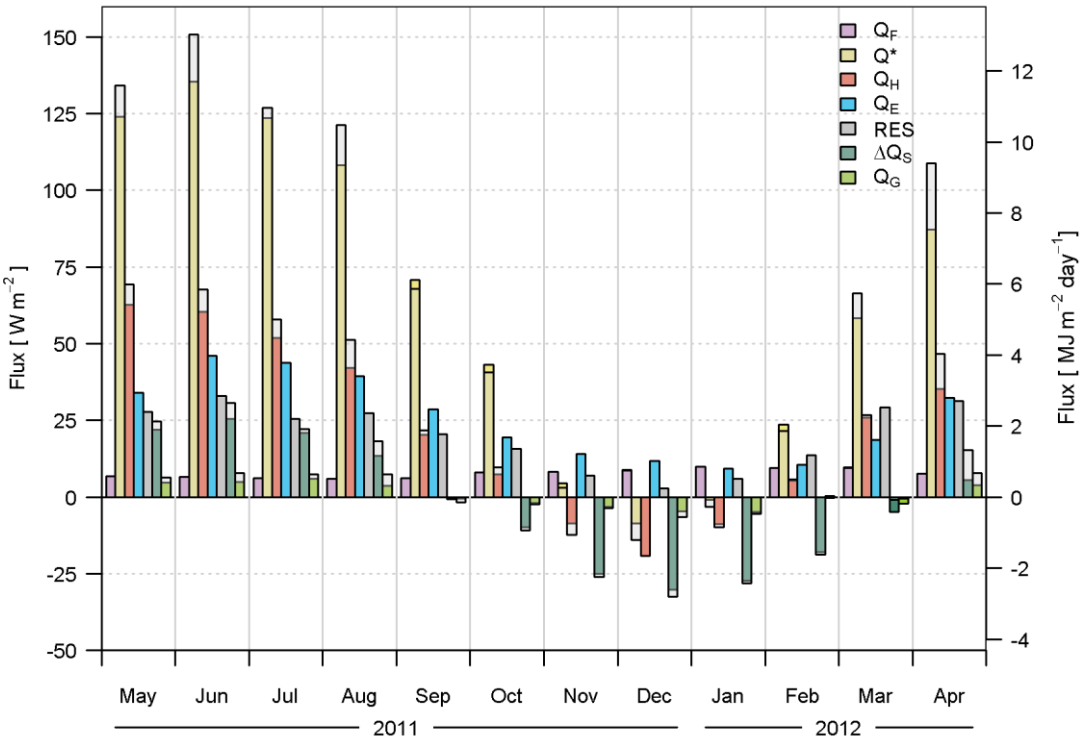

Figure 4-4 Monthly mean fluxes (average of 24 h ensemble median values for each month) for all available data (coloured bars) and for concurrent data only (unfilled bars). RES denotes the residual $(Q^* + Q_F) - (Q_H + Q_E)$.

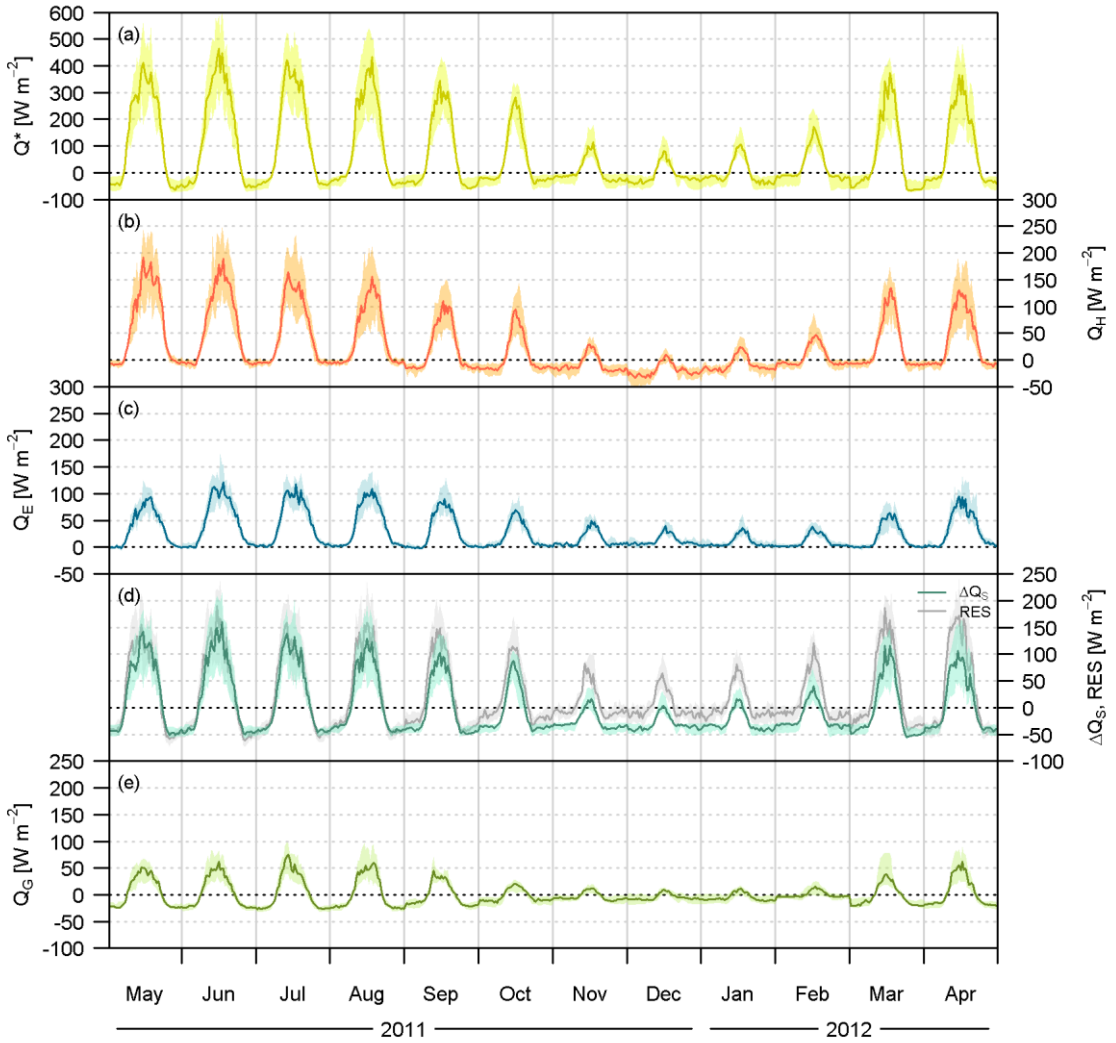

Figure 4-5 Median diurnal cycles (lines) and inter-quartile ranges (shading) of the energy fluxes for the study period.

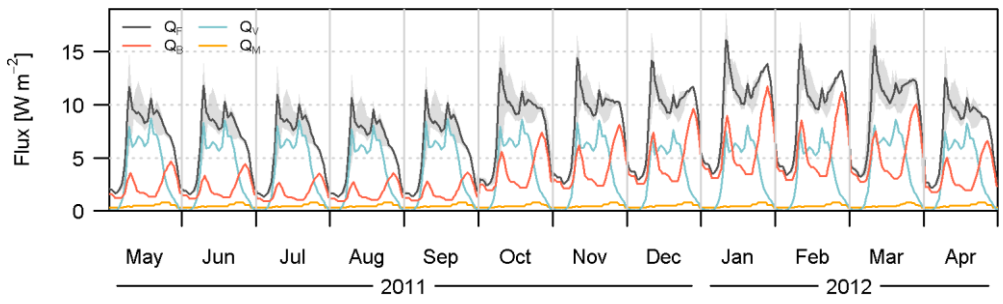

Figure 4-6 Mean diurnal cycles of building energy use (Q_B), vehicle emission (Q_V) and human metabolism (Q_M) contributions to total anthropogenic heat flux (Q_F) for the study period (see Section 4.7 for details). Shading indicates maximum and minimum Q_F values.

4.5.2 Controls on evaporation

For urban areas with similar vegetation fractions, the literature suggests typical midday or daytime Bowen ratios of 1-1.5 (Grimmond and Oke, 1995; Loridan and Grimmond, 2012). This is indeed matched quite well during summer 2011 in Swindon. However, midday (± 2 h) Bowen ratio values range from above 2.0 in spring to close to 0.5 in winter with a minimum of 0.05 in December when Q_H is at a minimum (Figure 4-7a). The range in daytime ($K_{\downarrow}$ > 5 W m^{-2}) Bowen ratios is greater and, as a result of the negative sensible heat flux except during the middle of the day, β is negative November-January, dropping to -0.6 in December. Nocturnal Bowen ratios are lower and more variable but follow a similar monthly pattern to the daytime values. They are often negative because Q_H < 0 W m^{-2}.

Rainfall was frequent in the second half of 2011 (Section 4.4). The longest dry periods were in mid-May 2011, following a very dry spring, and the end of March 2012. The highest midday Bowen ratios occurred during the driest conditions (May 2011, end of July and mid-October 2011, March 2012, Figure 4-7a) with frequent individual 30 min β values > 4. Figure 4-7b shows spring 2012 in more detail. February 2012 was drier than normal and in March less than one third of the average rainfall was recorded (Section 4.4). The Bowen ratio is seen to respond to the availability of water on a daily timescale, ramping up from < 1 following rainfall to > 4 as the surface dries out. Although the wind direction changes during this period, expected trends with vegetation fraction seem to be overridden by the limited availability of water – i.e. water supply is more important than surface cover in this case. After heavy rain on 3 April, median daytime β is mostly between 0 and 2 for the rest of the month, with a decreasing trend overall as extended rains provide abundant surface water and replenish soil moisture (not shown). Although not shown here, the remainder of 2012 was very wet and soil moisture remained high in contrast to 2011. As a result, observed Bowen ratios were lower during summer 2012 than 2011 (closer to 1 than 1.5).

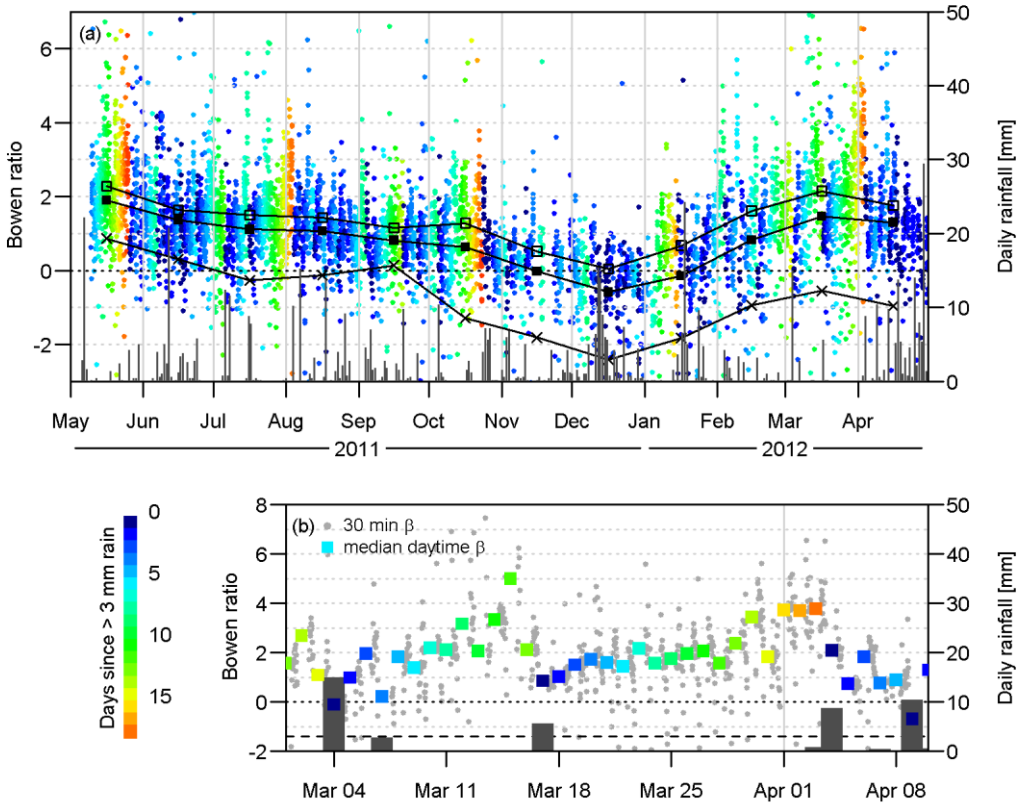

Figure 4-7 Daytime ($K_{\downarrow}$ > 5 W m^{-2}) Bowen ratio (30 min) coloured by number of days since rainfall (exceeding 3 mm) for (a) the study period and (b) spring 2012. Daily rainfall (bars) corresponds to the right-hand axes. In (a) monthly median midday (± 2 h) (open squares), monthly median daytime (solid squares) and monthly median night time (Q^* < 0 and $K_{\downarrow}$ ≤ 5 W m^{-2}) (crosses) Bowen ratios are plotted midmonth. In (b) the median daytime Bowen ratios for each day are shown (coloured squares).

Observed Q_E can be compared to the equilibrium evaporation, Q_{Eq} (Slatyer and McIlroy, 1961) for urban areas:

$$Q_{Eq} = \frac{s}{s+\gamma}(Q^* + Q_F - \Delta Q_S), \qquad (4\text{-}2)$$

where s is the slope of the saturation vapour pressure-temperature curve and γ is the psychrometric constant. Q_{Eq} is the energy limited but water unlimited evaporation rate for the ambient conditions. Note that since the ΔQ_S term is calculated here using OHM, it is also a function of Q^*. If instead the residual is used then the bracketed term reduces to the sum of the turbulent fluxes (Q_H + Q_E). The ratio Q_E/Q_{Eq} is the Priestley-Taylor aridity parameter (α_{PT}). For saturated surfaces (abundant moisture) α_{PT} = 1.26 and represents potential evaporation (Priestley and Taylor, 1972). Urban values of α_{PT} are considerably lower, e.g. 0.51 in humid Miami (Newton et al., 2007) and between 0.5 for well-irrigated suburban areas (Sacramento, California; Chicago, Illinois) and 0.1 for unusually dry conditions in Vancouver, Canada during an irrigation ban (Grimmond and Oke, 1999c). For Swindon in March-April 2012, α_{PT} = 0.52.

The low rainfall in early spring and increasingly dry conditions resulted in a marked reduction in α_{PT}, from 0.56 at 12 hours after rainfall to 0.28 during the longest dry period 10-16 days after rain (Figure 4-8). Despite the uncertainties in the energy balance terms, in particular ΔQ_S, the observed trend remains when the available energy is increased or decreased (adjusting ΔQ_S by ± 10% spreads the α_{PT} values by ±0.03). For this period, Q_E demonstrates a clear and strong response to surface moisture availability, even with source areas sometimes from the more treed sectors.

The measured suburban evaporation is well below the equilibrium value, implying that there is some control due to limited water supply even a few hours after rainfall (e.g. α_{PT} = 0.76 for 2-12 h, Figure 4-8). This conforms to expectations given the enhanced proportion of impervious surfaces, smaller vegetation fraction and reduced water storage compared to most natural environments. However, directly following rainfall, measured Q_E is significantly greater than Q_{Eq} (points > 1:1 line in Figure 4-8). For these instances Q_E is larger than would be expected given the available energy and likely represents rapid evaporation from rainfall that has either been intercepted by vegetation or buildings, or reached impervious road surfaces, that may be enhanced by micro-scale advection. Particularly if a warm, dry, impervious surface is suddenly wetted, energy is primarily directed into evaporation and Q_E can exceed Q^* via a negative Q_H as heat is supplied from the surroundings. For example, following a rain shower at 1200 UTC on 5 June 2011, β dropped from around 1.5 to -0.5 and Q_H remained negative throughout the afternoon (between -32 and -1 W m^{-2}). These sudden large water vapour fluxes are an important part of the urban water budget but are problematic to measure with open-path gas analysers (as instrument windows may remain wet for as long as the urban surface) and difficult to quantify through simple models.

There is also a considerable proportion of night time data when $Q_E > Q_{Eq}$ with small positive or negative values even when water is limited (i.e. many days after rain). This may result from inaccuracies in the night time storage heat flux. Uncertainties are likely to be small for Q^* (< 5%, e.g. Blonquist Jr et al. (2009)) but appreciable for observed Q_E (Section 4.5.1) and at these times α_{PT} is the ratio of two small numbers. Note, however, that exclusion of the night time data does not significantly change the regression slopes.

Despite clear trends in Figure 4-8, there is considerable scatter. Crudely accounting for a measure of water availability and applying this available energy-based estimation captures some of the trends in Q_E, but it does not accurately represent its variability. Also in Figure 4-9a, the lack of a diurnal trend in α_{PT} suggests a significant dependence on the energy available and supports the suggestion that the general model of Q_E responding to $Q^* + Q_F - \Delta Q_S$ is well-replicated across the daily timescale. Other relevant controls depend on the

timescale of interest, e.g. water availability through soil moisture usually changes over days to weeks whereas radiative forcing can change over minutes when cloud cover is patchy. The peaks in α_{PT} towards the end of the day result from Q_{Eq} values passing through zero and there is considerable variability associated with small fluxes at transition times and at night. After the very dry start to April 2012, the month as a whole was very wet (Section 4.4) and produces a relatively large value of α_{PT} (0.6-0.7) (Figure 4-9a). Evaporation was closest to equilibrium rates in November-December 2011, when there was fairly frequent, sometimes heavy rain and minimum solar energy input so that surfaces remained wet for much of the time. Due to the increased difficulties of estimating ΔQ_S at this time we suspect that the 'true' α_{PT} may be larger than shown here.

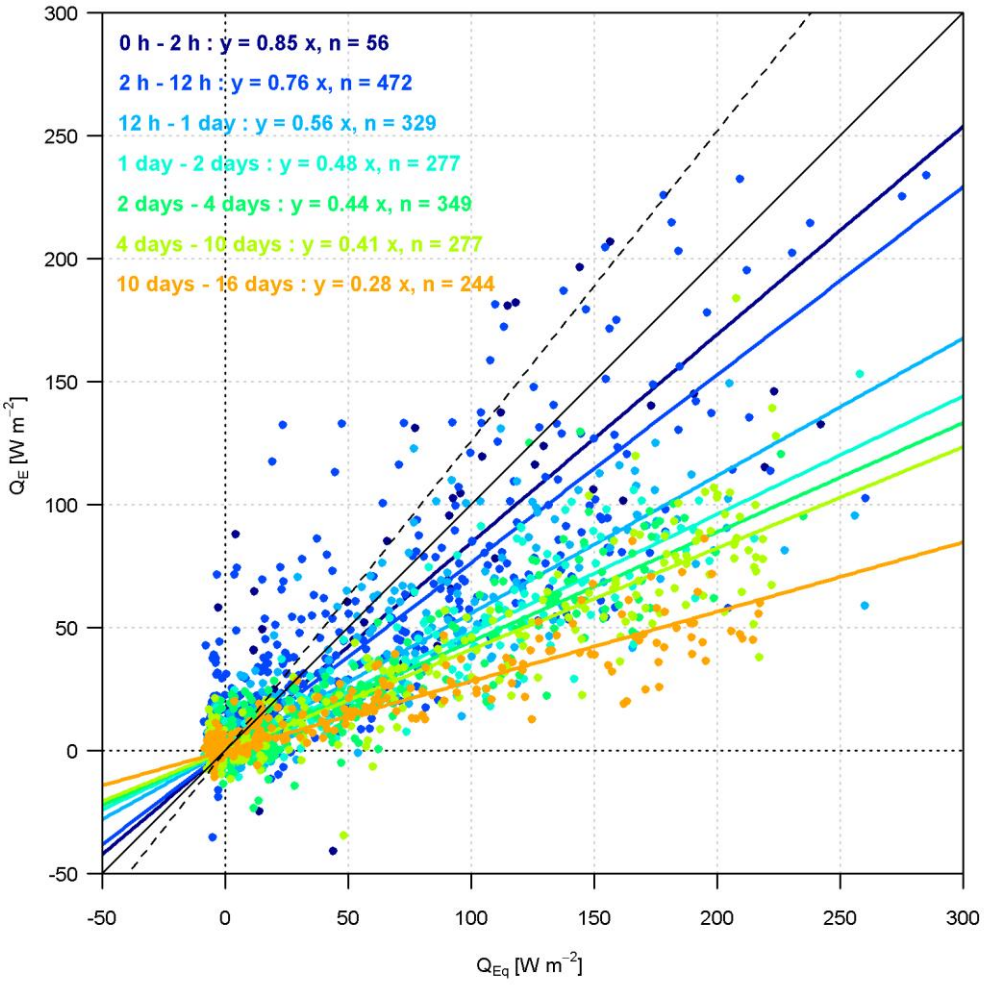

Figure 4-8 Measured evaporation (30 min) against equilibrium evaporation for contrasting water availability in March and April 2012, coloured according to time since rainfall. The slopes give the value of α_{PT}: 1.26, i.e. potential evaporation (dashed line), 1.00 (solid black line) and decreasing α_{PT} with increasing time since rain (coloured, inset).

The seasonal variability of Q_E in relation to the available energy (α_{PT}) differs from the relation to Q_H (β). The Bowen ratio has a clear diurnal cycle throughout the year (Figure 4-9b) and, again, night time results are highly variable being the ratio of small numbers (with appreciable uncertainties: the uncertainty on Q_H being the larger of 10% or 10 W m^{-2} (Mauder et al., 2006)). Negative β values for much of winter daytime reflects the tendency for Q_H < 0 W m^{-2} (Figure 4-5) and prevailing stable or near-neutral conditions. The small values of the stability parameter, ζ =(z_m - z_d)/L_{Ob} (L_{Ob} is the Obukhov length), even during spring and summer, appear perhaps surprising at first (Figure 4-9c). However, they are consistent with other studies (Weber and Kordowski, 2010) and are likely further suppressed by the wet conditions for this dataset; outside summer, dry March 2012 was fairly unstable. A combination of lower suburban Q_H than city centres (less heavily urbanised, more vegetation) but often similar displacement heights, means that suburban ζ can be low compared to both more urbanised and rural sites. This is exemplified by three sites along an urbanisation gradient in Montreal, Canada (Bergeron and Strachan, 2010).

The Penman-Monteith equation allows the calculation of the latent heat flux by incorporating the resistance of the surface (Monteith, 1965) and can therefore be applied in cases where water is not freely available. Grimmond and Oke (1991) modified the equation for urban areas:

$$Q_{E\_PM} = \frac{s(Q^* + Q_F - \Delta Q_S) + \rho c_p VPD / r_a}{s + \gamma(1 + r_s / r_a)}, \qquad (4\text{-}3)$$

where ρ is the density of air, c_p the specific heat capacity of air, VPD the vapour pressure deficit, r_a the aerodynamic resistance and r_s the surface resistance. The aerodynamic resistance in Equation 4-3 should be that for heat and water vapour (assumed equal) and can be calculated via (Grimmond and Oke, 1991)

$$r_a = \frac{\left[\ln\left(\frac{z_m - z_d}{z_{0m}}\right) - \psi_m\right]\left[\ln\left(\frac{z_m - z_d}{z_{0v}}\right) - \psi_v\right]}{\kappa_v^{\,2} U} = \frac{\left[\ln\left(\frac{z_m - z_d}{z_{0v}}\right) - \psi_v\right]}{\kappa_v u_*}, \qquad (4\text{-}4)$$

where κ_v is von Kármán's constant (0.4), U the horizontal wind speed, u_* the friction velocity and Ψ are stability functions for momentum (subscript *m*) or heat and water vapour (subscript *v*) (van Ulden and Holtslag, 1985; Högström, 1988). Here, the right-hand form of Equation 4-4 is used with the EC measured u_*. Following Järvi et al. (2011), the roughness length for water vapour was estimated using (Brutsaert, 1982),

$$z_{0v} = z_{0m} \exp\left[2 - a\left(\frac{u_* z_{0m}}{\nu}\right)^{0.25}\right], \quad (4\text{-}5)$$

where ν is the molecular viscosity of air, with the surface-dependent coefficient calculated using the parameterisation suggested by Kawai et al. (2009) for vegetated cities,

$$a = (1.2 - 0.9\lambda_V^{\,0.29}). \quad (4\text{-}6)$$

Aerodynamic resistances describe the impedance of scalars (momentum, heat, water vapour) to transfer by turbulence. Maximum r_a occurs when conditions are calm and mechanical turbulence is weak (wind speeds close to zero). Calculating r_a from Equation 4-4, enables the surface resistance to be estimated from observed Q_E and β (Monteith, 1965):

$$r_s = \left(\frac{s}{\gamma}\beta - 1\right) r_a + \frac{\rho c_p VPD}{\gamma Q_E}. \quad (4\text{-}7)$$

The resulting r_s values are effectively a measurement of the surface resistance obtained by inversion of Equation 4-3. For wet surfaces r_s approaches zero and Q_E is determined by the energy available. For dry conditions r_s comprises the mix of surface controls affecting Q_E and is a complex function of meteorological conditions and surface characteristics (e.g. incoming radiation, air temperature, humidity, wind speed, soil moisture, leaf area index (Järvi et al., 2011)), analogous to the bulk canopy resistance in forests made up of leaf stomatal resistance and contributions from the understory. Since r_s encompasses the range of controls determining the transport of water vapour between the surface and atmosphere, it would be highly desirable to be able to correctly parameterise this variable. Resistance can also be expressed as its reciprocal the surface conductance, $g_s = r_s^{-1}$.

Patterns in r_s are not always followed by those in r_a, indicating that the surface resistance cannot be explained by aerodynamic controls alone. The aerodynamic resistance shows remarkably little variability during daytime and all months exhibit a clear diurnal cycle of minimum resistance in the middle of the day (Figure 4-9e). Except during winter the daily cycle is smooth and fairly symmetrical. In contrast, the diurnal cycle of g_s is highly asymmetrical: surface conductance is usually highest in the morning and then reduces through the afternoon until close to zero at night (Figure 4-9f), which emerges from the combined shape of Q_E/VPD on a daily timescale. Night time conductances are significantly larger during winter than other seasons (around 3 mm s^{-1} compared to almost zero) when the surface often remains wet, the anthropogenic energy input is greatest and nocturnal wind speeds are high (Figure 4-9d). Uncertainty in the roughness length for momentum has a sizable effect on r_a but the impact on

g_s is small: increasing z_{0m} by 0.5 m increases the median value of r_a by 1.8 s m^{-1} and the average difference is 6%; the median value of g_s is unchanged and the average difference is 2%.

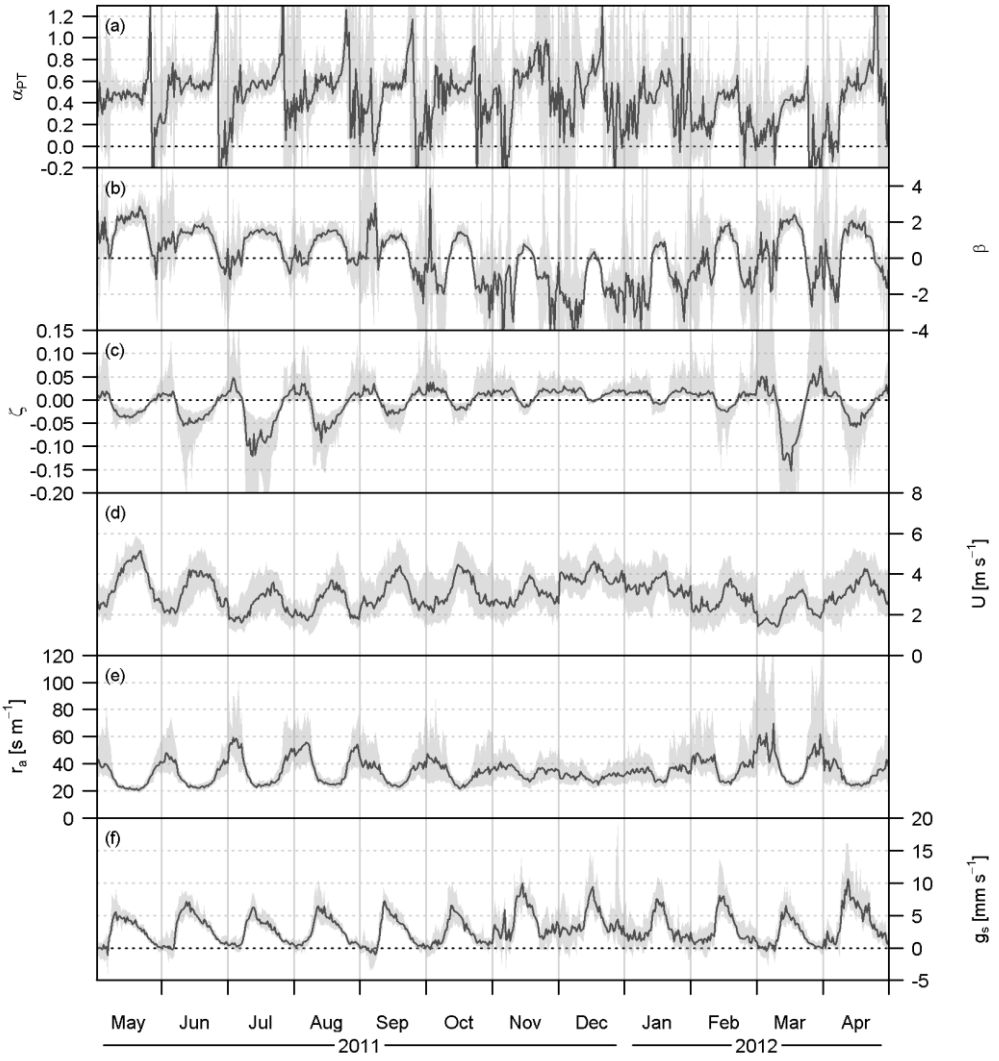

Figure 4-9 Monthly median diurnal cycles (lines) and inter-quartile ranges (shading) of (a) the aridity parameter, α_{PT}; (b) Bowen ratio, β; (c) stability parameter, ζ; (d) wind speed, U; (e) aerodynamic resistance, r_a; and (f) surface conductance, g_s, for all conditions. See text for methods.

During morning hours, the behaviour of g_s differs for days with and without dewfall (days with dew were identified by the surface wetness sensor and IRGA diagnostics, Figure 4-10). Negative Q_E during night times with dew results in negative surface conductances. Whilst Q_E measurements are scarce when heavy dew settles on and is evaporated from the IRGA windows, the data remaining after quality control (i.e. when moisture is not present on the instrument windows but likely remains over the surroundings) indicate larger surface conductances in the early morning compared to days with little or no dewfall. By the afternoon, the course of g_s is similar for dew and non-dew days. Note that irrigation of gardens

in Swindon is expected to be minimal, particularly overnight, unlike in many of the North American studies.

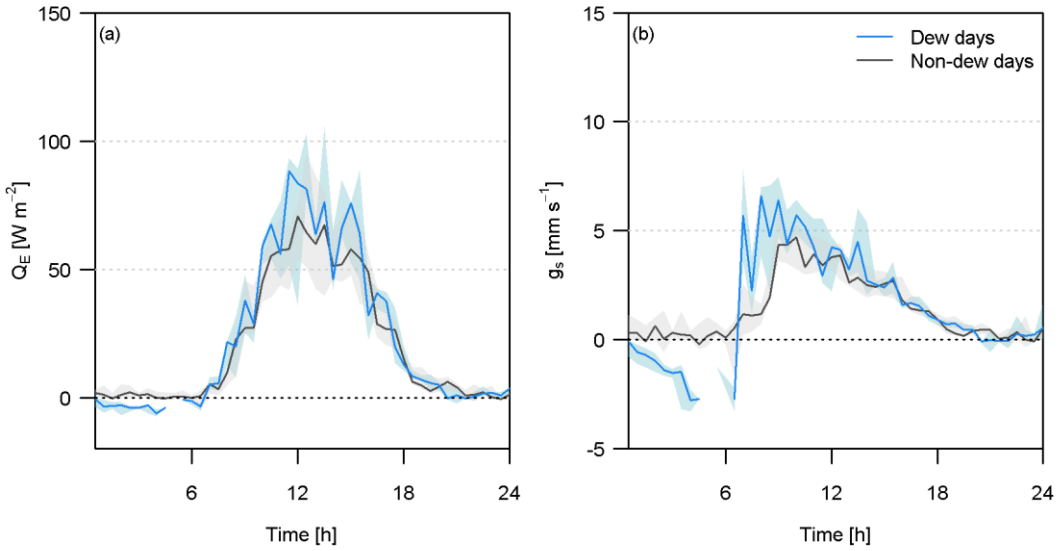

Figure 4-10 Median diurnal cycles (lines) and inter-quartile ranges (shading) of (a) latent heat flux and (b) surface conductance for selected days with heavy dewfall (23-26, 30 March 2012) and little or no dewfall (22, 27-29, 31 March 2012, 1-2 April 2012). Values of g_s > 40 mm s^{-1} or g_s < -10 mm s^{-1} have been excluded.

The dataset is divided into broad categories by season (summer (MJJA), autumn (SON), winter (DJF) and spring (MA)) and approximate wetness regimes (wet (1 to 6 h after rain), partially wet (6 h to 2 days after rain) and dry (≥ 2days since rain)). The largest Q_E values occur in spring and summer (Figure 4-11a) when the leaf area index increases, vegetation actively transpires and solar radiation is large (Section 4.5.1). Potential evaporation rates are rarely reached during the day, even for wet conditions, although by selecting data between 1 and 6 hours after rain some of the highest evaporation rates immediately following rainfall have been excluded (these can be highly variable and confuse underlying trends). The wintertime potential evaporation is thought to be over-estimated in Figure 4-11a due to the limitations of the OHM estimation of ΔQ_S. For all seasons there is an appreciable difference between wet and dry conditions, with the most marked contrast in spring 2012 when rainfall patterns were extreme (Section 4.4).

Differences in synoptic conditions, particularly cloud cover and Q^*, lead to differences in the potential evaporation rates between wetness subsets: daily potential evaporation is larger for dry conditions than wet conditions, yet observed daily evaporation totals are smaller for dry conditions than wet conditions. In winter, the potential evaporation is similar between subsets, at 0.87 mm day^{-1} and 0.89 mm day^{-1} for wet and dry conditions, respectively, whereas

the observed evaporation was 0.53 mm day^{-1} (61%) and 0.33 mm day^{-1} (38%), respectively. As expected, the greatest contrast is seen in March-April 2012 when observed evaporation reached 71% of potential for wet conditions and 28% for dry conditions. The largest mean daily evaporation rates were observed for summer (1.89 and 1.39 mm day^{-1}) as also predicted by the potential rates (3.10 and 3.33 mm day^{-1}) for both wet and dry conditions. On the whole, the potential evaporation shows the same seasonal trends as, but is much larger than, the observations and also the ratio of observed to potential evaporation varies considerably with season and surface conditions. This supports earlier findings that α_{PT} is dynamic (Figure 4-8 and Figure 4-9a). In addition, Figure 4-11b shows the dependence of the Bowen ratio on moisture availability for all seasons.

The surface conductance is significantly higher shortly after rainfall, when surfaces are likely to be wet, but Figure 4-11c suggests that setting r_s to 0 during these times may be too extreme. Median values of g_s reach about 17-20 mm s^{-1} in spring and summer and 12-15 mm s^{-1} in autumn and winter for data 1-6 h after rain. For dry conditions the peak of the diurnal cycle is around 5 mm s^{-1} (Figure 4-11c). Although peak values are similar across all seasons (6-9 mm s^{-1} for all conditions) the shape of the diurnal pattern varies. Some monthly variability seen in Figure 4-9f is averaged out across the seasons, such as the contrast in peak values between March and April 2012, whilst other trends remain visible, for example higher night time conductance in winter. Under wet conditions, Q_E and g_s are highly variable and show sharp changes from hour to hour, in contrast to the fairly smooth behaviour, particularly during daytime, when the surface is dry.

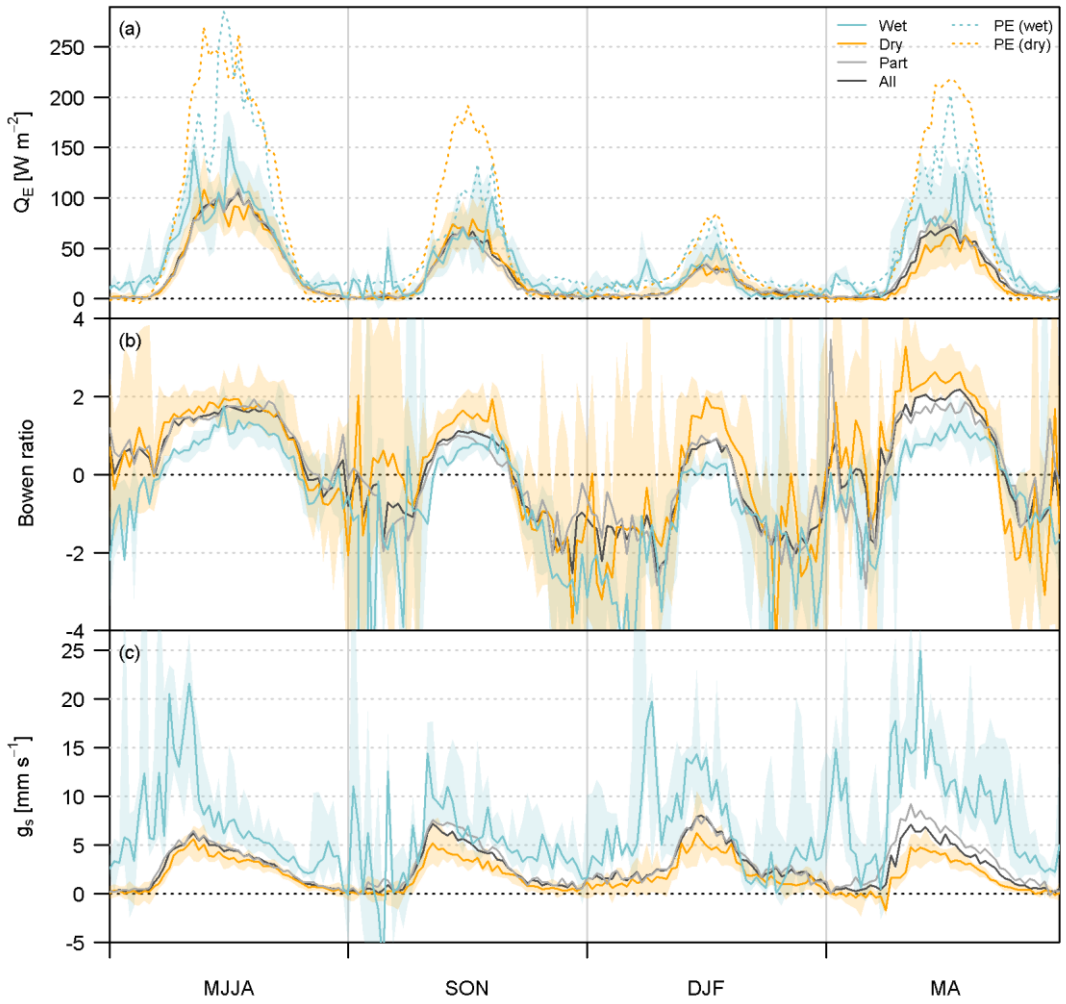

Figure 4-11 Median diurnal cycles and inter-quartile ranges (shading) of (a) measured and potential evaporation (PE), (b) Bowen ratio and (c) surface conductance by season and for different surface conditions: wet (1 to 6 h after rain), partially wet (6 h to 2 days after rain) and dry (≥ 2days since rain).

4.5.3 Carbon flux

There are often distinct sources and sinks of CO_2 with strong temporal signatures. Examples include natural processes such as seasonal and diurnal patterns of CO_2 uptake by plants and CO_2 release through respiration, as well as human drivers that include emissions from traffic, heating, industry or landfill sites. Carbon fluxes measured by eddy covariance above suburban areas are the net result of these surface controls.

There is a striking contrast between daytime CO_2 uptake in summer and release in winter (Figure 4-12). Summertime uptake by vegetation is largest in the middle of the day (-5 µmol m^{-2} s^{-1}) and total F_C exhibits strong correlation with photosynthetically active radiation (PAR, estimated as a proportion of $K_\downarrow$ following Papaioannou et al. (1993), Figure 4-13). Results are similar to those of Crawford et al. (2011) (see their Fig. 6): for high PAR

values (around 1500 µmol m^{-2} s^{-1}) the rate of uptake decreases, probably limited by stomatal closure and light saturation; for low PAR values the increase in uptake is more linear than the natural ecosystem comparisons. The Swindon fluxes are more positive (a larger source, smaller sink) than the natural ecosystem comparisons when reduced to similar vegetation fraction, demonstrating the impact of anthropogenic sources. Compared to the Baltimore site (λ_V = 0.67) (Crawford et al., 2011) the Swindon uptake is lower. Swindon has a smaller vegetative fraction, increased building density, and likely heavier traffic load closer to the measurement site (the crossroads to the southwest of the mast is probably the busiest junction within the study area). The Swindon data also show a weaker response to increasing PAR.

The Swindon site is a net source of carbon dioxide in all seasons despite uptake during daytime in the summer. The mean daily carbon release ranges from 0.56 g C m^{-2} day^{-1} in July to 9.5 g C m^{-2} day^{-1} in December (averages of monthly mean diurnal cycles). The vegetative draw-down is not large enough to compensate for the emissions on a daily basis but does go some way to offsetting the human impact.

Photosynthetic activity begins early in the year, with the diurnal cycle exhibiting midday uptake in March (Figure 4-12). The proportion of evergreen trees around the measurement tower is small so this is most likely due to grass growth in early spring, occuring before leaf-out of deciduous trees (Peters et al., 2011). Warmer temperatures in the urban environment can also encourage early onset of the growing season compared to rural areas (Zhang et al., 2004). These factors give urban vegetation an advantage in its effectiveness at helping to offset carbon emissions compared to agriculture, for example, where crops may be sown later in the year and harvested early, leaving bare soil for many weeks whilst the urban vegetation continues to photosynthesise, providing there is adequate water available.

From late summer and through autumn the CO_2 fluxes are larger at all times of day, except early morning hours when the flux remains fairly constant across the seasons at around 3 µmol m^{-2} s^{-1}. Anthropogenic activity is minimal for these night time hours, photosynthesis nil, and the observed fluxes can be attributed to respiration (soil, plant and human) with a probable slight contribution from emissions due to heating, industrial activities and occasional traffic. A small increase in night time CO_2 emissions is seen during December and February; these are likely from central heating. February was the coldest month with a mean temperature of 4.2°C and two snowy periods (5 February and 10-12 February). Other suburban studies have shown similar patterns (Coutts et al., 2007a), in contrast to more heavily urbanised sites where winter time fluxes are considerably higher than in summer for all hours of the day and throughout the night (Liu et al., 2012; Song and Wang, 2012). This is generally a

result of heating a greater density of buildings and heavier traffic loads, and may also be due to some 24 h industrial contributions.

The rise in carbon emissions from summer to winter illustrates the increasing seasonal impact of anthropogenic activity. Coupled with vegetation being largely dormant during winter, a shift is seen in the drivers of the diurnal F_C cycle. The main controls change from photosynthetic uptake – related to PAR, vegetation fraction and water availability, to human behaviour – the demand for building heating and traffic signals that are no longer masked by uptake (Figure 4-12).

To quantitatively examine the impact of anthropogenic activities, the release of CO_2 from the combustion of fossil fuels for heating or transport and from human exhalation is estimated following a similar method to Q_F (Section 4.7). The emissions from transport are a major source and a direct human impact on the atmosphere (Figure 4-14). Two prominent peaks are visible for the winter months and although strongest in winter, elevated CO_2 fluxes can be identified in August during these morning and evening peaks of activity (Figure 4-12). As with Q_F, these correspond to the daily pattern of human behaviour in residential areas, i.e. rush hour periods when roads are busiest, times of building and hot water heating demand (combustion of fossil fuels) and maximal metabolic release from respiration when residents are at home before and after work. With the addition of increased emissions from building heating in winter, these anthropogenic peaks in the diurnal cycle are considerable (> 10 µmol m^{-2} s^{-1} for 5 months of the year). Consistent with other studies, the morning peak is sharpest, with the widely spread evening peak reflecting the end of the school day, variable length of workdays and contributions from heating and cooking which occur throughout the evening. The peak morning flux is also likely enhanced as CO_2 stored overnight is flushed out by growth of the boundary layer (Coutts et al., 2007a). At night the shallower boundary layer restricts the dispersion of CO_2, causing an increase in concentration. In the morning, as the boundary layer grows again with the increase in vertical mixing, an enhanced flux may be observed as CO_2 is transported away from the surface (Reid and Steyn, 1997).

In winter, the morning and evening peaks are considerably larger on weekdays compared to weekends, when home heating (and probably leisure travel) contributes to larger positive fluxes during the middle of the day (Figure 4-14b, c). Summertime F_C is slightly more positive on weekdays compared to weekends, which is most noticeable during the morning (not shown). Differences between weekday and weekend human behaviour are incorporated into the model and agreement with observed fluxes is best on winter weekdays, but for both types of day the midday modelled fluxes are larger than the observations. This may be the small uptake by evergreen vegetation and grass that is unaccounted for, or more likely a

misrepresentation of daily patterns in traffic or building emissions. An overestimated traffic contribution seems likely, especially in the middle of the day, as when compared with estimates from the National Atmospheric Emissions Inventory[1] (NAEI), our values for vehicle emissions are larger (approximately double). However our values for the whole of Swindon match NAEI estimates more closely (10% underestimation), indicating our assumption of equal traffic distribution over all roads within the Borough of Swindon is a weakness. Human respiration is only really a significant contribution at night (alongside soil and plant respiration). Night time measured F_C is larger than the anthropogenic estimates in summer but about the same in winter (Figure 4-14), which could be attributed to increased soil and plant respiration with warmer temperatures.

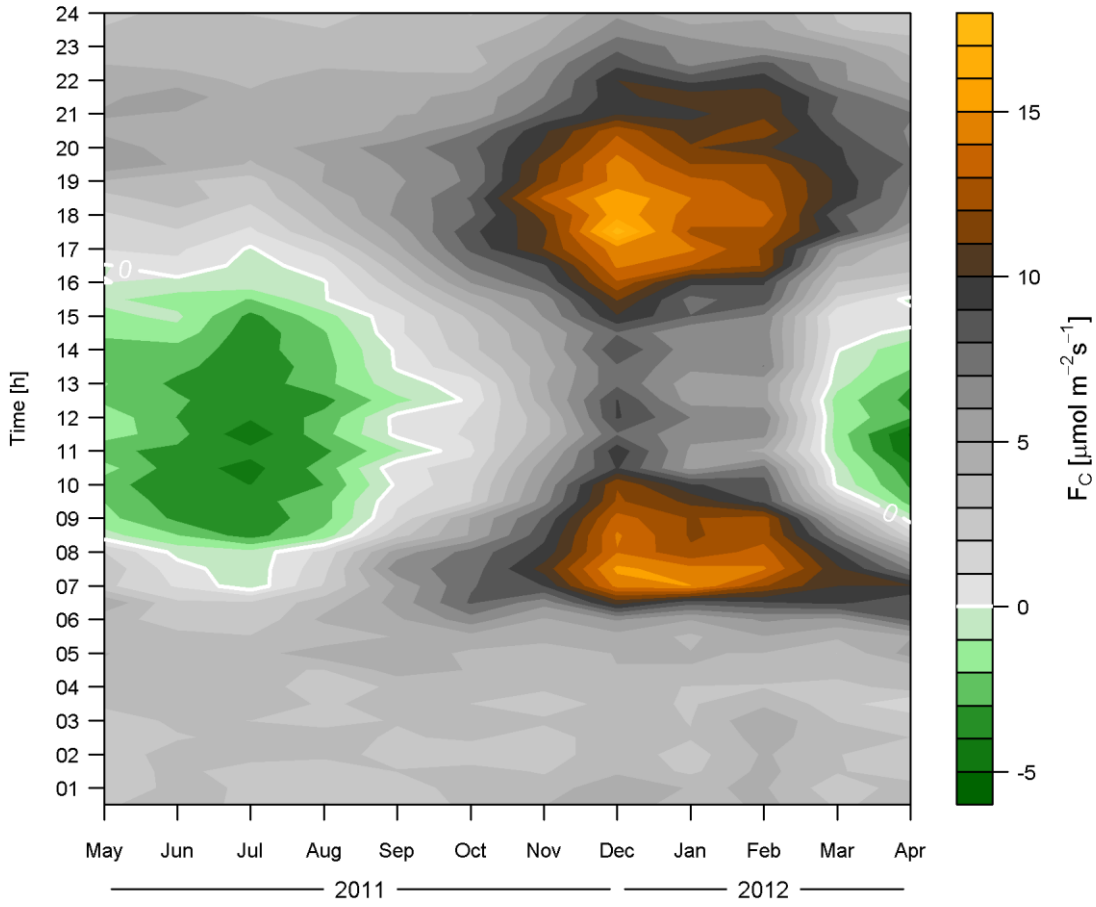

Figure 4-12 Temporal variation of monthly ensemble mean carbon fluxes by time of day.

[1] http://naei.defra.gov.uk, last access: 21 September 2011

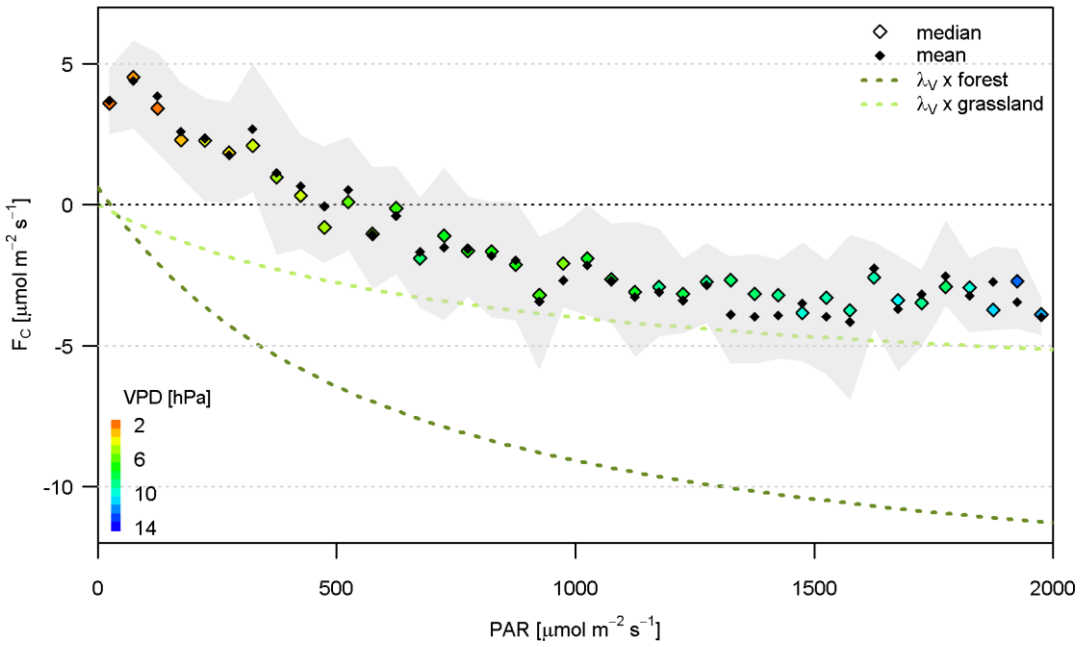

Figure 4-13 Summer (JJA) daytime ($K_{\downarrow}$ > 5 W m^{-2}) carbon flux as a function of photosynthetically active radiation (PAR, in bins of 50 µmol m^{-2} s^{-1}). Shaded area is the inter-quartile range; median values coloured by median vapour pressure deficit (VPD); the models of Schmid et al. (2000) for a mixed deciduous forest ecosystem and Flanagan et al. (2002) for temperate grassland, scaled by the vegetation fraction for Swindon, are shown.

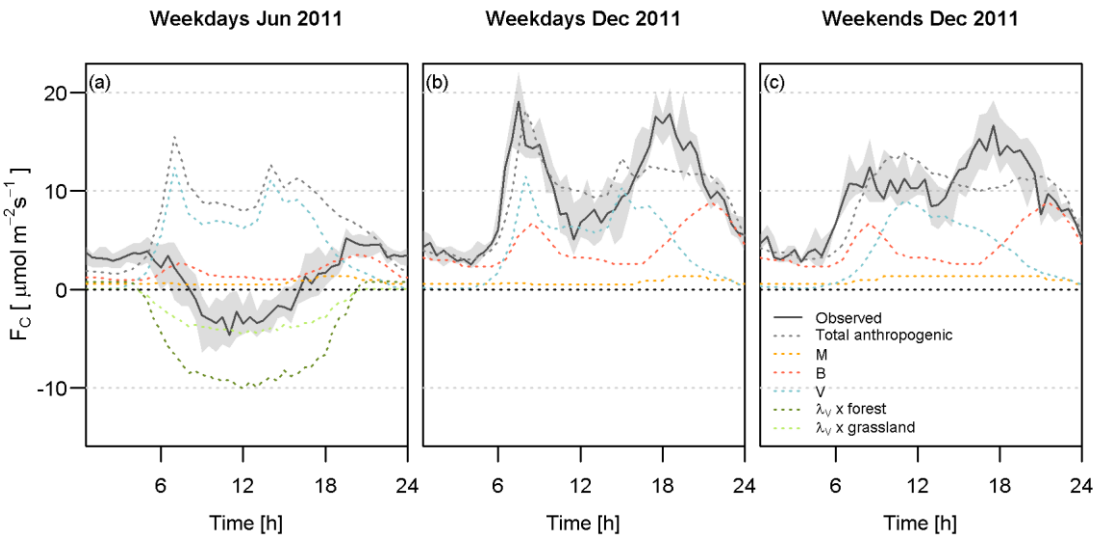

Figure 4-14 Diurnal cycle of measured (median: solid lines, inter-quartile range: shaded) and modelled anthropogenic (mean: dashed lines) carbon fluxes, including components from human metabolism (M), gas usage in buildings (B) and vehicle emissions (V). Uptake by vegetation is modelled for a mixed deciduous forest (Schmid et al., 2000) and temperate grassland (Flanagan et al., 2002) ecosystem scaled by the vegetation fraction for Swindon (a). Weekdays are shown for June 2011 (a) and weekdays and weekends for December 2011 (b, c).

4.5.4 Influence of surface cover on fluxes

The highest vegetation fraction is found to the north of the mast, particularly directly northeast where there are mature trees and lush gardens (Figure 4-1). In contrast the busy road, higher built fraction and increased impervious surfaces lie to the southwest (Figure 4-2). The sector 210-240° has the greatest difference between anthropogenic (0.60) and natural surface cover (λ_V is 0.35). When analysed by wind direction, summer daytime F_C is negative except for the most built-up sectors: the 0-90° sector with large lush gardens, quieter roads and a nature reserve beyond shows strong uptake (Figure 4-15a). Similarly, when the daytime latent heat flux is normalised by downwelling radiation ($Q_\downarrow = K_\downarrow + L_\downarrow$) a greater proportion of the incoming radiation is used in evaporation (just above 10%) for the most vegetated sectors ($\lambda_V \geq 0.45$) and slightly less for the least vegetated sectors (λ_V = 0.35-0.40, about 6-8%) (Figure 4-16a).

In autumn, with reduced photosynthesis and increased anthropogenic emissions (Section 4.5.3), F_C increases across all wind sectors (Figure 4-15b). The largest wintertime F_C release is from the sectors with the greatest proportion of buildings (180-240°). Trends in the latent heat flux are less clear but as the incoming radiation diminishes much is returned as outgoing radiation and a smaller fraction of $Q_\downarrow$ is converted to turbulent or storage fluxes during winter (Loridan and Grimmond, 2012). In autumn there is still quite high $Q_E/Q_\downarrow$ for the 90-180° sector, and also low F_C, which could be due to photosynthesis more likely from grass than deciduous trees (Peters et al., 2011) and evaporation from wet surfaces or moist soils.

In spring (Figure 4-15c, Figure 4-16c), spatial patterns similar to the summer emerge as plants become active again. Anthropogenic CO_2 emissions reduce as temperatures increase and daytime average F_C is negative for the more vegetated sectors as photosynthetic uptake begins (March and April, 0-90°) and transpiration contributes to the total suburban evaporation. As leaves emerge during March-April these trends of falling F_C and rising $Q_E/Q_\downarrow$ are seen fairly consistently across all wind sectors, which reflects the significant proportion of vegetation in the study area as a whole.

Previous studies have demonstrated clear links between surface cover and flux partitioning (Grimmond and Oke, 2002; Christen and Vogt, 2004; Offerle et al., 2006; Goldbach and Kuttler, 2013). For the analysis presented here, no detailed footprint model has been applied, nevertheless categorising the data by wind sector broadly supports these results. In heterogeneous environments it is important to consider the EC measurement bias introduced by the wind direction distribution during the study period. For example, in Helsinki variable

wind direction explains a 16% difference between annual carbon budgets due to source area characteristics (Järvi et al., 2012).

In Swindon, the predominant wind direction is from the southwest (Figure 4-3e), therefore the dataset is expected to be biased towards high CO_2 fluxes, relative to the study area as a whole. Some months have few data from particular wind directions (e.g. 0-90° in May and December). From the observations, Swindon is an annual source of CO_2, with a net release of 1.6 kg C m^{-2} y^{-1}. By considering monthly mean diurnal cycles for different wind sectors, the annual flux from the least vegetated quadrant with the busiest roads (180-270°) is estimated at 2.0 kg C m^{-2} y^{-1}, compared to 1.4 kg C m^{-2} y^{-1} for the 270-360° quadrant. These values are considerably lower than other UK studies: both London and Edinburgh emit around 10 kg C m^{-2} y^{-1} (Nemitz et al., 2002; Helfter et al., 2011), but comparable to other suburban studies worldwide, such as in Melbourne (Coutts et al., 2007a), Helsinki (Järvi et al., 2012) and Montreal (Bergeron and Strachan, 2011) where emissions are 2.32, 1.76 and 1.36 kg C m^{-2} y^{-1} respectively.

In the same way, the total evaporation measured by the EC system will be affected by the wind direction distribution, since vegetated areas promote evaporation through transpiration, access to deep water reserves and evaporation from soil, whilst impermeable surfaces can have very high evaporation rates for a short time immediately following rainfall. These large latent heat fluxes immediately after rain (as well as evaporation of intercepted rainfall over all surface types) are usually not captured by the IRGA, therefore the annual evaporation is likely to be an underestimate. From the measurements, annual evaporation is estimated to be 370 mm, compared to 650 mm of rainfall for the twelve months May 2011 – April 2012.

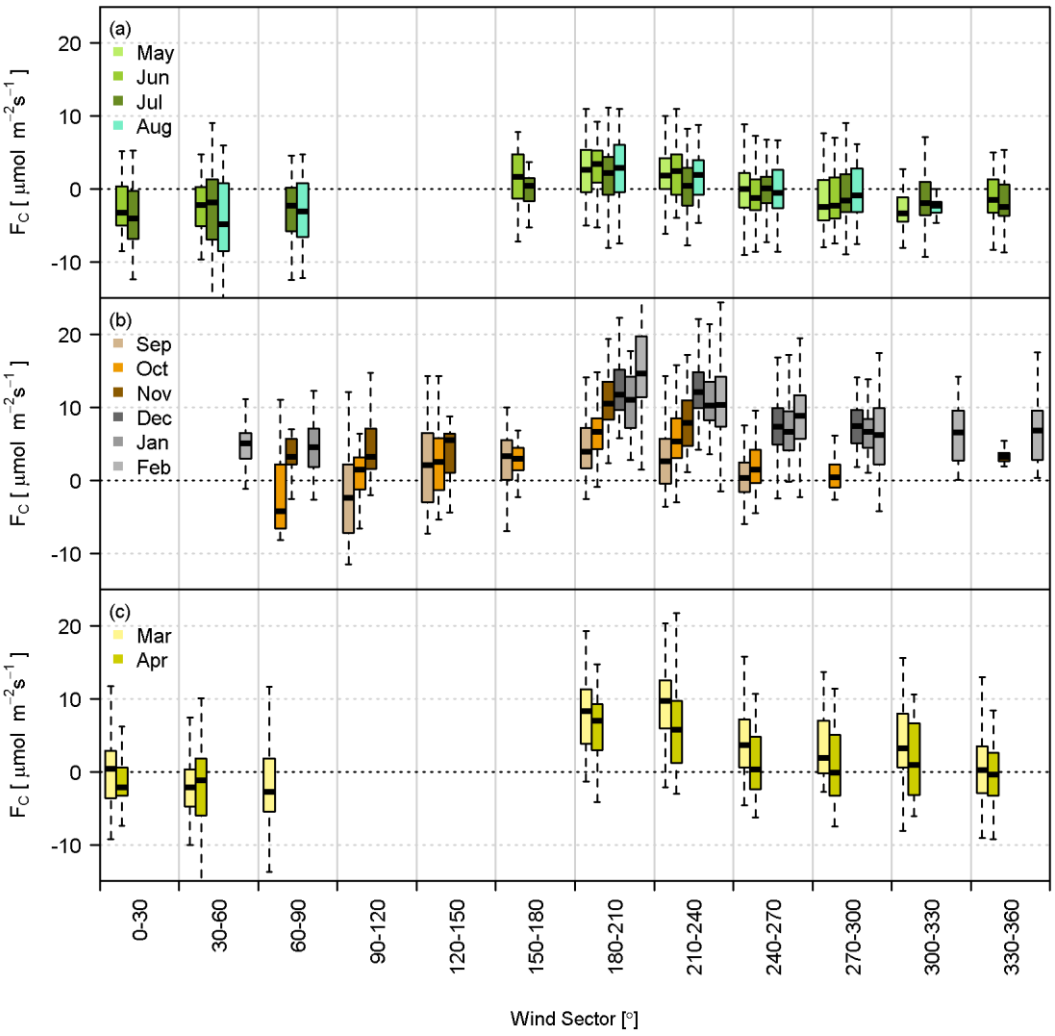

Figure 4-15 Monthly boxplots of daytime ($K_{\downarrow}$ > 5 W m^{-2}) carbon fluxes by wind direction for (a) summer, (b) autumn-winter and (c) spring. Boxes have a minimum of 20 samples.

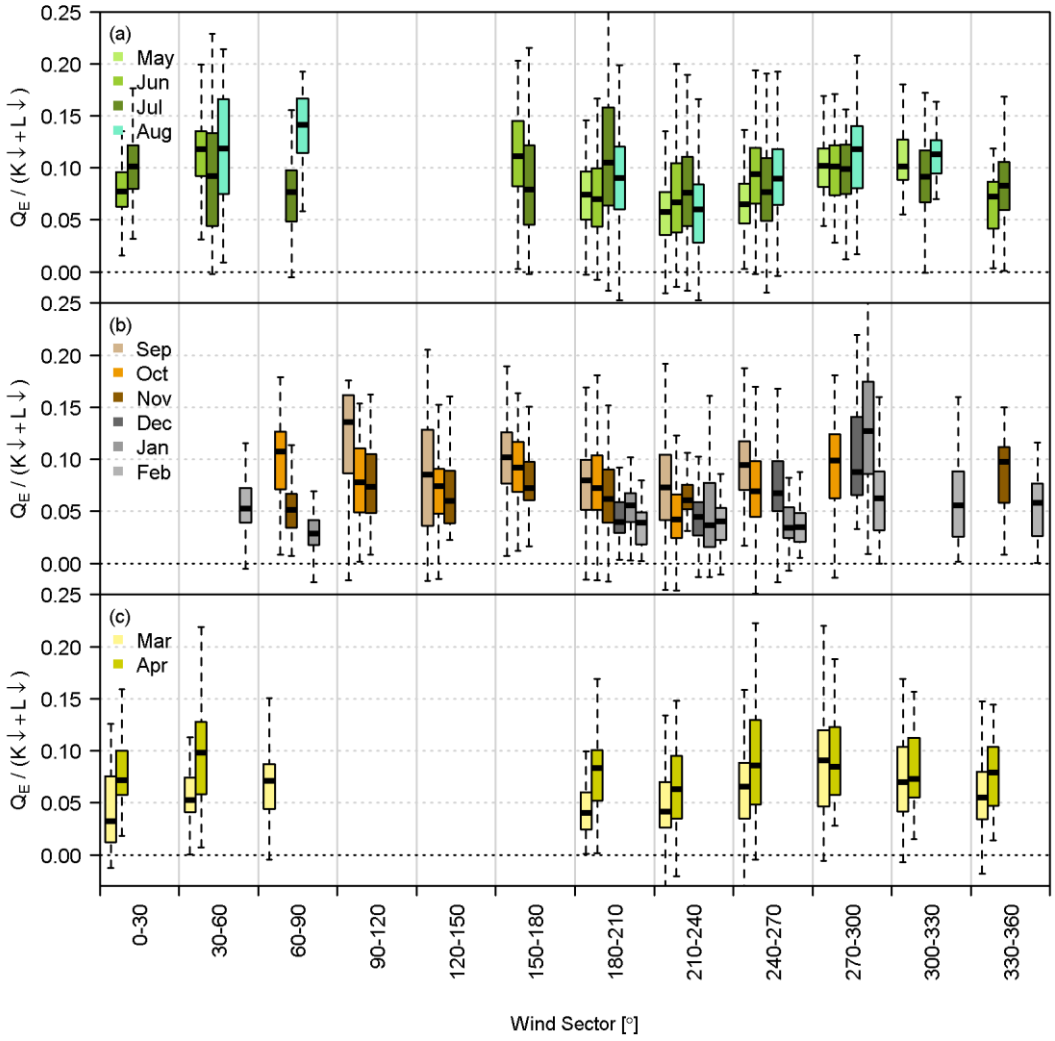

Figure 4-16 As for Figure 4-15 but for Q_E normalised by incoming radiation.

4.6 Conclusions

The first UK suburban measurements of energy, water and carbon fluxes are presented for a residential area in the town of Swindon for twelve months. The eddy covariance and meteorological data give comparable results to studies in similar environments: the storage flux is a major component of the energy balance all year round, the anthropogenic heat flux is small but important when Q^* is small, and more energy is directed into Q_H than Q_E during summer (Figure 4-4). In winter there are negative Q_H values (Figure 4-5) that can be explained by the suburban nature of the site with relatively low building density, small Q_F and relatively small ΔQ_S terms compared to sites that are more built-up – and more frequently studied.

A specific aim of this work was to identify the controls on evaporation within the suburban environment. Results show that the latent heat flux remains positive all year round so under limited radiative input energy is diverted to evaporation at the expense of Q_H. This results in

an annual cycle of the Bowen ratio that reaches a minimum of close to zero in December (Figure 4-7a). At this time daily (24 h) Q_H and Q_E have opposite signs (Figure 4-4). Negative Q_H is also observed during summer daytimes shortly after rainfall, when evaporation can exceed potential rates. Night time β exhibits a similar seasonal trend but is lower. At the other extreme, high values of β (> 4) are seen in both spring 2011 and 2012 when water is scarce (Figure 4-7). Significant deviations from the typical β of 1-1.5 expected given the vegetation fraction occur outside of summer and on daily timescales in response to water availability (Section 4.5.2).

To further investigate controls on evaporation, surface conductances were calculated using measured variables by season and by time since rainfall. These empirically-derived conductances may be useful for assessing or improving model values, e.g. to capture variability in time and across different surface conditions. The diurnal cycle of the observed g_s is asymmetrical, particularly outside of winter, being usually highest in the morning and declining through the afternoon until close to zero at night (Figure 4-9). This pattern results from the combined course of Q_E/VPD over the day. An early morning peak is seen as dew evaporates, the dewfall itself represented by negative values of g_s as Q_E is directed towards the surface (Figure 4-10). Nocturnal g_s is larger when water is abundant and wind speeds are high. Generally g_s follows a smooth diurnal course, however when the surface is wet values are larger and more erratic (Figure 4-11). After several days without rain, impervious surface materials limit evaporation compared to the pervious and vegetated areas. Hence the energy partitioning is strongly dependent on land cover fractions (Section 4.5.4). The active vegetation index proposed by Loridan and Grimmond (2012) to characterise urban surfaces in terms of energy exchange accounts for some seasonal variability through changing leaf area (as opposed to a fixed vegetation fraction), but does not currently parameterise water availability. However, the results presented here suggest linking water availability to surface cover and state of vegetation could offer improved accuracy for modelling the energy partitioning.

Analysis by wind direction reveals the significance of vegetation and traffic on carbon emissions. The annual net carbon release for residential Swindon (1.6 kg C m^{-2} y^{-1}) is consistent with other studies of similar source area characteristics and is considerably lower than other UK city-based observations. In Swindon, vegetation clearly helps to offset emissions, aided by extended growing seasons (Figure 4-12). Vehicle emissions and photosynthetic activity are responsible for the difference between overall daytime uptake and release for different wind sectors around the flux mast. However, even in summer when the diurnal trend is dominated by photosynthesis, daily fluxes (24 h) indicate CO_2 release. Comparison of the modelled anthropogenic CO_2 release with the measured fluxes demonstrates the impact of human

activities. In December when vegetation is dormant, the combination of traffic peaks and building emissions match the observed fluxes fairly well (Figure 4-14).

Key questions remain if we are to better understand the complex urban environment. Future work should focus particularly on lesser studied conditions – winter months and night times, demanding multi-seasonal observations such as the Swindon dataset presented here. From the analysis discussed above, the change in response of surface fluxes to moisture availability and seasonal controls, as well as to the variability in land cover characteristics, warrants further research.

4.7 Appendix A: Estimating the direct anthropogenic contributions of energy, water and carbon

The energy balance of urban environments can include a non-negligible addition of energy as a direct result of anthropogenic activities such as building or water heating, electricity use, transport and human metabolism. The heat released during these activities boosts the energy available (from solar input) for turbulent fluxes or storage. In addition to heat release, combustion processes and human respiration produce carbon dioxide and water vapour, hence the carbon and water cycles also have direct anthropogenic inputs which are not found in natural environments. The additional energy supplied via human activities is represented in the energy balance by Q_F, the anthropogenic heat flux, consisting of contributions from vehicular transport (Q_V), the energy used in buildings (Q_B) and human metabolism (Q_M) (Sailor and Lu, 2004):

$$Q_F = Q_V + Q_B + Q_M . \qquad \text{(4-A1)}$$

The aim here is a first order estimate to gauge the probable magnitude of these terms for Swindon using UK national statistics available at a range of spatial and temporal resolutions. Sub-daily and monthly variations are of interest for comparison with multi-seasonal eddy covariance observations. At the spatial scale and coarseness of our Q_F estimation it did not make sense to attempt to calculate differences with land cover (e.g. building density, percentage of road) for different wind sectors around the flux mast. However it should be kept in mind that, to a certain extent, the EC fluxes will reflect the variable source area measured. Daylight saving was accounted for in the following calculations.

4.7.1 Vehicular emissions

The total distance travelled by motor vehicles for each local authority in the UK (Department for Transport[1] (DfT)) was weighted by the area of road in the study area, assuming the weight of traffic is equal across all roads as in Ichinose et al. (1999). This resulted in 122 million vehicle km y^{-1}, which when divided by the representative area and converted from years to seconds gives the average vehicle km per unit area per second. Multiplying by emission factors for the amount of energy, CO_2 and water vapour released per km travelled yielded Q_V, the contribution of traffic to F_C and the anthropogenic water vapour flux from traffic. Emission factors from the Department of Energy and Climate Change[2] (DECC) and Moriwaki and Kanda (2004) of 0.2069 kg km^{-1} and 0.0990 kg km^{-1}, with a mean fuel economy of 8.5 km L^{-1} (Sailor and Lu, 2004), were used for CO_2 and H_2O respectively. For Q_V, a mean energy release of 3.97 MJ km^{-1} from Sailor and Lu (2004) has been used. No adjustment for fleet composition or variable fuel economy was made as no data specific to Swindon were available. Temporal changes were modelled using typical daily (Monday-Friday, Saturday, Sunday) and monthly profiles from the National Travel Survey 2010[3] (DfT).

4.7.2 Building energy use

To estimate the outputs of energy use in buildings the following assumptions were made:

1. All energy released from fuel consumption or electricity use in buildings is eventually dissipated as heat.
2. No allowance is made for time lags between energy consumption and release to the surroundings.
3. Only domestic energy use is considered as residential areas are judged to be the predominant land use. There are a few institutional buildings (mainly schools) and small supermarkets plus a row of shops to the southwest (Figure 4-1). Domestic energy use data are probably an underestimate and may misrepresent the daily and seasonal patterns (non-domestic energy use typically remains high throughout the workday and decreases in the evening, see Hamilton et al. (2009), and shows less variation across seasons) – but the prevalence of residential buildings means the likely impact is small.
4. Whilst the dissipation of heat from electricity used in the home but generated at out of town power plants will result in additional heating that contributes to the observations, the emissions from these power plants do not contribute to CO_2 measured at the flux tower.

Annual domestic electricity and gas consumption statistics were available up to 2009 for different areas within Swindon, whilst consumption in 2011-12 was available quarterly for gas

[1] http://www.dft.gov.uk/statistics/series/traffic, last access: 28 June 2012
[2] http://www.decc.gov.uk, last access: 04 October 2012
[3] http://www.dft.gov.uk/statistics/releases/national-travel-survey-2010, last access: 3 April 2012

and monthly for electricity for the UK (DECC). The latter provides more information on temporal changes which can be determined, for example, by the weather (mild winter in 2011) and cost of fuel. In 2009, approximately 0.3% of the UK's total electricity and gas use was consumed by Swindon Borough, of which about 85% was used by Swindon Town. These proportions are assumed to remain similar for 2011-12 to obtain quarterly and monthly energy use. CO_2 and water vapour release were estimated based on consumption of natural gas (Moriwaki and Kanda, 2004). Other energy sources (e.g. burning of biomass, coal, oil) were neglected. The sub-daily variation was modelled using Hamilton et al. (2009), linearly interpolated to 30 min profiles.

4.7.3 Human metabolism

Night and day time population densities from the 2001 census were used to estimate heat and gas emissions from human metabolism. For the study area the population has not changed significantly (-1.5%) between 2001 and 2010 (Office for National Statistics[1]), although the population of Swindon Town has grown significantly (+ 14%) as development has rapidly progressed to the north and west. Following Bergeron and Strachan (2010), night time population densities were used for weekday night times (1800-0600), weekends and holidays; lower daytime population densities were used for weekdays when residents would be at work (0800-1600); and linear interpolation filled the transition times. The daytime (175 W person^{-1}, 0800-2100 on weekdays, 0900-2100 on weekends/holidays), night time (75 W person^{-1}, 2300-0600 on weekdays, 2300-0700 on weekends/holidays) and transition period (125 W person^{-1}, between times) heat released depending on activity is based on Sailor and Lu (2004). Figures for CO_2 and water vapour release are adjusted for day, night and transition times (280, 120 and 200 µmol CO_2 s^{-1} person^{-1}; 31.5, 13.5 and 22.5 W person^{-1}) based on Moriwaki and Kanda (2004). Combining the population densities with the per capita emissions yielded fluxes of anthropogenic heat, CO_2 and latent heat due to human metabolism.

These estimates do not account for details such as residents on holiday, night shifts, more or less active lifestyles, or people travelling into the area for education, to work or shop. However, many of these contributing factors tend to compensate. The methodology could be refined by more intensive data collection and increased complexity of models, as has been trialled in other studies: Nemitz et al. (2002) obtained hourly gas supply data for Edinburgh; detailed traffic monitoring was available in London (Helfter et al., 2011). For suburban areas an order of magnitude figure may be sufficient to demonstrate that Q_F is a relatively small contribution to the overall energy balance; improving the accuracy of CO_2 emission estimates

[1] http://www.statistics.gov.uk/hub/population, last access: 21 September 2011

might be more relevant. The water vapour released through anthopogenic activities was found to be a negligible component of the total Q_E as shown in other studies (Moriwaki and Kanda, 2004), except near cooling towers (Moriwaki et al., 2008).

4.8 Appendix B: Net storage heat flux estimation

The net storage heat flux, a significant term in the urban energy balance, is difficult to measure directly. As shown in Figure 4-4, the residual term can be very large and was judged a poor estimate of the likely storage flux for this dataset. Several heat flux plates were installed within different materials in Swindon (under soil, vegetation and rubble, between a roof and roof lining) to give a qualitative indication of the different behaviour between the multiple material types that make up the urban fabric. The practicalities of obtaining sufficient spatial representation and the assumptions required to use such measurements to determine a representative storage term demand a different approach. To avoid these issues we estimate the storage heat flux using the Objective Hysteresis Model (OHM) of Grimmond et al. (1991). The method uses Camuffo and Bernardi's (1982) hysteresis regression approach with net all-wave radiation and a rate of change term for the hysteresis between Q* and ΔQ_S. The coefficients are applied objectively based on the different land cover types weighted by their relative proportions of the surface. Thus, the storage flux is estimated from (Grimmond et al., 1991)

$$\Delta Q_S = \sum_i \{a_{1i} Q^* + a_{2i} (\partial Q^* / \partial t) + a_{3i}\} f_i \,, \qquad \text{(4-B1)}$$

where t is time and $a_{1,2,3}$ are coefficients for each land cover type, i, covering an area fraction f_i. For Swindon the plan area fractions (Table 4-1) were used. Coefficients used were taken from Table 1 of Grimmond et al. (1991), using an average of the values given for each land cover type, asphalt for roads and bare soil for surfaces classified as 'Other'. The resulting coefficients obtained for Swindon (a_1 = 0.39, a_2 = 0.35, a_3 = -27.0) are comparable to those at Sunset, Vancouver.

These coefficients were used all year round. Anandakumar (1999) derived a set of coefficients for asphalt which revealed seasonal variation, notably the large negative values of a_3 found during summer became smaller and even positive during winter. For the Swindon data, fitting Equation 4-B1 to the soil heat flux Q_G suggested similar seasonal variation of the coefficients, particularly a_3. Clearly this topic warrants further research. A further limitation is that the proportion of incoming energy dissipated by conduction can vary when surfaces are wet compared to dry (Offerle et al., 2005b; Kawai and Kanda, 2010). Ideally the estimation of

ΔQ_S would incorporate changing seasonal and surface conditions, but the variety of surface types and lack of long-term datasets means this is beyond the scope of the present study.

Acknowledgements

We wish to thank the owners of the Swindon property who very kindly agreed to have the flux mast installed in their garden. We appreciate the constructive comments of both anonymous reviewers. This work was funded by the Natural Environment Research Council, UK.

Chapter 5 Multi-scale sensible heat fluxes in the urban environment from large aperture scintillometry and eddy covariance

5.1 Introduction

Understanding the interactions between the land surface and the atmosphere is central to developing our capabilities in weather forecasting, air quality, thermal comfort, flood risk and developing tools for urban design. Differences in observed energy fluxes, both within and between cities, have been attributed to differences in land use and land cover. This has been achieved largely through eddy covariance (EC) measurements at multiple sites in a city (see, for example, the work in Los Angeles (Grimmond et al., 1996), Basel (Christen and Vogt, 2004), Łódź (Offerle et al., 2006), Melbourne (Coutts et al., 2007b), Montreal (Bergeron and Strachan, 2010), Dublin (Keogh et al., 2012), Essen (Weber and Kordowski, 2010), Oberhausen (Goldbach and Kuttler, 2013) and Helsinki (Nordbo et al., 2013)); and through comparison of fluxes from different cities (e.g. Grimmond and Oke (1995; 2002)). Also, studies at individual sites have combined footprint models and land cover maps to capture differences in the surface cover sampled as the source area of the measurements changes with atmospheric conditions (Vesala et al., 2008; Järvi et al., 2012; Goldbach and Kuttler, 2013). Relations between surface cover and fluxes offer a valuable indication of the underlying processes and form a basis for modelling turbulent fluxes (Grimmond and Oke, 2002; Järvi et al., 2011; Loridan and Grimmond, 2012).

Scintillometry provides a means of estimating fluxes at a much larger scale, of the order of several km^2 (Hoedjes et al., 2007; Guyot et al., 2009; Kleissl et al., 2009a). Path-averaging along the optical beam of the scintillometer means that measurements are inherently spatially integrated, offering a particular advantage over heterogeneous surfaces (Beyrich et al., 2002b; Meijninger et al., 2002b; Beyrich and Mengelkamp, 2006; Samain et al., 2011a; Evans et al., 2012). Despite the complexity of the urban surface, patches of impervious land cover (roads, car parks, paved areas) adjacent to green spaces (parks, gardens) are not very different to the juxtaposition of fields containing differently ripening and senescing crops in mixed agricultural landscapes. In such studies, measuring sufficiently high above the surface ensures the influences of surface heterogeneity are well-blended at the height of the measurement and

reliable fluxes can be obtained (Meijninger et al., 2002b; Ezzahar et al., 2007). In addition to the increased spatial representativeness of such large-area measurements, the increased scale facilitates comparison with satellite remote sensing products or land-surface models. Studies comparing model output with scintillometry data include the work of Cheinet et al. (2011), Samain et al. (2011b) and Steeneveld et al. (2011). After testing three aggregation schemes for surface temperature obtained from remote sensing against scintillometry data, Chehbouni et al. (2000a) concluded that model development should focus on developing relationships to replicate observations made at the large-scale.

The use of scintillometers in urban environments can be divided into two groups: (a) studies involving small aperture instruments, usually deployed within or near the top of the roughness sub-layer on path lengths of the order of 100 m, e.g. in Tokyo (Kanda et al., 2002), Basel (Roth et al., 2006) and London (Pauscher, 2010); (b) larger scale studies over much longer path lengths (500 m – 10 km) using large aperture scintillometers. This study is concerned with the latter. Large aperture scintillometry offers unique advantages over other established techniques such as eddy covariance. The much larger sampling volume enables robust retrieval of turbulence statistics and the measurement sensitivity is greatest near the centre of the path, away from the instruments and their mounting structures, such that the influence of locally-produced turbulence around these structures has minimal impact on the measurements. Furthermore, direct access to the measurement area is not required – an electromagnetic beam is simply transmitted high above the surface – unlike point measurements requiring *in situ* mounting. This remote sensing capability makes the scintillometry technique particularly valuable in the urban environment.

There are an increasing number of studies using large aperture scintillometry in urban areas. Lagouarde et al. (2006) present results from a three week trial in summer 2001 in which two large aperture scintillometers were used over Marseille. Other studies include work in London (Gouvea and Grimmond, 2010), Nantes (Mestayer et al., 2011), Łódź (Zieliński et al., 2012) and Helsinki (Wood and Järvi, 2012).

To date, the use of large aperture scintillometry in urban areas has been to derive the sensible heat flux. In order to directly estimate the latent heat flux, a second scintillometer of longer wavelength is required (Hill et al., 1988; Andreas, 1989) but these are not yet commercially available. Hence there are only a handful of two-wavelength studies documented (Kohsiek and Herben, 1983; Green et al., 2001; Meijninger et al., 2002a; Meijninger et al., 2006; Evans, 2009). For this project, a millimetre-wave scintillometer was installed alongside one of the infrared scintillometers. These first two-wavelength results from the urban environment are presented in two companion papers (Chapters 7 and 8).

The goal of this study is to investigate the influence of the surface on sensible heat fluxes across different spatial and temporal scales in the suburban environment. Eddy covariance measurements are analysed together with large aperture scintillometers installed on 2.8 km and 5.5 km paths in Swindon, UK (Section 5.2). The long time-series enables analysis of seasonal and inter-annual patterns (Section 5.4.1) as well as the short-term response of heat fluxes to solar radiation (Section 5.4.2). Consideration is given to the experimental uncertainties, including the representativeness of point measurements required as inputs for scintillometry algorithms (Section 5.2.3) and the challenges associated with urban environments. Path-averaged wind speed is compared to point measurements (Section 5.3). Source area modelling is applied and the contribution of different land cover classes is related to the observations at each scale (Section 5.4.3).

5.2 Methodology

5.2.1 Derivation of the sensible heat flux from single-wavelength scintillometry

Scintillometers measure the changing intensity of an electromagnetic beam as it propagates through the turbulent atmosphere, yielding the structure parameter of the refractive index of air (C_n^2). First, these refractive index fluctuations must be related to temperature fluctuations (Wesely, 1976),

$$C_T^2 = \frac{T^2}{A_T^2} C_n^2 (1 + 0.03\beta^{-1})^{-2}, \tag{5-1}$$

where C_T^2 is the temperature structure parameter, A_T is the structure parameter coefficient which depends on temperature (T), pressure (p) and weakly on humidity (Hill et al., 1980; Andreas, 1988) and β is the Bowen ratio. Because β is not known *a priori* and there are major uncertainties involved in estimating the available energy in urban areas, this correction is not implemented here. The effect of this is discussed in Section 5.2.3.

The conversion from structure parameters to fluxes entails iteration of similarity functions using Monin-Obukhov Similarity Theory (MOST) and the effective height of the scintillometer, z_{ef}, the wind speed, U, measured at height z_U, displacement height, z_d, and roughness length, z_0. Commonly used forms of the similarity functions (f_{MO}) are

$$f_{MO}(\zeta) = c_{T1}(1 - c_{T2}\zeta)^{-2/3} \tag{5-2}$$

for unstable conditions and

$$f_{MO}(\zeta) = c_{T1}(1 - c_{T3}\zeta^{2/3}) \quad (5\text{-}3)$$

for stable conditions. The stability parameter ζ is given by $(z_m\text{-}z_d)/L_{Ob}$, where L_{Ob} is the Obukhov length and z_m the measurement height, or z_{ef}/L_{Ob} when z_{ef} has been calculated incorporating the displacement height (Hartogensis et al., 2003). Different values of the empirically derived constants $c_{T1\text{-}3}$ are used in the literature (Andreas, 1988; Hill et al., 1992a; De Bruin et al., 1993), and alternative functional forms appear too (Thiermann and Grassl, 1992). The values found by Wyngaard (1973) were adjusted by Andreas (1988) to give c_{T1} = 4.9, c_{T2} = 6.1 and c_{T3} = 2.2 (hereafter An88). De Bruin et al. (1993) found c_{T1} = 4.9, c_{T2} = 9 and c_{T3} = 0 (hereafter DB93). The friction velocity, u_*, is estimated from the logarithmic wind profile adjusted for stability and solved iteratively with

$$L_{Ob} = \frac{u_*^2 T}{g\kappa_v T_*}, \quad (5\text{-}4)$$

where g is the acceleration due to gravity, κ_v von Kármán's constant and T_* is the temperature scaling variable. Finally the sensible heat flux is obtained using

$$Q_H = -\rho c_p u_* T_*, \quad (5\text{-}5)$$

where ρ is the density of air and c_p the specific heat capacity at constant pressure. In the following, Q_{H_BLS} and Q_{H_LAS} are used to denote the sensible heat flux for the 5.5 km path and 2.8 km path, respectively (see Section 5.2.2). The sensible heat flux from the EC station is denoted Q_{H_EC}.

One drawback of scintillometry is that the sign of the heat flux is unknown and must be assigned based on other information. Samain et al. (2012) compared possible algorithms and recommended using the minima in the diurnal cycle of C_n^2 to indicate a transition of stability. This methodology is followed here, which has the key advantage that it is based on path-averaged information.

5.2.2 Site description and experimental details

This study took place in Swindon, UK (population 175 000), situated 120 km west of London (top right, Figure 5-1). Typical of the UK suburban landscape, Swindon consists mainly of residential areas with houses of varying ages extending outwards from the town centre, interspersed with greenspace, small parades of shops and institutional buildings. Larger industrial and commercial zones are mostly situated towards the edges of the development. The town centre comprises commercial areas, with some pedestrianised streets, offices, public

buildings and transport hubs. Building density in the town centre is greater than in the surrounding suburbs and buildings are taller, larger and more variable in height. Outside of the urban core, the buildings are more uniform – houses are mostly 1-3 storeys, semi-detached or terraced and usually have at least a small garden. There are a few small blocks of flats (4-5 storeys) and larger warehouses in the industrial areas. Trees are of a similar height to the buildings and found mostly in undeveloped green corridors between residential areas, along roadsides and in gardens. The area is relatively vegetated (cover fraction 53%), largely due to the prevalence of grassed areas: parks, playing fields, green corridors, gardens, verges and a large nature reserve near the centre of the study area (Figure 5-1).

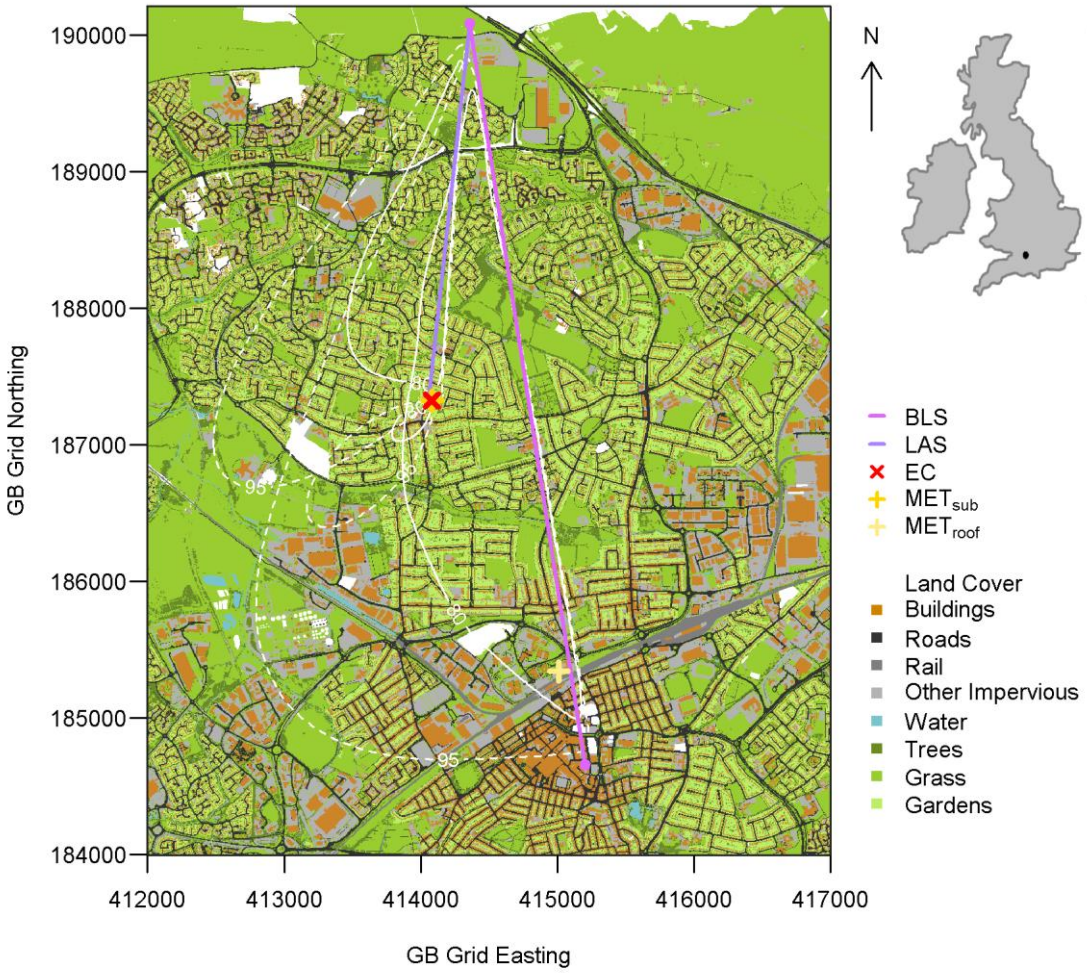

Figure 5-1 Land cover map of the study area with locations of the two scintillometer paths (BLS and LAS), eddy covariance station (EC) and two meteorological stations (MET_{sub} and MET_{roof}). Example footprints for typical atmospheric conditions (wind direction = 225°, L_{Ob} = -200 m, u_* = 0.5 m s^{-1} and σ_v = 0.9 m s^{-1}) are indicated by the cumulative source area: the region within the solid (dashed) line contributes 80% (95%) to the measured flux. The location of Swindon within the British Isles is shown (top right). Details of the land cover classification are given in the text. Where data were unavailable areas are left unclassified (white).

Observations at multiple scales are achieved using the eddy covariance technique and two scintillometer paths. The largest measurement scale reaches between the town centre and the rural fringe at the northern edge of the settlement: an infrared scintillometer, the BLS900 (Scintec, Rottenburg, Germany), was installed on a 5.5 km path orientated approximately north-south. A second infrared scintillometer, a LAS 150 (Kipp and Zonen, Delft, The Netherlands), was aligned on a shorter path of length 2.8 km. This path is located over relatively recently developed suburbs (in the last ~20 years) 3-5 km north of the town centre. Both are large aperture scintillometers operating at a wavelength of 880 nm. Although LAS often stands for large aperture scintillometer, in this study BLS is used to denote the scintillometer on the long path and LAS the scintillometer on the short path. The eddy covariance (EC) system was installed approximately 3 km north of the town centre, close to the middle of the long path.

Footprint models can be used to aid the interpretation of observed fluxes by relating them to the probable area of the surface that influenced the measurements. Although some of the assumptions may be challenged by complex environments, footprint models have been used successfully in urban areas (Schmid et al., 1991; Järvi et al., 2009; Hiller et al., 2011). Meijninger et al. (2002b) extended the theory to scintillometer footprints by combining source areas calculated for a single point measurement with the scintillometer path weighting function. This has since been adopted by other studies (Meijninger et al., 2006; Hoedjes et al., 2007; Samain et al., 2011a; Evans et al., 2012; Liu et al., 2013). A range of footprint models exist; we use the analytical model of Hsieh et al. (2000) and assume the lateral dispersion is Gaussian (Schmid, 1994; Detto et al., 2006).

Results of the footprint model for each of the three systems are shown in Figure 5-1 for typical atmospheric conditions (wind direction = 225°, L_{Ob} = -200 m, u_* = 0.5 m s^{-1} and standard deviation of lateral wind σ_v = 0.9 m s^{-1}). Source areas vary depending on atmospheric conditions and wind direction, as well as measurement height and surface roughness. Nevertheless, the difference in measurement scales is apparent. The sizes of the areas contributing 80% (95%) of the observed fluxes are approximately 0.06, 1.0 and 3.0 km^2 (0.5, 3.0 and 7.5 km^2) for the EC, LAS and BLS, respectively. The size of the footprints increases with stability.

Beam heights, land cover and building and tree height were obtained using a spatial database incorporating surface cover information (OS MasterMap 2010 ©Crown Copyright), a digital terrain model and digital surface model from lidar (2007, ©Infoterra Ltd) and aerial photography (2009, ©GeoPerspectives). Further details are given in Chapter 4; for this study a

spatial resolution of 5 m was used. Some of the residential area at the far northwest of the study area has very recently been completed, with some development of the rural outskirts ongoing during the study period. The overall effect here may be a small overestimation of the vegetated land cover fraction for the LAS path when winds are from the west or northwest and in stable conditions.

The roughness length for momentum, z_0, was estimated based on the mean height of the roughness elements within the area influencing the measurements using the approximation $z_0 = 0.1z_H$ (Garratt, 1992). The resulting values (Table 5-1) are reasonable based on comparison with the literature, however there is appreciable uncertainty associated with this (and other) methods (Section 5.4.1). The zero plane displacement height, z_d, is estimated at $0.7z_H$ and incorporated into the effective height calculation for the scintillometers, after Hartogensis et al. (2003) (their Equation 15).

Both infrared scintillometer transmitters were installed on a telecommunications mast at the northern edge of the suburbs at 27.9 m (BLS) and 26.6 m (LAS) above ground level. The LAS receiver was bolted to a 1.7 m high post at the same property as the EC mast, whilst the BLS receiver was mounted on a building in the town centre at 26.2 m. The topography (Figure 5-2) combined with mounting on existing structures provides sufficient beam height for the scintillometers to be above the blending height (which is estimated to be between 15 and 30 m (Pasquill, 1974; Garratt, 1978)).

Instrumentation	Dates	Location	z_m [m]	z_{ef} [m]	Path length [m]	Bearing [°]	z_0 [m]	z_d [m]
BLS	12 Jan 2011 – 31 Dec 2012	51°36'33.9" N 1°47'38.6" W (Tx) 51°33'38.1" N 1°46'55.3" W (Rx)	44.3	45.0	5492	170	0.7	4.9
LAS	22 Jun 2011 – 31 Dec 2012	51°36'33.9" N 1°47'38.6" W (Tx) 51°35'4.9" N 1°47'53.0" W (Rx)	32.4	35.9	2761	184	0.6	4.5
EC	09 May 2011 – 31 Dec 2012	51°35'4.6" N 1°47'53.2" W	12.5	-	-	-	0.5	3.5
MET_{sub}	09 May 2011 – 31 Dec 2012	51°35'4.6" N 1°47'53.2" W	10.6 (WXT) 10.1 (NR01)	-	-	-	0.5	3.5
MET_{roof}*	01 Jan 2011 – 31 Dec 2012	51°34'0.3" N 1°47'5.3" W	2.0 (WXT) 1.1 (NR01)	-	-	-	-	-

Table 5-1 Details of the instrumental setup. Tx denotes transmitter, Rx receiver. For the scintillometers, the mean heights of the beams above the surface (z_m) and the effective measurement heights (z_{ef}) are given. The date range refers to the data used here. *For MET_{roof} the heights above the roof surface are given; z_0 and z_d were not calculated for this site.

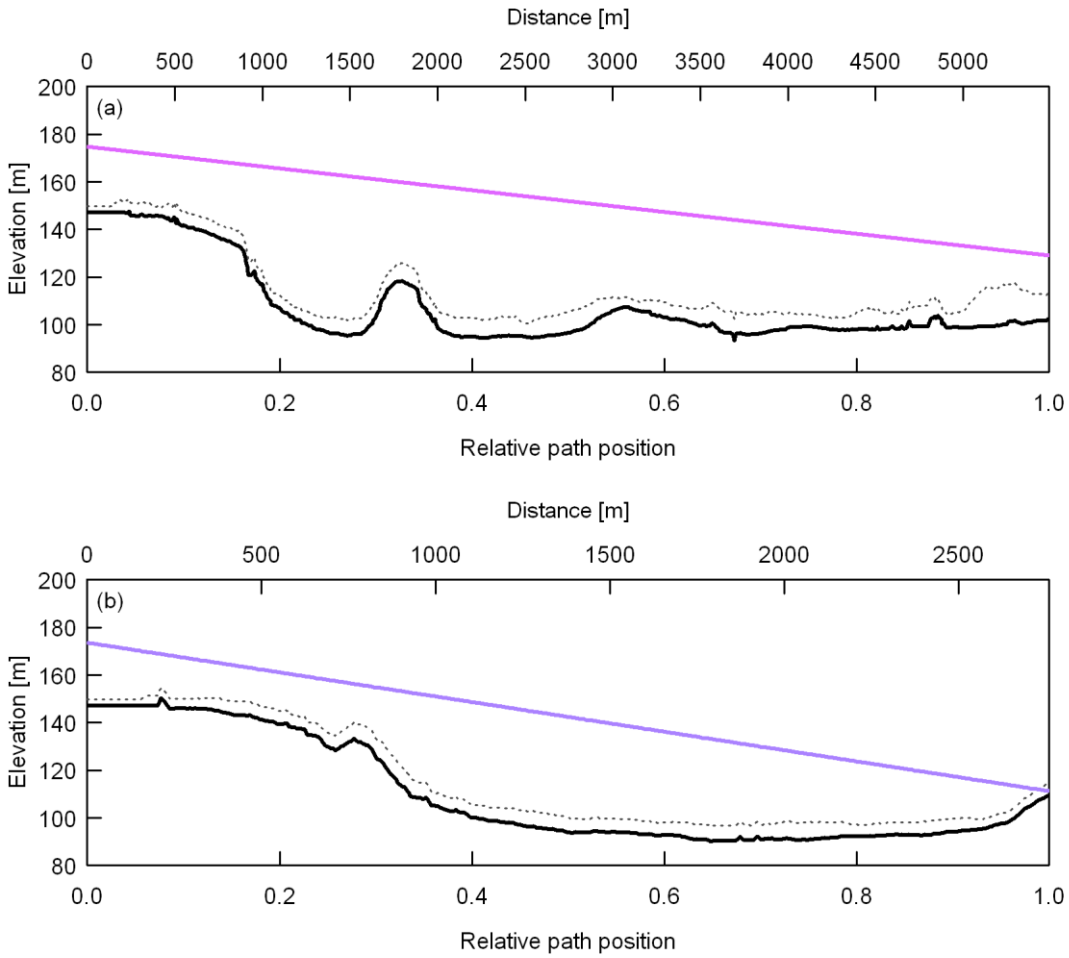

Figure 5-2 Cross section of the topography (solid black line) and mean obstacle height (dotted line, buildings and trees within a radius of 100 m) along the (a) BLS and (b) LAS paths (coloured lines).

A CR5000 datalogger (Campbell Scientific Ltd., Loughborough, UK) sampled the intensity of the received LAS signal at 500 Hz and measured the logarithm of the C_n^2 signal (calculated onboard the instrument) every second, which was then output at 1 min intervals and these averaged to 10 min. For the BLS, the mean and standard deviation of the beam intensity of each disk (the BLS900 is a dual disk instrument with two transmitting apertures) were obtained from the supplied signal processing unit at 30-second intervals, then converted to log-amplitude variances and C_n^2 and averaged up to 10 min. Data from a single disk are presented here, except for the wind speed comparison which requires the dual-disk functionality (Section 5.3).

The EC system consists of a sonic anemometer (R3, Gill Instruments, Lymington, UK) and open-path infrared gas analyser (LI-7500, LI-COR Biosciences, Lincoln, USA) at a height of 12.5 m. This is 2-3 times the height of the surrounding buildings and trees and therefore

sufficiently high to deliver fluxes representative of the local-scale. Data were processed using EddyPro (v3.0.0beta, LI-COR) following the conventional procedure. Further details of the EC measurements can be found in Chapter 4.

Meteorological instruments were installed on the same mast as the EC equipment (denoted MET_{sub}). A second set of meteorological data were collected at a rooftop site close to the town centre (MET_{roof}). Both stations included a four-component radiometer (NR01, Hukseflux, The Netherlands), automatic weather station (WXT, Vaisala, Finland) and tipping bucket rain gauge (0.2 mm tip, Casella CEL, Bedford, UK). At MET_{sub}, the radiometer was installed at a height of 10.1 m so that the downward-facing field of view comprises a mixture of surfaces: grass lawns and verges, road, pavement, hedges and small trees, bare soil, gravel, roofs of garages, small sheds and single-storey extensions and walls (brick and painted). At MET_{roof}, the radiometer was installed at 1.1 m above the roof surface made of grey synthetic material and black rubber matting. Additionally at MET_{roof}, a heat flux plate (HFP01, Hukseflux) was installed between the roof surface and rubber sheet, providing an approximation of the change in storage through the roof. At both sites the meteorological data were logged at 1 min intervals (CR1000, Campbell Scientific Ltd.) and subsequently averaged up to 10 min resolution for calculation of the scintillometer fluxes (Section 5.2.1) or 30 min for comparison with EC. The 10 min scintillometer fluxes were also averaged to 30 min for comparison with EC results. Details of the experimental setup are summarised in Table 5-1.

To provide nearly continuous auxiliary data required for scintillometry processing, results from the two meteorological stations were combined. When available, data from MET_{sub} is used as the siting of this station is more appropriate. Based on the regression of concurrent data (9 May 2011 - 31 December 2012), temperature, relative humidity (RH), pressure and wind speed at MET_{roof} were adjusted to gap-fill the combined dataset, including the period prior to installation of MET_{sub} on 9th May 2011. This is considered further below (Section 5.2.3).

All data were subject to quality control routines. Data were removed at times of known instrument malfunction. Meteorological data were excluded when they (or their standard deviations) fell outside physically reasonable thresholds. Quality control of the scintillometry data included rejecting times when the received signal intensity dropped below half of the value in clear conditions, which usually indicated rain or fog. Data points neighbouring those that failed the intensity check were also removed. Out of the total data collected, 84% of BLS and 82% of LAS data (10 min) remained for analysis.

Both scintillometers were corrected for the effects of saturation using the modulation transfer function of Clifford et al. (1974). According to the threshold value suggested by Kleissl et al. (2010), 16% of the BLS data and 0.2% of the LAS data might be expected to suffer from saturation. Overall, the correction increased C_n^2 by 4% and 1% for the BLS and LAS respectively (naturally the corrections are larger with increased scintillation and rise to 8% and 2% considering midday periods only).

Recent studies have indicated sometimes severe discrepancies between certain scintillometers, in particular the LAS 150 model, whereas the BLS900 model tends to give more reproducible results (Kleissl et al., 2009b). Prior to deployment in Swindon, the LAS and BLS were run alongside each other at a fairly homogenous grass test site at Chilbolton Observatory, Hampshire, UK (17 April 2010 – 25 May 2010). Observed C_n^2 ranged between 10^{-16} $m^{-2/3}$ and 10^{-12} $m^{-2/3}$ which spans the range of values observed for the Swindon paths. Results suggested the response of the LAS is reasonable but compared to the BLS C_n^2 is overestimated by 9.8%. This adjustment has been applied to the LAS for the Swindon data.

5.2.3 Assessment of the input meteorological data

First, the suitability of the combined meteorological input data used to process the scintillometry fluxes is considered. To calculate Q_H from single-wavelength scintillometry, air temperature, pressure and humidity are required to first obtain the structure parameter of temperature, C_T^2. Both T and RH differ by less than 3% and there is high correlation $r^2 > 0.98$ between the (MET_{sub} and unadjusted MET_{roof}) sites. Sensitivity of Q_H to these input meteorological variables is small (Hartogensis et al., 2003) and indeed these very small differences have minimal impact on the fluxes. The average difference in Q_H is < 0.5% when calculated using T, RH and p from each site. Use of this combined dataset is therefore judged unproblematic and to be a sufficiently accurate representation of T, RH and p across the study area.

An initial estimate of the Bowen ratio is recommended to account for the contribution of humidity and combined temperature-humidity fluctuations to optical C_n^2 (Wesely, 1976). Usually the value of β is arrived at iteratively through incorporation of the available energy (e.g. Meijninger et al. (2002b)). However, estimating the available energy is challenging in urban areas as the net storage heat flux (ΔQ_S) plays a more significant role in the energy balance than for most rural areas (e.g. grassed or agricultural land), yet it is very difficult to measure directly (Offerle et al., 2005a; Roberts et al., 2006). Other (rural) studies have used β measured at a nearby station (Hoedjes et al., 2002; Samain et al., 2011a) or have calculated Q_H using a series of values of β (Meijninger and De Bruin, 2000). When β is expected to be large

(e.g. > 0.6 for Chehbouni et al. (2000b); Moene (2003) advises > 1) the correction may be neglected. Given the uncertainty in estimating the available energy and the lack of representative EC data across the whole area, the Bowen ratio correction has not been applied for the results presented here. The potential impact is an average overestimation in Q_H from the scintillometers of less than 5% for $\beta > 1$, and less than 10% for $\beta = 0.5$.

To process scintillometry data, the friction velocity is usually estimated from wind speed measured at a single point and adjusted to beam height using the logarithmic profile accounting for stability. Over complex topography and heterogeneous surfaces the wind field varies spatially (e.g. Oke (1987)) and the friction velocity associated with the point measurement may differ to the path-averaged value. As with the other meteorological inputs, wind speed from MET_{roof} was adjusted to produce the combined dataset with optimum availability of input data. Concurrent Q_H values calculated using the MET_{sub} wind speed or the adjusted MET_{roof} wind speed differ by less than 3%, r^2 is high (0.98) and there is little scatter (RMSE < 10 W m^{-2}).

5.3 Comparison of wind speeds

The dual-disk capability of the BLS900 enables the path-averaged crosswind to be measured, i.e. the component of the wind speed perpendicular to the scintillometer path. The retrieval is based on the time-lagged cross-correlation of the signals from each disk (Scintec, 2009) but details of the algorithm are unpublished. Here, the crosswind output by the BLS is compared to crosswind calculated from the sonic wind speed and direction and scaled to beam height using stability (L_{Ob}) from EC and a local value of z_0 = 0.5 m and z_d = 3.5 m. Overall there is good agreement between BLS and EC estimates of crosswind and both instruments indicate the same trends across a range of wind speeds and directions (as an example 20 days in July 2010 are shown in Figure 5-3). The correlation between the datasets is high (r^2 = 0.957 for all available data, Figure 5-4), suggesting that the EC data generally capture the variability of the wind field at the larger scale. This supports the assumption that the measurements are made above the roughness sub-layer.

However, the BLS tends to overestimate the EC crosswind, even after scaling to the effective beam height (regression slope of 0.763). This height scaling depends on z_0: larger z_0 gives larger wind speeds. The spatial variability in z_0 and difficulty of accurate parameterisation increases the uncertainty on the scaled wind speeds (and hence on the friction velocity for calculation of the fluxes). The mean wind speed measured by the sonic anemometer is 3.1 m s^{-1} at 12.5 m ($z_m - z_d$ = 9 m); when scaled to the effective beam height (of 45.0 m) the mean wind speed is 5.1 m s^{-1} for z_0 = 0.50 m, 4.7 m s^{-1} for z_0 = 0.25 m and 5.7 m s^{-1} for z_0 = 1.00

m. The scaled EC crosswind matches the BLS crosswind for z_0 close to 2 m (Figure 5-3). Although anemometric estimates of the surface roughness vary around the EC site and the simple morphometric parameterisation $z_0 = 0.1 z_H$ suggests a larger roughness length for the source area of the BLS compared to EC (Table 5-1), values much above 1.5 m seem unrealistically high.

Experimental evaluations of the BLS crosswind measurement, such as with a network of anemometers, have not been reported in the published literature. Van Dinther et al. (2013) made a comparison between a single sonic anemometer and a short path of 426 m over a flat homogeneous grass site and found that the method used by the BLS overestimated the crosswind by about 20% and performed less well than their proposed algorithms which use a single disk. Issues with obtaining crosswind from scintillometry over less ideal sites are discussed in Poggio et al. (2000) and in Appendix A. Despite the complex environment in Swindon, the crosswind comparison looks promising in terms of capturing the variability but it is not possible to validate the BLS data with the current experimental setup. Given the uncertainties in characterising the surface and the large difference between the sonic height and beam height, we cannot judge whether the BLS represents the wind field accurately, but overestimation seems likely given the large value of z_0 apparently required to match the BLS wind speed data with height scaled EC data. The purpose of this comparison is to check that the wind data at the EC site are a realistic proxy for the wind field over the scintillometer source area. The strong correlation between EC and BLS crosswinds gives confidence in the use of wind speed measured at the suburban garden site in the scintillometry processing. The wind speed measured by the WXT at the MET_{sub} site (10.6 m on the EC mast) also demonstrates strong correlation with the EC data. The WXT data was used to process the scintillometer fluxes to maintain independence between the EC and scintillometer datasets. The EC (3-D sonic) data were used in the above comparison so that the stability (L_{Ob}) could be accounted for in the crosswind scaling.

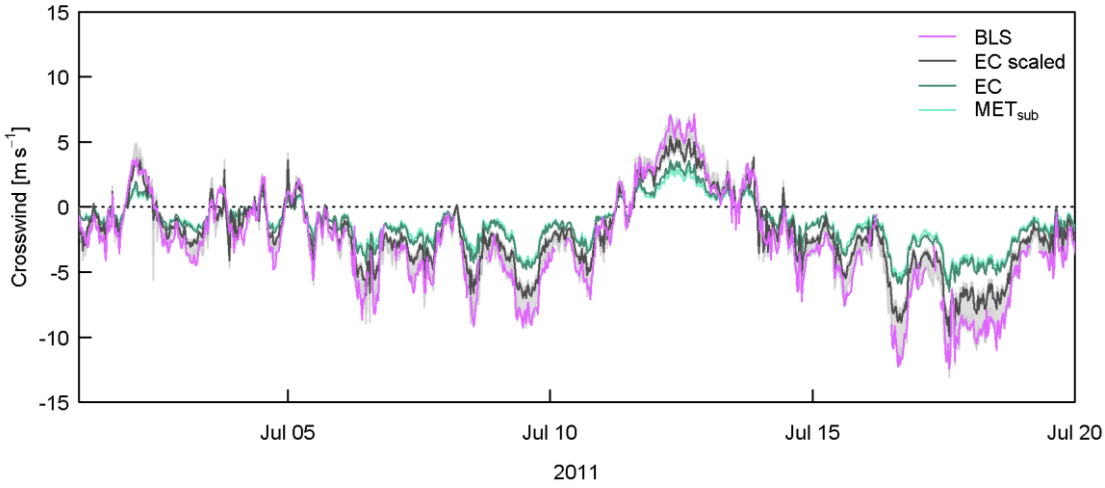

Figure 5-3 Crosswind for 1-20 July 2011 calculated using different methods: (1) measured by the BLS; (2) the component of the wind speed at 12.5 m perpendicular to the BLS path measured by the sonic (EC); (3) the wind speed of (2) scaled to the BLS effective height using stability from EC and z_0 of 0.5 m (EC scaled) (shading indicates the scaled wind speed range for z_0 = 0.25-2.00 m); and (4) the component of the wind speed at 10.6 m perpendicular to the BLS path measured by the 2-D sonic on the WXT (MET$_{sub}$).

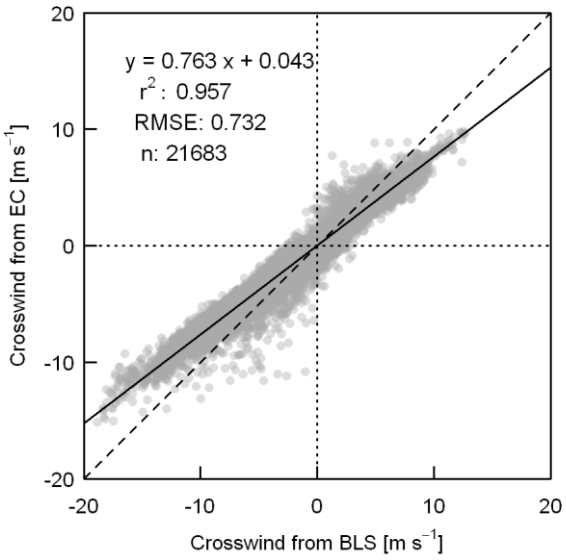

Figure 5-4 Crosswind calculated from EC data and scaled to beam height against crosswind measured by the BLS for all available data (30 min means). The BLS crosswind was removed whenever C_n^2 failed quality control checks.

5.4 Analysis of sensible heat fluxes

5.4.1 Assessment of seasonal cycles and annual variations

Large-area sensible heat fluxes from the 5.5 km scintillometer path are presented for two years 2011-12, alongside 18 complete months of data from the shorter 2.8 km scintillometer path and almost 20 months of eddy covariance data (Figure 5-5). The annual cycle is evident,

with mean daily (24 h) Q_H reaching a maximum in early summer (May-June in 2011, May in 2012) and minimum in December (Figure 5-5a). In December, the average Q_H is negative even during daytime (defined as incoming shortwave radiation $K_{\downarrow}$ > 5 W m^{-2}, see Figure 5-5b) as the typical diurnal course of Q_H becomes positive only for a few hours around midday (Figure 5-6). This behaviour is observed consistently across the three datasets and in both years but contrasts with the majority of urban studies in more built-up areas, where greater heat release from storage and anthropogenic activity can maintain a positive sensible heat flux all year round (Offerle et al., 2005a; Kotthaus and Grimmond, submitted-a). For two sites in Oberhausen, Germany, Goldbach and Kuttler (2013) found Q_H to be positive for most of the daytime throughout the year at their urban site, whereas their suburban site exhibits similar behaviour to Swindon. Besides the smaller storage and anthropogenic heat flux in suburban areas, more of the available energy is partitioned into evaporation, owing to increased moisture availability from soil surfaces and greater total evapotranspiration from a larger vegetation fraction.

Within the trends of the expected annual cycle, there are notable differences between the two years studied. Peak Q_H is larger in summer 2011 compared to 2012 and month-to-month variation is smaller in 2011. Broadly speaking, much of 2011 was under threat of drought, with dry soil moisture conditions and low ground water levels. Despite frequent rain and very few clear sky days the annual rainfall total was 530 mm compared to the average 780 mm for southern England[1]. Dry conditions continued through early spring 2012, until early April. Very wet weather followed and remained throughout 2012 (total rainfall 1020 mm), with brief drier and warmer spells in late July and early September.

June 2012 was particularly wet and cloudy (sunshine hours were only 70% of normal[2]; mean daytime $K_{\downarrow}$ was 174 W m^{-2} in 2012 compared to 212 W m^{-2} in 2011). Monthly mean daily Q_H was 19% and 32% lower than in June 2011 for the BLS and EC, respectively. August 2012 also had a notably lower Q_H during daytime compared to 2011 (also shown in Figure 5-6), despite similar radiative energy inputs in both years. A long dry spell and generally sunny weather in September 2012 allowed surfaces to dry out and Q_H to increase, resulting in a larger average value than for the previous month. Large negative nocturnal Q_{H_BLS} in February 2011 means the daily average is negative, whereas it is positive in 2012 (Figure 5-5).

[1] Met Office climate statistics (1971-2000), http://www.metoffice.gov.uk/climate, last accessed 29 March 2013

[2] Met Office climate statistics (1971-2000), http://www.metoffice.gov.uk/climate, last accessed 29 March 2013

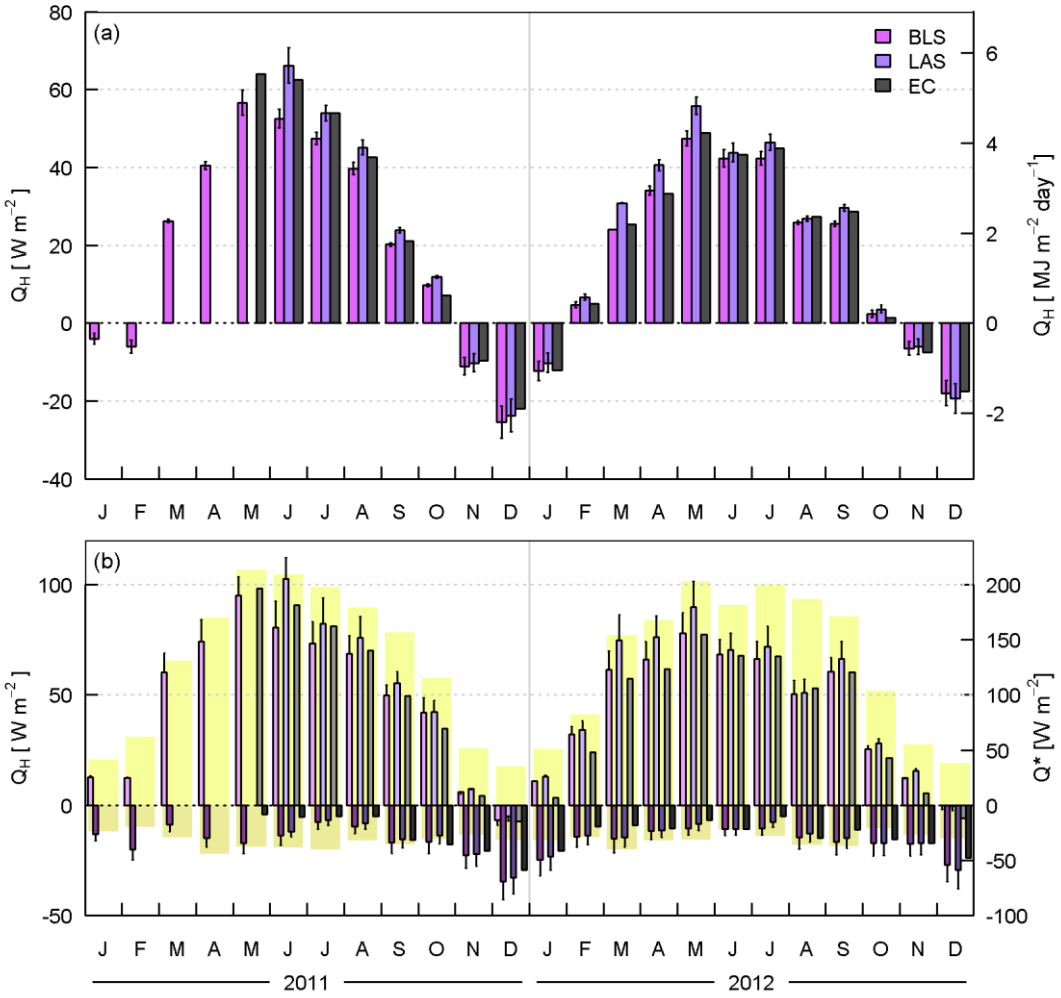

Figure 5-5 Monthly mean sensible heat flux observations from scintillometry (BLS and LAS) and eddy covariance (EC) for (a) all available data over 24 h and (b) separated into day ($K_{\downarrow}$ > 5 W m^{-2}) and night times. Partial months in relation to the installation dates (Table 5-1) are January 2011 (BLS), May 2011 (EC) and June 2011 (LAS). Error bars indicate the impact on the scintillometer fluxes of altering the input roughness length by ± 0.2 m (a) or using the similarity functions of De Bruin et al. (1993) (b). The net radiation (shading) is shown in (b) on the right-hand axis.

Overall there is remarkably good agreement across the three areal extents and between techniques, which captures seasonal similarities and inter-annual variability. The different source areas of each instrument, and that the BLS measures across a large proportion of northern Swindon, suggest that these trends are local-to-city-scale responses to regional weather variability. Furthermore, this agreement implies that any bias in the monthly averages due to the effect of the wind direction distribution on the measurement footprints is outweighed by the changes in surface conditions, prevailing weather and the resulting surface-atmosphere interactions. Given the much smaller source area of the EC technique compared to scintillometry, it is reasonable to expect that heterogeneity of the surface has a larger influence on the EC observations than the scintillometry observations (Section 5.4.3).

Typically, the uncertainty in z_0 is large as z_0 can vary spatially, with time of day and stability (Grimmond et al., 1998; Hoedjes et al., 2007; Zilitinkevich et al., 2008), and with shape, density and arrangement of surface structure (Grimmond and Oke, 1999a). For the study area, the true value is expected to be within the range 0.4 to 1.0 m based on values in the literature. The impact on Q_H of changing the prescribed values of z_0 by ±0.2 m is ±7% (error bars in Figure 5-5a). Although the flux is fairly sensitive to the value of z_0 used, the overall trends do not change significantly. No adjustment was made to account for seasonal variation in z_0 (or z_d) which may be 10-20% smaller in winter (Grimmond et al., 1998). Using a smaller value of z_0 during leaf-off periods would decrease the wintertime fluxes slightly (the error bars in Figure 5-5a represent a change in z_0 of about ±30%).

Allowing a ±5% uncertainty in z_{ef} (±2.25 m) affects the fluxes by ±3%. This uncertainty in z_{ef} includes measurement accuracy and variation of the effective height with stability as well as accounting for spatial differences in obstacle height (hence z_d) and topography. The large beam height and relatively small displacement height help to keep the sensitivity to z_{ef} (and z_d) small.

The LAS tends to give the largest Q_H, particularly during daytime, compared to both EC and the BLS. In summer 2012 the EC and BLS average values do not reach above 150 W m^{-2}, in contrast to Q_{H_LAS} (Figure 5-6). During winter months (November 2011-January 2012) and at night the BLS gives the largest fluxes. Daily average Q_{H_EC} often lies between the two scintillometer averages but during winter (November-December 2011, December 2012) and at night the scintillometers tend to give larger magnitude Q_H. Larger scintillometer fluxes in neutral-to-stable conditions likely reflect the performance of the similarity functions. This can be seen in Figure 5-6: the absolute size of Q_H from the scintillometers is larger (e.g. around transition times in December), whether positive or negative, whereas for EC values are much closer to zero.

Using the De Bruin et al. (1993) similarity functions rather than those of Andreas (1988) increases Q_H by about 13-14% (bars in Figure 5-5b). This is similar to results in Marseille (Lagouarde et al., 2006) and within the 10-15% range given by Beyrich et al. (2012). The large uncertainty introduced through similarity functions is a major limitation of the scintillometry technique across all environments; it is not confined to urban sites although there is the added question of whether functions developed over homogeneous terrain should be applied to more heterogeneous locations. Kanda et al. (2002) and Roth et al. (2006) both derived 'urban forms' of the similarity functions for their small aperture scintillometer studies, however their paths were closer to, or within, the roughness sub-layer. Other large aperture studies in urban

environments have used the more common functions (Lagouarde et al., 2006; Zieliński et al., 2012).

The choice of similarity function is an ongoing issue in scintillometry and often limits the accuracy with which the fluxes can be known. Investigation into the scaling of C_T^2 with stability is presented in more detail elsewhere (Chapter 8). Using the functions of a conventional form, such as An88 and DB93, is found to overestimate Q_H in neutral conditions (f_{MO} is too small so the T_* obtained is too large). Thus Q_H values close to zero are underrepresented or not obtained. However, as the absolute magnitude of these fluxes is small we implemented the widely used An88 functions for these results.

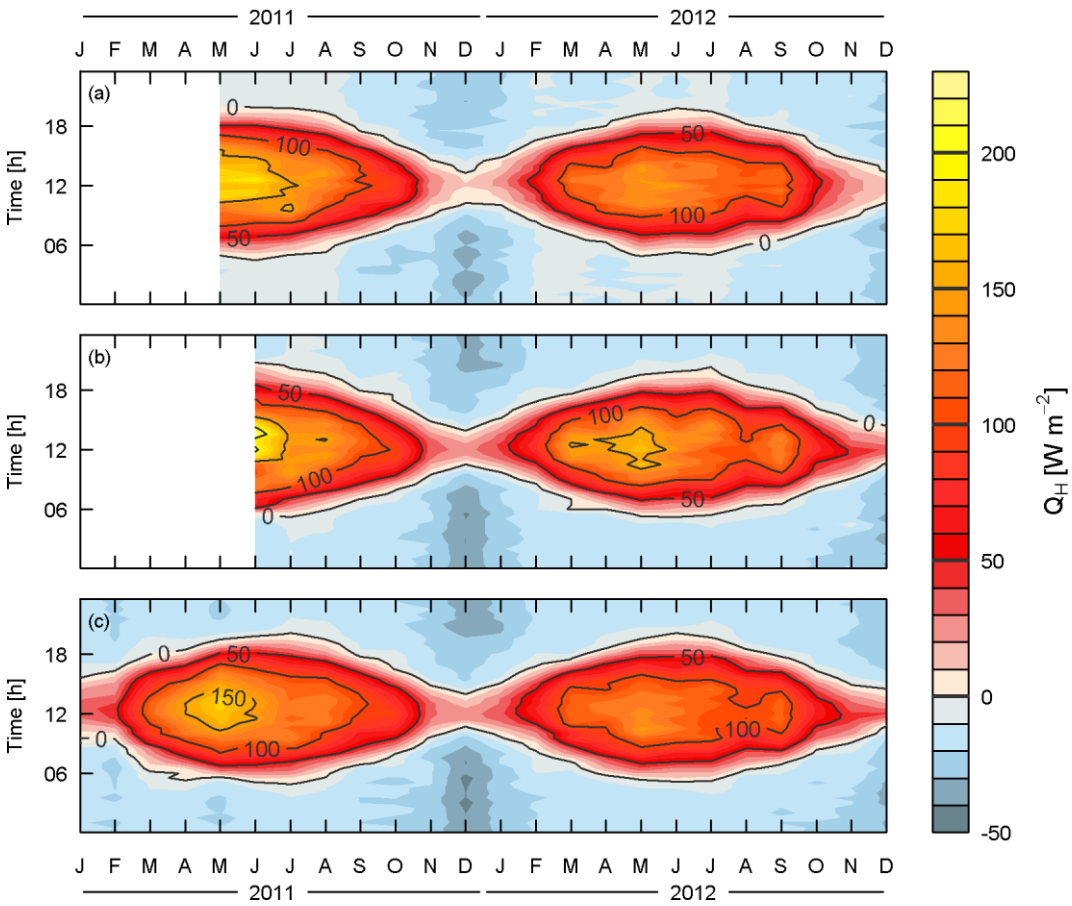

Figure 5-6 Temporal variation of monthly mean sensible heat fluxes from (a) eddy covariance, (b) the LAS and (c) the BLS by time of day.

5.4.2 Short-term variability

Direct comparison of 30 min sensible heat fluxes obtained from scintillometry and EC (Figure 5-7) indicates reasonably good agreement between the measurement techniques and across the scales with strong correlation (r^2 ≈ 0.87). The slope of the regression between

Q_{H_LAS} and Q_{H_EC} is close to 1, with a small positive offset, whereas the BLS tends to give lower Q_H than EC particularly towards large values of Q_H. Whilst the linear fit between Q_{H_LAS} and Q_{H_EC} is a good match to the data, for the BLS the distribution of data points appears more curved at high Q_{H_EC}. When the EC and scintillometer results are expected to be representative of the same or similar surface, this curvature can often indicate saturation of the scintillometer (Meijninger et al., 2006). For the Swindon setup, however, the source area of the EC and BLS are quite different, which may also explain why the highest EC fluxes are not matched by the BLS. Specifically, the area to the south and southwest of the EC mast has a particularly high proportion of built and impervious surfaces and little vegetation, whilst the BLS source area always includes open green spaces. Thus when the EC footprint is over the least vegetated sector (180-240°), the measured Q_{H_EC} tends to be larger compared to other wind sectors around the flux mast as well as to the scintillometer results. This effect would be amplified when surface water is scarce.

When summertime data are stratified by wind direction (Figure 5-8), both Q_{H_LAS} and Q_{H_BLS} are lower than Q_{H_EC} when the wind is from the south. For more westerly wind (240-270°) the EC source area contains more vegetation and there is closer agreement between Q_{H_EC} and Q_H from the scintillometers. Despite having corrected the scintillometers for saturation (Section 5.2.2), it is possible that the BLS data may still be affected. Other studies have suggested that the effects of saturation may still be observed above commonly-used thresholds (Kohsiek et al., 2006). Some curvature remains in Figure 5-8, although Q_H does not seem to be saturating at a particular value with many data points between 200-300 W m^{-2}.

During night and transition times, the agreement between the datasets is poorer (r^2 decreases to around 0.4). This is to be expected for several reasons: (1) the limitations in instrument performance are reached when fluxes are small; (2) atmospheric conditions do not always satisfy the assumptions required for the measurement theory (e.g. weak turbulence, non-stationarity, poorer performance of similarity functions); (3) the time of stability transition may vary with location, even along the scintillometer paths, so that the three values of Q_H obtained for a given time period may not have the same sign. Removing the night time data causes the regression slopes in Figure 5-7 to decrease slightly to 0.77 (BLS) and 0.94 (LAS), and the intercepts to increase to 13 W m^{-2} (BLS) and 9 W m^{-2} (LAS). The increase in intercepts likely results from the overestimation of small fluxes by the most widely used similarity functions (Chapter 8). For night time data only, the intercepts are similar in size but of opposite sign. Lagouarde et al. (2006) also noted an overestimation (15 W m^{-2}) of small night time Q_H values using An88 and DB93 (unstable forms). Considering all data together (Figure 5-7) the lack of

small Q_H values from the scintillometers can be identified around zero. Although this is undesirable, the small size of the fluxes at these times means that absolute errors are small.

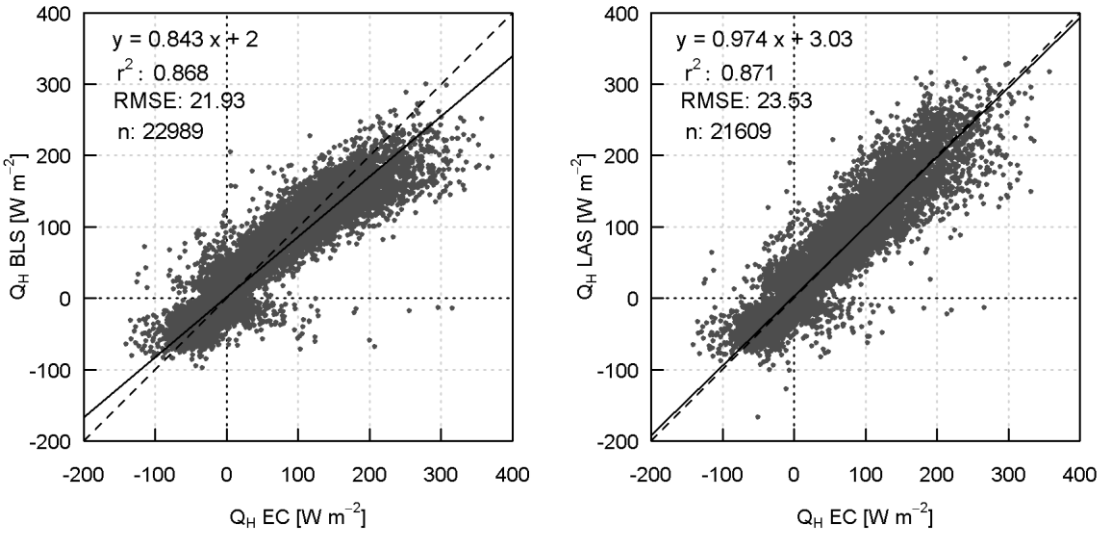

Figure 5-7 Comparison of 30 min sensible heat fluxes derived from the scintillometers (BLS, LAS) and eddy covariance (EC) for all available data.

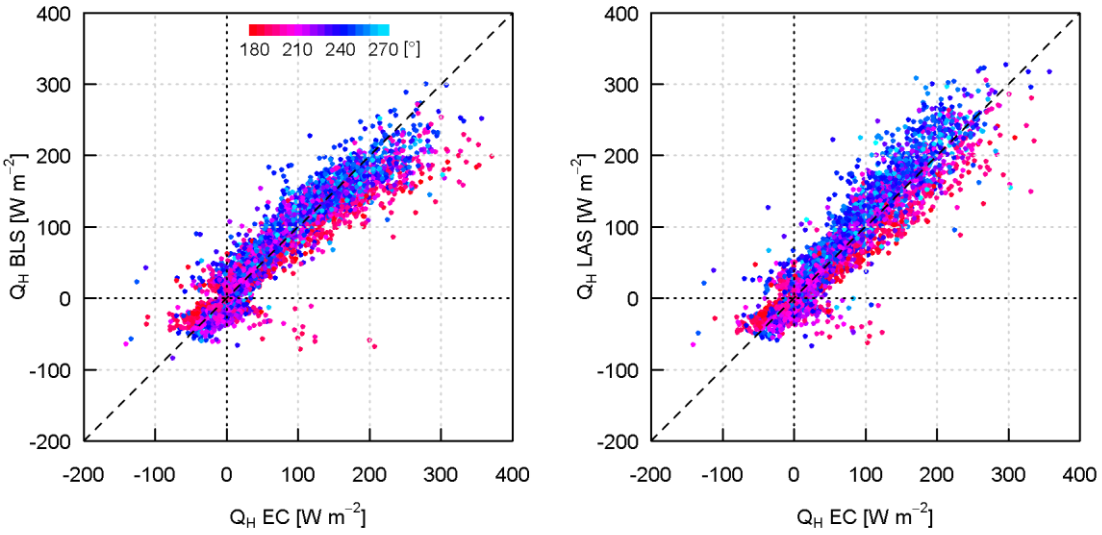

Figure 5-8 As for Figure 5-7 but for summertime (May-September 2011-12) data only and for wind directions 180-270° (colours).

The diurnal course of Q_H obtained from the three systems follow each other closely: example days from July 2012 are shown in Figure 5-9. No rainfall was observed during these mostly clear-sky days although the influence of cloud cover can be seen on the morning of 22 July and afternoon of 25 July. On 22 July the fluxes respond consistently to changes in the net radiation and the peaks and troughs are closely matched between EC, LAS and BLS

observations. Data from MET_{roof}, approximately 3 km southwards (Figure 5-1), closely matches the variation in Q^* measured at the EC site. Time-lapse photography reveals fairly uniform, almost full cloud cover at sunrise which clears throughout the morning. On the afternoon of 25 July, however, the situation is quite different. Rapidly changing patchy cloud cover creates spatial variability in the radiation balance components. The responses of the two radiometers are less well correlated (compare Q^* and Q^*_{roof} in Figure 5-9) and Q_H is seen to respond differently across the different measurement scales. Not surprisingly, Q_{H_EC} most closely matches Q^* as both are measured at the same location and have more similarly sized and at least partially coincident source areas. In general, the scintillometers yield a more smoothly varying diurnal course than EC, often attributed to the greater spatial averaging by scintillometers (e.g. Lagouarde et al. (2006), Guyot et al. (2009)). The BLS appears to vary more smoothly than the LAS (e.g. 24 July) which is consistent with the size of their source areas.

For clear days, the phase of Q_H is lagged relative to Q^*: at the three scales Q_H peaks after Q^* and remains positive later into the evening than Q^*. One component of the urban net heat storage flux is approximated by a heat flux plate installed under the roof covering at MET_{roof} (ΔQ_{S_roof} in Figure 5-9). This flux increases earlier in the day and becomes negative long before Q^*. In this way, release of stored energy enables Q_H to remain positive even when Q^* is negative (Oke and Cleugh, 1987; Lemonsu et al., 2004). Normalising these fluxes by the net radiation clearly demonstrates the opposing hysteresis patterns of Q_H compared to ΔQ_{S_roof} (Figure 5-9b). The proportion of Q^* directed into sensible heat increases throughout the day whereas the proportion of energy used to heat the surface decreases. Strong hysteresis is evident on clear days but it tends to be less obvious on cloudier days. Similar patterns have been observed at other urban sites at the local-scale (Grimmond and Oke, 2002; Grimmond et al., 2004). Here we demonstrate that the phase lag between Q_H and Q^* is observed right across the urban environment, from the local-scale up to the city-scale. The shift in peak Q_H around midday and into early afternoon can also be seen to some extent in the average monthly values (Figure 5-6), particularly in spring and early summer 2011.

Other than under conditions of rapidly changing Q^*, and its associated high spatial variability, the diurnal patterns in Q_H derived from EC and the scintillometers match those of Q^* measured at the EC site (Figure 5-10). On 21, 22 and 27 July 2011 the sudden drop in Q^* during the middle of the day is also seen in Q_H. The day-to-day variation in these two quantities is also very similar. For example Q^* and Q_H steadily increase to reach over 600 W m^{-2} and 200-300 W m^{-2}, respectively, on 25 July when peak Q_{H_BLS} is about 2/3 of Q_{H_LAS}. Both Q^* and Q_H are lower during the following few days until 29 July when the net radiation remained very small throughout the day (< 100 W m^{-2}) and conditions were mostly

near-neutral (according to the EC data). On this day the agreement between the scintillometers and EC is poorer, although the fluxes show some agreement in responding to the dip in Q^* in the afternoon. The small scintillometer fluxes are possibly overestimated by similarity scaling (Section 5.4.1).

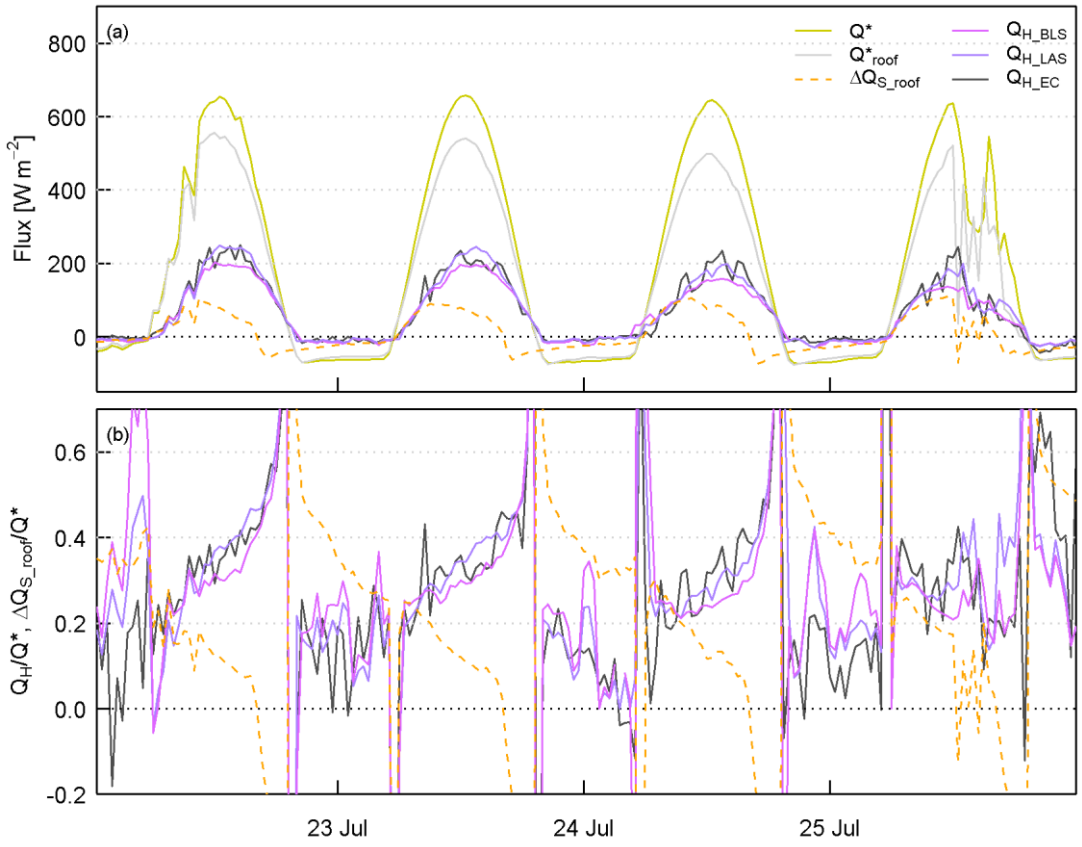

Figure 5-9 Diurnal variation in sensible heat flux (Q_H) and net radiation (Q^*) for four days in July 2012. Data from a heat flux plate installed on a rooftop, representing one component of the storage heat flux (ΔQ_{S_roof}) and a second radiometer located on the rooftop (Q^*_{roof}) are also shown. In (b) the fluxes are normalised by the net radiation measured at the EC site (Q^*).

The sign of the scintillometer sensible heat flux must be assigned during processing. Here, the stability was assumed to change from stable to unstable at the first minimum in C_n^2 on each day, and from unstable to stable at the second minimum. Hence for each 24 h period this always results in some stable and some unstable data and the proportion of each depends on the observed behaviour of C_n^2 (effectively how long between the morning and evening minima). As is evident from the data, this method generally performs well in Swindon, where EC data suggests Q_H tends to be positive for some duration around midday and negative at night (Chapter 4). However, there are some days when the stability transition does not occur and either unstable conditions prevail throughout the night or stable conditions throughout

the day. In these cases the sign of the fluxes from the scintillometers may be incorrect but these occasions are observed infrequently and the size of the fluxes tends to be small so the impact is fairly unimportant.

The day-to-day (night-to-night) changes in amplitude are usually captured (e.g. decreasing magnitude of nocturnal Q_H 24-27 July 2011 in Figure 5-10b) and for some days the evolution of Q_H throughout the night is similar (e.g. decreasing 20-21, increasing 25-26 and 26-27 July 2011, Figure 5-10b). This clear relationship between the scintillometer and EC fluxes gives confidence that the measurement heights are suitable; in particular that the scintillometers are not measuring above the surface layer. In the winter months, occasionally there are periods of a few hours to days when the shallow surface layer means the scintillometer measurements cannot be related to surface fluxes via MOST (Braam et al., 2012). The EC data further supports these findings with very few cases of strongly stable stratification observed (ζ_{EC} < 0.1 for 89% of data).

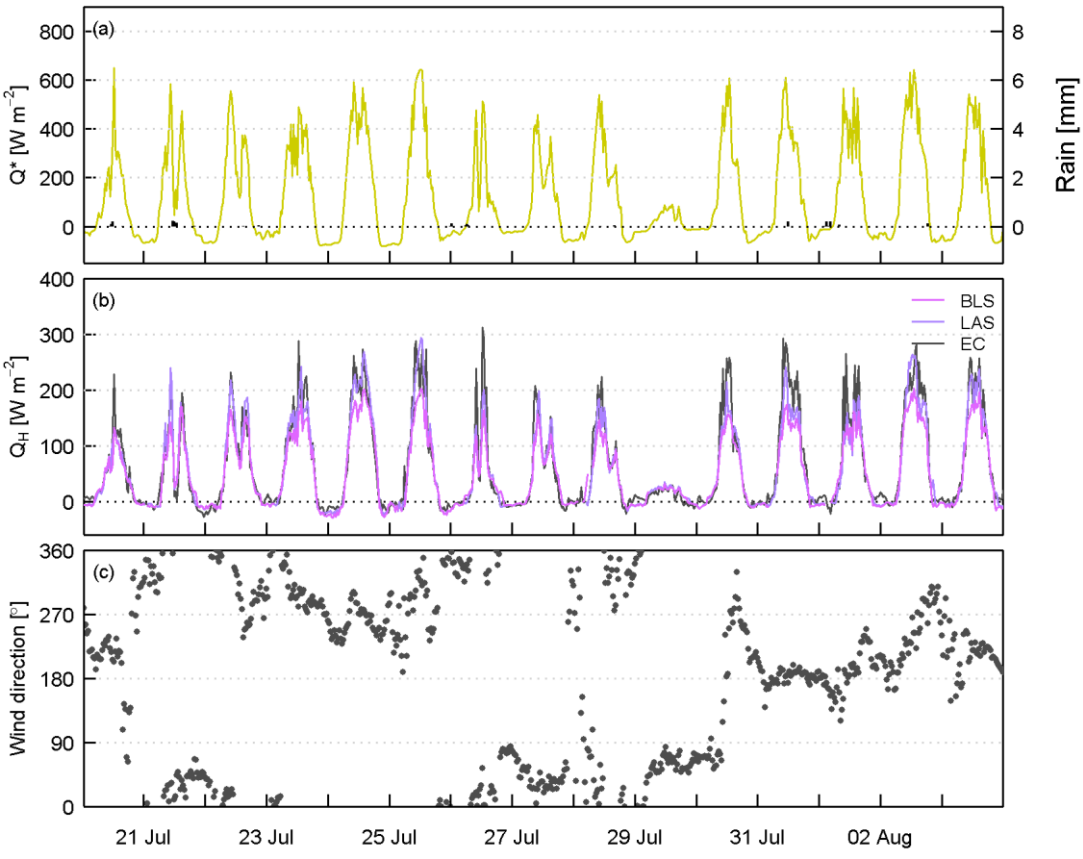

Figure 5-10 Sensible heat fluxes from EC and the scintillometers alongside net all-wave radiation from the EC site (Q*), rainfall and wind direction (also measured at the EC site) for two weeks in July-August 2011.

5.4.3 Influence of the surface

Comparing the relative sizes of the fluxes can offer insight into key controls. Towards the end of the case study in Figure 5-10 (30 July-01 August 2011), Q_{H_EC} peaks at larger values than from either of the scintillometers, whilst Q_{H_LAS} is generally largest near the beginning of the period (21-25 July). The wind direction (Figure 5-10c) provides a partial explanation due to the variation in source areas. For westerly to northerly winds, Q_{H_LAS} tends to be largest. All three fluxes become similar during northerly winds, when there is a greater vegetation fraction within the source area of each instrument. For the scintillometers the footprint will extend to include some of the rural farmland beyond the edge of the suburbs; at the EC site the increased vegetation is due to more gardens to the north of the mast (see Chapter 4).

The period shown in Figure 5-11 (21 May – 31 July 2012) coincides with sudden vegetation growth in response to warm, sunny conditions at the end of May, completing the leaf-out period to reach maturity. Vegetation is then fully active throughout June and July. In this period a range of synoptic conditions (cloudy, mixed and clear days), frequent rainfall and a wide distribution of wind directions (although southwesterly was still dominant) occurred.

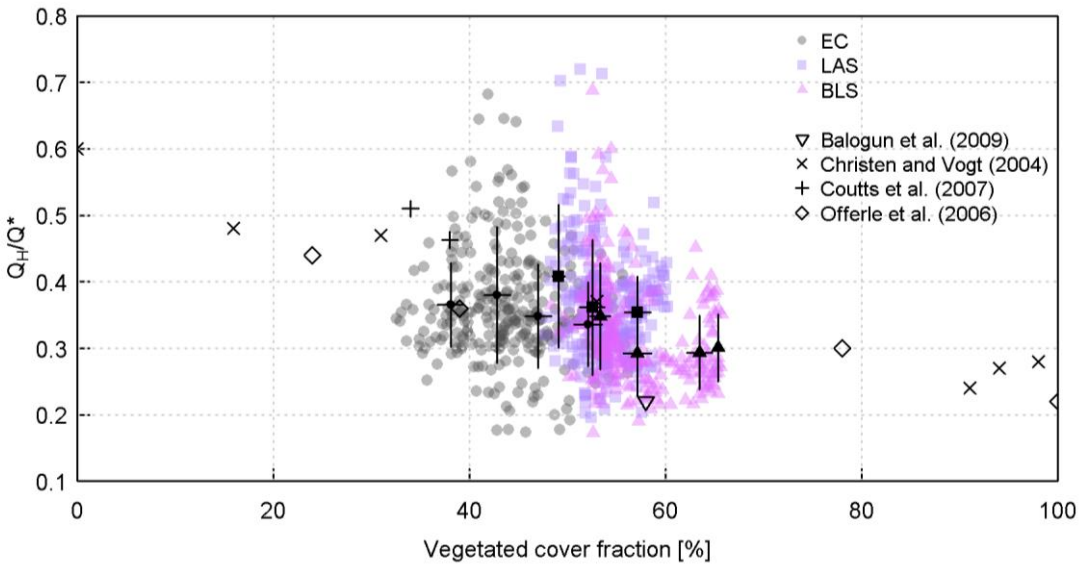

Figure 5-11 Ratio of observed sensible heat flux to net all-wave radiation versus the proportion of vegetation within the flux footprint of the EC station, LAS and BLS in Swindon. Points are 30 min values around midday (1100-1500 UTC) for the period 21 May – 31 July 2012. Data are excluded for times during and ≤ 2h after rainfall and when $K_{\downarrow} \leq 200$ W m^{-2}. Black symbols with error bars represent the mean ± standard deviation of the respective observed values binned in 5% intervals of the vegetated cover fraction (bins with > 10 data points are plotted). Average summertime values from various sites in the literature are shown for comparison (see references for details).

Footprint calculations for each 30 min period reveal an overall ranking of the vegetation fraction for each instrument that is in accordance with broad expectations given their respective sitings (EC < LAS < BLS). The mean vegetation fractions (± standard deviations) are 44.1 (±5.0) %, 53.9 (±2.9) % and 56.9 (±4.5) % for EC, LAS and BLS, respectively, for the data shown in Figure 5-11. The standard deviation is largest for the EC site, as might be expected (a) given the far smaller size of the source area and (b) the differences in surface cover with wind sector around the mast. The vegetation fraction ranges between 32.6% and 56.8% according to the EC footprint estimation for this period. The LAS source area characteristics are much less variable (minimum 47.7%, maximum 60.2%). The prominent retail park to the west of the path (Figure 5-1) constitutes a small proportion of the total source area and for westerly wind directions there is only a small increase in the built and impervious fractions. Despite having the largest area, the BLS footprint shows appreciable variability (48.3% – 65.7%), mostly associated with northerly or southerly winds when the town centre and nearby industrial areas (Figure 5-1) or rural surroundings are included in the footprint. For other wind directions the variability is much smaller. In addition to the directional aspect of the surface heterogeneity, the total area included in the scintillometer footprint is smaller when the wind direction is parallel, as opposed to perpendicular, to the scintillometer path (Meijninger et al., 2002b).

The ratio of Q_H to Q^* decreases as the proportion of vegetation within each instrument's source area increases (Figure 5-11). Normalising the turbulent fluxes by an indicator of the energy available largely removes this otherwise often dominant dependence (e.g. on insolation). The observed relation between vegetation cover and partitioning of energy into Q_H is in agreement with other published studies, including summertime data from Kansas City (Balogun et al., 2009), seven sites in Basel (Christen and Vogt, 2004), two sites (high and medium density) in Melbourne (Coutts et al., 2007b) and four sites in Łódź (Offerle et al., 2006). Use of the scintillometers in Swindon enables this comparison to be extended to larger scales.

These relationships between land cover and energy partitioning have mostly been developed for summer months, when the majority of field campaigns have taken place and do not account for differences in surface or synoptic conditions. Whilst there is generally good agreement between summertime datasets across a range of sites, those studies extending to winter demonstrate very different behaviour of Q_H/Q^*. In dense urban areas, the anthropogenic heat flux and much larger storage flux can sustain a positive sensible heat flux all year round (Goldbach and Kuttler, 2013; Kotthaus and Grimmond, submitted-a). In these locations, building density may be a more appropriate variable to use than vegetation fraction and the effect of the anthropogenic heat flux can result in Q_H that is significantly greater than

Q^*. The few campaigns spanning multiple seasons indicate temporal evolution of daytime Q_H/Q^*, e.g. between about 0.30 (winter) and 0.55 (summer) in Melbourne (Coutts et al., 2007b), and between 0.29 (December) and 0.49 (July) in Tokyo (Moriwaki and Kanda, 2004). The data presented here reveal daytime Q_H/Q^* peaks in spring between 0.4 and 0.5 and drops to about 0.2 in winter for Swindon. These seasonal changes incorporate multiple effects: the anthropogenic influences already mentioned, vegetative activity and the amount of incoming radiation are major factors, but do not account for inter-annual variability in meteorological conditions or rainfall. Average Q_H/Q^* for September 2012 is higher than expected from the seasonal cycle, which is unsurprising given the fair weather (see also Figure 5-5 and Figure 5-6). In February 2012 the limited moisture availability likely contributed to atypically high Q_H/Q^* of around 0.4.

At shorter timescales, the meteorological conditions and local stability both have an influence. Reduced availability of moisture constrains the latent heat flux and allows the sensible heat to increase (demonstrated in Swindon in Chapter 4). Inter-annual variations in rainfall can lead to differences in the size of the fluxes from year to year that cannot only be attributed to variations in Q^* (Figure 5-5). Although normalising by Q^* removes much of the dependence on the radiative energy, whether conditions are clear or cloudy can affect the response of the surface. Some studies have stratified results by cloud cover conditions (Grimmond and Oke, 1995; Balogun et al., 2009) although the effect on Q_H/Q^* is small. In Figure 5-11, data are excluded for $K_{\downarrow} \leq 200$ W m^{-2} and most of the remaining points greater than 0.6 occur under low insolation. The sensible heat flux is dependent on the amount of energy stored and released, which itself depends on the season (Offerle et al., 2005a), surface wetness (Kawai and Kanda, 2010) and cloud cover (Grimmond and Oke, 1995). The ability of the surface to store or dissipate heat depends primarily on the physical properties of the constituent materials, but may also be affected by changes in surface conditions, for example a wet surface may have a lower albedo than when dry (e.g. in Cairo (Frey et al., 2011)) and soil moisture can affect its conductivity. Different materials respond differently to direct and diffuse radiation (Kotthaus and Grimmond, submitted-b). In combination with surface morphology and changing solar elevation with latitude and time of year, this determines the impact of shadowing. To account for shading patterns in energy flux parameterisation schemes Loridan and Grimmond (2012) propose an 'active' built index. The latent heat flux also depends on these, and other, factors. To further develop understanding of such processes and interactions it will be necessary to focus more attention on the interdependencies between energy fluxes and how these are affected by surface conditions in urban areas.

Finally, although the Bowen ratio correction has not been applied to the data here, the biggest impact of the correction would be at small β. For β = 0.5, scintillometric Q_H is overestimated by 9% which would result in mean Q_H/Q^* being overestimated by 0.04. Implementing the β correction would act to further decrease Q_H/Q^* with vegetation fraction. As β itself has been shown to depend on the vegetation fraction, smaller β at larger vegetation fraction again acts to amplify rather than reduce the trend.

5.5 Conclusions

This work demonstrates the applicability of large aperture scintillometry for making spatially integrated observations over urban areas. With selection of a suitable path, adequately sited auxiliary meteorological measurements and knowledge of the land surface, sensible heat flux estimates are obtained that are representative of several neighbourhoods or across the settlement. Whilst EC measurements are representative of the local-scale (0.5 km^2), the scintillometer data in this study have a much larger source area: 3.0 and 7.5 km^2 (95% contribution) for the LAS and BLS, respectively.

Remarkable temporal agreement is observed across the three different areal extents for both short-term variability (e.g. the response to radiation patterns over a few hours to days) and seasonal trends. Differences in magnitudes of the fluxes between sites are attributed primarily to the role of vegetation. Comparison with large-area fluxes at the city-scale provides some context for the EC dataset and confirms that the site selection was appropriate. However, some important differences are also observed. As has been noted previously, the scintillometer fluxes tend to be smoother as a result of the greater spatial averaging. The large-scale flux measurements are much less sensitive to source area variability, for example due to changing wind direction over heterogeneous surfaces. These large-area fluxes are more representative of the study area and suffer less from sampling bias. EC measurements are easily influenced by variable land cover or surface characteristics around the mast. The effect can be decreased by measuring at a greater height, but in general the land cover must be carefully examined for each wind sector before drawing conclusions on the representativeness of data from a single EC site.

For many purposes we are interested in fluxes at large scales, whether the application is input data for, or evaluation of, land-surface models or numerical weather prediction, assessment of satellite remote sensing products or representative observational datasets to characterise a particular environment. Scintillometry offers a promising way forward, but there are still limitations. A major source of uncertainty arises from the MOST functions. This is an area that would benefit from further attention for all sites and has implications beyond

improving the accuracy of fluxes from scintillometry. Single-wavelength scintillometry may be best suited to urban areas with little vegetation as the higher the Bowen ratio the smaller the error due to neglecting the β-correction (Equation 5-1). Given the potential for saturation, particularly if the sensible heat flux is large, it is recommended that an extra-large aperture scintillometer is considered for very long paths. Future work will likely focus on the development of the scintillometry technique and the application for routine monitoring at large-scales (e.g. Kleissl et al. (2009a)).

Acknowledgements

We gratefully acknowledge the support of the following CEH staff: Alan Warwick and Cyril Barrett for design and construction of the scintillometer mountings, Geoff Wicks for assistance with the electronics and Dave McNeil for helping to build the rooftop weather station. This work would not have been possible without the generous co-operation of several people in Swindon who very kindly gave permission for equipment to be installed on their property. We also wish to thank the Science and Technology Facilities Council staff at Chilbolton Observatory for use of their test range for the scintillometer comparison. This work was funded by the Natural Environment Research Council, UK.

Chapter 6 A critical revision of the estimation of the latent heat flux from two-wavelength scintillometry[1]

6.1 Introduction

There is considerable demand for reliable and accurate measurements of surface fluxes over different land surfaces to develop better understanding of land-atmosphere interactions in order to improve models and prediction capability. A key component in both water and energy balances is the evaporation, or latent heat flux. Catchment-scale information on the water balance is essential for assessing flood risk and, especially important where supplies may be limited, for managing fresh water provision (e.g. irrigation scheduling).

Two-wavelength scintillometry offers the ability to estimate the latent heat flux over large areas (e.g. 2-5 km^2) (Kohsiek, 1982; Hill, 1997; Green et al., 2001; Meijninger et al., 2002a; Meijninger et al., 2006). Studies have shown that measurements of turbulent heat fluxes integrated over an area of this order offer suitable comparison data for evaluating land surface schemes in numerical weather prediction models (Beyrich et al., 2002a; Beyrich and Mengelkamp, 2006), hydro-meteorological models (Samain et al., 2011) or satellite retrievals of similar scales (Hoedjes et al., 2007; Kleissl et al., 2009a).

Two-wavelength scintillometry requires one visible or near-infrared instrument (here referred to as optical) and another at millimetre or radio wavelengths (Andreas, 1989), positioned so that their beams are close together (Lüdi et al., 2005). The intensity fluctuations of each beam are converted into a measure of the refractive index fluctuations of air at the corresponding wavelength using turbulence and wave propagation theory (Tatarski, 1961; Wheelon, 2006). The quantity retrieved is the path-averaged refractive index structure parameter, C_n^2 (Wang et al., 1978). At optical wavelengths, the refractive index fluctuations are almost entirely due to temperature fluctuations, whereas longer wavelengths have greater sensitivity to humidity fluctuations. For each wavelength C_n^2 can be written in terms of temperature (C_T^2) and humidity (C_q^2) structure parameters and the cross-structure parameter (C_{Tq}). Solving simultaneously yields the contributions from temperature and humidity, using

[1] Ward, H.C., Evans, J.G., Hartogensis, O.K., Moene, A.F., De Bruin, H.A.R. and Grimmond, C.S.B., 2013b. A critical revision of the estimation of the latent heat flux from two-wavelength scintillometry. Q. J. R. Meteorol. Soc.

the two measured values of C_n^2 plus an estimate of the temperature-humidity correlation coefficient r_{Tq} (Hill et al., 1988). Alternatively the cross-structure parameter can be found directly by correlating the signals at each wavelength: this bichromatic method enables the correlation between temperature and humidity to be measured and thus removes the need to assume a value for r_{Tq} (Beyrich et al., 2005; Lüdi et al., 2005). Monin-Obukhov Similarity Theory (MOST) is then used to calculate the scaling variables of temperature and humidity, from which sensible and latent heat fluxes are found (Kohsiek, 1982; Hill, 1997; Green et al., 2001; Meijninger et al., 2002a; Meijninger et al., 2006).

Previously, the absolute humidity (Q, i.e. the mass of water vapour per volume of moist air, kg m^{-3}) has been used to represent the water vapour content of the atmosphere. The original derivations (Hill et al., 1980; Andreas, 1988) partitioned the refractive index fluctuations into temperature fluctuations and absolute humidity fluctuations. Hill (1989) uses absolute humidity to derive structure parameters and scaling variables; Kohsiek (1982), Kohsiek and Herben (1983), Hill et al. (1988), Green et al. (2001), Meijninger et al. (2006) and Evans (2009) all employ absolute humidity in the calculation of the latent heat flux, denoted L_vE, where L_v is the latent heat of vaporisation and E is the evaporation. Possibly the use of Q in these studies is because Wyngaard and Clifford (1978) stated that $E = w'Q'$ (where w' represents fluctuations in vertical wind speed). This is not always correct, especially for high Bowen ratio (β, turbulent sensible to latent heat flux ratio) conditions. Wesely (1976), one of the first to suggest deriving fluxes from scintillometry, used water vapour pressure (e, Pa).

Unfortunately, the symbols used in the literature are not consistent. Nevertheless, specific humidity q ($= Q/\rho$, kg kg^{-1}, where ρ is the density of moist air, kg m^{-3}) has been little used in the two-wavelength literature. Hill (1997) and Moene (2003) remark that conserved quantities (i.e. potential temperature and specific humidity) should be used in MOST. In Hill's (1997) detailed discussion of two-wavelength algorithms, the structure parameters C_Q^2 and C_{TQ} are obtained from C_n^2 and then converted to C_q^2 and C_{Tq} for use in MOST, but he gives the latent heat flux in terms of the absolute humidity scaling variable, Q_*.

It is argued that specific humidity should be used for this application: firstly, it is independent of temperature; secondly, it is conserved, thus suitable for use in MOST; and thirdly, it is an appropriate variable to use to estimate the latent heat flux. Whilst Q is defined with respect to a volume, which changes with temperature (due to thermal expansion) or pressure fluctuations of vertical motions, q uses relative densities (mass of water vapour per mass of moist air). Thus specific humidity is considered a conserved quantity (Lee and Massman, 2011) in the lower part of the atmosphere (for dry adiabatic processes) whereas Q

is not. Since the latent heat flux is concerned with the transport of water vapour it is necessary to avoid contamination through changes in temperature.

Figure 6-1 provides an overview of the processing stages discussed. The surface moisture flux can be obtained from measured C_n^2 via two paths, using either specific humidity (route a) or absolute humidity (route b), although as will be shown here, route b is not recommended. Previously, step 1b has been used to find C_Q^2, usually followed by 2b and 3b. The main source of error is from following the b route and taking $u_* Q_*$ as the evaporation (i.e. stopping after 3b) which is incorrect. Additionally, step 2b is not strictly valid. Errors also arise from inconsistency, such as mistakenly arriving at C_q^2 after applying 1b.

As Q contains temperature information, it is not an ideal measure of humidity. C_q^2 is a useful statistic to describe fluctuations in water content, whereas C_Q^2 is contaminated by temperature fluctuations. The requirements for MOST scaling are satisfied by q_* (but not necessarily Q_*). Thus q_* is a much more appropriate variable to use to estimate the latent heat flux and properly account for density effects.

Since ρ depends on the water vapour content (relative molecular mass of moist air decreases with water vapour content) the resulting $L_v E$ is (usually slightly) underestimated when the mass of water vapour is considered relative to moist air, i.e. even when using q, a (small) density effect occurs due to the latent heat flux itself. Bakan (1978) concluded that the most suitable quantity to determine the latent heat flux is the mass mixing ratio relative to the density of dry air ($r = Q/\rho_d$, kg kg^{-1}, where ρ_d is the density of dry air). Scintillometry data could be processed using r, yielding the structure parameter of mixing ratio (C_r^2) and $L_v E$ found from a scaling variable of mixing ratio (r_*). In practice other uncertainties in the measurements, processing and assumptions in the derivation of equations outweigh the difference between using r or q, for example instrumental noise, absorption and limitations of MOST (Medeiros Filho et al., 1983; Meijninger et al., 2006; Beyrich et al., 2012). Mixing ratio formulations are given in the Appendix (Section 6.7).

The objective of this paper is to present the key scintillometry equations in terms of the specific humidity, giving the formulations necessary to calculate specific humidity structure parameters and correctly estimate latent heat fluxes. Section 6.2 outlines the theory, comparing the use of q and Q. Equations to correctly calculate the latent heat flux from two-wavelength scintillometry are given and the analogy with other measurement techniques is made in Section 6.3. In light of these findings, recommendations are given for processing and analysis (Section 6.4), implications are discussed (Section 6.5) and conclusions drawn (Section

6.6). Note that only the real part of the refractive index fluctuations is considered here (i.e. no absorption).

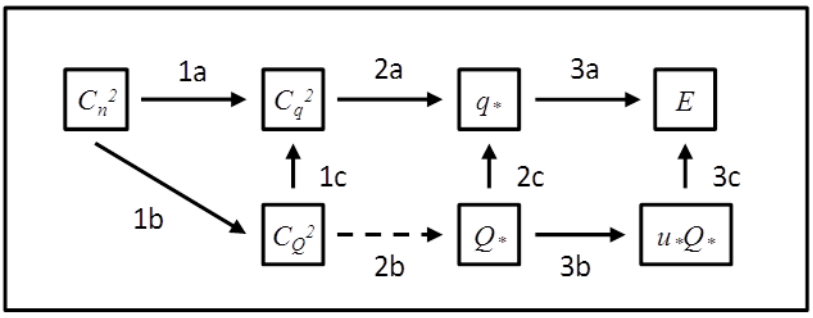

Figure 6-1: Summary of processing routes for absolute (Q) and specific (q) humidity formulations: 1. Partitioning of refractive index fluctuations into temperature and moisture fluctuations; 2. MOST; 3. Definition of evaporation (Equation 6-17). Stage 2b is invalid as Q is not a conserved variable. Conversions from absolute to specific humidity variables can be performed at stage 1c (Equation 6-14), 2c or 3c (Equation 6-18). See text for further explanation.

6.2 Scintillometry theory re-examined

6.2.1 Formulating the refractive index

Following Hill et al. (1980) and Andreas (1988), the refractive index (n) can be expressed as refractivity, defined as $10^6(n-1)$, and related to the contributions from dry air (n_d) and water vapour (n_v),

$$10^6(n-1) = n_d + n_v = m_1\left[\frac{p-e}{T}\right] + m_2\frac{e}{T} \qquad (6\text{-}1)$$

where the values of m_1 and m_2 have been found empirically and are given by Owens (1967) for wavelengths (λ) in µm:

$$m_{1\_opt} = 0.237134 + \frac{68.39397}{130-\lambda^{-2}} + \frac{0.45473}{38.9-\lambda^{-2}} \qquad (6\text{-}2a)$$

$$m_{2\_opt} = 0.648731 + 0.0058058\lambda^{-2} - 0.0000711505\lambda^{-4} + 0.0000088501\lambda^{-6} \qquad (6\text{-}2b)$$

for optical wavelengths ($0.36 > \lambda_{opt} > 3$ µm). For millimetre wavelengths ($\lambda_{mw} > 3$ mm) (Bean and Dutton, 1966):

$$m_{1\_mw} = 0.776 \tag{6-3a}$$

$$m_{2\_mw} = m_{2a\_mw} + m_{2b\_mw}(T) = 0.720 + \frac{3750}{T} \tag{6-3b}$$

p is the atmospheric pressure (Pa) and T air temperature (K). For optical wavelengths the refractivity is wavelength dependent through m_{1_opt} and m_{2_opt}, whereas there is no wavelength dependence in the millimetre range but m_{2_mw} depends inversely on T. Contrary to Hill et al. (1980) and Andreas (1988), who used absolute humidity, we use the ideal gas law to rewrite the vapour pressure (e) in terms of the specific humidity:

$$10^6(n-1) = m_1 \frac{p}{T} + (m_2 - m_1)R_v \frac{pq}{RT}. \tag{6-4}$$

R is the specific gas constant for moist air: $R = R(q) = R_d + q(R_v - R_d)$ with R_d and R_v the specific gas constants for dry air and water vapour, respectively. This stage differs from the original derivations which substituted e/T as R_vQ (ideal gas law). We reformulate this in terms of specific humidity ($R_v\rho q$) and write the density as p/RT to obtain n as a function of T, q, and p. Thus for millimetre wavelengths:

$$10^6(n_{mw} - 1) = 0.776 \frac{p}{T} + (0.720 + \frac{3750}{T} - 0.776)R_v \frac{pq}{RT}. \tag{6-5}$$

This was first presented by Hartogensis and Moene (2011). Moene et al. (2004) give the specific humidity formulation for optical wavelengths.

6.2.2 Re-derivation of structure parameter coefficients

Equation 6-4 expresses the refractive index in terms of three variables (T, q and p), recalling that the gas constant for moist air is a function of q. Thus the change in n can be written in terms of partial derivatives:

$$\partial n = \frac{\partial n}{\partial T}\partial T + \frac{\partial n}{\partial q}\partial q + \frac{\partial n}{\partial p}\partial p, \tag{6-6}$$

where each derivative is found while holding the other variables constant. If the absolute humidity is used, the differentiation with respect to T, for example, creates the artificial situation of a temperature change which is forbidden from changing Q, whereas, a parcel of moist air will expand when warmed, causing Q to decrease. The use of specific humidity avoids this as T and q are independent variables.

Considering relative changes in T, q and p, Equation 6-6 can be re-written:

$$n' = A_t \frac{T'}{\overline{T}} + A_q \frac{q'}{\overline{q}} + A_p \frac{p'}{\overline{p}} \qquad (6\text{-}7)$$

with primes indicating fluctuations, overbars indicating mean values, and the structure parameter coefficients defined for a scalar, y, as:

$$A_y = \overline{y} \frac{\partial n}{\partial y}. \qquad (6\text{-}8)$$

The humidity variable chosen results in different coefficients for specific (A_t, A_q) or absolute humidity (A_T, A_Q). The difference in the coefficients for temperature occurs due to the definition (Equation 6-8): for the derivation in terms of absolute humidity, A_T is formed from the partial differential of n with respect to T *at constant absolute humidity*; if specific humidity is used then A_t is obtained from the partial differential of n with respect to T *at constant specific humidity*. Note that A_T and A_t are both derivatives with respect to temperature, whereas A_Q and A_q are derivatives with respect to absolute and specific humidity respectively. Following the same convention, in the case of the mass mixing ratio A_τ is formed from the partial derivative of n with respect to T at constant mass mixing ratio and A_r from the partial derivative with respect to r at constant temperature, see Appendix (Section 6.7).

As for the original derivations, pressure terms are not included (Andreas, 1988; Hill, 1997). Following Moene et al. (2004), who demonstrated that pressure fluctuations are negligible for optical wavelengths, we conclude that they can also be ignored for millimetre wavelengths. Table 6-1 compares the magnitude of each term in Equation 6-7. Small relative fluctuations in p mean the pressure terms remain small enough to be ignored. This is also fortunate, since the two-wavelength method relies on a pair of simultaneous equations to solve for the two unknowns – temperature and humidity fluctuations (Hill et al., 1988).

Scalar y	Mean $\overline{y}$	Fluctuation y'	Relative fluctuation $y'/\overline{y}$	Optical		Millimetre	
				A_y	$A_y\, y'/\overline{y}$	A_y	$A_y\, y'/\overline{y}$
T [K]	288	1	3×10^{-3}	-2.70×10^{-4}	-9×10^{-7}	-4.13×10^{-4}	-1.4×10^{-6}
q [kg kg^{-1}]	10^{-2}	10^{-4}	10^{-2}	-6.85×10^{-7}	-6.9×10^{-9}	7.14×10^{-5}	7.1×10^{-7}
p [Pa]	10^{5}	10^{-2}	10^{-7}	2.70×10^{-4}	2.7×10^{-11}	3.40×10^{-4}	3.4×10^{-11}

Table 6-1: Sensitivity of the refractive index at optical and millimetre wavelengths to fluctuations in T, q and p. Estimates of turbulent fluctuations of T, q and p are from Moene et al. (2004) and A_y values assume typical atmospheric conditions (T = 288 K, p = 10^5 Pa, q = 0.010 kg kg^{-1}). A wavelength of 0.880 µm was used for the optical region.

The explicit forms of the structure parameter coefficients are given in Table 6-A1 (Section 6.7) and illustrated in Figure 6-2. When formulated in terms of specific humidity the coefficients gain additional terms due to the presence of T in the density ($\rho = p/RT$). For optical scintillometry, the difference between absolute and specific humidity formulations is negligible as nearly all refractive index fluctuations are caused by temperature variations and humidity plays a very small role (Figure 6-2a). The additional terms (Table 6-A1) contribute less than 1% to the structure parameter coefficients. Therefore for single-wavelength (optical or near-infrared) scintillometry, the effect of the choice of humidity variable is practically negligible. However, for longer wavelengths, A_q is very slightly smaller than A_Q (again < 1%) but the magnitude of A_t is about 20% larger (more negative) than A_T under typical atmospheric conditions. This arises mostly from the additional differentiation of the n_{v_mw} term with respect to T when specific humidity is used (arrow, Figure 6-2a). The dependence of m_{2_mw} on temperature coupled with the representation of specific humidity requiring a $1/T$ dependence is responsible for this term appearing twice in A_t compared to the same term appearing once in A_T.

The size of the structure parameter coefficients varies with atmospheric conditions (Figure 6-2b). The temperature is relevant for optical wavelengths (higher T results in less negative A_T and A_t) but both temperature and humidity affect the structure parameter coefficients for the millimetre region. Smaller Q results in smaller absolute values of the temperature and humidity structure parameter coefficients (compare coefficients for decreasing relative humidity (RH) at constant temperature) and a smaller difference between absolute and specific humidity formulations: A_t is 8% larger than A_T for a relative humidity of 30% (Q = 0.0038 kg m^{-3} at T = 288 K). At constant RH increasing T is accompanied by larger Q and an increase in the magnitude of the millimetre wavelength structure parameter coefficients (and a larger difference between A_t and A_T), whereas the magnitudes of optical A_t and A_T decrease. Pressure has a small effect: ± 5 × 10^3 Pa variation alters the difference between millimetre A_t and A_T by less than 1%.

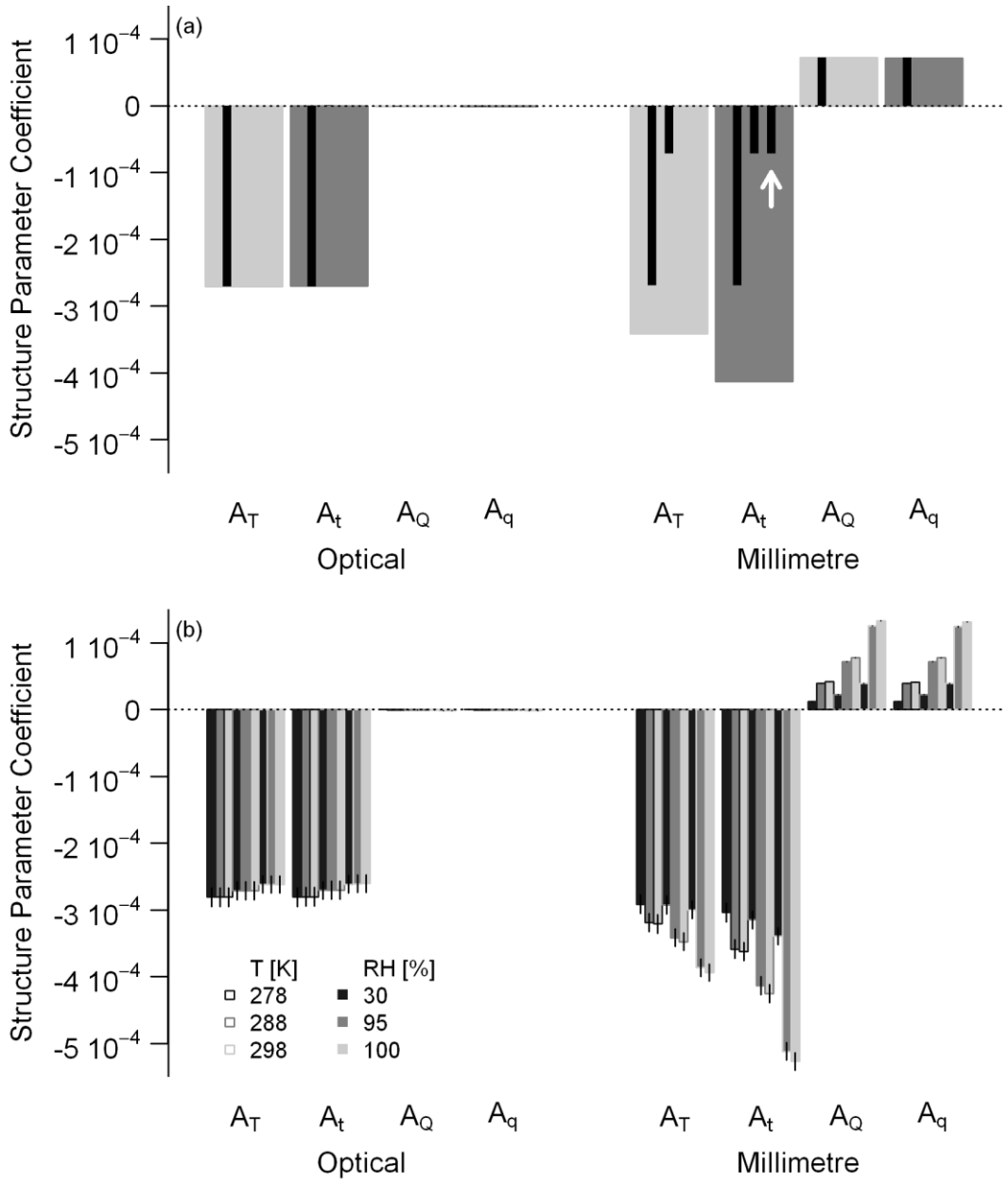

Figure 6-2: (a) Comparison of structure parameter coefficients (shaded bars) and contributions from each term in Table 6-A1 (black) for typical atmospheric conditions (*viz.* T = 288 K, p = 10^5 Pa, Q = 0.012 kg m^{-3}, after Meijninger (2003)) for optical and millimetre wavelengths using absolute and specific formulations. The difference in millimetre wave A_t and A_T is caused by the differential of n_{v_mw} with respect to T appearing twice in A_t (arrow) and only once in A_T. The difference in optical A_Q and A_q is negligible (see Section 6.7). (b) Variation of the structure parameter coefficients for different temperatures and relative humidities (values in key). The central bar in each group (T = 288 K, Q = 0.012 kg m^{-3}) is equivalent to (a). Impact of pressure variations of ±5 × 10^3 Pa are shown by the thin vertical lines.

The layout of Table 6-A1 and Figure 6-2a is intended to aid comparison between Q and q formulations. The q formulation can be found for the optical region in Moene et al. (2004) but has not previously been given in the literature for millimetre wavelengths. The mixing ratio formulations are not known to have been presented before. The most useful structure

parameter coefficients, A_t and A_q, are summarised in Table 6-2 with simplified notation so that both wavelength regions have the same general form. This is intended to be a reference, and as such shows the full expressions.

	$A_t = -\frac{\bar{p}}{\bar{T}}\left(b_{t1} + b_{t2}\frac{R_v}{R}\bar{q}\right)$	$A_q = \frac{\bar{p}}{\bar{T}}\frac{R_v}{R}\bar{q}b_{q2}\left(1-\frac{\bar{q}}{\bar{R}}(R_v - R_d)\right)$
Optical	$b_{t1} = 10^{-6}m_{1\_opt}$ $= \left(0.237134 + \frac{68.39397}{130-\lambda^{-2}} + \frac{0.45473}{38.9-\lambda^{-2}}\right)\times 10^{-6}$ $b_{t2} = 10^{-6}(m_{2\_opt} - m_{1\_opt})$ $= (0.648731 + 0.0058058\lambda^{-2} - 0.000071150\lambda^{-4}$ $+ 0.000008851\lambda^{-6})\times 10^{-6} - b_{t1}$	$b_{q2} = b_{t2}$
Millimetre-wave	$b_{t1} = 10^{-6}m_{1\_mw}$ $= 0.776\times 10^{-6}$ $b_{t2} = 10^{-6}m_{2b\_mw} + 10^{-6}(m_{2\_mw} - m_{1\_mw})$ $= \left(\frac{7500}{\bar{T}} - 0.056\right)\times 10^{-6}$	$b_{q2} = 10^{-6}(m_{2\_mw} - m_{1\_mw})$ $= \left(\frac{3750}{\bar{T}} - 0.056\right)\times 10^{-6}$

Table 6-2: Simplified forms of the temperature and humidity structure parameter coefficients for optical and millimetre wavelengths, in terms of specific humidity. Using this notation A_t and A_q have the same form for both wavelength regions, with the b-coefficients containing the wavelength (in μm) and temperature dependence. For optical regions b_{t1}, b_{t2} and b_{q2} depend on wavelength: for $\lambda_{\_opt}$ = 0.880 μm b_{t1} = 0.781 × 10-6 K Pa^{-1} and b_{t2} = b_{q2} = -0.124 × 10-6 K Pa^{-1} (to 3 significant figures); for millimetre wavelengths b_{t1} is constant, b_{t2} and b_{q2} depend on temperature.

6.2.3 Structure parameter relations and the interpretation of structure parameters

Critically, the alternative structure parameter coefficients relate to *different* structure parameters. Writing C_n^2 using the general definition of the structure parameter for a scalar y (Monin and Yaglom, 1971):

$$C_y^2 = \overline{(y'(x) - y'(x+\delta))^2}\,\delta^{-2/3}, \qquad (6\text{-}9)$$

where x is location and δ is the separation distance, and substituting Equation 6-7 and tidying the right hand side gives:

$$C_n^2 = \frac{A_t^2}{\overline{T}^2} C_T^2 + 2\frac{A_t A_q}{\overline{T}\,\overline{q}} C_{Tq} + \frac{A_q^2}{\overline{q}^2} C_q^2 . \qquad (6\text{-}10)$$

The structure parameters obtained here are C_{Tq} (K kg kg^{-1} m$^{-2/3}$) and C_q^2 (kg^2 kg^{-2} m$^{-2/3}$), which are clearly different physical quantities to C_{TQ} (K kg m^{-3} m$^{-2/3}$) and C_Q^2 (kg^2 m^{-6} m$^{-2/3}$). Although the coefficients A_T and A_t are different, C_T^2 is the same whether the derivation uses absolute or specific humidity. The difference in structure parameter coefficients is compensated for by the fundamental differences in the structure parameters of humidity (C_Q^2 compared to C_q^2) and cross-structure parameters (C_{TQ} compared to C_{Tq}). Both methods separate the refractive index fluctuations into contributions from temperature, humidity and correlated temperature-humidity fluctuations, however, the meaning of humidity fluctuations is not the same, as illustrated by using the ideal gas law to relate changes in q to changes in Q. From the definition of q and the ideal gas law:

$$q = \frac{QRT}{p} . \qquad (6\text{-}11)$$

Using Reynolds decomposition, and keeping only first order terms, the fluctuations in Q can be written (see Hill (1997) for details):

$$\frac{Q'}{\overline{Q}} = \frac{q'}{\overline{\gamma}\,\overline{q}} - \frac{T'}{\overline{T}} + \left(\frac{p'}{\overline{p}} \right) \qquad (6\text{-}12)$$

(where γ is R/R_d). Neglecting pressure fluctuations (column 4, Table 6-1) and using Equation 6-9, the structure parameter for absolute humidity can be written in terms of the structure parameters for the independent variables of temperature and specific humidity:

$$\frac{C_Q^2}{Q^2} = \frac{C_q^2}{\gamma^2 q^2} + \frac{C_T^2}{T^2} - 2\frac{C_{Tq}}{\gamma T q} . \qquad (6\text{-}13)$$

Hill (1997) gives the specific parameters in terms of the absolute parameters (and also the cross-structure parameter) in his Equations 14a, b:

$$\frac{C_q^2}{\overline{\gamma}^2 \overline{q}^2} = \frac{C_Q^2}{\overline{Q}^2} + \frac{C_T^2}{\overline{T}^2} + 2\frac{C_{TQ}}{\overline{T}\,\overline{Q}} \qquad (6\text{-}14)$$

and

$$\frac{C_{Tq}}{\gamma \overline{T}\overline{q}} = \frac{C_T^2}{\overline{T}^2} + \frac{C_{TQ}}{\overline{T}\overline{Q}}. \qquad (6\text{-}15)$$

The additional $1/T$ on the left of Equation 6-15 is believed to be missing in Hill (1997). These equations clearly show that the partitioning of temperature and humidity fluctuations varies between the specific and absolute approach. Substituting Equations 6-14 and 6-15 into Equation 6-10 recovers the more familiar C_n^2 equation (with A_T and A_Q, C_T^2, C_Q^2 and C_{TQ}). Both absolute and specific humidity structure parameters are valid in their own right – but C_Q^2 can be non-zero even when there is no evaporation.

In order to calculate heat fluxes from C_n^2 at both wavelengths, we first calculate structure parameters via the two-wavelength methodology given in Hill (1988). Both the original absolute humidity formulation and the new specific humidity route are evaluated here. We assume $C_{Tq} = r_{Tq}(C_T^2 C_q^2)^{1/2}$ with $r_{Tq} = \pm 1$, and likewise for Q. To demonstrate differences between the two approaches, heat fluxes are calculated using MOST which requires parameter specification. The following arbitrary values for demonstration are used: a measurement height of 10 m, roughness length of 0.01 m and wind speed of 10 m s^{-1}. The Andreas (1988) stability functions are used, with identical functions assumed for temperature and humidity. Unless otherwise stated T = 288 K, $p = 10^5$ Pa and Q = 0.012 kg m^{-3} (typical values from Meijninger (2003)). To represent different atmospheric conditions available energies of 500 W m^{-2} and -50 W m^{-2} are shown as examples of day and night time energy regimes. The optical wavelength used throughout is 0.880 µm.

Figure 6-3a illustrates the contributions of each term in Equation 6-10 to the total millimetre-wavelength C_n^2 for the absolute and specific humidity formulations. As discussed, C_T^2 is the same in each case and the difference between $(A_T^2/T^2)C_T^2$ and $(A_t^2/T^2)C_T^2$ is due to the structure parameter coefficients. The contributions of humidity and temperature-humidity fluctuations to C_n^2 are different between the two approaches, due to both a difference in structure parameter coefficients and the structure parameters themselves. Figure 6-3b shows the difference between C_q^2 and C_Q^2 (divided by ρ to obtain compatible units).

It should be noted that the two-wavelength approach does not yield a single unique solution as there is an ambiguity in the sign of the cross-structure term (Hill et al., 1988; Hill, 1997), resulting in two possible Bowen ratios for a given C_n^2 (solid line in Figure 6-3a). Applications of the two-wavelength method to date reported in literature (Kohsiek, 1982; Hill, 1997; Green et al., 2001; Meijninger et al., 2002a; Meijninger et al., 2006) refer to conditions where β is to the left of the C_n^2 minimum (Figure 6-3a). For drier conditions (i.e. higher β) it is more difficult to select the correct solution without additional information on the true value of

β, either from other measurements such as eddy covariance (EC) or site characteristics. It is outside the scope of this paper to discuss in detail this feature. However the bichromatic method offers the key advantage of providing a measurement of C_{Tq} (Lüdi et al., 2005) so the sign ambiguity is not relevant.

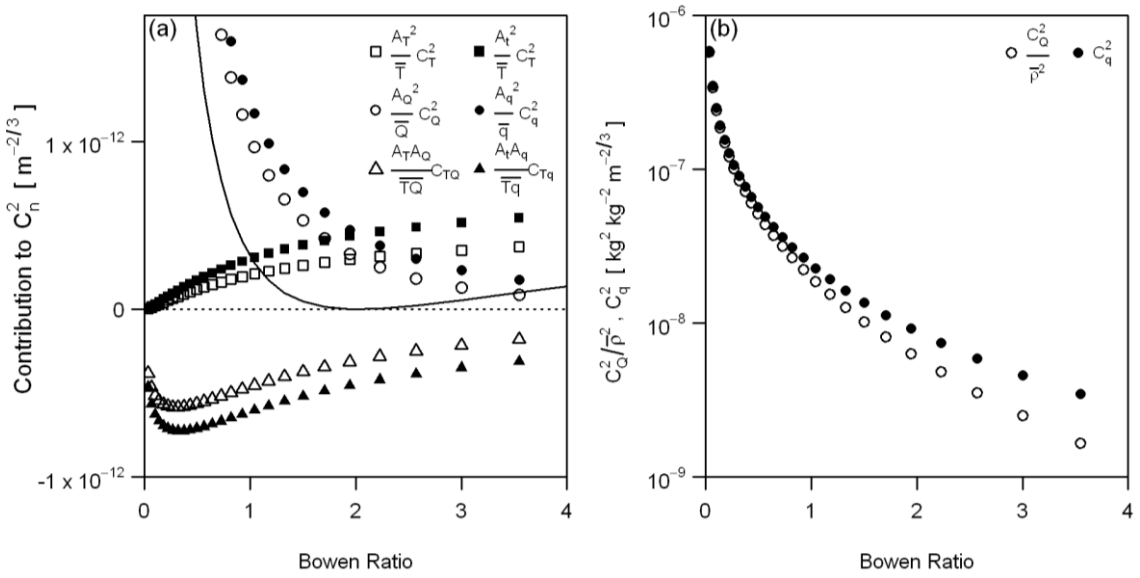

Figure 6-3: (a) Contribution of temperature, humidity and temperature-humidity fluctuations to the total C_n^2 (solid line) for millimetre wavelengths for the absolute and specific humidity methods, and (b) comparison between humidity structure parameters for a range of Bowen ratios with an available energy of 500 W m^{-2} and assuming the free convection limit.

6.2.4 Similarity theory scaling

Monin-Obukhov Similarity Theory is the required mechanism to establish fluxes from scintillometry measurements. It uses dimensionless relations to parameterise the variability of atmospheric quantities based on empirically derived profiles and the surface fluxes. A prerequisite for MOST is that the quantity being modelled is a conserved scalar.

Strictly, potential temperature should be used in similarity theory, but if pressure fluctuations are neglected then potential temperature changes are proportional to temperature changes and this does not create a problem (Hill, 1997). However, as absolute humidity is not a conserved variable, it is not necessarily suitable for use with MOST scaling. Despite its prevalence in the literature, it is therefore questionable to apply MOST to C_Q^2/Q_*^2 as noted by Moene (2003) and Hill (1997). Furthermore, if the intention is to study scaling relations, in particular whether heat and moisture behave similarly (e.g. Kohsiek (1982), Roth and Oke (1995), Moene and Schüttemeyer (2008)), it is preferable to compare independent measures (T and q), as in Kohsiek and Bosveld (1987), De Bruin et al. (1993) and Li et al. (2011),

rather than use Q which contains an inherent T dependence. Although errors in misapplying MOST to Q may be small (especially compared to e.g. assuming identical functions for temperature and humidity), the propagation of the temperature fluctuations through ${C_Q}^2$ to Q_* is a more significant issue (discussed in Section 6.2.5).

6.2.5 Formulation of the latent heat flux

We determine the latent heat flux based on u_*q_* rather than u_*Q_* (Hill, 1997; Green et al., 2001; Meijninger et al., 2006) where u_* is the friction velocity. According to Webb et al. (1980), the water vapour mass flux is given by:

$$E = \frac{\overline{\rho}}{(1-\overline{q})}\overline{w'q'} \tag{6-16}$$

to a close approximation. Analogously, to estimate the latent heat flux from two-wavelength scintillometry via scaling variables, one should use:

$$L_v E = -\frac{\overline{\rho}}{(1-\overline{q})} L_v u_* q_* . \tag{6-17}$$

The $(1-q)^{-1}$ factor arises because the water vapour flux itself causes a density change, as detailed in Webb et al. (1980) and mentioned in Section 6.1. When the latent heat flux is positive, L_vE derived from absolute humidity ($-L_vu_*Q_*$) is expected to be an underestimation (overestimation) of the true flux for positive (negative) H (which follows from Equation 6-12 multiplied by w' and averaged). The underestimation of the latent heat flux increases with increasing H. The magnitude of a negative latent heat flux will be underestimated (overestimated) by a negative (positive) H. This means that for positive β the magnitude of L_vE is underestimated; for negative β it is overestimated.

Figure 6-4a shows the sensible and latent heat fluxes obtained using both humidity methods as a function of Bowen ratio. The sensible heat flux is unaffected by the choice of humidity variable (grey hollow and filled shapes are coincident). However, for unstable conditions (H > 0) and positive β, the latent heat flux calculated using the absolute humidity ($-L_vu_*Q_*$) can considerably underestimate the true latent heat flux calculated from Equation 6-17. If H is negative but L_vE is positive, $-L_vu_*Q_*$ overestimates L_vE. Such conditions may occur in the nocturnal boundary layer with small available energies (squares) or during daytime over a wet surface (De Bruin et al., 2005) with larger available energies (circles). The biggest differences between absolute and specific formulations of the latent heat flux occur when the magnitude of the sensible heat flux is largest (i.e. at large Bowen ratios). The percentage error

in latent heat flux is plotted in Figure 6-4b. At low Bowen ratios the effect is small to negligible (< 5% for β < 0.5); at higher Bowen ratios the correction becomes appreciable (> 10% for β > 1.0). The small underestimation visible at low β is due to the density effect caused by the latent heat flux itself (Section 6.1).

With β = 1 and an available energy of 500 W m^{-2} (H = L_vE = 250 W m^{-2}) the absolute humidity method yields 225 W m^{-2}, i.e. an underestimation of 25 W m^{-2} or 10%. When β = 3 (H = 375 W m^{-2}, L_vE = 125 W m^{-2}) the larger sensible heat flux gives rise to a greater underestimation, with -$L_v u_* Q_*$ = 91 W m^{-2}, which translates as an absolute error of 34 W m^{-2} and a percentage error of 27%. The percentage error in the latent heat flux increases with the size of β (Figure 6-4b), but it must be noted that the total latent heat flux also decreases with increasing β for a given available energy (e.g. a 23% error corresponds to a smaller absolute error of 5.6 W m^{-2} at β = -3, H = -75 W m^{-2}, L_vE = 25 W m^{-2}). With respect to atmospheric conditions, the percentage error is largest for higher T and RH, whilst changes in p have a smaller effect (not shown). For Figure 6-4b a wide range of T, RH and p is shown so for most setups the variation encountered will be much smaller than indicated here. The percentage error is unaffected by stability, site characteristics or wind speed – the curves in Figure 6-4a collapse onto the single solid line in Figure 6-4b. The error depends on the partitioning of H and L_vE and is affected by T, Q and p (Section 6.3).

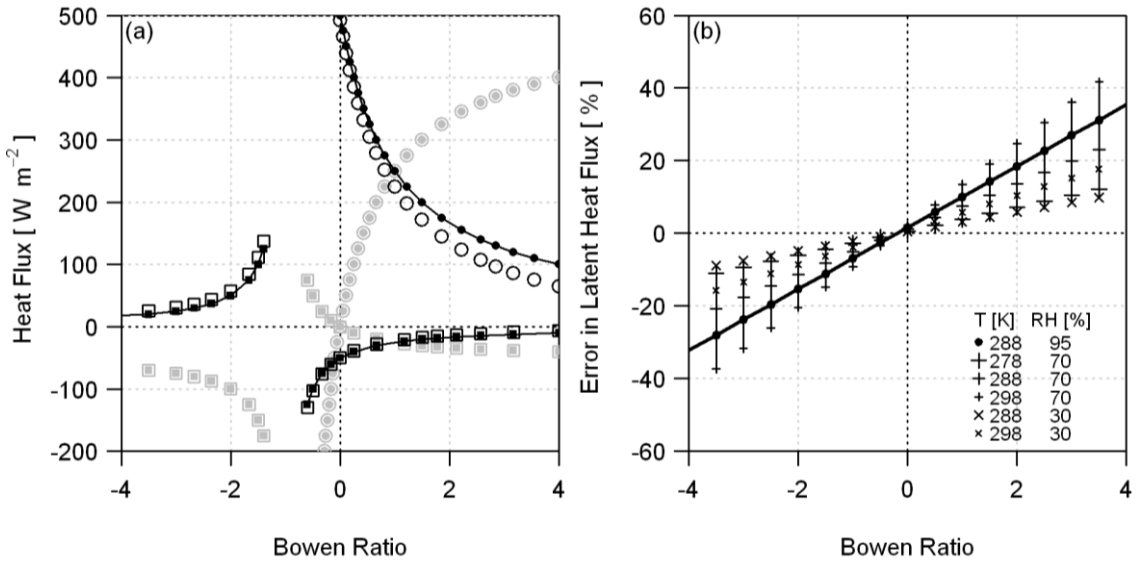

Figure 6-4: (a) Turbulent sensible (grey) and latent (black) heat fluxes as a function of Bowen ratio using absolute (hollow) and specific (filled) humidity formulations. Results when the available energy is 500 W m^{-2} (circles) and -50 W m^{-2} (squares) are shown and T = 288 K, p = 10^5 Pa, Q = 0.012 kg m^{-3}. Sensible heat flux is unaffected by the choice of humidity whereas L_vE via the absolute formulation (-$L_v u_* Q_*$) underestimates (overestimates) the magnitude of the true latent heat flux (Equation 6-17) for β > 0 (β < 0). (b) Percentage error in latent heat flux: ([1 – (-$L_v u_* Q_*$)]/ L_vE according to Equation 6-17) as a function of Bowen ratio, determined for typical T, p and Q as in (a) (solid line, solid circles) with vertical lines illustrating the effect of different atmospheric conditions (key).

6.3 Density corrections for open-path gas analysers

The conclusions reached in Section 6.2 are in accordance with the key ideas of the Webb et al. (1980) (WPL) correction for latent heat flux measured by open-path gas analysers in combination with sonic anemometers. In the eddy covariance method, fast-response gas density and temperature measurements are combined with fast-response vertical wind speed observations. The sensible and latent heat fluxes obtained are proportional to the covariances of the vertical wind speed with temperature and humidity respectively (MOST is not required). Open-path gas analysers measure absorption of radiation, which is proportional to the density of a gas, e.g. the absolute humidity. The latent heat flux is obtained from $w'Q'$ but this must be corrected for density effects using the WPL correction before a true latent heat flux measurement can be obtained.

Both gas analysers and scintillometers effectively sense changes in density along an optical (or millimetre wavelength) path. If the density measurement is expressed in terms of the absolute humidity, this will suffer the influence of temperature and water vapour fluctuations and either $w'Q'$ (for EC) or u_*Q_* (for scintillometry) will require a correction to account for the difference from the true latent heat flux. If specific humidity is used ($w'q'$ or u_*q_*), the difference is almost zero, with only a small correction for water vapour required – of the order of $(1-\bar{q})^{-1}$, as appears in Equations 6-16 and 6-17.

When data cannot be reprocessed from measured C_n^2 values, it is useful to have a correction to the latent heat flux calculated from u_*Q_* to account for density effects using a WPL-style correction. The evaporation may be expressed as:

$$E = -\frac{\bar{\rho}}{(1-\bar{q})} u_* q_* = -(1+\frac{\bar{Q}}{\bar{\rho}_d}\frac{R_v}{R_d})(u_* Q_* + \frac{\bar{Q}}{\bar{T}} u_* T_*), \qquad (6\text{-}18)$$

which is very similar to the familiar WPL form (Equation 25 of Webb et al. (1980)). When corrected for density effects via Equation 6-18, the absolute formulation agrees with Equation 6-17 (solid lines in Figure 6-4a).

The Bowen ratio should be specified in terms of specific humidity:

$$\beta = \frac{H}{L_v E} = (1-\bar{q})\frac{-\bar{\rho} c_p u_* T_*}{-\bar{\rho} L_v u_* q_*} = (1-\bar{q})\frac{c_p}{L_v}\frac{T_*}{q_*}, \qquad (6\text{-}19)$$

where c_p is the specific heat capacity of air at constant pressure, so that when T and q are assumed to obey the same similarity scaling,

$$\beta = \pm(1-\bar{q})\frac{c_p}{L_v}\sqrt{\frac{C_T^2}{C_q^2}} \approx \pm\frac{c_p}{L_v}\sqrt{\frac{C_T^2}{C_q^2}}\,. \qquad (6\text{-}20)$$

Combining Equations 6-18 and 6-19, the error in the latent heat flux can be found as a function of Bowen ratio:

$$\left(1-\frac{u_* Q_*}{\frac{\bar{\rho}}{(1-\bar{q})}u_* q_*}\right)\times 100\% = \left(1-\frac{1}{(1+\frac{\bar{Q}}{\bar{\rho}_d}\frac{R_v}{R_d})}+\frac{\bar{Q}}{\bar{T}}\frac{L_v}{\bar{\rho}c_p}\beta\right)\times 100\%, \qquad (6\text{-}21)$$

shown in Figure 6-4b.

Although the form of the correction to find L_vE is analogous to the WPL correction for eddy covariance (Webb et al., 1980), it does not rely on vertical wind speed. Lee and Massman (2011) present a derivation of the corrections for density fluctuations (for trace gas measurements by EC) founded on the ideal gas law. Therefore it becomes apparent that WPL is not confined to EC but is a necessary consideration when using Q, in order to properly account for density changes in the humidity variable measured.

6.4 Recommendations

The fact that absolute humidity is not conserved formally precludes its use in MOST and this alone means it is not a suitable variable for obtaining fluxes via similarity scaling. Therefore either a composite method as set out in Hill (1997), where $C_Q{}^2$ is converted to $C_q{}^2$ for use in MOST to find q_*, can be used; or the new structure parameter coefficients presented here (Table 6-1) can be applied and the data processed entirely using specific humidity formulations. Note that where Hill's (1997) method has been followed, the final stage of computing the latent heat flux differs from the argument presented here (he converts back to Q_* in order to find -$L_v u_* Q_*$). It is noted here that all published two-wavelength scintillometry estimates of the latent heat flux appear to contain this error, which has not been recognised before. To correctly account for the density effects, Equation 6-17 should be used instead.

Ideally, the specific humidity should be used throughout the calculations. When scintillometric fluxes have been calculated based on absolute humidity and it is not possible to reprocess the data, then the density correction (Equation 6-18) should be applied retrospectively. This will allow interpretation of published results, as often it may be possible to approximately correct the latent heat flux using the information contained within the publication. Although this still incorporates Q_* obtained using an inappropriate method (MOST

for a non-conserved quantity) these errors may be small when similarity functions for temperature and moisture are almost identical.

To summarise (Figure 6-1), if route 1b is used to find C_Q^2, this can be converted to C_q^2 via 1c or Q_* to q_* via 2c. In principle MOST requires conserved variables, making 2b invalid, although under perfect MOST conditions T-q similarity is obeyed and 2a and 2b would become equivalent. Taking u_*Q_* as the evaporation gives an inaccurate estimation of the evaporation and the WPL-style correction of Equation 6-18 should be applied to find the true value (step 3c). However, the recommended route is to use specific humidity throughout, following route 1a, 2a and 3a, in order to estimate the surface moisture flux from measured C_n^2.

6.5 Implications

It has been shown here that the widespread use of absolute humidity in latent heat fluxes derived from two-wavelength scintillometry will likely result in an error in the estimation of the true latent heat flux. For campaigns over agricultural land, such as the Flevoland (Meijninger et al., 2002a) and LITFASS (Meijninger et al., 2006) experiments, Bowen ratios were generally low (< 1), suggesting an underestimation of a few percent, but this will be larger (perhaps 10%) for drier fields. Future two-wavelength observations over areas with larger β would be expected to show a greater discrepancy.

Formulating the refractive index in terms of specific rather than absolute humidity changes how that measurement is interpreted. However the C_n^2 measurement itself is unchanged. Therefore the recommendations made here do not alter the effective height scaling method as outlined in Evans and De Bruin (2011), which is based around the effective measurement height of C_n^2 and occurs before the partitioning of refractive index fluctuations into temperature and humidity contributions.

Through the choice of humidity variable, it may appear that the instrument sensitivity to humidity fluctuations has changed. However, this is not the case – it is simply that the sensitivity to specific humidity is more relevant than the sensitivity to absolute humidity. The suitability of different wavelength combinations (such as the three-wavelength method (Andreas, 1990) or the two-wavelength analysis (Andreas, 1991)) could be reformulated using q. The reduced C_n^2 sensitivity of millimetre-wave scintillometers at certain Bowen ratios ($\beta \approx 2$-3), brought about by the negative C_{Tq} term and noted by Otto et al. (1996), cannot be avoided by choosing to work with specific rather than absolute humidity (Figure 6-3a). Further research is required on this topic.

At optical wavelengths the choice of specific or absolute humidity makes little difference because at those wavelengths the fluctuations are almost entirely due to temperature variation. Fortunately, this means that the single-wavelength scintillometry equations are not noticeably different between humidity variables (< 1% difference in structure parameter coefficients) and no changes are necessary for the single-wavelength method. Furthermore, with a single scintillometer setup the latent heat flux is estimated from the surface energy balance. Thus neither the sensible nor latent heat fluxes estimated from single-wavelength scintillometry require significant adjustment as a result of the work presented here.

6.6 Conclusions

Through re-examination of the methodology to estimate the latent heat flux from two-wavelength scintillometry it is concluded that the common use of absolute humidity is not advised for two main reasons: (a) Q is not a conserved variable and so should not be used in MOST, and (b) changes in Q are not independent of changes in temperature. The latter is more significant: not accounting for density effects can result in an underestimation of the daytime latent heat flux by more than 20% for very dry conditions, and around 5-15% for more typical conditions.

The use of specific humidity to represent the water vapour content of the atmosphere overcomes both issues; it is a conserved variable and independent of temperature. Importantly, changes in specific humidity are related to a surface source or sink of water molecules and cannot arise solely from variations in temperature. After re-deriving the central equations required to process scintillometry data in terms of q, different structure parameters are obtained (C_q^2 and C_{Tq}) leading to the scaling variable of specific humidity (q_*). The latent heat flux is then calculated using q_*, ensuring that a temperature change alone cannot give rise to an apparent latent heat flux. The resulting flux properly accounts for density effects due to temperature, and by including the $(1-q)^{-1}$ factor in accordance with Webb et al. (1980), the additional small correction for the water vapour flux is applied.

The new formulation for the latent heat flux is in accordance with the open-path eddy covariance work in Webb et al. (1980). For scintillometry there is the advantage of being able to choose to work with q at an early stage. It is recommended to use specific humidity throughout so density effects and MOST requirements are inherently taken care of. By working with independent variables, it is possible to separate the influences of temperature and water vapour. Most critically, this ensures comparisons can be made with other measurement techniques, model output or theoretical predictions.

Accounting for density effects rectifies the underestimation in the latent heat flux when β is positive/overestimation when β is negative. Previous studies have tended to indicate that latent heat fluxes estimated from scintillometry are already quite high (Green et al., 2000), perhaps suggesting there are other problems with the methodology or instrumentation that have not been considered. In order to progress, the methodology must have a sound physical basis according to current understanding. Other significant areas of uncertainty remain, for example knowledge of the stability functions (De Bruin et al., 1993; Hoedjes et al., 2002; Moene et al., 2004; Meijninger et al., 2006) and accurate rejection of absorption fluctuations (represented by the imaginary part of the refractive index) particularly for millimetre wavelengths (Nieveen et al., 1998; Green et al., 2001; Meijninger et al., 2002a; Van Kesteren, 2008; Evans, 2009). To refine and improve the technique further careful experimental comparisons are required.

This improved methodology, based on theoretical considerations, should be applied to ensure that obtained latent heat fluxes are as accurate as possible; and meet the accepted definition of surface flux, so are comparable with other methods (such as eddy covariance).

6.7 Appendix

In Table 6-A1 the structure parameter coefficients for absolute humidity (Q), specific humidity (q) and mass mixing ratio (r) formulations are given. These were derived starting from Equation 6-1, in each case substituting e/T as $R_v Q$, $R_v \rho q = R_v pq/RT$, or $R_v \rho_d r = R_v pr/(R_d + R_v r)T$, which are obtained combining the ideal gas law and Dalton's law of partial pressures. The terms are broadly arranged into columns pertaining to the differentiation process. The structure parameter coefficients A_Q, A_q and A_r are all similar as are the temperature structure parameter coefficients for optical wavelengths. The significant difference occurs between A_T and A_t or A_τ due to the third term, which is the differential of density with respect to temperature. A_t and A_τ are identical because neither q nor r is dependent on T.

It is valid to use any of the above pairs of structure parameters to partition C_n^2 into temperature and moisture fluctuations (via an equation of the form of 6-10). Only q or r should be used with MOST. The latent heat flux can be found using q_* (Equation 6-17) or r_*:

$$L_v E = -\overline{\rho_d} L_v u_* r_* = -\overline{\rho}(1-\overline{q}) L_v u_* r_* . \qquad \text{(6-A1)}$$

Since both Equation 6-17 and Equation 6-A1 require a $(1-q)^{\pm 1}$ factor to find $L_v E$, there is no obvious preference for choosing r over q.

Temperature Coefficients				
Optical	$A_{T\_opt} = -10^{-6} m_{1\_opt} \frac{\overline{p}}{\overline{T}}$			
	-271	-271	-	-
	$A_{t\_opt} = -10^{-6} m_{1\_opt} \frac{\overline{p}}{\overline{T}}$		$-10^{-6}(m_{2\_opt} - m_{1\_opt}) R_v \frac{\overline{pq}}{\overline{RT}}$	
	-270	-271	-	0.689
	$A_{\tau\_opt} = -10^{-6} m_{1\_opt} \frac{\overline{p}}{\overline{T}}$		$-10^{-6}(m_{2\_opt} - m_{1\_opt}) \frac{R_v \overline{pr}}{\overline{T}(R_d + R_v \overline{r})}$	
	-270	-271	-	0.689
Millimetre-wave	$A_{T\_mw} = -10^{-6} m_{1\_mw} \frac{\overline{p}}{\overline{T}} - 10^{-6} m_{2b\_mw} R_v \overline{Q}$			
	-342	-269	-72.1	-
	$A_{t\_mw} = -10^{-6} m_{1\_mw} \frac{\overline{p}}{\overline{T}} - 10^{-6} m_{2b\_mw} \frac{R_v \overline{pq}}{\overline{RT}}$		$-10^{-6}(m_{2\_mw} - m_{1\_mw}) \frac{R_v \overline{pq}}{\overline{RT}}$	
	-413	-269	-72.1	**-71.8**
	$A_{\tau\_mw} = -10^{-6} m_{1\_mw} \frac{\overline{p}}{\overline{T}} - 10^{-6} m_{2b\_mw} \frac{R_v \overline{pr}}{\overline{T}(R_d + R_v \overline{r})}$		$-10^{-6}(m_{2\_mw} - m_{1\_mw}) \frac{R_v \overline{pr}}{\overline{T}(R_d + R_v \overline{r})}$	
	-413	-269	-72.1	**-71.8**
Humidity Coefficients				
Optical	$A_{Q\_opt} = 10^{-6}(m_{2\_opt} - m_{1\_opt}) R_v \overline{Q}$			
	-0.689	-0.689	-	
	$A_{q\_opt} = 10^{-6}(m_{2\_opt} - m_{1\_opt}) \frac{R_v \overline{pq}}{\overline{RT}}$		$-10^{-6}(m_{2\_opt} - m_{1\_opt}) \frac{R_v \overline{pq}}{\overline{RT}} \left[\frac{\overline{q}}{\overline{R}} (R_v - R_d) \right]$	
	-0.685	-0.689	0.00416	
	$A_{r\_opt} = 10^{-6}(m_{2\_opt} - m_{1\_opt}) \frac{R_v \overline{pr}}{\overline{T}(R_d + R_v \overline{r})}$		$-10^{-6}(m_{2\_opt} - m_{1\_opt}) \frac{R_v \overline{pr}}{\overline{T}(R_d + R_v \overline{r})} \left[\frac{\overline{q}}{\overline{R}} R_v \right]$	
	-0.678	-0.689	0.110	
Millimetre-wave	$A_{Q\_mw} = 10^{-6}(m_{2\_mw} - m_{1\_mw}) R_v \overline{Q}$			
	71.8	71.8	-	
	$A_{q\_mw} = 10^{-6}(m_{2\_mw} - m_{1\_mw}) \frac{R_v \overline{pq}}{\overline{RT}}$		$-10^{-6}(m_{2\_mw} - m_{1\_mw}) \frac{R_v \overline{pq}}{\overline{RT}} \left[\frac{\overline{q}}{\overline{R}} (R_v - R_d) \right]$	
	71.4	71.8	-0.433	
	$A_{r\_mw} = 10^{-6}(m_{2\_mw} - m_{1\_mw}) \frac{R_v \overline{pr}}{\overline{T}(R_d + R_v \overline{r})}$		$-10^{-6}(m_{2\_mw} - m_{1\_mw}) \frac{R_v \overline{pr}}{\overline{T}(R_d + R_v \overline{r})} \left[\frac{\overline{q}}{\overline{R}} R_v \right]$	
	70.7	71.8	-1.15	

Table 6-A1: Structure parameter coefficients for optical and millimetre wavelengths for absolute humidity (A_T, A_Q), specific humidity (A_t, A_q) and mass mixing ratio (A_τ, A_r) formulations. New formulations shown here are optical A_τ and A_r and millimetre-wave A_t and A_q, and A_τ and A_r. Values are shown for typical atmospheric conditions (T = 288 K, p = 10^5 Pa, Q = 0.012 kg m^{-3}) below each term, including the total value of each structure parameter coefficient (shaded) to three significant figures. The values shown are scaled by a factor of 10^6, so that e.g. A_{t_mw} = -4.13 × 10^{-4}. A wavelength of 0.880 μm was used for the optical region. The additional term appearing in A_t and A_τ is significant (bold type), contributing around an extra 20% to the total structure parameter coefficients.

Acknowledgements

We would like to thank Wim Kohsiek for his valuable discussions and the reviewers for their suggestions to strengthen the paper. This work was partly funded by the Natural Environment Research Council, UK.

Chapter 7 Infrared and millimetre-wave scintillometry in the suburban environment – Part 1: structure parameters

7.1 Introduction

Scintillometry provides turbulent heat fluxes representative of much larger scales than is possible with traditional point-based or small area measurements, such as eddy covariance. Scintillometry is suited to heterogeneous regions because the measurements are spatially integrated, providing average values representative of the area as a whole (Hoedjes et al., 2002; Meijninger et al., 2002b; Evans et al., 2012). The scintillometry technique relates fluctuations in the intensity of light ('scintillations', observed as shimmering or 'heat-haze' on a hot day) to the strength of turbulence in the atmosphere. A transmitter provides a beam of electromagnetic radiation that is detected some distance (0.1-10 km) away by a receiver. Variations in the received intensity result from refraction as turbulent eddies move through the beam. The refractive indices of constituent air parcels are determined by their density which, in turn, can be related to their temperature and moisture content (see e.g. Meijninger (2003) or Moene et al. (2004) for details). The refractive index also depends on the wavelength of radiation; in the optical or near-infrared range temperature-induced fluctuations dominate the refractive index fluctuations, whereas for longer wavelengths (millimetre or radio-wave regions) humidity is more important. The peak sensitivity of the scintillometer measurement is towards the centre of the path, i.e. away from the transmitter and receiver and their mountings. Thus the atmosphere above a city (or valley) can be sampled remotely – a major practical advantage in areas where it would be very difficult to install other equipment *in situ*.

Scintillometer measurements have been conducted at sites spanning a range of complexities, from tests of the technique under simple conditions (Hill and Ochs, 1978; De Bruin et al., 1993), to studies investigating some of the complexities of non-ideal terrain, such as heterogeneous land cover (Beyrich et al., 2002a; Meijninger et al., 2002a; Meijninger et al., 2006; Ezzahar et al., 2007) or complex topography (Poggio et al., 2000; Evans, 2009; Evans et al., 2012). On the whole, these studies have shown that scintillometers installed above or close to the blending height provide valuable area-averaged fluxes.

Depending on the application, different scintillometers may be used. These are distinguished by the aperture size and wavelength of the source. With careful selection of a suitable path, the scintillometry technique has been successfully used in urban areas. Kanda et al. (2002), the first to derive the sensible heat flux in an urban setting (a dense residential area of Tokyo), used two small aperture scintillometers installed at different heights on a 250 m path. Other small aperture studies in cities include measurements made over rooftops and a street canyon in Basel (Roth et al., 2006) and comparison of fluxes above a courtyard and rooftop in London (Pauscher, 2010). Large aperture scintillometers are increasingly being used over longer urban paths, for example in Marseille (Lagouarde et al., 2006), Łódź (Zieliński et al., 2012), Helsinki (Wood and Järvi, 2012), London (Gouvea and Grimmond, 2010; Wood et al., 2013) and Nantes (Mestayer et al., 2011). These studies use infrared (or optical) scintillometers, which must rely on the residual of the energy balance if the latent heat flux is to be estimated. However, given the complexity of the energy balance (Oke, 1987), in particular the significant storage heat flux component (Oke et al., 1999; Offerle et al., 2005a) and a contribution from anthropogenic activities (Klysik, 1996; Allen et al., 2011) – both very difficult to measure – this is usually not attempted in urban areas.

A two-wavelength scintillometer system has the advantage that it is sensitive to both humidity and temperature fluctuations. Thus, the structure parameter of humidity can be obtained in addition to the structure parameter of temperature, from which both sensible and latent heat fluxes can be found (Hill et al., 1988; Andreas, 1989). Several studies have reported successful estimates of latent heat fluxes using the two-wavelength method (Meijninger et al., 2002a; Meijninger et al., 2006; Evans, 2009; Evans et al., 2010). However, this technique requires a value of the temperature-humidity correlation coefficient, r_{Tq}, to be assumed. Often r_{Tq} is taken to be ±1, indicating perfect correlation, as in Green et al. (2001) and Meijninger et al. (2002a), but other values have also been used: Kohsiek and Herben (1983) used r_{Tq} = 0.87; Evans (2009) used r_{Tq} = 0.8; Meijninger et al. (2006) used measured r_{Tq} from a nearby EC station with values between -0.5 and 0.9.

To overcome the need to assume a value for r_{Tq}, Lüdi et al. (2005) outlined a method to obtain path-averaged values of r_{Tq} using a two-wavelength scintillometer system. This 'bichromatic method' is an extension of the two-wavelength technique and involves correlating the signals from each scintillometer to enable determination of the combined temperature-humidity fluctuations and r_{Tq}. To date, there are only two (known) studies where the bichromatic method has been applied. The first, during LITFASS-2003, showed promising results. The methodology, sensitivity analysis and experimental findings are presented in Lüdi

et al. (2005) and the structure parameters are compared to eddy covariance in Beyrich et al. (2005). The second study, during LITFASS-2009, is introduced by Beyrich et al. (2012).

Aside from enabling more accurate structure parameters and fluxes to be obtained from scintillometry, improved knowledge of r_{Tq} has wider applications. Correlations between scalars are thought to be useful indicators for the violation of Monin-Obukhov Similarity Theory (MOST) (Hill, 1989; Andreas et al., 1998) and also offer insight into turbulent transport processes and physical quantities, such as the eddy diffusivities for heat and water vapour, fundamental to many models. In almost all previous studies measurements of r_{Tq} were made using point sensors. The literature suggests r_{Tq} is typically expected to be slightly less than +1 during the day, but negative and of smaller magnitude at night (Kohsiek, 1982; Andreas et al., 1998; Meijninger et al., 2002a; Beyrich et al., 2005; Lüdi et al., 2005; Meijninger et al., 2006). Some studies have suggested that r_{Tq} varies with stability (Li et al., 2011; Nordbo et al., 2013), although others have shown no clear relation (De Bruin et al., 1993; Roth, 1993). Explanation of $|r_{Tq}| \neq 1$ is often related to surface heterogeneity (Roth, 1993; Andreas et al., 1998; Lüdi et al., 2005), but lower values have been obtained over homogeneous surfaces too (Kohsiek, 1982; De Bruin et al., 1993). Such contrasts in published data highlight the importance of making these measurements.

In this study, a unique 94 GHz millimetre-wave scintillometer is deployed alongside an infrared scintillometer over the town of Swindon, UK. This is the first use of such a system in the urban environment. The overall objectives of this research are to measure structure parameters and obtain large-area sensible and latent heat fluxes for a suburban area. In this chapter, structure parameters from the two-wavelength system are compared to structure parameters calculated from eddy covariance and measured values of r_{Tq} are discussed. In Part 2 (Chapter 8), determination of the turbulent sensible and latent fluxes is presented and results analysed. These spatially integrated scintillometer measurements represent the behaviour of the suburban surface over an area of 5-10 km^2. The influence of energy and water availability, vegetation cover and seasonality is explored in both chapters.

7.2 Theory

The structure parameter for a variable, y, is defined (Tatarski, 1961),

$$C_y^2 = \frac{\overline{[y(x+\delta) - y(x)]^2}}{\delta^{2/3}}, \tag{7-1}$$

where δ is the spatial separation between two points and $y(x)$ is the value of the variable at location x. The cross-structure parameter between two variables is defined analogously. For

example the cross-structure parameter between temperature, T, and specific humidity, q, is written in terms of the averaged product $[T(x+\delta)-T(x)]\,[q(x+\delta)-q(x)]$.

7.2.1 Obtaining structure parameters from scintillometry

The refractive index structure parameter (C_n^2) is fundamental to scintillometry. For each wavelength (λ), it can be written,

$$C_n^2 = \frac{A_T^2}{T^2}C_T^2 + 2\frac{A_T A_q}{Tq}C_{Tq} + \frac{A_q^2}{q^2}C_q^2, \qquad (7\text{-}2)$$

where C_T^2 is the structure parameter of temperature, C_q^2 the structure parameter of specific humidity, C_{Tq} the temperature-humidity cross-structure parameter and A_T and A_q are the structure parameter coefficients for temperature and specific humidity respectively, given in Chapter 6, as A_t and A_q (see Table 6-2). These coefficients contain the wavelength dependence of C_n^2, whereas C_T^2, C_q^2 and C_{Tq} are properties of the atmosphere.

Each C_n^2 measurement is made up of a combination of the three unknowns: C_T^2, C_q^2 and C_{Tq}. As C_n^2 from large aperture optical or near-infrared scintillometers is almost entirely made up of temperature fluctuations (C_T^2), the (usually small) contributions from C_{Tq} and C_q^2 can be approximated using the Bowen ratio, β, (Wesely, 1976; Moene et al., 2004):

$$C_n^2 = \frac{A_T^2}{T^2}C_T^2\left(1+\frac{A_q}{q}\frac{T}{A_T}\frac{c_p}{L_v}\beta^{-1}\right)^2 \approx \frac{A_T^2}{T^2}C_T^2(1+0.03\beta^{-1})^2, \qquad (7\text{-}3)$$

where c_p is the specific heat capacity of air at constant pressure, L_v is the latent heat of vaporisation and the value 0.03 is for typical atmospheric conditions. The required Bowen ratio may be found by iteration to obtain the sensible heat flux, with the available energy as an input (e.g. Green and Hayashi (1998), Meijninger et al. (2002b), Solignac et al. (2009)). For single-wavelength scintillometry, calculation of the latent heat flux must then rely on the residual of the energy balance (Ezzahar et al., 2009; Guyot et al., 2009; Samain et al., 2011b; Evans et al., 2012).

As demonstrated by Hill et al. (1988) and Andreas (1989), a two-wavelength scintillometer system enables retrieval of both C_T^2 and C_q^2 via simultaneous equations (Equation 7-2 for each wavelength). The two-wavelength method has the significant advantage of providing both sensible and latent heat fluxes directly, but a value for the temperature-humidity correlation coefficient r_{Tq} must be assumed in the substitution $C_{Tq} = r_{Tq}(C_T^2 C_q^2)^{1/2}$.

The bichromatic method (Lüdi et al., 2005) uses the combination of optical and millimetre wavelength scintillometers, as in the two-wavelength method, but exploits the correlation between optical and millimetre-wave signals to obtain a third equation for the cross-structure parameter, C_{n1n2},

$$C_{n1n2} = \frac{A_{T1}A_{T2}}{T^2}C_T^2 + \left(\frac{A_{T1}A_{q2} + A_{T2}A_{q1}}{Tq}\right)C_{Tq} + \frac{A_{q1}A_{q2}}{q^2}C_q^2, \qquad (7\text{-}4)$$

where the subscripts 1 and 2 refer to different wavelengths. In this study, λ_1 denotes optical (specifically 880 × 10^{-9} m) and λ_2 millimetre (3.2 × 10^{-3} m) wavelengths. Thus all three unknown meteorological structure parameters (C_T^2, C_q^2 and C_{Tq}) can be found from the three measured refractive index structure parameters by inverting the matrix equation,

$$(C_{n1n1} \quad C_{n2n2} \quad C_{n1n2}) = \mathbf{M}\begin{pmatrix} C_T^2 \\ C_{Tq} \\ C_q^2 \end{pmatrix}, \qquad (7\text{-}5)$$

where the inverse matrix $\mathbf{M}^{-1}$ is given by,

$$\mathbf{M}^{-1} = \frac{T^2q^2}{(A_{T1}A_{q2} - A_{T2}A_{q1})^2}\begin{pmatrix} \frac{A_{q2}^2}{q^2} & \frac{A_{q1}^2}{q^2} & \frac{-2A_{q1}A_{q2}}{q^2} \\ \frac{-A_{T2}A_{q2}}{Tq} & \frac{-A_{T1}A_{q1}}{Tq} & \frac{(A_{T1}A_{q2} + A_{T2}A_{q1})}{Tq} \\ \frac{A_{T2}^2}{T^2} & \frac{A_{T1}^2}{T^2} & \frac{-2A_{T1}A_{T2}}{T^2} \end{pmatrix}. \qquad (7\text{-}6)$$

As mentioned above, the structure parameter coefficients A_T and A_q should be those formulated using specific humidity.

For the bichromatic method the value of C_{Tq} obtained can therefore be used to effectively measure the temperature-humidity correlation coefficient:

$$r_{Tq} = \frac{C_{Tq}}{\sqrt{C_T^2C_q^2}}. \qquad (7\text{-}7)$$

The Bowen ratio is defined as the ratio of the sensible to latent heat flux. If MOST assumptions (i.e. T-q similarity) are satisfied, the Bowen ratio can be calculated from the structure parameters (Andreas, 1990; Lüdi et al., 2005),

$$\beta = \mathrm{sgn}[C_{Tq}]\frac{c_p}{L_v}\sqrt{\frac{C_T^2}{C_q^2}}\,. \tag{7-8}$$

When the cross-structure parameter has not been measured, the structure parameters C_T^2 and C_q^2 can be calculated from the two-wavelength equations, after Hill et al. (1988):

$$C_T^2 = \frac{A_{q2}^2 C_{n1n1} + A_{q1}^2 C_{n2n2} + 2r_{Tq}A_{q1}A_{q2}S_{2\lambda}\sqrt{C_{n1n1}C_{n2n2}}}{(A_{T1}A_{q2} - A_{T2}A_{q1})^2 T^{-2}}, \tag{7-9}$$

$$C_q^2 = \frac{A_{T2}^2 C_{n1n1} + A_{T1}^2 C_{n2n2} + 2r_{Tq}A_{T1}A_{T2}S_{2\lambda}\sqrt{C_{n1n1}C_{n2n2}}}{(A_{T1}A_{q2} - A_{T2}A_{q1})^2 q^{-2}}, \tag{7-10}$$

where $S_{2\lambda}$ is ±1 (for the positive square root). This choice of sign is an inherent ambiguity of the two-wavelength method and represents the two possible solutions to C_{n2n2} (Hill et al., 1988; Hill, 1997). For low β when humidity fluctuations dominate C_{n2n2} then $S_{2\lambda}$ = +1; $S_{2\lambda}$ = -1 is required at larger β. The sign of $S_{2\lambda}$ is not known *a priori* but must be assumed. Often the two solutions for β indicate which is the most likely solution for the atmospheric conditions and site characteristics (Hill, 1997).

The sensible heat flux (Q_H) and latent heat flux (Q_E) are obtained iteratively from structure parameters using MOST. Details are given in Chapter 8.

7.2.2 Obtaining structure parameters from eddy covariance

Conversion between temporal and spatial domains enables calculation of structure parameters from point measurements, such as those from eddy covariance instrumentation. The spatial structure function, D_{yy_x}, can be written (e.g. Stull (1988))

$$D_{yy\_x}(\delta) = C_y^2\delta^{2/3} = \overline{[y(x+\delta) - y(x)]^2}\,. \tag{7-11}$$

Analogously, the temporal structure function, D_{yy_t}, is given by

$$D_{yy\_t}(\tau) = \overline{[y(t+\tau) - y(t)]^2}\,, \tag{7-12}$$

where τ is the temporal separation and $y(t)$ is the value of the variable at time t. Bosveld (1999) gives the conversion between temporal and spatial structure functions using the horizontal wind vector, U, and the variances of the three wind components, $\sigma^2_{u,v,w}$:

$$D_{yy\_x}(\delta) = \frac{D_{yy\_t}(\delta / U)}{\left(1 - \frac{1}{9}\frac{\sigma_u^2}{U^2} + \frac{1}{3}\frac{\sigma_v^2}{U^2} + \frac{1}{3}\frac{\sigma_w^2}{U^2}\right)}. \quad (7\text{-}13)$$

Thus the temporal structure functions can be calculated from eddy covariance measurements, converted to spatial structure functions (Equation 7-13) and used to find the structure parameters (Equation 7-11).

7.3 Experimental details

7.3.1 Instrumental setup and site description

The millimetre-wave scintillometer (MWS) (Evans, 2009), designed and built by the Centre for Ecology and Hydrology (CEH) and Rutherford Appleton Laboratory (RAL), was used in combination with a commercially available large aperture infrared scintillometer, the BLS900 (Scintec, Rottenburg, Germany). Both scintillometers were installed on a 5.5 km path over Swindon, UK. The path is orientated approximately north-south and extends from the rural fringes at the edge of the settlement to the town centre (Figure 7-1). An eddy covariance (EC) system was positioned near the centre of the path, consisting of a sonic anemometer (R3, Gill Instruments, Lymington, UK) and open-path infrared gas analyser (IRGA) (LI-7500, LI-COR Biosciences, Lincoln, USA) mounted at 12.5 m on a pneumatic mast. The EC site was equipped with an automatic weather station (WXT, Vaisala, Finland) which provides the additional input data required to process the scintillometer data: temperature, relative humidity (RH), pressure (p) and wind speed (U) are measured at a height of 10.6 m. A four-component radiometer (NR01, Hukseflux, The Netherlands) was installed at 10.1 m on the same mast and a tipping bucket rain gauge (0.2mm tip, Casella CEL, Bedford, UK) near the base of the mast. These were installed in the garden of a residential property approximately 3 km north of the town centre, where the surrounding land use is predominantly residential, consisting of 1-2 storey houses with gardens. Full details are given in Chapter 4. In addition to the meteorological instrumentation at the EC site (MET_{sub}), a second weather station was established on the rooftop of a modern office building close to the town centre (MET_{roof}). A summary of the instrumental setup is given in Table 7-1 and Figure 7-1. To provide a combined dataset of continuous input variables required for scintillometry processing, T, RH, p and U from MET_{roof} were linearly adjusted to gap-fill MET_{sub} (required for < 1% of T, RH and p and < 2% of U data), based on regressions with concurrent data from MET_{sub} (9 May 2011 - 31 December 2012).

Northern Swindon is typical of suburban areas, comprising different land use and land cover types, often with contrasting characteristics, in close proximity. The town centre at the

south of the study area has the highest density of buildings and roads (Figure 7-1). Industrial areas to the north and east have little vegetation and consist of mainly impervious surfaces but do not form a significant contribution to the typical measurement source areas. The area as a whole has a large proportion of vegetation, including grass verges, gardens, parkland, playing fields and intentionally undeveloped green corridors. There is also a large nature reserve just north of the centre of the study area, which lies directly underneath the scintillometer path. The area shown in Figure 7-1 comprises the following land cover fractions: 14% buildings, 31% impervious, 53% vegetation, 1% water and 2% pervious.

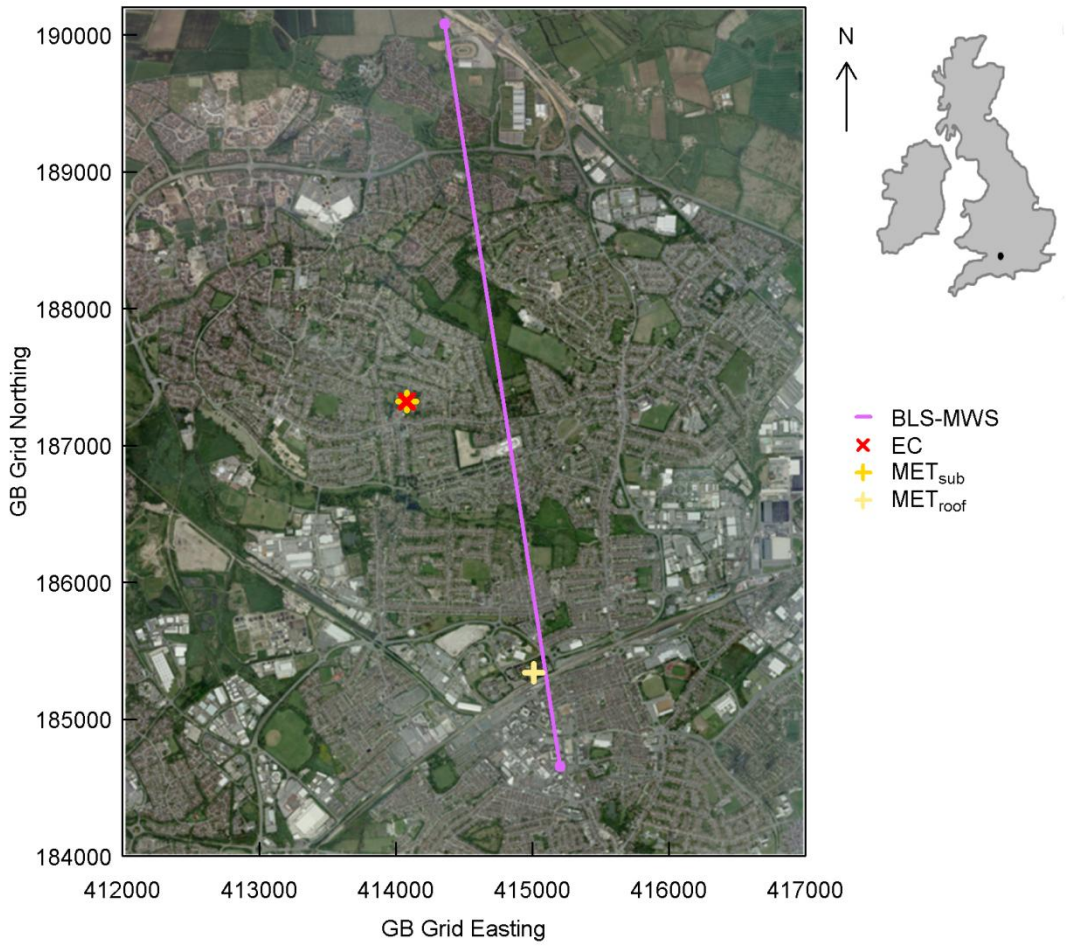

Figure 7-1 Aerial photograph (2009, ©GeoPerspectives) of the study area showing the locations of the two-wavelength scintillometer path (BLS-MWS), eddy covariance station (EC) and two meteorological stations (MET_{sub}, MET_{roof}). The location of Swindon within the British Isles is shown (top right).

Within the residential zones, local supermarkets with car parks and schools with playgrounds create patches with different land cover characteristics to the surrounding houses and gardens. Away from these patches, many neighbourhoods appear fairly homogeneous at a scale of a few hundred metres. To obtain representative measurements it is important to be high enough above the surface that quantities are sufficiently well-blended, although recent

studies have shown successful use of scintillometers even below the blending height (Meijninger et al., 2002b; Ezzahar et al., 2007). Based on the average height of the roughness elements (i.e. buildings and trees) the blending height is estimated at about 15-30 m for the BLS-MWS source area (Pasquill, 1974; Garratt, 1978).

To achieve sufficient beam height, topography and existing structures were exploited. The scintillometer transmitters were mounted on custom built brackets and installed at 28 m above ground level (a.g.l.) on a television transmitter at the northern edge of the town. The receivers of the BLS-MWS system were mounted at 26 m a.g.l. on the roof of a building in Swindon town centre. The resulting path is slanted (Figure 7-2). Within the practical constraints of finding sites in urban areas, this path: (a) ensures sufficient beam height particularly over the central portion of the path, (b) avoids east-west alignment which can allow coupling of solar radiation at low sun angles into the BLS receiver and (c) is not aligned with the southwesterly prevailing wind.

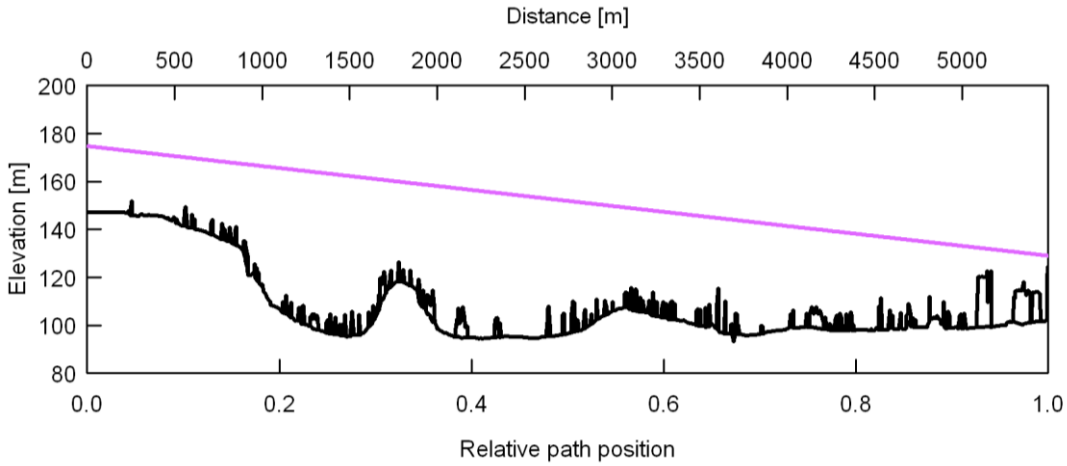

Figure 7-2 Cross section of the land surface and height of obstacles along the BLS-MWS path (coloured line).

The effective heights of the scintillometers are given in Table 7-2, calculated according to Equation 15 of Hartogensis et al. (2003). These estimates include adjustment to account for the curvature of the earth and the zero plane displacement height (Table 7-1). The displacement heights were calculated from the mean height of the roughness elements, z_H, within a distance of ±1000 m perpendicular to the scintillometer path (and +500 m in the direction parallel to the path), using the rule-of-thumb $z_d = 0.7z_H$ (Garratt, 1992). Estimation of a path weighted z_d gave very similar values. The difference in path weighting functions, which describe the sensitivity of the instruments as a function of position along the path (Figure 7-3), means that the BLS, MWS and combined BLS-MWS covariance measurements are

representative of different heights even though the BLS and MWS beams essentially traverse the same path (Evans and De Bruin, 2011). In the case of the EC station, z_H was calculated within 500 m of the EC mast. The average height of the surrounding roughness elements is lower here, and the height of the EC mast is 2-3 times z_H (Chapter 4).

Instrumentation		Height [m]	Location	Path length [m]	Bearing [°]	z_0 [m]	z_d [m]
Two-wavelength scintillometer system	BLS MWS	44.3	51°36'33.9" N 1°47'38.6" W (Tx) 51°33'38.1" N 1°46'55.3" W (Rx)	5492	170	0.7	4.9
Eddy covariance station	Sonic anemometer Infrared gas analyser	12.5	51°35'4.6" N 1°47'53.2" W	-	-	0.5	3.5
MET_{sub}	Weather station Radiometer	10.6 (WXT) 10.1 (NR01)	51°35'4.6" N 1°47'53.2" W	-	-	0.5	3.5
MET_{roof}	Weather station Radiometer	2.0 (WXT) 1.1 (NR01)	51°34'0.3" N 1°47'5.3" W	-	-	-	-

Table 7-1 The instrumental setup. For the scintillometers, the mean height of the beam above the land surface (z_m) is given (for the effective measurement heights (z_{ef}) see Table 7-2); for MET_{roof} the heights above the roof surface are given. The roughness length, z_0, and displacement height, z_d, were not calculated for rooftop site. Tx denotes transmitter, Rx receiver.

Scintillometer	Instrument characteristics		Site dependent characteristics		
	Wavelength [m]	Aperture diameter [m]	Fresnel zone [m]	Effective height [m]	Scaling (S) factor
BLS (C_{n1n1})	880×10^{-9}	0.145	-	45.0	-
MWS (C_{n2n2})	3.2×10^{-3}	0.25	4	42.8	0.952
BLS-MWS (C_{n1n2})	-	-	-	43.1	0.958

Table 7-2 Instrumental and site dependent characteristics for the scintillometer systems. See text for methods used.

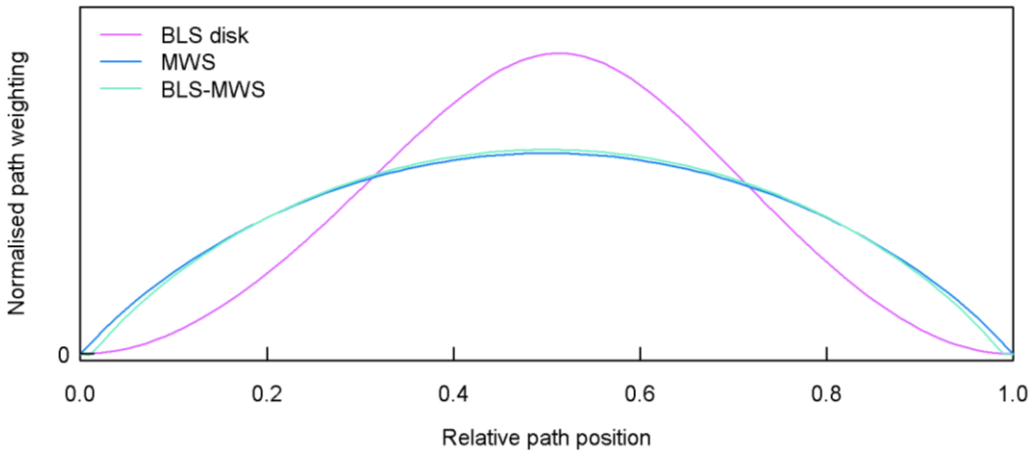

Figure 7-3 Path weighting functions for the infrared scintillometer (BLS disk), the MWS and the BLS-MWS combination, normalised so that the total area under each curve equals one.

For the BLS-MWS system the beams must be close together (Lüdi et al., 2005). The separation between MWS and BLS beams was minimised (< 0.35 m) and the configuration reversed at each end so that the beams crossed near the centre of the path. To protect against electrical interference, it was necessary to shield the power and signal cables at the scintillometer sites. Scintillometer data can sometimes be affected by vibrations of the mounting structures (Von Randow et al., 2008; Beyrich et al., 2012). The brackets were designed with this in mind and the scintillometer spectra do not suggest that the setup suffers from vibrational contamination.

From January 2012 to April 2012 the MWS was not operational due to a fault. The data presented here constitute the complete months when the scintillometer system was functioning: July-December 2011 and May-December 2012.

7.3.2 Data collection, processing and quality control

7.3.2.1 Scintillometry

To calculate the meteorological structure parameters as described in Section 7.2, C_n^2 must be obtained from the scintillometers. In this study, C_{n1n1} is used to denote the refractive index structure parameter for the BLS, to distinguish from C_{n2n2} (MWS) and C_{n1n2} (BLS-MWS cross-term).

The BLS900 is a dual-beam scintillometer with two transmitter disks (results of only one disk are presented here) and was supplied with its own signal processing unit. The signal intensity of each BLS disk was sampled and stored at 500 Hz (raw data) and statistics including the mean and standard deviation of signal intensity were provided at 30-second intervals by the Scintec software (SRun v1-07). Additionally, the signal intensities of both BLS disks and of the MWS were sampled at 100 Hz by a CR5000 datalogger (Campbell Scientific Ltd., Loughborough, UK). These data were processed using code written in R (The R Foundation for Statistical Computing). The data were subjected to initial quality control involving the removal of dropouts (when the BLS makes a background measurement) and despiking. The BLS and MWS signals were bandpass filtered to remove contributions below 0.06 Hz and above 20 Hz for the calculation of C_{n2n2} and C_{n1n2}. The high-pass filter minimises the effect of low frequency absorption fluctuations. The unfiltered infrared signals were used for C_{n1n1}. At 10 min intervals, the variances, covariances and mean values of the signals were calculated as described in Lüdi et al. (2005), from which the log-amplitude (co)variances (σ^2_χ) were obtained. To convert between the log-amplitude (co)variances and refractive index (cross-)structure parameters the following equations were used:

$$C_{n1n1} = 4.48 D^{7/3} L^{-3} \sigma^2_{\chi 1} \qquad (7\text{-}14)$$

$$C_{n2n2} = 8.33k^{-7/6}L^{-11/6}\sigma_{\chi 2}^2 \quad (7\text{-}15)$$

$$C_{n1n2} = 8.93k^{-7/6}L^{-11/6}\sigma_{\chi 1\chi 2}, \quad (7\text{-}16)$$

where D refers to the aperture diameter of the infrared scintillometer (here, the BLS, D_{BLS} = 0.145), k to the optical wavenumber ($2\pi/\lambda$) of the millimetre-wave scintillometer and L to the path length of the two-wavelength system (Table 7-1, Table 7-2). These equations can be derived from the full forms of the log-amplitude (co)variances, which express the path weighting of the instrument, aperture averaging by the finite size of transmitter and receiver, the turbulence spectrum (assumed to be the Kolmogorov spectrum, e.g. Monin and Yaglom (1971)) and separation of the beams if applicable (Equations 7-A1, 7-A2, Section 7.7). Equation 7-16 is relevant for the bichromatic method but is only applicable to the installation described here. Equation 7-15 is obtained using the full formula (Equation 7-A2) instead of the small aperture approximation (in which the Bessel functions accounting for aperture averaging are excluded) and is also specific to this setup. For longer wavelengths, the approximation results in an inaccuracy even for long paths (Section 7.7). The equation for the infrared scintillometer (Equation 7-14) is a standard result and was first demonstrated by Wang et al. (1978).

Data were rejected during periods of low signal strength (usually caused by rain or fog), or when the measured structure parameters were outside physically reasonable thresholds. BLS data were rejected when the received signal intensity dropped below 0.5 of the daily maximum value. For the MWS a threshold of 0.33 of the daily maximum intensity was used, and MWS data were also removed when the BLS signal intensity was below the 0.5 threshold indicating obscuration along the BLS-MWS path. The data points directly adjacent to those failing the signal strength checks were also removed. Rain was recorded at the EC site for 10% of the dataset and fog often occurred particularly during autumn and winter mornings (based on observations during site visits). Values of C_n^2 above reasonable thresholds were excluded (nine C_{n1n1} values and one C_{n1n2} value). The resulting data available for analysis constituted 79% of the total possible 10 min values (N = 61776, which represents 429 days).

Kleissl et al. (2010) suggest an empirical threshold for the onset of saturation for infrared large aperture scintillometers of $C_{n1n1} > 0.074D^{5/3}\lambda^{1/3}L^{-8/3}$. Approximately 21% of the BLS data were above this threshold of 3.2×10^{-15} $m^{-2/3}$ and were corrected for saturation using a look up table of numerical values based on the modulation transfer function of Clifford et al. (1974). The correction increased C_{n1n1} by around 5% overall (~15% during summer daytimes). Where the estimated correction was larger than 25% data were removed instead (46 values in total). The MWS data and the BLS-MWS cross-correlation were not corrected. MWS data were well

below the saturation threshold of 5.0×10^{-11} $m^{-2/3}$ (Clifford et al., 1974) and a methodology for the cross-correlation is yet to be determined (Beyrich et al., 2012), so there is increased uncertainty in these measurements due to the extent of currently applicable theory.

To scale C_{n2n2} from the MWS and C_{n1n2} from the BLS-MWS to the same effective height as C_{n1n1} from the BLS, the S factors (Evans and De Bruin, 2011) given in Table 7-2 were applied to C_{n2n2} and C_{n1n2}. These factors account for the difference in effective heights between the three refractive index structure parameter measurements as a result of the combination of weighting functions and beam elevation. The S factors are relatively close to unity as the height differences are reasonably small for this setup.

Having obtained compatible 10 min values of C_n^2 from each of the BLS, MWS and BLS-MWS combination, the calculation of the meteorological structure parameters then proceeds as described in Section 7.2. Data were processed using each of the three techniques to investigate their respective merits, although the main focus is on the two-wavelength and bichromatic methods. No Bowen ratio correction was applied for the single-wavelength method (Equation 7-3), given the difficulties in estimating the available energy in urban environments. For the two-wavelength method r_{Tq} = ±0.8 was assumed and the solution corresponding to $S_{2\lambda}$ = +1 was chosen. The positions of twice-daily minima in C_{n1n1} were used to indicate stability transitions (Samain et al., 2012) and assign positive or negative r_{Tq} for the two-wavelength method. To distinguish between the methods applied, the subscripts '2λ' and 'bi' are used.

7.3.2.2 Eddy covariance

For comparison with scintillometer data, structure parameters were also derived from 20 Hz raw EC data. Sonic and IRGA data were time aligned by seeking maximum covariance between variables. Initial quality control incorporated threshold checks, outlier detection and despiking. A fixed temporal separation of 1 s was used after investigation into suitable values in the inertial subrange. Structure parameters of temperature and humidity and the temperature-humidity cross-structure parameter were calculated incorporating the Schotanus et al. (1983) correction for sonic temperature as discussed in Braam (2008) and Braam et al. (2012). Equation 7-7 was used to calculate r_{Tq} from the EC data.

The resulting 30 min structure parameters were quality controlled in accordance with the corresponding EC fluxes. Data were removed during times of known instrument malfunction, when the IRGA diagnostic indicated obstruction of the optical path, when rainfall could adversely affect the measurements and if values exceeded physically reasonable ranges.

7.4 Instrument performance

An unidentified instrumental noise problem affecting the CEH-RAL MWS has been reported elsewhere (Van Kesteren, 2008; Evans, 2009; Beyrich et al., 2012). Following extensive testing, the cause was finally established and the instrument repaired in June 2011. The spectra obtained are now close to the ideal shapes predicted by theory and suggest good instrument performance with a low noise floor (Figure 7-4). An upper estimate for the MWS noise limit is $C_{n2n2} \sim 1 \times 10^{-15}$ m$^{-2/3}$. The observed noise limit of the BLS is of the order of $C_{n1n1} \sim 5 \times 10^{-17}$ m$^{-2/3}$ in agreement with the manufacturer's specification (Scintec, 2009).

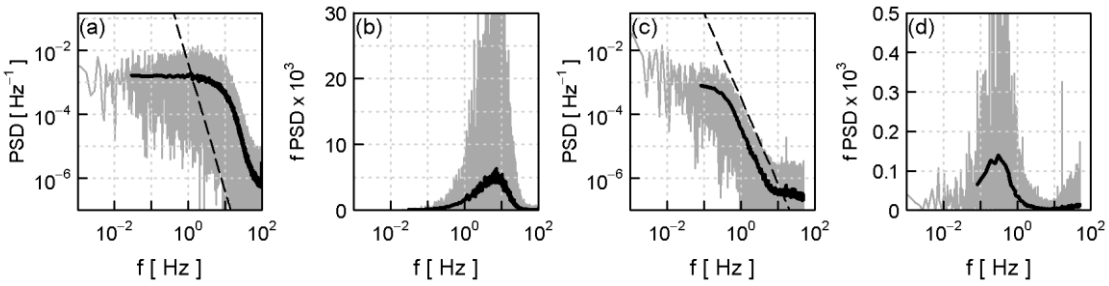

Figure 7-4 Example power spectral density (PSD) and frequency (*f*) spectra for (a, b) the BLS and (c, d) unfiltered MWS for 1430-1500 UTC on 02 July 2011. The dashed lines represent the theoretically predicted slopes of -12/3 and -8/3 for the BLS and MWS respectively.

7.5 Results and discussion

7.5.1 Structure parameters of the refractive index

For the two-wavelength scintillometer system, the refractive index structure parameters measured by the BLS, C_{n1n1}, and MWS, C_{n2n2}, and the cross-structure parameter from the covariance of the BLS-MWS signals, C_{n1n2}, follow clear diurnal cycles throughout the study period (Figure 7-5). The cross-structure parameter can be positive or negative depending on whether the signals are correlated or anti-correlated. As observed elsewhere C_{n1n2} tends to be negative during the daytime and positive at night (Lüdi et al., 2005). The main results are in broad agreement with those of the LITFASS campaigns, the only other published bichromatic scintillometry studies known to the authors (Beyrich et al., 2005; Lüdi et al., 2005; Beyrich et al., 2012). Since Figure 7-5 combines data across all months in the study period, the tendency is to average out seasonal differences. When examined by month (Figure 7-6) seasonal changes become evident, diurnal trends are better defined and changing day length is more apparent, particularly in the zero-crossing of C_{n1n2}.

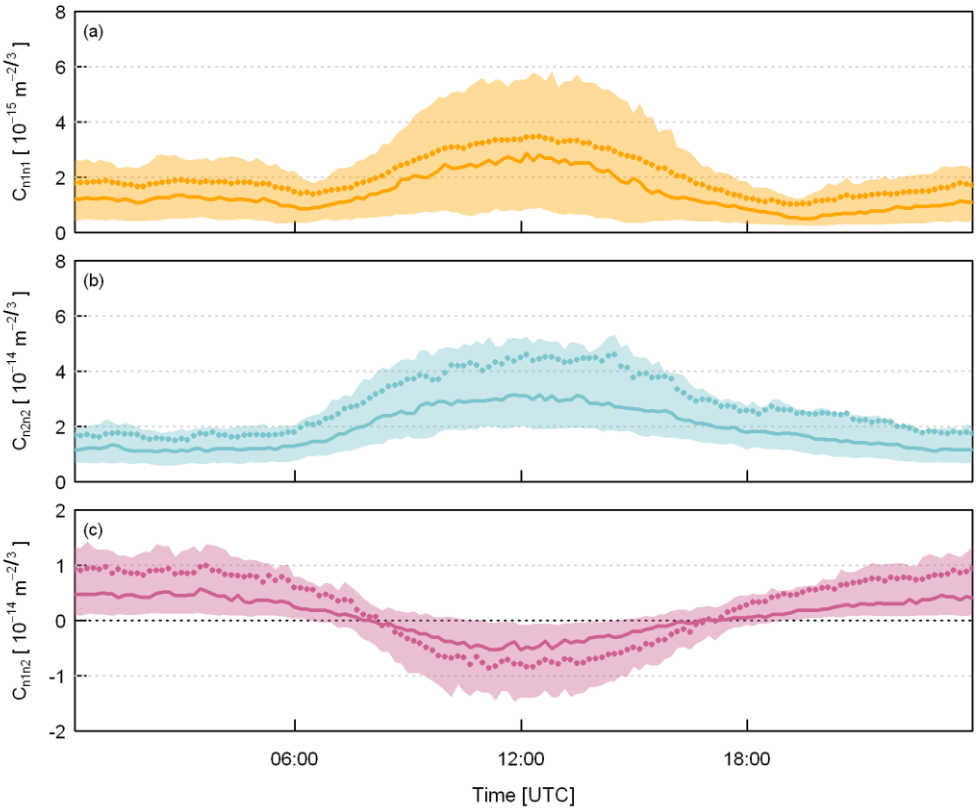

Figure 7-5 Mean (points) and median (lines) diurnal cycles and inter-quartile range (shading) of the structure parameters of the refractive index of air as measured by (a) the BLS, C_{n1n1}, and (b) MWS, C_{n2n2}, and (c) the cross-structure parameter as measured by the BLS-MWS combination, C_{n1n2}, for all data.

C_{n1n1} is largest during the day, passes through minima at sunrise and sunset and increases again at night. But during winter, reduced radiative input means the midday maximum is small and C_{n1n1} can be greatest at night. For millimetre wavelengths the diurnal course is less distinct, being generally flatter and wider, with no clear minima; instead C_{n2n2} remains low throughout the night. Daytime values of C_{n1n1} are about an order of magnitude smaller than C_{n2n2}, more so during winter as C_{n1n1} shows a greater seasonal reduction compared to C_{n2n2}. The diurnal cycle in C_{n1n2} is maintained across all months measured, has the largest amplitude during summer and changes in the position of the zero-crossings are influenced by the day length. In December C_{n1n2} is negative only for a short period during the middle of the day. The results presented here are thus in agreement with previous findings, and also extend the observations to a different climatic region, different land cover type and across multiple seasons.

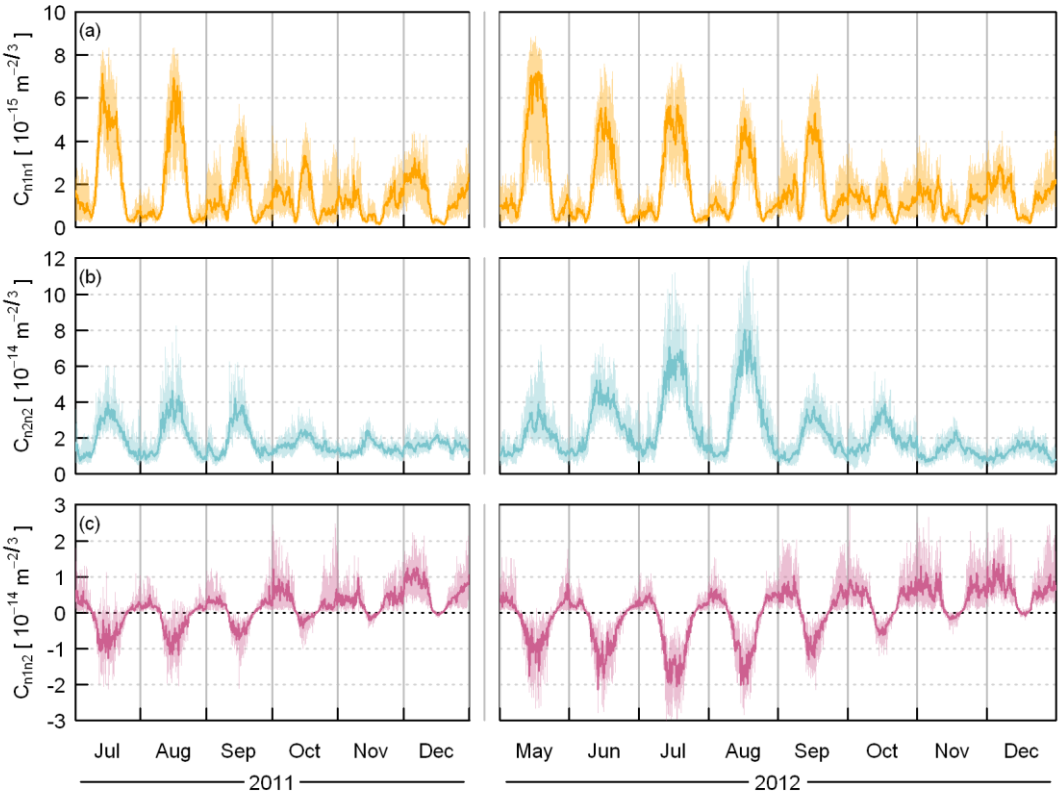

Figure 7-6 Median diurnal cycles and inter-quartile range (shading) of the structure parameters of the refractive index of air as measured by (a) the BLS, C_{n1n1}, and (b) MWS, C_{n2n2}, and (c) the cross-structure parameter as measured by the BLS-MWS combination, C_{n1n2}, separated by month.

There are notable differences in the structure parameters between months and between the same months in different years. For example, July-August 2011 has larger C_{n1n1} and smaller C_{n2n2} than in the same months in 2012, attributed to drier conditions in 2011 and very wet conditions in 2012. Infrared scintillometers are most sensitive to temperature fluctuations, hence C_{n1n1} is dominated by C_T^2 with a small contribution from C_{Tq} (of about 5%, which decreases as the Bowen ratio increases (Green et al., 2001)). The cross-structure parameter, C_{n1n2}, consists mostly of the C_{Tq} term and a contribution from C_T^2. The dominant term in C_{n2n2} depends on the Bowen ratio (Chapter 6): C_q^2 usually dominates at low β but the C_{Tq} term is important too and forms a negative contribution to C_{n2n2} during daytime when C_{Tq} is positive. As has been noted elsewhere (Hill et al., 1988; Otto et al., 1996; Leijnse et al., 2007), at higher Bowen ratios the terms in Equation 7-2 can cancel out leaving C_{n2n2} close to zero.

This minimum in C_{n2n2} is predicted from theory whilst, in practice, the finite instrumental noise floor and other experimental uncertainties mean zero C_{n2n2} will not be observed. Instead a measurement problem of reduced sensitivity is created around the region of minimum C_{n2n2}, where the true signal is close to, or below, the detection limit of the instrumental setup. From

the literature, the problematic region is expected to occur for $\beta \approx$ 2-3 (Leijnse et al., 2007). For the Swindon path, as for most of the previous two-wavelength campaigns, typical β values are expected to lie below this region. Other urban studies suggest daytime β of around 1-1.5 for suburban sites, lower when precipitation is frequent (Grimmond and Oke, 1995) and strongly dependent on the amount of vegetation (Grimmond and Oke, 1999c; Grimmond and Oke, 2002; Christen and Vogt, 2004). However, changing surface conditions can drive down the evaporation on the timescale of a few days (e.g. the drying out of impervious urban surfaces (Chapter 4) or, at agricultural sites, senescing crops (Evans et al., 2012)) producing significant excursions from the average β. Such excursions are seen in this dataset, particularly in the EC results and also in the bichromatic data. But the Bowen ratios measured by the two-wavelength method appear to be limited to around $\beta_{2\lambda} \leq 1.3$. There are two issues here: (a) the two-wavelength sign ambiguity discussed in Section 7.2 and (b) the region of reduced sensitivity around the C_{n2n2} minimum due to limiting instrument performance. Selecting $S_{2\lambda}$ = +1 automatically restricts the retrieved $\beta_{2\lambda}$ to values below that at which the terms in Equation 7-2 cancel out ($\beta_{2\lambda\_min}$ is 2.0-2.6 for this dataset). It is thought that the finite noise floor of the setup further constrains the measured value of $\beta_{2\lambda}$. Combined, these effects have a wider impact at lower values of β than suggested in the literature.

For a few cases (when β is large), the true structure parameters should be obtained from the alternative two-wavelength solution ($S_{2\lambda}$ = -1). Deciding when to choose which solution appears to be an intractable problem, however, unless an alternative reliable estimate of β or Q_E is available for the scintillometer source area. The bichromatic method does not have this same ambiguity and therefore could be used to identify times of high β (but limitations of the bichromatic method are discussed in Section 7.5.3). For this dataset $\beta_{bi} > \beta_{2\lambda\_min}$ for a very small proportion of the data (< 0.3% of daytime values); the corresponding C_T^2 and C_q^2 were excluded from further analysis. The more significant issue is the reduced measurement capability for $\beta_{2\lambda} > 1.3$. Comparison with β_{bi} suggests this could affect 3-8% of data. In these cases $\beta_{2\lambda}$ is likely an underestimate of the true β, hence the corresponding C_q^2 (and Q_E) will be overestimated. These data have not been removed but their impact on the results is discussed.

7.5.2 Structure parameters of temperature and humidity

The clear response to seasonal changes and robust diurnal cycles of C_n^2 give confidence that, in general, the scintillometer setup is responding reasonably. The meteorological structure parameters from the two-wavelength scintillometer system are shown in Figure 7-7. In Figure 7-8 some individual days are examined more closely and compared to EC. It is not expected that the BLS-MWS and EC values of C_T^2 and C_q^2 would agree exactly, firstly because

they have not been scaled to the same height and secondly, they are representative of different source areas with different land cover. However, the independent measurements are often remarkably comparable, with similar responses to changes in the driving meteorology and boundary layer conditions.

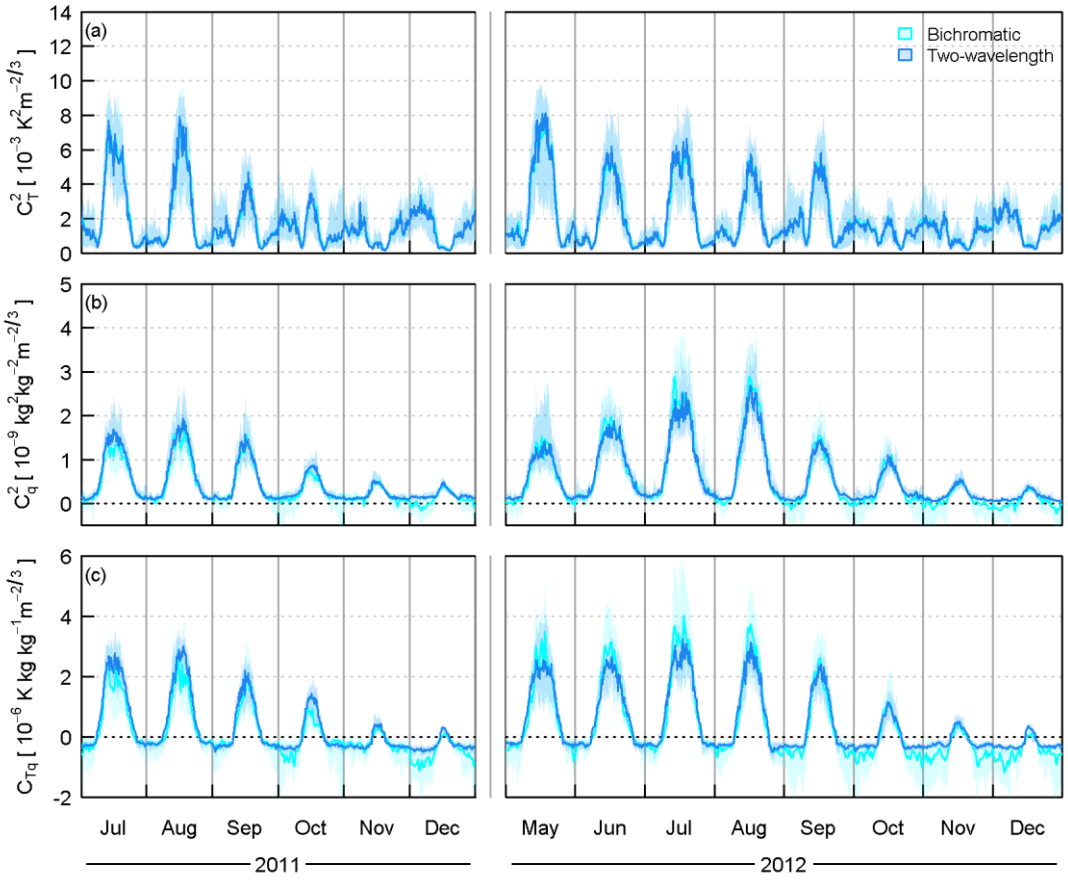

Figure 7-7 Median diurnal cycles and inter-quartile range (shading) of the meteorological structure parameters calculated using the bichromatic (30 min) and two-wavelength (10 min) techniques. In (c) C_{Tq} for the two-wavelength technique is given by $\pm 0.8(C_T^2 C_q^2)^{1/2}$.

In general, C_T^2 derived from EC is larger than from the BLS-MWS system whereas the estimates of C_q^2 are much closer together. Assuming identical height-scaling of temperature and humidity this suggests greater evaporation from the BLS-MWS source area than the EC source area. The EC C_T^2 measurements are larger most likely due to a combination of (a) being made closer to the surface and (b) being representative of an area with more energy partitioned into heating the atmosphere than evaporating water.

The three estimates of C_T^2 for the BLS-MWS path are similar (on average within 6%) whether the bichromatic, two-wavelength or single-wavelength approach is used. Larger deviations are seen between the bichromatic and two-wavelength estimates of C_q^2 when r_{Tq}

measured by the bichromatic method differs from the value assumed (±0.8) in the two-wavelength method (e.g. 21 August 2011, Figure 7-8).

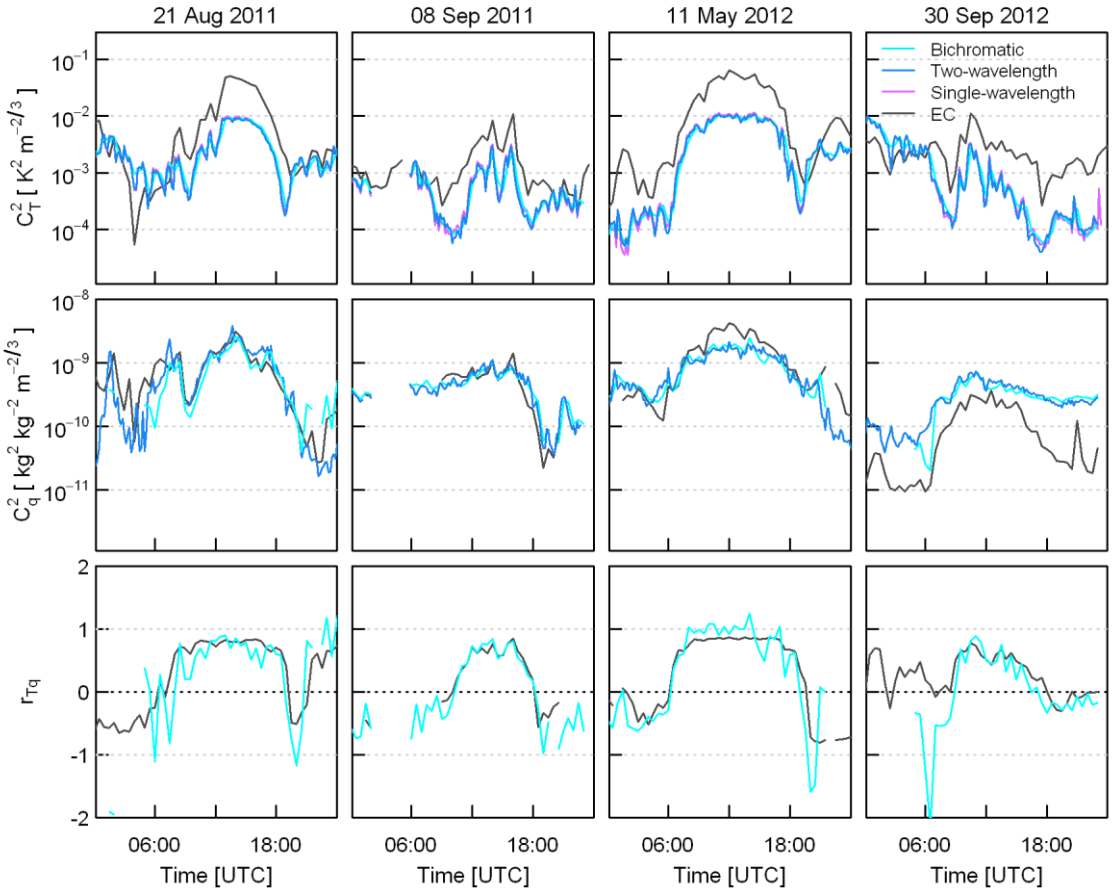

Figure 7-8 Structure parameters of temperature and humidity and the temperature-humidity correlation for selected days, derived from eddy covariance measurements (EC) and for the BLS-MWS system using the single-wavelength, two-wavelength and bichromatic techniques. For the two-wavelength method, r_{Tq} is prescribed as ±0.8. Single-wavelength and two-wavelength data represent 10 min intervals; EC and bichromatic statistics are for 30 min intervals.

Despite the differences in magnitude, structure parameters from the BLS-MWS system and from EC exhibit the same trends over the course of the year (Figure 7-9). Month-to-month changes in C_T^2 and C_q^2 are generally replicated in both scintillometer and EC datasets. Daytime values of the structure parameters decrease from mid-summer through to winter, but the decrease in C_T^2 is faster than that in C_q^2 and occurs earlier. Therefore β also decreases. C_T^2 is largest earlier in the year, whilst C_q^2 peaks in July and August (Figure 7-7, Figure 7-9). In summer 2012, C_q^2 is larger and C_T^2 smaller compared to the same months in 2011. The Bowen ratio exhibits similar seasonal behaviour in both years but is significantly lower for the BLS-MWS than for the EC data (daytime $\beta_{BLS\text{-}MWS}$ ~ 0.5 and β_{EC} ~ 1.0 in summer 2011, both are

smaller in 2012). In winter β becomes negative as a result of reduced radiative input. In terms of the energy exchange, evaporation continues throughout winter whereas the sensible heat flux is directed towards the surface for much of the daytime, only becoming positive for a short time around midday when there is sufficient energy (Chapter 4). Although it is more straightforward to consider this aspect in terms of the fluxes (discussed further in Chapter 8), the same conclusions can be inferred from the diurnal course of r_{Tq} (see Figure 7-10) and the positions of C_{n1n1} minima.

Two-wavelength C_q^2 is slightly larger than bichromatic-derived C_q^2 in 2011, but the opposite is true for most of 2012 (Figure 7-7). This could be explained by higher bichromatic-measured values of r_{Tq} in 2012 (Figure 7-10). Higher values of r_{Tq} result in smaller C_T^2 but larger C_q^2, when $r_{Tq} > 0$. The value of r_{Tq} has a greater impact on C_q^2 than C_T^2 (compare error bars in Figure 7-9a, c). Had r_{Tq} been assumed to be ±1 instead of ±0.8 for the two-wavelength method, average daytime C_q^2 would have been up to 9% higher and C_T^2 2% lower.

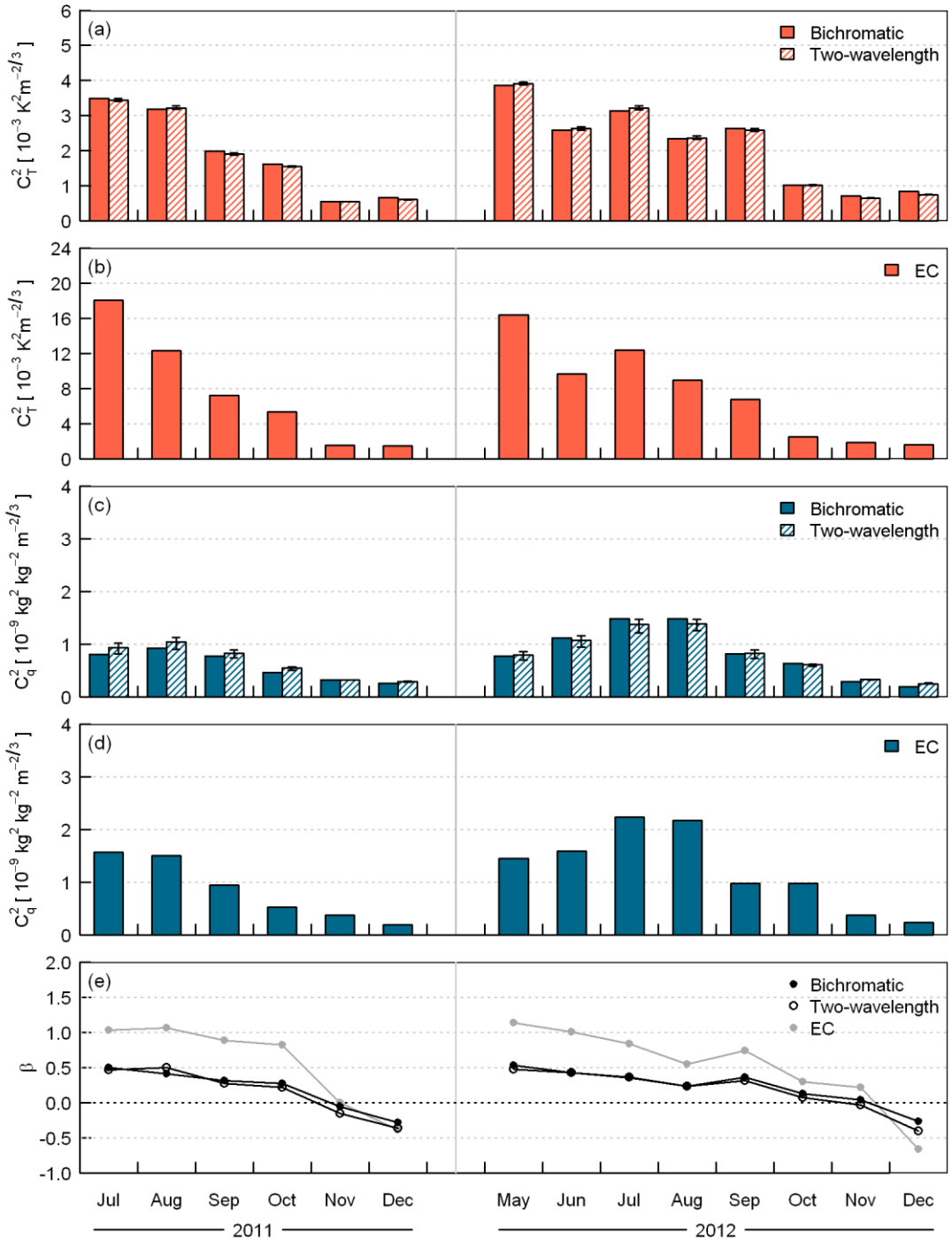

Figure 7-9 Mean daytime (incoming shortwave radiation $K_{\downarrow}$ > 5 W m^{-2}) (a-d) structure parameters and (e) Bowen ratio using Equation 7-8 for each month calculated for the BLS-MWS system (bichromatic and two-wavelength approaches) and eddy covariance (EC) data. For the two-wavelength results r_{Tq} = ±0.8; error bars (a, c) indicate r_{Tq} = ±0.5 and r_{Tq} = ±1.0. Note different y-axes in (a) and (b).

7.5.3 Temperature-humidity correlation

In Sections 7.5.1 and 7.5.2, application of the bichromatic method enabled the measurement of C_{Tq}. However, the BLS-MWS covariance term C_{n1n2} can be highly variable and this variability is transferred to the bichromatic structure parameters and r_{Tq}. As a result, 10 min structure parameters from the bichromatic method show greater variability than from the two-wavelength method, particularly C_q^2 and C_{Tq} which have a greater dependence on C_{n1n2} than C_T^2 does (e.g. C_q^2 in Figure 7-8). Inspection of the time-series reveals that bichromatic r_{Tq} almost always follows a typical diurnal course but individual points may vary about the general trend and some unrealistic values of $|r_{Tq}| > 1$ are observed (e.g. 21 August 2011, 11 May 2012, 30 September 2012 Figure 7-8, Figure 7-10). Since r_{Tq} is a correlation coefficient these values (> 1) do not have a physical interpretation and they indicate limitations in the measurement. Lüdi et al. (2005) also reported frequent occurrences of $|r_{Tq}| > 1$. From the time-lagged cross-covariance of BLS and MWS signals, the estimated uncertainty in C_{n1n2} is around 10-20% during times when the bichromatic correlation appears most robust and the best performance is seen. This is of a similar size to the 20% estimate suggested by Lüdi et al. (2005). To calculate r_{Tq}, the structure parameters must be combined (Equation 7-7) and so r_{Tq} amasses the uncertainties in each of the measurements.

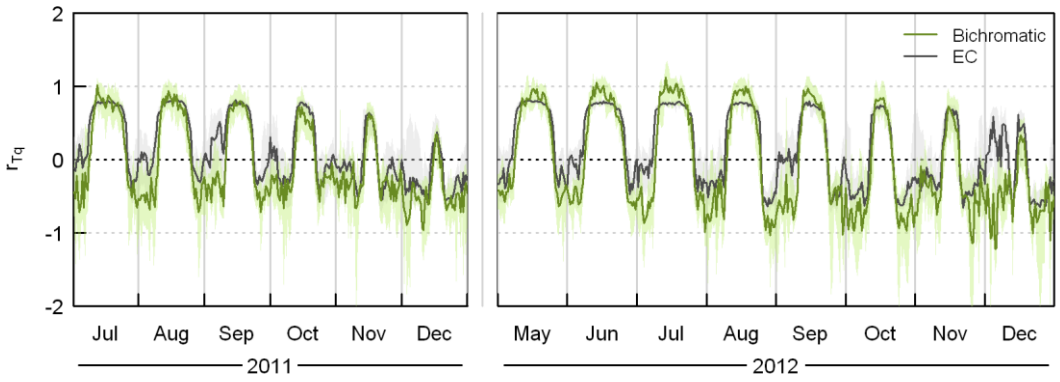

Figure 7-10 Monthly median diurnal cycles and inter-quartile range (shading) of the temperature-humidity correlation coefficient calculated using the BLS-MWS system via the bichromatic method and from the structure parameters from EC.

The bichromatic method was generally observed to perform best on days with moderate to high crosswinds (the wind speed component perpendicular to the BLS-MWS beams). At these times, the distribution of r_{Tq} is clearly bimodal with values centred around 0.8 to 1 for unstable daytime conditions and -0.3 to -0.5 for stable conditions and the variability between 30 min intervals is small. At times of low or near-zero crosswinds (< 2 m s^{-1}), however, $|r_{Tq}| > 1$ is

commonly observed, the variability of r_{Tq} is much higher and the retrieved values less robust, resulting in large fluctuations so that r_{Tq} frequently changes sign (even during the day when both turbulent fluxes are reasonably expected to be positive and the EC data do not suggest the contrary). When the crosswind is low, turbulent eddies decay as they are blown slowly through the beam (Taylor's hypothesis is violated) changing the intensity fluctuations. The correlation between the received scintillation pattern from one sample to the next decreases compared to higher crosswind cases (Poggio et al., 2000). The scintillation signals detected by the BLS and MWS will also have a less well-defined correlation, hence C_{n1n2} varies more from sample to sample. Furthermore, a locally homogenous and isotropic atmosphere is assumed in wave propagation theory upon which scintillometry is based (e.g. Tatarski (1961), Wang et al. (1978)). When wind speeds are low, turbulence may be sporadic and not well-developed over the whole path length. Perhaps sudden gusts or turbulence events can also cause spuriously high correlation between BLS and MWS signals which outweighs the correlated scintillation signal that the technique aims to measure. Given the complexity of this suburban site it is difficult to speculate further on this apparent effect of crosswind on bichromatic scintillometry but further research over simpler terrain would be beneficial.

The region of reduced sensitivity of C_{n2n2} (Section 7.5.1) also compromises the performance of the bichromatic method. In the vicinity of β_{min} measured C_{n2n2} will be mostly made up of noise contributions relative to the near-zero true value of C_{n2n2}. It follows that the correlation between BLS and MWS signals in this region is expected to be dominated by common instrumental or atmospheric effects such as absorption, or any electrical interference, mounting vibrations or obscuration along the path, although these effects were not found to be problematic generally. The most likely explanation is probably contamination by absorption, which is usually small and minimised by filtering, but which could become significant when the refraction signal diminishes. As previously discussed, the proportion of data with low sensitivity is believed to be small (Section 7.5.1). Some unphysical values of $C_q^2 < 0$ are also observed for the bichromatic method, usually at night when C_{n2n2} is small but C_{n1n1} and C_{n1n2} may be large (Figure 7-7b). Absorption or entrainment processes could be responsible for large C_{n1n2} at these times.

Despite the high uncertainty associated with individual bichromatic measurements, average r_{Tq} values provide information on the typical temperature-humidity correlation along the scintillometer path. This is an important quantity in its own right, as well as for accurate estimation of structure parameters and fluxes and as an indication of MOST violations. Measured r_{Tq} from the bichromatic method shows similar trends to the EC data (Figure 7-10). During summer, there is a clear plateau of close to +1 during daytime and the transition times

when r_{Tq} changes sign are of short duration compared to the day length. In winter r_{Tq} remains below zero for most of the day but peaks at positive values around midday, though the average midday r_{Tq} is less than 1.

The bichromatic data suggest larger daytime r_{Tq} in 2012 compared to 2011 but this is not seen in the EC data. The contrast between patches of hot, dry impervious areas and cool, wet vegetation may be reduced by generally wetter surfaces in 2012, which is thought to increase correlation between temperature and humidity (Moene and Schüttemeyer, 2008), but it is difficult to see why this would affect the scintillometer footprint more than the EC footprint. On the other hand, Lüdi et al. (2005) find that lower r_{Tq} coincides with lower β, which would suggest r_{Tq} values in 2012 would be smaller, not larger. Clearly more research is needed to better understand the performance of the bichromatic technique, and indeed the behaviour of r_{Tq}, under different conditions.

Typical values of r_{Tq} measured in this study are explored in Figure 7-11. Data are separated into unstable and stable conditions (based on the Obukhov length, L_{Ob}, from EC data and the timing of stability transitions according to C_{n1n1} for the scintillometer data). During unstable conditions measured r_{Tq} is positive and around 0.6 to 0.9, whereas the stable values tend to be smaller at around -0.3 to -0.5 and more variable. In winter r_{Tq} is smaller and more variable (median r_{Tq_EC} decreases from > 0.7 in summer to < 0.5 in December for unstable conditions). Some studies have indicated a dependence of temperature-humidity correlation on L_{Ob}, with larger deviations from MOST as neutral conditions are approached (Li et al., 2011; Nordbo et al., 2013), although other studies differ (De Bruin et al., 1993; Roth, 1993). The relatively small number of published studies available highlights the value of making these measurements. The scaling of temperature and humidity with stability is further explored in Chapter 8.

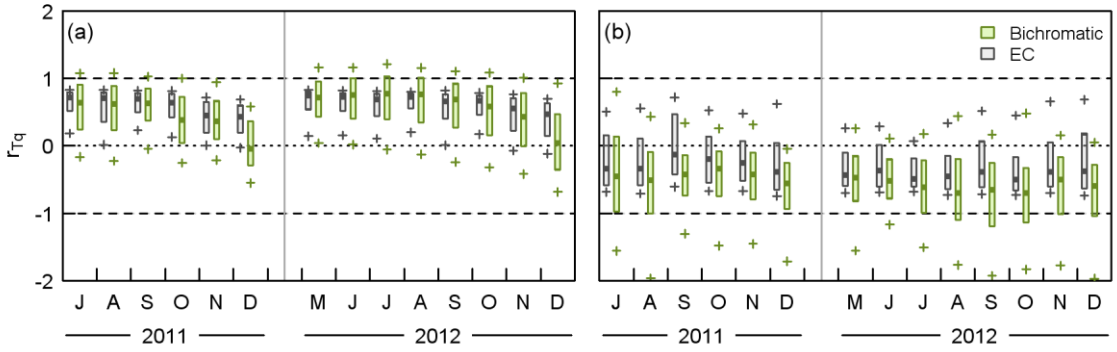

Figure 7-11 Boxplots of r_{Tq} from eddy covariance (EC) and the BLS-MWS bichromatic method for (a) unstable and (b) stable conditions. Crosses indicate the 10th and 90th percentiles, boxes the inter-quartile range (25th to 75th percentiles) and heavy lines the medians.

The EC data are always within the physically reasonable limits of ±1 and rarely exceed the range -0.75 to 0.85. The bichromatic data have a wider distribution with sometimes as much as 25% of data exceeding the upper limit of 1, especially in summer 2012. Nevertheless, the overall agreement between methods is encouraging and indicates generally large r_{Tq} for this suburban site so that MOST violations are usually small. Other studies also suggest daytime r_{Tq} tends to be smaller than 1, typically around 0.8. Kohsiek (1982) reported a value of 0.75 from a flat, homogeneous site at Table Mountain, Colorado using fast response temperature and humidity sensors. Andreas et al. (1998) find r_{Tq} = ±0.76, using EC over sandy soil with patchy vegetation in the Sevilleta, New Mexico. Meijninger et al. (2002a) find values between 0.7 and 0.95 for unstable conditions over heterogeneous farmland in Flevoland, The Netherlands. Roth (1993) presents values between 0.2 and 0.8 for an eight day period in July 1989 in suburban Vancouver. Nocturnal values of r_{Tq} down to -1 are rarely seen (Andreas et al., 1998; Beyrich et al., 2005; Lüdi et al., 2005; Meijninger et al., 2006). Our measurements do not indicate lower T-q correlation for this urban environment. It is thought that the EC-derived r_{Tq} likely underestimate the true values (as the sonic and IRGA are spatially separated and no spectral loss correction has been applied). The two-wavelength assumption r_{Tq} = +0.8 is seen to be reasonable for unstable conditions, although probably r_{Tq} = -0.8 is too large during stable conditions. These assumptions are also less justified in winter.

During winter, the transition periods last for a larger proportion of the daylight hours so that, as indicated in Figure 7-10, r_{Tq} only reaches its maximum value for a short time around midday. Several of the measurement issues in wintertime are also relevant at night. Turbulence tends to be weaker which calls into question some of the assumptions required for measurement theory; and stable stratification is more common which may mean that sometimes the measurement heights are outside the surface layer. Due to the rough surface, near-neutral conditions were far more common than stable and for the most part there remains a close match between EC and scintillometer measurements suggesting they are responding to the same forcing. On the few occasions when strongly stable conditions were observed at the EC station, the scintillometer time-series indicated times when the BLS-MWS was likely to be outside the surface layer, and potentially affected by other processes such as entrainment.

Some instances of positive nocturnal r_{Tq} are observed when the fluxes have the same signs – i.e. either unstable (Q_H > 0) conditions prevail, or more frequently observed is dewfall (Q_E < 0) under stable conditions, as on 21 August 2011 after 2130 (Figure 7-8). In these cases the two-wavelength method is limited as negative r_{Tq} must be assumed in the absence of other information, whereas the bichromatic method often captures this behaviour. For the most part

the nocturnal structure parameters and fluxes tend to be small so the absolute errors introduced by r_{Tq} of the wrong sign are fairly small, though they will always be biased in the same direction so will accumulate over time.

7.6 Conclusions

In this chapter, the first use of a two-wavelength scintillometer system in an urban area is reported and the behaviour of structure parameters is investigated at daily and seasonal timescales. By examining the structure parameters themselves, it is possible to gain more direct insight into the performance of the measurement technique; comparison of fluxes introduces the uncertainties of similarity functions which can be significant. These quantities are also important in their own right. Summertime behaviour is broadly in agreement with other published trials (Beyrich et al., 2005; Lüdi et al., 2005) and the long time-series offers insight into the dynamics of turbulent transport and their variation with season and surface characteristics. During summer C_T^2 is largest during the day, but daytime values are much smaller in winter. Whilst C_T^2 passes through clear minima at the stability transitions twice a day, C_q^2 follows a smoother diurnal course and remains larger during daytime than night time. The influence of seasonal variations in day length, or more specifically in available energy, has a clear impact on the structure parameters and r_{Tq}.

The Bowen ratio calculated from the measured structure parameters decreases across the two summer-to-winter periods studied here. Both EC and scintillometry exhibit similar month-to-month variations but β is smaller for the scintillometer system compared to EC, which can be explained by different source area characteristics. Overall, the structure parameters calculated from the EC data often exhibit remarkably similar behaviour to the scintillometry values, especially given the different scales and heights of the measurements. Chapter 8 explores these topics further and deals with the calculation and analysis of the turbulent fluxes.

As well as extending the two-wavelength technique to a new environment, several recently developed improvements are implemented in the processing. To obtain the structure parameter of refractive index from the millimetre-wave scintillometer, the validity of the small aperture approximation is considered (Section 7.7) and the more accurate full formula used instead (Equation 7-15, for this setup). To adjust for the difference in effective heights between the BLS and MWS, the S factor approach of Evans and De Bruin (2011) was used. Furthermore, the structure parameters were calculated following the formulation in terms of specific humidity as outlined in Chapter 6. The cross-correlation between BLS and MWS signals

enabled estimation of the temperature-humidity correlation coefficient, thus extending the application of the bichromatic method to the suburban surface.

These bichromatic results allow the extent to which r_{Tq} deviates from ±1 to be assessed. Both the path-averaged and eddy covariance r_{Tq} estimates are in accordance with studies over different land surfaces. However, the bichromatic method sometimes returns values outside the physically meaningful range $|r_{Tq}| \leq 1$. The inherent variability of the cross-structure parameter C_{n1n2} limits the accuracy of any particular measurement, whereas the two-wavelength results are more robust over shorter periods of 10 min. On average, the results closely follow the expected diurnal cycle of correlated temperature and humidity during the day and anti-correlated at night. Measured r_{Tq} is approximately 0.6-0.9 in unstable conditions; stable values are more variable but tend to be smaller in magnitude, averaging around -0.3 to -0.5. Observed r_{Tq} was furthest from ±1 during winter and in near-neutral conditions. Bichromatic r_{Tq} often captures the behaviour of r_{Tq} observed at the EC station, i.e. the shape of the diurnal cycle on a particular day and times when the assumed two-wavelength value will be wrong such as during dewfall. There may also be times when the local stability at the EC station is different to the stability for the BLS-MWS source area, which highlights the benefit of making a path-averaged measurement of r_{Tq}. Nordbo et al. (2013) demonstrate stability differences across Helsinki, although the contrasts in anthropogenic activities and building density between their study sites are much greater.

Two-wavelength scintillometer systems have considerable potential to deliver large-area measurements representative of complex environments, but it will be necessary to have a better understanding of the limitations in order to make further progress. Advantages of the bichromatic method include more accurate structure parameters derived using measured values of r_{Tq} rather than relying on assumptions. A measurement of r_{Tq} provides additional information about the atmospheric conditions, e.g. the relative sign of the heat fluxes and to what extent MOST conditions are satisfied. The bichromatic method also removes the sign ambiguity of the two-wavelength method, providing a single solution rather than two alternatives. For the minimal extra hardware requirements the recommendation is therefore to measure the bichromatic correlation even if the additional information is not used directly in data processing. Future work should focus on the performance under different conditions, such as whether there is an effect of crosswind, and the impact of differences in footprint and effective height between instruments.

Limitations of the two-wavelength method include ambiguity due to the possibility of multiple solutions, arising out of the choice of sign for C_{Tq} and the minimum in C_{n2n2} at moderate Bowen ratios. The region of reduced sensitivity around the C_{n2n2} minimum needs

more research, firstly to better understand its behaviour and secondly to focus on possible improvements to the experimental system or post-processing to overcome or at least minimise the impact. The large proportion of vegetation and cool, wet summers helped to maintain a low Bowen ratio in Swindon and no data were collected during spring time when β is typically larger. In drier years or at more built-up urban sites the results may have been less useable. To grasp the full potential and limitations of two-wavelength scintillometer systems, theoretical development combined with careful experimental testing is required. Comparison data (structure parameters and fluxes) from different methods will be required for thorough evaluation of these techniques.

7.7 Appendix: Validity of the small aperture approximation for millimetre-wave scintillometers

The log amplitude covariance of a scintillometer system can be written in a generalised form as (e.g. Lüdi et al (2005)),

$$\sigma_\chi^2 = 4\pi^2 k_1 k_2 0.033 C_n^2 \int_0^\infty dK \int_0^L dx K K^{-11/3} \sin\left(\frac{K^2 x(L-x)}{2k_1 L}\right) \sin\left(\frac{K^2 x(L-x)}{2k_2 L}\right) \times \left[\frac{2J_1(0.5KD_{r1}x/L)}{0.5KD_{r1}x/L}\right]\left[\frac{2J_1(0.5KD_{t1}(1-x/L))}{0.5KD_{t1}(1-x/L)}\right] \times \left[\frac{2J_1(0.5KD_{r2}x/L)}{0.5KD_{r2}x/L}\right]\left[\frac{2J_1(0.5KD_{t2}(1-x/L))}{0.5KD_{t2}(1-x/L)}\right] J_0(K|d|) \quad \text{(7-A1)}$$

where σ_χ^2 is the covariance of log amplitude, C_n^2 the refractive index structure parameter, K the eddy wavenumber and x the position along the path of length L; k is the optical wavenumber and D the aperture diameter of the receiver (subscript *r*) or transmitter (subscript *t*) for each instrument (subscript 1 or 2) separated by a distance d. J_0 and J_1 are Bessel functions. The three-dimensional Kolmogorov spectrum $\Phi_n(K) = 0.033 C_n^2 K^{-11/3}$ is assumed.

For a single instrument, this reduces to the standard formula for a large aperture scintillometer (Hill and Ochs, 1978):

$$\sigma_\chi^2 = 4\pi^2 k^2 0.033 C_n^2 \int_0^\infty dK \int_0^L dx K K^{-11/3} \sin^2\left(\frac{K^2 x(L-x)}{2kL}\right) \times \left[\frac{2J_1(0.5KD_r x/L)}{0.5KD_r x/L}\right]^2 \left[\frac{2J_1(0.5KD_t(1-x/L))}{0.5KD_t(1-x/L)}\right]^2. \quad \text{(7-A2)}$$

For cases when aperture averaging is unimportant, the standard formula for small aperture scintillometers,

$$\sigma_{\chi}^2 = 4\pi^2 k^2 0.033 C_n^2 \int_0^{\infty} dK \int_0^{L} dx K K^{-11/3} \sin^2\left(\frac{K^2 x(L-x)}{2kL}\right), \qquad \text{(7-A3)}$$

which gives

$$\sigma_{\chi}^2 = 0.124 k^{7/6} L^{11/6} C_n^2 \qquad \text{(7-A4)}$$

on integration, is often applied (Meijninger et al., 2002a; Lüdi et al., 2005; Meijninger et al., 2006).

Here we consider the validity of applying the small aperture approximation to millimetre-wave, microwave and radio-wave systems. For the effects of aperture averaging to be insignificant, the aperture diameter must be sufficiently small compared to the size of the Fresnel zone (F). With F around 10 times D, the small aperture approximation causes an appreciable (7%) underestimation of C_n^2 compared to evaluating the full formula (Figure 7-A1). The relatively long path over Swindon means the difference between formulations is quite small here (3%), but will be more important for shorter paths, shorter wavelengths or larger aperture diameters. Use of the full equation also modifies the path weighting function slightly; for Swindon the difference in effective heights between using the approximation and full form is 0.15 m.

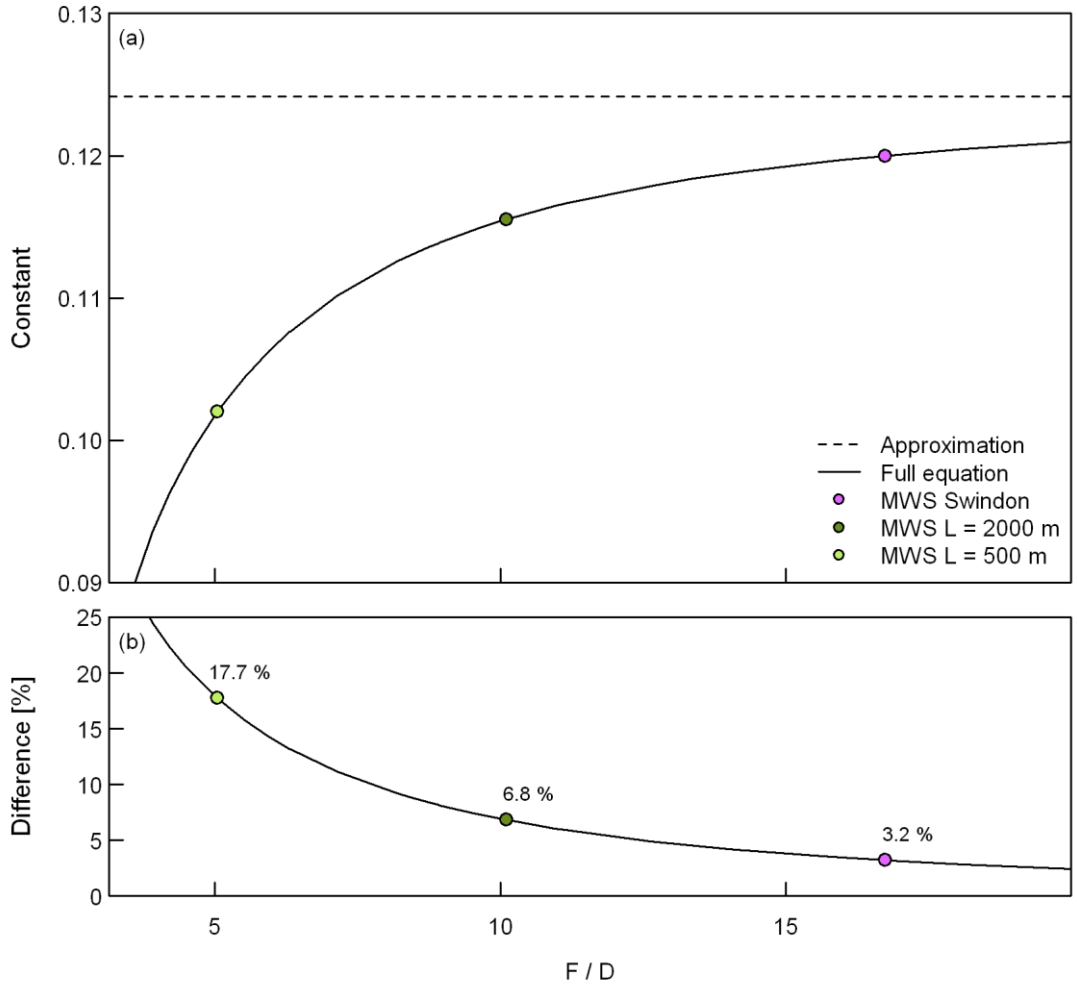

Figure 7-A1 (a) Value of the 'constant' in Equation 7-A4 when calculated using the full equation (Equation 7-A2) as a function of the ratio of Fresnel zone F to aperture diameter D and (b) percentage difference from the small aperture approximation (Equation 7-A3). Some example experimental setups are selected for the CEH-RAL MWS.

Acknowledgements

We would like to thank Alan Warwick and Cyril Barrett for constructing the scintillometer mounting brackets, Geoff Wicks for assisting with the electronics and the residents of Swindon who very kindly gave permission for equipment to be installed on their property. We are grateful to Wim Kohsiek and Oscar Hartogensis for their helpful discussions regarding the work presented in Section 7.7. This work was funded by the Natural Environment Research Council, UK.

Chapter 8 Infrared and millimetre-wave scintillometry in the suburban environment – Part 2: large-area sensible and latent heat fluxes

8.1 Introduction

The demand for large-area estimates of evaporation is considerable. Observations of catchment-scale evaporation are required for hydrological modelling, both to evaluate model performance and as forcing data for real-time river flow and water balance models and flood forecasting. For rural environments knowledge of evaporation is vitally important for irrigation scheduling, crop management and crop yield prediction – applications which will become increasingly important with the demands of food and water security as the world's population continues to grow. Given its key role in both the water and energy balance of ecosystems, evaporation is highly relevant across a range of applications including eco-hydrology (e.g. the ecological effects of drought) and in biogeochemistry for the modelling of large-scale greenhouse gas exchange through links with soil moisture and turbulent transport processes.

In urban areas evaporation has been shown to be a significant component of the energy and water balance and strongly dependent on surface water availability and vegetation cover (Grimmond and Oke, 1995; Grimmond and Oke, 2002; Christen and Vogt, 2004). Accurate measurement and prediction of evaporation, and its energy equivalent the latent heat flux, is important for assessing thermal comfort, flood risk and the merits of urban design options (such as green roofs, street trees, types of vegetation), management schemes (irrigation bans) and sustainable urban drainage tools (Xu and Chen, 2005; Mitchell et al., 2008).

Scintillometry offers a solution for routine monitoring of heat fluxes with significant advantages of being spatially representative over a large area, of high temporal resolution (30 min or less), continuous (i.e. not limited to cloud-free days as with some satellite products), able to inherently cope with heterogeneity, practical to install and low maintenance (e.g. Kleissl et al. (2009a)). Scintillometers measure the intensity of an electromagnetic beam transmitted through the turbulent atmosphere. Changes in intensity due to refraction by eddies of differing densities are related to changes in temperature and humidity, expressed as the temperature and humidity structure parameters, from which the fluxes of heat and water

vapour are obtained. At infrared (or optical) wavelengths, temperature fluctuations dominate, so these instruments are suitable for deriving the sensible heat flux. Longer wavelengths (e.g. microwaves, radio-waves) are more sensitive to humidity fluctuations so that, in combination with infrared, both sensible and latent heat fluxes can be obtained more directly (Hill et al., 1988; Andreas, 1989); with a single infrared instrument estimation the latent heat flux relies on closure of the energy balance.

One of the first studies to estimate evaporation from radio-wave scintillation was Kohsiek and Herben (1983), but there was no optical scintillometer used. Hill et al. (1988) outlined the theory and demonstrated the viability of the two-wavelength technique by comparison with structure parameters and fluxes from other micrometeorological methods at a very homogeneous farmland site in Flatville, Illinois. The technique has since been used to estimate heat fluxes over a vineyard (Green et al., 2000), pasture (Green et al., 2001), mixed agricultural landscapes (Meijninger et al., 2002a) and mixed agriculture with complex topography (Evans et al., 2010). The LITFASS campaigns (Beyrich and Mengelkamp, 2006) include heavily instrumented comparisons across different land cover types, mainly mixed agriculture. Aggregated eddy covariance results compared with two-wavelength scintillometry estimates indicated generally good performance for the trial of 11 days (LITFASS-2003, Meijninger et al. (2006)). In addition, the bichromatic correlation method was developed and tested (Beyrich et al., 2005; Lüdi et al., 2005), enabling a path-averaged measurement of the temperature-humidity correlation coefficient, thus removing the need to assume its value as with the traditional two-wavelength method. In the overview paper of LITFASS-2009, Beyrich et al. (2012) present structure parameters from two example days, 12-13 July 2009. Two-wavelength scintillometry remains a specialist technique as a longer wavelength instrument is not available commercially at present. A three-wavelength method has also been proposed as a solution to obtaining the combined temperature-humidity fluctuations, but would require at least three scintillometers and sensitivity analyses suggest results may not be significantly improved over the two-wavelength method (Andreas, 1990).

Single-wavelength (large aperture) scintillometry is now a fairly well-established technique and deployed in a variety of locations, although its use in urban environments has only developed recently. A three week experiment in Marseille demonstrated good agreement between scintillometer and eddy covariance sensible heat fluxes over the ‘reasonably homogenous’ built surface (Lagouarde et al., 2006). A much longer campaign in Łódź looks at diurnal and seasonal variability (Zieliński et al., 2012). Both studies compare the similarity functions used to estimate the sensible heat flux from structure parameters. Other urban sites include London (Gouvea and Grimmond, 2010), Toulouse (Masson et al., 2008), Nantes

(Mestayer et al., 2011) and Helsinki (Wood and Järvi, 2012). These studies concern the sensible heat flux. Results from Swindon using the single-wavelength method (i.e. infrared scintillometers only) are presented in Chapter 5.

In this study we report on the first large-area sensible and latent heat fluxes obtained from a two-wavelength scintillometer system installed over the urban environment. This chapter presents the estimation of fluxes from the structure parameters (obtained in Chapter 7) and analysis of those fluxes. Results are contrasted against eddy covariance measurements representative of a much smaller scale. Following the theoretical (Section 8.2) and experimental (Section 8.3) details, the performance of the scintillometry techniques is critically examined (Section 8.4.1). Three approaches are considered here: the single-wavelength, two-wavelength and bichromatic methods. For each wavelength (or combination of wavelengths) the conversion of the observed refractive index structure parameters to temperature (C_T^2) and humidity (C_q^2) structure parameters and the temperature-humidity cross-structure parameter (C_{Tq}) is described in Part 1 (Chapter 7). The two-wavelength results and eddy covariance fluxes are used in case studies to demonstrate the capabilities of the method (Section 8.4.2) and explore the important physical processes determining the energy partitioning (Section 8.4.3). Finally, the whole dataset (fourteen months) across two consecutive years, 2011-12, is presented (Section 8.4.4).

8.2 Theory: obtaining fluxes from scintillometry

Here the goal is to relate the structure parameters of temperature (C_T^2) and humidity (C_q^2) to the surface fluxes of heat and water vapour. The theory for calculating these structure parameters is described in detail in Chapter 7. Briefly, the two-wavelength scintillometer system provides three refractive index structure parameters (C_n^2), denoted C_{n1n1} from the optical scintillometer, C_{n2n2} from the millimetre-wave scintillometer and C_{n1n2} from the correlation between wavelengths. Conversion to the temperature and humidity structure parameters involves either the single-wavelength, two-wavelength or bichromatic method. For the two-wavelength method C_{n1n1} and C_{n2n2} are combined to give C_T^2 and C_q^2, which also requires an assumption about the temperature-humidity correlation coefficient, r_{Tq}. The assumption used in this study is r_{Tq} = ±0.8. The bichromatic method additionally measures the cross-structure parameter C_{n1n2} to remove the need for the r_{Tq} assumption and the three refractive index structure parameters (C_{n1n1}, C_{n2n2}, C_{n1n2}) allow the three meteorological structure parameters (C_T^2, C_q^2, C_{Tq}) to be found by solving simultaneous equations. A summary is given in Figure 8-1 and the reader is referred to Chapter 7 for full details.

The established method to convert structure parameters to fluxes is through Monin-Obukhov similarity theory (MOST). Through dimensionless combinations of atmospheric quantities and empirically observed vertical profiles, the variability of temperature, T, or specific humidity, q, (or other conserved scalars) can be related to surface fluxes. For example (Wyngaard et al., 1971),

$$\frac{C_T^2(z_m - z_d)^{2/3}}{T_*^2} = \frac{C_q^2(z_m - z_d)^{2/3}}{q_*^2} = f_{MO}\left(\frac{z_m - z_d}{L_{Ob}}\right), \tag{8-1}$$

where T_* and q_* are the scaling variables of temperature and humidity, respectively; z_m is the measurement height, z_d the displacement height, L_{Ob} the Obukhov length and f_{MO} is a similarity function describing the height dependence of the structure parameters as a function of stability. For the path-averaged quantities obtained from scintillometry, the effective height, z_{ef}, is used in place of ($z_m - z_d$) as described in Hartogensis et al. (2003). The stability parameter, ζ, is defined as $(z_m - z_d)/L_{Ob}$ for the EC station and z_{ef}/L_{Ob} for the scintillometer system.

Several forms of the similarity functions exist in the literature. Useful discussions can be found in Braam et al. (2012) and Beyrich et al. (2012) in the context of scintillometry, and in Kanda et al. (2002) for consideration of urban environments. The choice of similarity function for this dataset is investigated in Section 8.6. As in previous scintillometry studies identical functions for T and q are assumed here. The widely used forms with the constants suggested by Andreas (1988) are used,

$$f_{MO}(\zeta) = c_{T1}(1 - c_{T2}\zeta)^{-2/3} \qquad (\zeta < 0) \tag{8-2}$$

$$f_{MO}(\zeta) = c_{T1}(1 - c_{T3}\zeta^{2/3}) \qquad (\zeta > 0) \tag{8-3}$$

with c_{T1} = 4.9, c_{T2} = 6.1 and c_{T3} = 2.2 (hereafter An88).

The scaling variables and stability are determined by iteration (e.g. Moene et al. (2004)). The Obukhov length is calculated from $L_{Ob} = u_*^2 T / g\kappa_v T_*$, where g is the acceleration due to gravity and κ_v is von Kármán's constant. The required friction velocity (u_*) input is usually obtained from a point measurement of wind speed and an estimate of the roughness length (z_0).

The sensible heat flux is calculated using

$$Q_H = -\rho c_p u_* T_*, \tag{8-4}$$

where ρ is the density of air and c_p the specific heat capacity at constant pressure. The latent heat flux is calculated following Chapter 6,

$$Q_E = -\rho L_v u_* q_* , \tag{8-5}$$

where L_v is the latent heat of vaporisation. When q_* is not known (as for the single-wavelength method), Q_E may be estimated as the residual of the surface energy balance if all other terms are known, but the complexity of energy partitioning in urban areas makes this very difficult. The urban energy balance can be written (Oke, 1987),

$$Q^* + Q_F = Q_H + Q_E + \Delta Q_S , \tag{8-6}$$

where Q^* is the net all-wave radiation, Q_F the anthropogenic heat flux and ΔQ_S the net storage heat flux. The Bowen ratio, β, is expressed in terms of the fluxes as Q_H/Q_E.

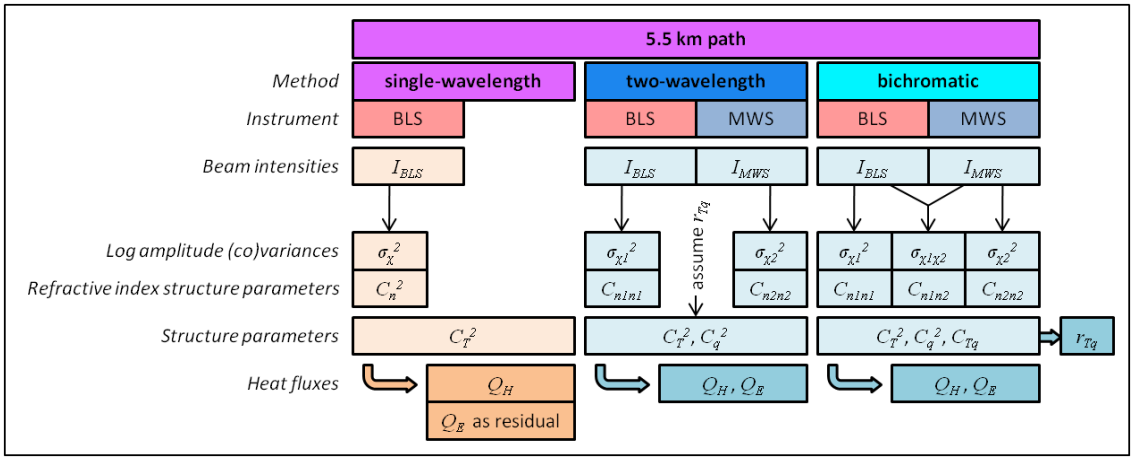

Figure 8-1 Methods to obtain heat fluxes from scintillometry as applicable to the experimental setup in Swindon. See Section 8.3 for details of the instrumentation, including an optical large aperture scintillometer (BLS) and a millimetre-wave scintillometer (MWS).

8.3 Experimental details

A two-wavelength scintillometer system was deployed on a 5.5 km path over an extensive suburban area of Swindon, UK. This system comprises an infrared scintillometer, the BLS900 (Scintec, Rottenburg, Germany), and a millimetre-wave scintillometer (MWS) designed and built by the Centre for Ecology and Hydrology (CEH) and Rutherford Appleton Laboratory (RAL). The MWS operates at 94 GHz, see Evans (2009) for further details. Near the centre of the scintillometer path an eddy covariance (EC) station was installed at a height of 12.5 m in

the garden of a residential property. The instrument locations and typical source areas of the fluxes are shown in Figure 8-2.

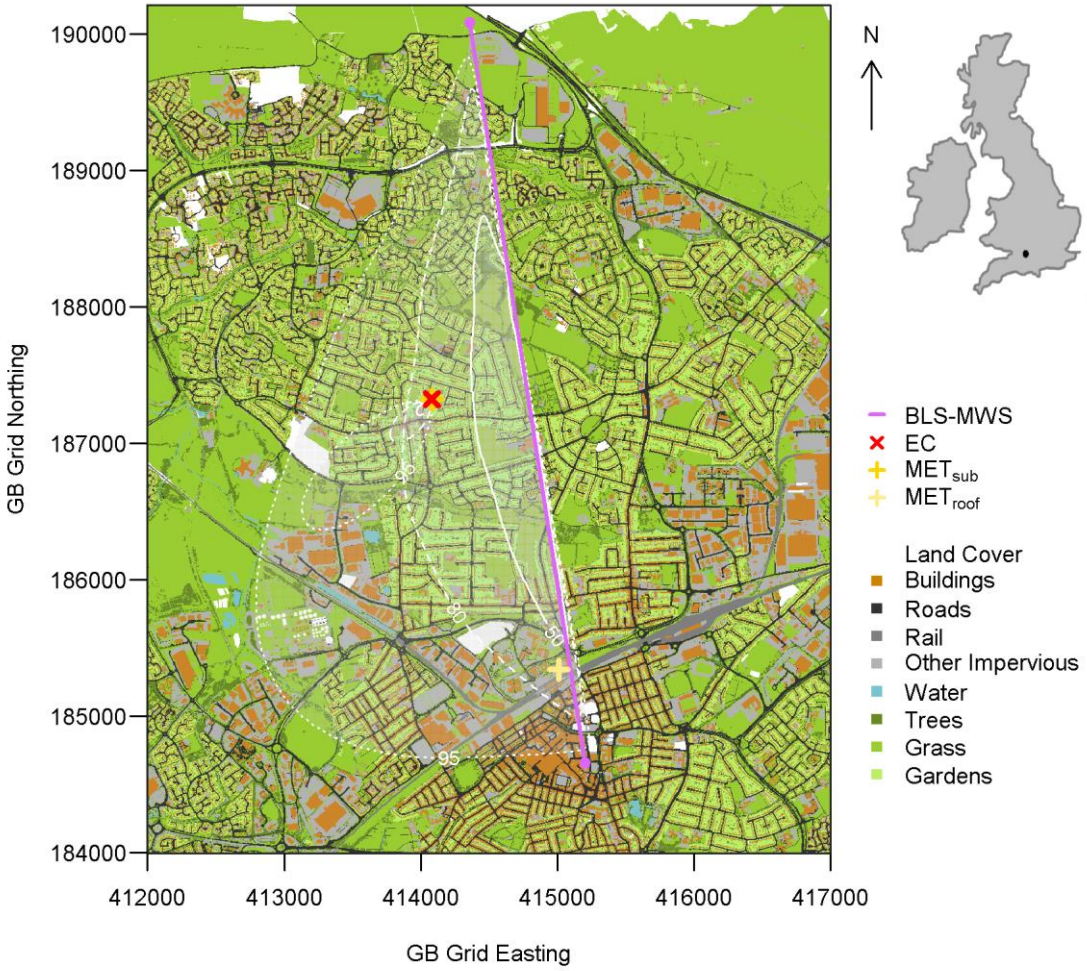

Figure 8-2 Land cover map of the study area showing the two-wavelength scintillometer path (BLS-MWS) and location of the eddy covariance station (EC) and two meteorological stations (MET_{sub}, MET_{roof}). Land cover classification was based on a geodatabase (OS MasterMap 2010 © Crown Copyright), lidar data (2007, ©Infoterra Ltd) and aerial photography (2009, ©GeoPerspectives). Where data were unavailable areas are left unclassified (white). Example footprints indicate the area contributing 50%, 80% and 95% of the observed fluxes for typical atmospheric conditions (see text for details). The location of Swindon within the British Isles is shown (top right).

Table 8-1 summarises the instrumental setup and site characteristics. The effective height of the scintillometer system is given as the effective height of the BLS according to Equation 15 of Hartogensis et al. (2003) and includes the displacement height. Displacement height and roughness length are based on the mean height of buildings and trees (z_H) (within 500 m of the EC site and 1000 m of the scintillometer path) and the relations $z_0 = 0.1z_H$, $z_d = 0.7z_H$ (Garratt, 1992). Source area estimation combines an analytical model (Hsieh et al., 2000) with the scintillometer path weighting (e.g. Meijninger et al. (2002b)) and is calculated for typical

atmospheric conditions (southwesterly wind (225°), u_* = 0.5 m s^{-1}, standard deviation of lateral wind σ_v = 0.9 m s^{-1} and L_{Ob} = -200 m (200 m for stable conditions)). For these conditions the relative contribution of vegetation to the footprint (λ_V) is 32% for EC and 53% for the BLS-MWS (33% and 48% in stable conditions). At the EC site the southwesterly wind sector (210-240°) is the least vegetated and the northeasterly sector the most vegetated (λ_V = 52-53%, for a wind direction of 45° and other atmospheric conditions as above); the average vegetation fraction over twelve 30° wind sectors is 45%, but note this does not account for the observed wind direction distribution, which is predominantly southwesterly. For the BLS-MWS the average λ_V over all wind sectors is 56% and the different sectors range between 53-65%. In stable conditions the average of the typical footprints for each sector is 50%. The larger source area means the town centre and industrial areas to the southeast (Figure 8-2) have a greater influence, with $\lambda_V \approx$ 40% for the sectors 90-210°; the north is more vegetated (λ_V up to 64%).

					Source area [km^2] unstable (stable)		
Instrumentation	**Location**	**Height [m]**	**z_0 [m]**	**z_d [m]**	**95%**	**80%**	**50%**
BLS-MWS scintillometer system	51°36'33.9" N 1°47'38.6" W (Tx) 51°33'38.1" N 1°46'55.3" W (Rx)	45.0* [39.0-45.0]	0.7 [0.5- 1.1]	4.9 [4.4-5.4]	7.5 (10.2)	3.0 (6.9)	0.9 (3.2)
Eddy covariance station	51°35'4.6" N 1°47'53.2" W	12.5	0.5 [0.4-0.9]	3.5 [3.0-4.0]	0.5 (0.7)	0.06 (0.1)	0.007 (0.01)

Table 8-1 Details of the scintillometer and eddy covariance systems. Tx denotes transmitter; Rx denotes receiver. *The height of the scintillometer system is given as the effective height of the BLS. Values in square brackets represent the probable range of each quantity: for the effective height these are the limiting stabilities; for z_0 and z_d these are based on the literature (e.g. Grimmond and Oke (1999a)). See text for details of the source area estimation.

Other meteorological instrumentation was also installed at the EC site (denoted MET_{sub}). An automatic weather station (WXT, Vaisala, Finland) at a height of 10.6 m provides the temperature, pressure, humidity and wind speed inputs required to process the scintillometry data. A four-component radiometer (NR01, Hukseflux, The Netherlands) at 10.1 m on the same mast provides incoming and outgoing shortwave ($K_\downarrow$, $K_\uparrow$) and longwave ($L_\downarrow$, $L_\uparrow$) radiation and the net all-wave radiation. A tipping bucket rain gauge (0.2 mm tip, Casella, Bedford, UK) was situated near the base of the mast. Data from a second similarly instrumented meteorological station on a rooftop near the town centre (MET_{roof}, Figure 8-2) were linearly adjusted and used to gap-fill MET_{sub} to provide a more complete set of continuous input variables, though these were only required in a few cases (mainly to cover power failure at MET_{sub}). Less than 2% of the combined dataset consisted of the adjusted MET_{roof} data.

The EC sensible and latent heat fluxes were calculated for 30 min intervals. Raw data were sampled from a sonic anemometer (R3, Gill Instruments, Lymington, UK) and an open-path infrared gas analyser (IRGA) (LI-7500, LI-COR Biosciences, Lincoln, USA) at 20 Hz (CR3000, Campbell Scientific Ltd., Loughborough, UK). Flux processing included despiking of raw data; correction for angle of attack; time-lag compensation; double co-ordinate rotation; and corrections for sonic temperature (Schotanus et al., 1983), high and low frequency losses (Moncrieff et al., 1997) and gas densities (Webb et al., 1980). EddyPro software (LI-COR Biosciences) was used to implement these stages. Quality control excluded data during times of instrumental fault or when rain could adversely affect readings (e.g. IRGA diagnostic flag set) and data were subject to physically reasonable range checking. More information about the EC system can be found in Chapter 4.

A CR5000 datalogger (Campbell Scientific Ltd.) sampled the BLS and MWS signal intensities at 100 Hz. Raw BLS and MWS signals were bandpass filtered between 0.06 Hz and 20 Hz for the calculation of C_{n2n2} and C_{n1n2}; C_{n1n1} was calculated from the unfiltered BLS signal. The low-frequency cut-off reduces the influence of absorption fluctuations. Quality control comprised initial raw data despiking, rejection of data during rain or fog (when the signal intensity dropped below 0.5 (0.33) of the BLS (MWS) daily maximum and removal of values adjacent to these), threshold checking of C_n^2 and removal of data strongly affected by saturation (if the estimated correction was greater than 25%). The remaining BLS data were corrected for saturation using the modulation transfer function of Clifford et al. (1974) which increased C_{n1n1} by 5% on average. Kleissl et al. (2010) derived an empirical threshold for the onset of saturation; 21% of BLS data were above this value. The MWS data were well below the saturation threshold (Clifford et al., 1974) and no correction was applied to the MWS data or the BLS-MWS cross-correlation. As discussed in Chapter 7, the two-wavelength method does not provide a unique solution for the structure parameters, but two possible values at low and high Bowen ratios (Hill et al., 1988; Hill, 1997). In most applications to date where β < 2-3 the lower Bowen ratio solution has been correctly chosen. For the Swindon dataset two-wavelength structure parameters were rejected when β was believed to exceed this threshold and assuming the lower β solution would therefore be incorrect (< 0.3% of data), but we could not be sufficiently certain to adopt the higher β solution for these cases.

The calculation of fluxes from scintillometry proceeds as described in Section 8.2. During daytime hours between minima in C_{n1n1}, the similarity functions for unstable conditions were used; at other times stable conditions were assumed. The two-wavelength results were calculated assuming positive r_{Tq} during unstable conditions (Q_H > 0, Q_E > 0) and negative r_{Tq} under stable conditions (Q_H < 0, Q_E > 0). Clearly the two-wavelength method will suffer a

positive bias in Q_E resulting from these assumptions, i.e. dewfall (Q_E < 0) is never detected. The bichromatic method, in principle, provides more information than the two-wavelength method. Initially, unstable conditions during daytime and stable conditions at night are assumed. Then for cases of observed r_{Tq} < 0 during daytime (between C_{n1n1} minima) Q_E is assumed to remain positive but Q_H to switch to being negative, so the stable similarity function is used. This may be expected to occur following rainfall when surfaces are wet. During the night it is more difficult to determine the stability regime for the scintillometer source area, as r_{Tq} > 0 can indicate either stable conditions and dewfall (Q_H < 0, Q_E < 0) or unstable conditions and evaporation (Q_H > 0, Q_E > 0). Because r_{Tq} only describes the relative sign of the fluxes these two situations cannot be distinguished by the bichromatic method, although it does indicate the occurrence of one or other of these situations. Here, nocturnal r_{Tq} > 0 is taken to indicate dewfall. A time-step of 10 min was used for two-wavelength C_T^2 and C_q^2, yielding Q_H and Q_E at 10 min. To allow for the variability of the bichromatic structure parameters (Chapter 7), the corresponding fluxes were calculated at 30 min intervals using 30 min mean C_T^2 and C_q^2.

In the following, the subscript 'EC' refers to quantities derived from the eddy covariance measurements and 'BLS-MWS' those from scintillometry. Results using structure parameters calculated from the two-wavelength or bichromatic methods are subscripted '2λ' and 'bi' respectively. Data are presented for 14 months when all instrumentation was functioning: July-December 2011 and May-December 2012.

8.4 Results and discussion

8.4.1 Comparison of methods

Fluxes computed from the bichromatic and two-wavelength methods and measured by eddy covariance are shown for four days in Figure 8-3. The sensible heat flux calculated using the single wavelength method is also plotted (no Bowen ratio correction has been applied, see Chapter 7). Differences in the sensible heat flux from the three scintillometry techniques are small and the scintillometry values quite closely match the EC values despite the different source areas of the measurements. Notable differences can be seen on the early morning of 30 September 2012 when Q_H from the scintillometers is more negative than Q_{H_EC} until around 0900, and on 11 May 2012 Q_{H_EC} is 50-100 W m^{-2} larger than for the scintillometric data. In general, and as seen in Figure 8-3, Q_E from the scintillometers tends to be larger than for EC. This should be expected as there is a greater proportion of vegetation within the source area of the BLS-MWS.

Figure 8-3 includes, to our knowledge, the first fluxes derived from structure parameters where the measured combined temperature-humidity fluctuations have been included via the bichromatic method. Differences between the bichromatic fluxes and the two-wavelength fluxes are mostly small, since the observed and assumed r_{Tq} values are mostly similar (±0.8). At times when measured r_{Tq} deviates from the assumed value, the fluxes differ accordingly and Q_E is affected more than Q_H. On 21 August 2011 r_{Tq} changes sign at the evening transition, as might be predicted, but also changes sign again a few hours later – EC and the bichromatic method capture both changes. Closer inspection reveals that Q_{E_EC} and Q_{E_bi} are both negative following r_{Tq} becoming positive, i.e. the bichromatic results capture the dewfall observed by EC that is not accounted for in the two-wavelength assumptions (which cause $Q_{E\_2\lambda}$ to remain positive). Comparison with the net radiation on the morning of 21 August also suggests that the lower bichromatic fluxes are more realistic given the available energy. At other times the bichromatic results appear less reasonable. Firstly, there are incidences of $|r_{Tq}| > 1$, which do not have a meaningful physical interpretation and indicate measurement limitations. Secondly, large fluctuations in r_{Tq} lead to sudden spikes in the fluxes (e.g. in Q_{E_bi} on the morning and evening of 11 May 2012). Such variability of the bichromatic data influences the fluxes and at times results in data that are almost certainly unduly influenced by the performance of the method. As discussed in Chapter 7, the small signal-to-noise ratio of the cross-structure parameter C_{n1n2} and the accumulation of uncertainties in r_{Tq} can contribute to large errors in individual measurements. The scintillometric fluxes presented below are calculated from two-wavelength structure parameters.

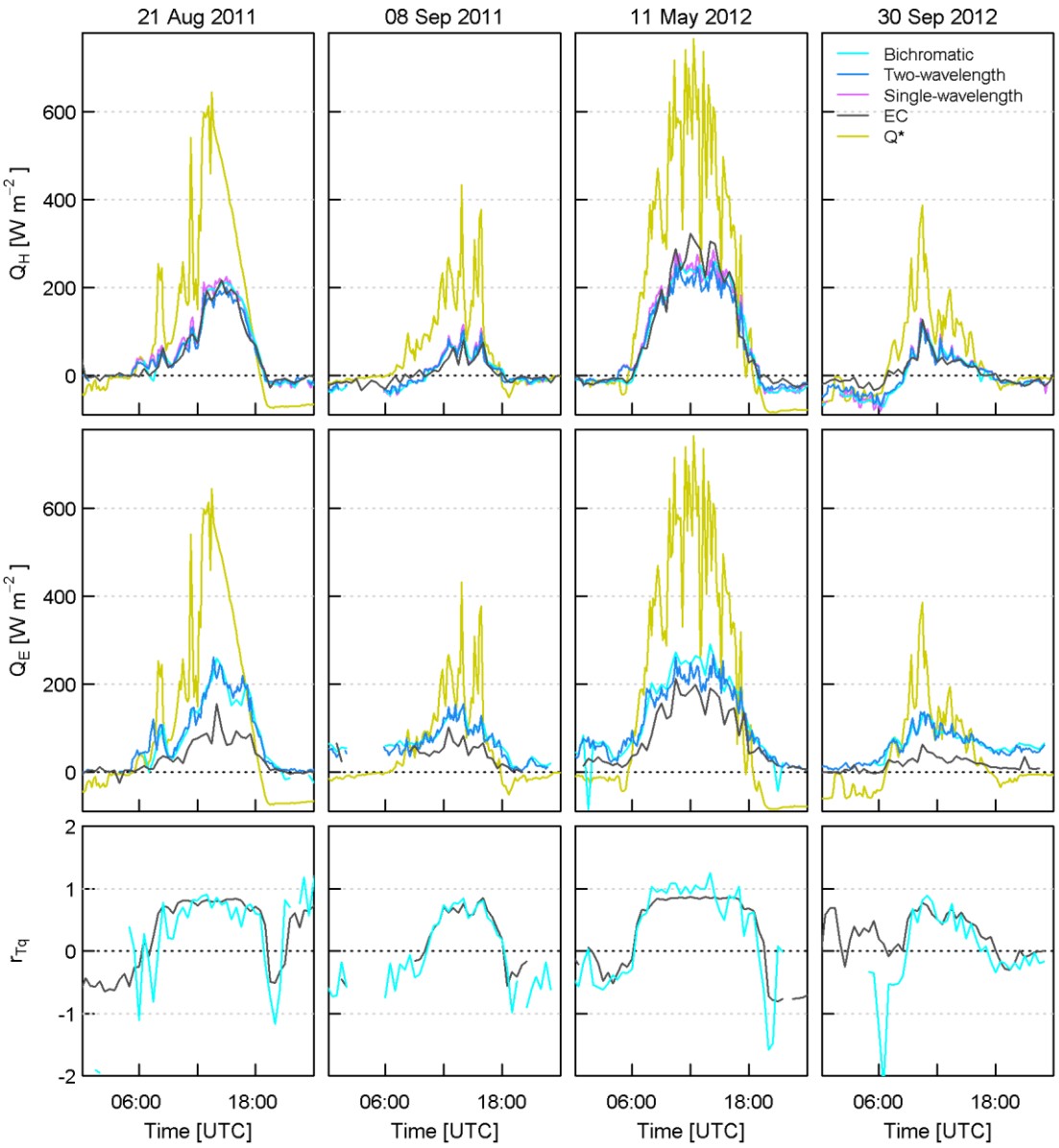

Figure 8-3 Sensible and latent heat fluxes, net radiation (Q*) and the temperature-humidity correlation coefficient for selected days. Single-wavelength and two-wavelength results are for 10 min intervals; EC and bichromatic statistics are at 30 min intervals (structure parameters for the same days are shown in Figure 7-8).

8.4.2 Evaporation following rainfall

In addition to providing fluxes that are representative of a large area, two-wavelength scintillometry has the potential to provide them directly following rainfall when water droplets on open-path gas analyser windows may preclude Q_E measurements by eddy covariance. Closed-path IRGAs permit flux measurements during or soon after rainfall, but water droplets may wet filters and high relative humidity may cause condensation in the sample tubing. Scintillometer measurements can be made as soon as the propagation path is clear following a rain shower even when the land surface (or IRGA window) has not had time to dry. The

drawback is that neither Q_H nor Q_E can be reliably obtained while the scintillometer path is obstructed, whereas EC is usually capable of providing fairly continuous Q_H measurements except during very heavy rainfall. As an example, fluxes from three days in July 2012 are shown in Figure 8-4. The sensible heat fluxes measured by the two techniques are closely matched and clearly respond to the energy available, primarily net all-wave radiation. Out of the 72 hours shown, scintillometer data were available for 56.7 hours, Q_{H_EC} for 66.5 hours and Q_{E_EC} for only 32.5 hours. Rainfall in the evening of 11 July meant the IRGA windows remained wet throughout the night. The BLS-MWS system shows an increase in Q_E after rainfall and non-zero evaporation through the night (0.6 mm between 2130 and 0800 on 12 July when no Q_{E_EC} was available). During the night, negative Q_H partly compensates for the energy used in evaporation. Very high rates of evaporation can be observed when surface water is abundant and there is considerable energy input from net radiation, such as in the middle of the day on 11 July 2012. Latent heat fluxes reached almost 500 W m^{-2} and the variability in Q_E clearly responds to the incoming radiation and cloud cover.

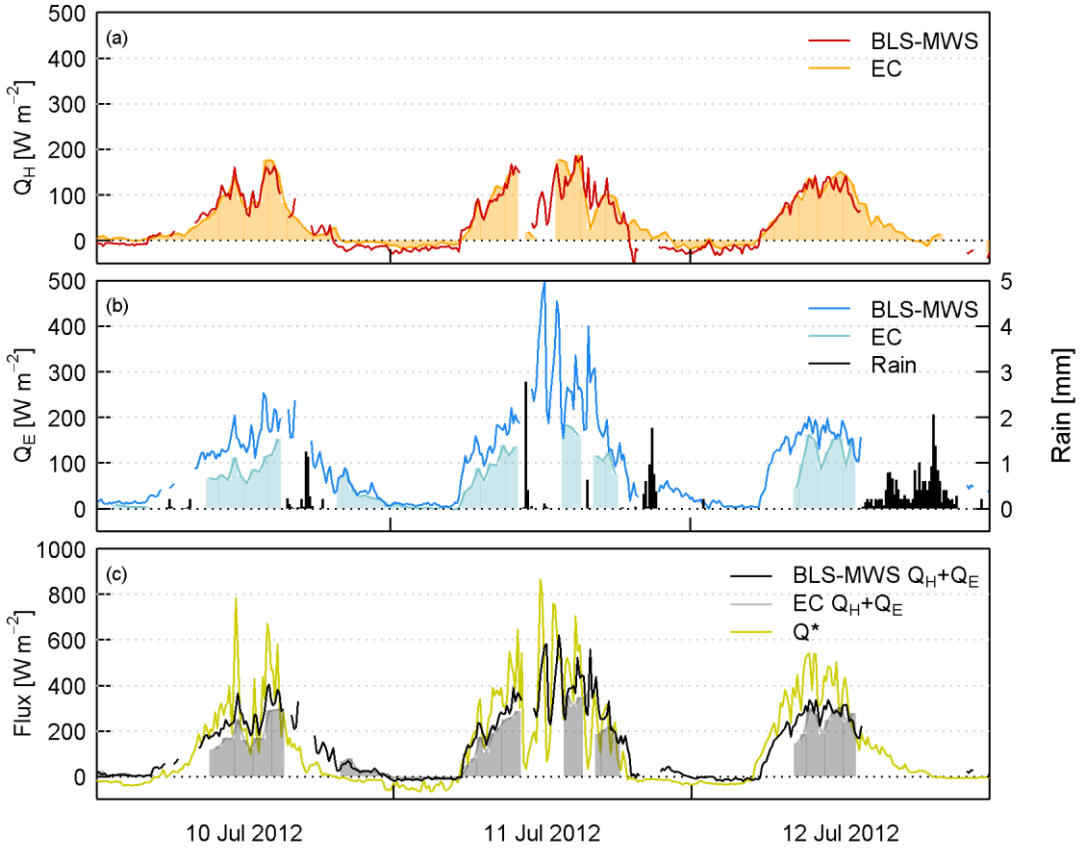

Figure 8-4 Response of (a) sensible and (b) latent heat fluxes to rainfall (right-hand axis) and net all-wave radiation (c). Shading indicates availability of EC data. EC data are at 30 min intervals; all other data are at 10 min intervals.

8.4.3 Case study: Changing phenology, surface conditions and meteorology

Closer analysis of shorter periods offers insight into the physical processes determining the partitioning of energy fluxes. In combination with the changing vegetation phenology, surface conditions and meteorology, the wind direction has a significant influence on the fluxes observed, particularly for the smaller EC source area (Chapter 4). A case study at the end of spring 2012 is presented in Figure 8-5. Following a very wet April and May with frequent rainfall and generally cloudy conditions, water is readily available and soil moisture high. During the run of clear days starting 22 May 2012, warmer temperatures and sunlight promotes leaf-out. Time-lapse photography reveals sudden plant growth and leaf development from 22 May to 28 May. Over these days, Q_E increases rapidly and β decreases as transpiration rates rise. Once the leaves are on the trees, the continued availability of sunlight drives photosynthesis and rapidly depletes soil moisture. Given the availability of near-surface moisture, evaporation from the soil and other pervious areas also contributes. The highest rates of evaporation are observed on 25-27 May. Conditions are then very favourable for evapotranspiration – high available energy, abundant water, warm and windy (reaching 25°C, 6 m s^{-1} on 25-26 May) with a high vapour pressure deficit (20 hPa) and plants are leafy. The EC-measured carbon flux also indicates strong photosynthetic uptake on these days (not shown). On 23, 27 and 29 May, clouds give rise to sudden changes in Q^*. For the EC data, Q_H rapidly adjusts – particularly evident as the sharp peak on 29 May. For the scintillometer system the radiation patterns are replicated to a lesser extent by Q_H and more closely matched by Q_E. Although night time data have larger uncertainties, EC and scintillometry are often in good agreement, for example the large negative Q_H during night time on 25-26 and 26-27 May.

More energy is directed into Q_{E_EC} than Q_{H_EC} for 25-26 May when leaves have developed and winds are northeasterly, and the source area contains a large proportion of active vegetation. Once the wind direction becomes more southwesterly again β_{EC} increases and continues to increase, peaking on 31 May when the urban surface has dried out. For this wind sector, Q_{E_EC} is likely water limited as there are few trees and a lower proportion of pervious or grassed areas with access to reserves in the soil. Meanwhile, trees, shrubs and grass in the scintillometer source area continue to be supplied with water from beneath the surface, maintaining a moderate latent heat flux (> 100 W m^{-2}). Once the wind direction changes and rain arrives on 1 June β_{EC} drops again.

The much larger source area of the scintillometer system means that measurements are less susceptible to variation in sampled land cover (as they are already averaged over a large

area). This offers significant advantages in terms of collecting representative data for the study area. Furthermore, integration into modelling studies, either as input data or evaluation of outputs, is facilitated since most models will not account for footprint differences.

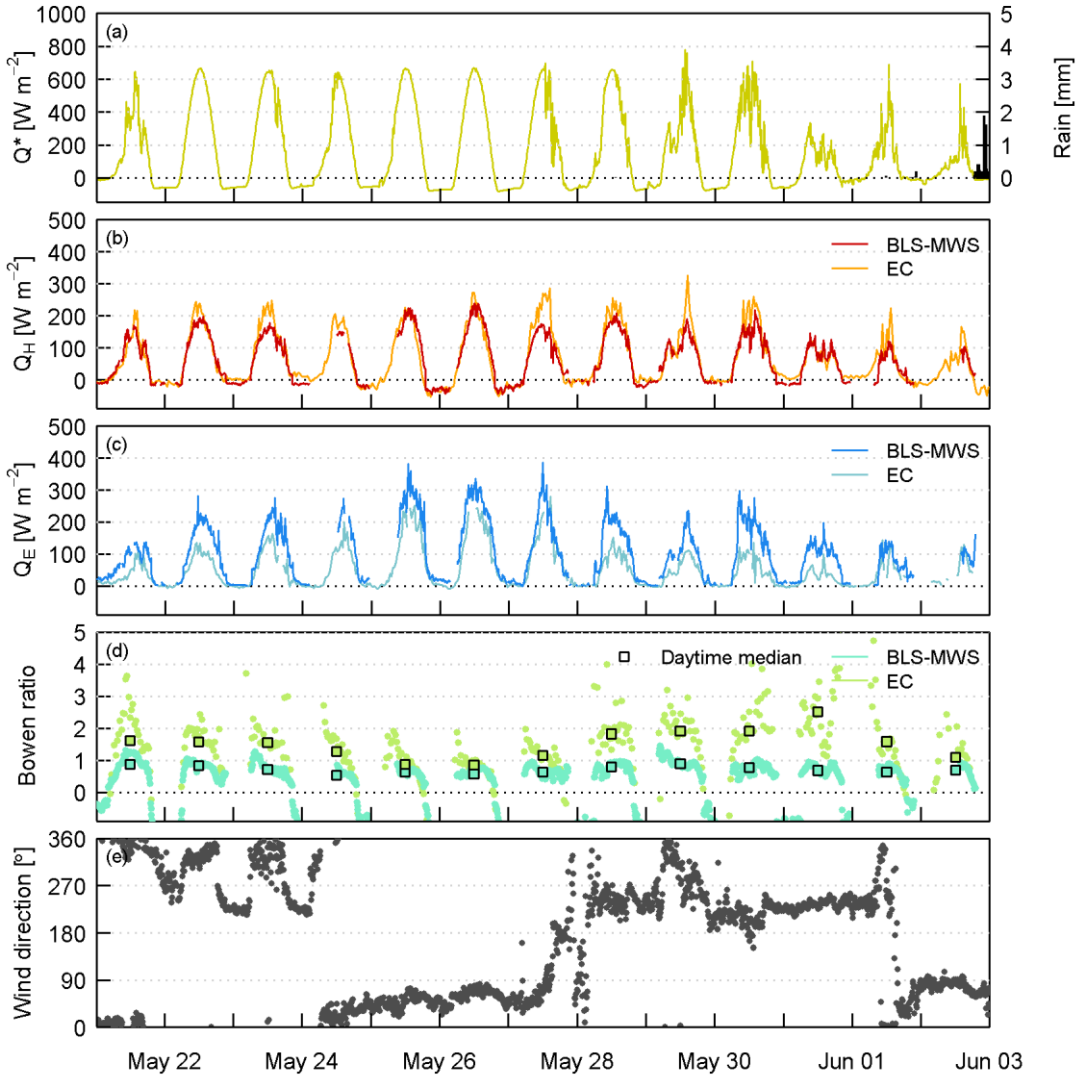

Figure 8-5 Energy partitioning according to eddy covariance and scintillometry during a warm, dry period in spring 2012. In (d), only daytime data are shown.

8.4.4 Climatology of the suburban environment

The average daily evaporation from the BLS-MWS is 1.5-3 times larger than from EC (Figure 8-6). These observations are broadly consistent with the instruments' different source area characteristics. The relatively large proportion of vegetation of the typical scintillometer footprint, including a large nature reserve located near the centre of the scintillometer path,

offers more potential for transpiration than the impervious surfaces around the EC mast. These footprint effects are further enhanced given that for the prevailing southwesterly wind the EC source area is more built-up (with more buildings, roads and impervious surfaces and less vegetation) than for other wind sectors (Section 8.3). The scintillometer system enabled measurements that are representative of a much larger portion of the suburban surface and these results suggest that vegetated suburban areas are able to support high rates of evaporation.

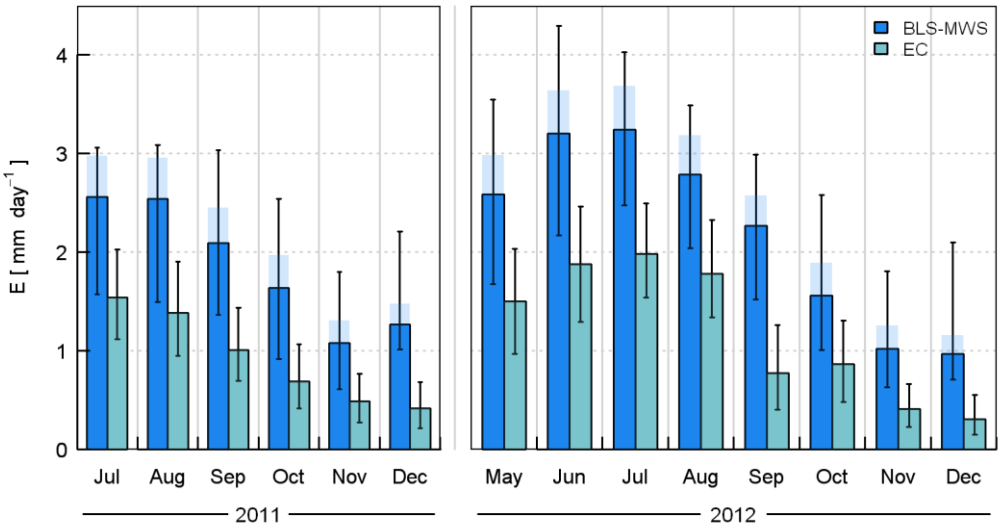

Figure 8-6 Average daily evaporation by month: bars represent the sum over the median daily cycle of evaporation for each month; error bars indicate the upper and lower quartiles; shading indicates the impact of using the De Bruin et al. (1993) similarity function.

8.4.4.1 Consideration of uncertainties

As discussed in Section 7.3, the two-wavelength method cannot distinguish times of dewfall and 'counts' these instances of negative Q_E as positive Q_E. According to the EC data, dewfall ($Q_E < 0$) was recorded for 8% of the study period, amounting to 4.9 mm in total. Based on this, the total BLS-MWS evaporation for the whole study period may be overestimated by ~10 mm. When there is heavy dewfall, however, this will often settle on the IRGA windows leading to those data being rejected, so the EC data are also expected to underestimate dewfall. In Swindon it is thought that dewfall is fairly small in comparison to (a) the total evaporation and (b) the other uncertainties involved, but nevertheless represents a systematic bias in the two-wavelength technique.

Moreover, measurement of night time fluxes presents challenges for both EC and scintillometry. The (usually) smaller magnitude of nocturnal fluxes may be close to the detection limit of the instruments and also means that the relative uncertainties can be large.

Weak turbulence and non-stationarity violate the assumptions required for both EC and scintillometry measurement theory and MOST. The collapse of the boundary layer may mean that measurements are made outside the surface layer under stable stratification, may be influenced by other processes such as entrainment, and may no longer relate to the surface fluxes (e.g. Braam et al. (2012)). In Swindon the rough suburban surface helped to maintain turbulent mixing, which reduces the occurrence of these issues.

The impact of the choice of similarity function can alter the daily evaporation by 0.20-0.45 mm, i.e. ~15-20% or more. In Figure 8-6 the average daily evaporation calculated using the De Bruin et al. (1993) similarity functions (DB93) is shown in comparison to the values derived using An88. Compared to the uncertainty associated with the similarity functions, other uncertainties in the derivation of fluxes are mostly quite small. Out of the required input quantities, uncertainties in the beam height, z_0 and wind speed are important; the long path length reduces the impact of inaccuracies in estimating its length and sensitivity to the other meteorological input variables is small (Hartogensis et al., 2003).

The general shape of the observed temperature and humidity scaling, based on EC values, is broadly described by similarity functions given in the literature (Section 8.6). Agreement is often quite good in unstable conditions (e.g. for An88 and DB93) but the fits are poorer in near-neutral and stable conditions as the data become more scattered. There are differences between the behaviour of temperature and humidity for neutral stability – the temperature scaling diverges. The humidity scaling tends towards an approximately constant value approaching neutral conditions and under stable conditions which appears to be larger than suggested by An88 (or DB93). Consequently, Q_E will be overestimated in these regions. Andreas et al. (1998) found that humidity scaling was 28% larger than for temperature using dimensionless standard deviations of these variables collected over patchy vegetation. In general, there is a tendency for the similarity functions to overestimate very small fluxes. Large scatter during stable and neutral times demonstrates the limitation of similarity theory scaling and cautions that the flux estimates are less reliable at these times.

Reduced sensitivity of the MWS around the region of minimum C_{n2n2} at $\beta \approx$ 2-3 (Leijnse et al., 2007) may have introduced a bias towards larger Q_E. As discussed in Chapter 7, the instrumental noise floor and experimental limitations are thought to widen the region of reduced sensitivity outside the theoretical prediction of the position of the minimum. The two-wavelength method tends to give Bowen ratios less than about 1.3 but the bichromatic results suggest higher β for about 3% of the data. For these 3%, the corresponding evaporation is 17 mm according to the two-wavelength method and 13 mm by the bichromatic method which

corresponds to an average overestimation for these 3% of about 30 W m^{-2} by $Q_{E\_2\lambda}$ compared to Q_{E_bi}. Although this represents a small proportion of the total dataset, it could have a major effect in drier conditions and restricts the ability of two-wavelength datasets to capture changing energy partitioning as conditions increase above $\beta \approx 1.3$.

The sum of the turbulent fluxes for each 30 min period is larger for the BLS-MWS results compared to EC. Regression of $Q_H + Q_E$ against Q^* yields slopes of 0.65 (BLS-MWS) and 0.59 (EC) with substantial offsets of 36 W m^{-2} (BLS-MWS) and 15 W m^{-2} (EC). A small positive offset is expected given the contribution of the anthropogenic heat flux, peak values are estimated at about 10-15 W m^{-2} for suburban Swindon (Chapter 4) and are within the expected range for similar environments (Christen and Vogt, 2004; Bergeron and Strachan, 2010). Regression of $Q_{H\_BLS\text{-}MWS} + Q_{E\_BLS\text{-}MWS}$ with $Q_{H\_EC} + Q_{E\_EC}$ gives a slope of 1.03 and intercept of 22.9 W m^{-2}. The non-negligible offset between the two datasets seems to be caused by the overestimation of fluxes by the similarity functions. The higher density of buildings and anthropogenic materials directly surrounding the EC mast could explain why the sum of the EC turbulent fluxes is smaller: their large thermal masses are able to effectively absorb and later release heat and therefore have a greater associated storage heat flux than vegetated areas. In addition, other methodological differences could result from the widely documented under-closure of the energy balance, commonly by as much as 10-20%, which may be partly due to underestimation of the turbulent fluxes by EC (Wilson et al., 2002; Frank et al., 2013). To reiterate, for this setup it is not expected that the EC and BLS-MWS systems give the same results.

Previous studies that have made direct comparisons have generally found reasonable agreement between methods within the experimental uncertainties, though two-wavelength estimates of Q_E are often quite large. Meijninger et al. (2002a) found a difference of 8% between EC and two-wavelength Q_E. Meijninger et al. (2006) find two-wavelength Q_E (using *in situ* r_{Tq} from EC) is 26% larger than Q_E from EC aggregated over the source area. Their corresponding two-wavelength Q_H data overestimate EC values by 7% and for small fluxes (< 150 W m^{-2}) $Q_H + Q_E$ is larger than the estimated available energy.

8.4.4.2 Interpretation of results

Whilst latent fluxes from the BLS-MWS are considerably higher than those from EC, the sensible heat fluxes are slightly smaller during the day and more negative at night (Figure 8-7). During winter the behaviour is more similar between BLS-MWS and EC datasets and the daytime Bowen ratios converge. At this time vegetation is largely dormant so there is less of a contrast between treed and built areas or grass and impervious surfaces compared to when vegetation is actively transpiring (Offerle et al., 2006). In Swindon, evaporation continues from

wet surfaces and pervious areas all year round, which means Q_H is negative for much of the day as energy is limited. Similar energy partitioning has been noted at other suburban sites (e.g. Goldbach and Kuttler (2013)) in contrast to city centre studies where typically the water availability is reduced and the energy input is supplemented by a larger anthropogenic component (Kotthaus and Grimmond, submitted-a). Peters et al. (2011) present evaporation rates from residential and recreational areas in suburban Minneapolis-Saint Paul, Minnesota of around 3 mm day^{-1} in summer, comparable to the BLS-MWS results shown here, but near zero in winter. This wintertime difference highlights the need to make observations across a range of climate zones: the UK's maritime climate experiences milder winters than the continental North American and European studies. Zieliński (2012) present several months of Q_H data from scintillometry in Łódź. Whilst the broad seasonal trends observed are similar to those in Swindon, Q_H is larger particularly in wintertime, which is not surprising given the higher density of buildings at the central Łódź site (Fortuniak et al., 2013).

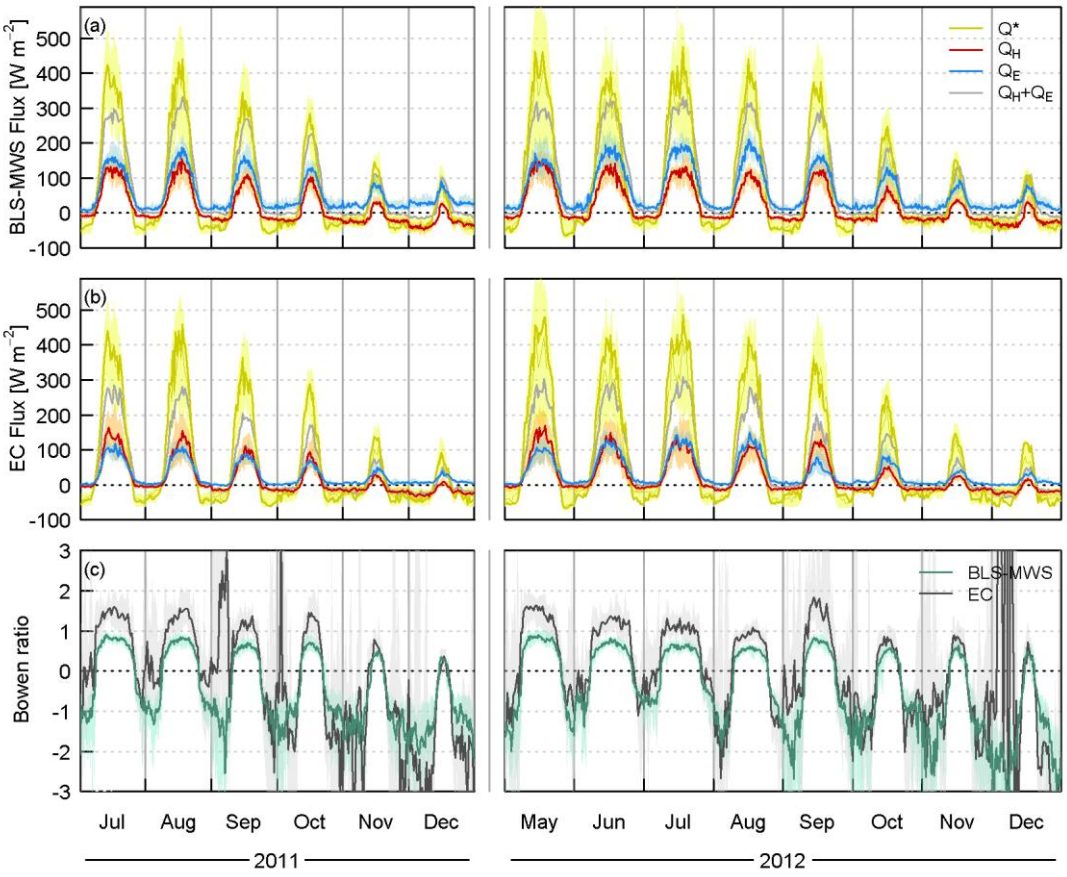

Figure 8-7 Monthly median diurnal cycles (lines) and inter-quartile range (shading) of sensible and latent heat fluxes as determined using (a) two-wavelength scintillometry and (b) eddy covariance; (c) the Bowen ratio. The net all-wave radiation and sum of turbulent fluxes (30 min) are also shown, where Q* has been selected according to the availability of (a) BLS-MWS and (b) EC fluxes; the thin line represents all available Q* data and is therefore the same in (a) and (b).

Seasonal trends are evident in the Swindon fluxes, yet there is also substantial inter-annual variability. Latent heat fluxes tend to be larger and sensible heat fluxes smaller for similar months in 2011 compared to 2012, particularly in summer. Rainfall was below average in 2011, with an annual total of 530 mm. Dry conditions continued through to March 2012, but after April 2012 flooding became a more immediate risk than drought. Total rainfall in 2012 was 1020 mm, with over 900 mm between April and December 2012. The average annual rainfall for southern England is 780 mm[1]. Contrasts in water availability are reflected in the energy partitioning: average β is significantly smaller in 2012 compared to 2011. September 2012 deviates from the general trend of decreasing β from summer to winter. EC averages are possibly less representative than for other months due to lower data availability, but both datasets suggest a larger β than might be expected. This can mainly be attributed to a lack of freely available water (surface water and near-surface soil moisture) and fairly sunny weather during the first half of the month; by 23 September near-surface soil moisture had reached its lowest value for the period studied in 2012. The effect of dry impervious surfaces on the EC observations is further enhanced due to predominantly southwesterly winds during September 2012, which kept the EC measurement footprint over built-up areas with less vegetation. Across the dataset as a whole, the variability in daytime energy partitioning (β) is much smaller for the BLS-MWS than EC (Figure 8-5 and Figure 8-7c).

The Swindon results are comparable to other published findings, but it is rare to find concurrent Q_H and Q_E data representative of such different scales. The low Bowen ratios from the BLS-MWS system are similar to other highly vegetated sites, such as Kansas City, Missouri (58% vegetation fraction). The observed daytime Bowen ratio of 0.47 for their August study period is one of the lowest amongst the urban literature (Balogun et al., 2009). For Swindon, average $\beta_{BLS\text{-}MWS}$ is 0.5-0.6 close to midday in August 2012, but larger in 2011 (~0.8); daytime averages are smaller due to the shape of the diurnal cycle. In Kansas City, water supplied by rainfall is further supplemented by automated irrigation, as for many of the North American studies and particularly sites with warm, dry summers (Grimmond and Oke, 2002). Wetter weather in Swindon during summer 2012 also reduced insolation, limiting evaporation despite abundant moisture (June 2012 was particularly cloudy). The two sets of Q^* in Figure 8-7a,b demonstrate energy availability under different conditions: for May-July 2012, average Q^* calculated using only data when there is concurrent EC data (i.e. mainly excluding times of rain) is considerably higher than the average calculated using all available Q^* data.

The local-scale Swindon results are in good agreement with the findings of Grimmond and Oke (1995), that frequent rainfall during summer reduces the expected Bowen ratio from

[1] Met Office climate average (1971-2000), http://www.metoffice.gov.uk/climate

between 1.0 and 1.5 to 0.8-1.0. In both years β is considerably lower for the more vegetated, larger-scale BLS-MWS dataset. Observations of decreasing β with increasing vegetation fraction (e.g. Grimmond and Oke (2002), Christen and Vogt (2004)) are mostly based on summertime observations. The need to incorporate seasonality in such parameterisations is illustrated by Loridan and Grimmond (2012) and supported by the Swindon data. Differences between years indicate the advantage of not just seasonal but multiple-year datasets to obtain representative data for long-term modelling studies and to improve the reliability of parameterisations.

8.5 Conclusions

The first observations of large-area latent heat fluxes for the urban environment using the two-wavelength scintillometry technique are presented. Contrasting conditions between the two summer-to-winter periods studied highlight the importance of making longer-term observations in order to capture seasonal and inter-annual variability to enable reliable inferences about the controlling processes. Higher evaporation rates from the BLS-MWS (1-3 mm day^{-1} on average) compared to the EC measurements (0.5-2 mm day^{-1}) are mainly attributed to the larger proportion of vegetation contained in the typical BLS-MWS source area. Summertime Bowen ratios are similar to those observed at other significantly vegetated suburban sites in the literature (midday summertime β_{EC} ≈ 0.8-1.5, $\beta_{BLS\text{-}MWS}$ ≈ 0.5-0.9). Both scintillometer and EC data suggest that the available energy is mainly partitioned into Q_E during the winter, with negative Q_H providing energy to some extent. However, Q_E derived from scintillometry is expected to be more significantly overestimated during winter when MOST may be less applicable as the frequency of stable and near-neutral conditions (for which similarity scaling is less reliable) is greater.

The analysis presented herein offers insight into the surface-atmosphere interactions above suburban areas and above mixed land use in general. Whilst vegetation is able to access sub-surface moisture, evaporation is restricted at the local-scale for areas with a large proportion of impervious surface (β_{EC} often rises to > 3 when water is limited). Exploration of the underlying controls in terms of available energy, access to water, vegetative activity and meteorological conditions offers explanations of the observed trends with season and surface characteristics, and reveals which processes are important for model development. The contrasts seen in Swindon highlight the role of water availability and the need for datasets spanning multiple years as well as multiple seasons. Long-term observations such as these, across a range of scales, climate zones, land cover types, synoptic conditions and water availabilities are urgently needed.

The range of energy partitioning is smaller for the scintillometer data than for the EC data, as scintillometer data are already spatially integrated over a large area, the changes in source area with meteorological conditions make less of an impact on the average composition of land cover. This offers significant advantages when using long-term datasets to parameterise or test models. The spatially integrated scintillometer data are representative of a scale of a few km, comparable to models or satellite pixels. To down-scale to individual land use types the EC method, or shorter scintillometer paths, can provide more specific information. Transforming local-scale measurements to representative values at the scale of model grids or satellite pixels is non-trivial over heterogeneous surfaces. For example, evaporation from urban greenspace can be significantly enhanced by warm surroundings (Spronken-Smith et al., 2000; Moriwaki and Kanda, 2004). Flux measurements over large areas are required for algorithm development to move between scales.

Northern Swindon has a relatively large proportion of vegetation so that deployment of an MWS in urban areas with less vegetation, or during drier periods, may be less successful due to the reduced sensitivity at moderate Bowen ratios. With the currently applied technology it appears the bichromatic method does not provide a full solution to the limitations of the two-wavelength method but information on path-averaged temperature-humidity correlation can be used to aid the interpretation of results. The performance of both methods should be more closely examined and current understanding must be tested experimentally. Appreciable uncertainties are introduced into the scintillometer fluxes through (a) lack of consensus on similarity functions and (b) times when data do not conform to the MOST framework. Improvements to MOST (or an alternative solution) should be a main focus of future work – and would have wider implications than scintillometry. More comparisons between different instruments and independent methods are necessary both to learn more about the advantages and shortcomings of the techniques and also to develop a better understanding of surface-atmosphere interactions.

8.6 Appendix: Choice of a suitable similarity function

To evaluate suitable similarity functions for Swindon, EC data were used. Dimensionless quantities formed from the structure parameters of temperature and humidity (f_{MO_T}, f_{MO_q}) were examined in terms of stability and compared to functions from the literature (Figure 8-A1). On the whole, the observed scaling follows a similar form to the range of functions given in the literature. For temperature and humidity, f_{MO} increases with decreasing instability then starting to flatten out around $\zeta \approx -0.03$ as neutral conditions are approached. Humidity scaling becomes approximately constant and independent of stability in neutral and stable conditions. For unstable to near-neutral conditions An88 and DB93 describe the behaviour

fairly well. DB93 seems to best capture the observed behaviour with stability but the resulting fluxes are larger than reasonably expected, sometimes unfeasibly so compared to the energy available, and larger than the fluxes measured directly with the conventional EC method (fluxes directly obtained from EC can be compared to fluxes calculated via structure parameters and MOST scaling). Under stable conditions the scatter is much greater.

Instead of approaching a constant value as predicted by many of the functions in the literature, f_{MO_T} diverges at neutral conditions, becoming very large. Similar behaviour has been observed at a rooftop site in Basel (Roth et al., 2006), and for the normalised standard deviation of temperature (Fortuniak et al., 2013; Nordbo et al., 2013). It occurs as T_* becomes very small to compensate for large u_* in order to maintain a small heat flux (Equation 8-4) as neutrality is approached, and thus is a limitation of scaling in this way. Over smoother surfaces this effect may be observed less frequently as u_* is smaller so T_* can be larger for a given Q_H. Using functions of a conventional form (Equations 8-2 and 8-3), such as those of An88 and DB93, can therefore considerably overestimate Q_H in neutral conditions (f_{MO_T} is too small so the T_* obtained is too large) and means Q_H values close to zero are underrepresented or simply not obtained. Using the function fitted directly to the Swindon EC data improves estimation of these smaller Q_H values. The observational fits have the conventional functional form in unstable and stable conditions, plus two extra terms to account for the divergence towards neutral conditions:

$$f_{MO}(\zeta) = \frac{C_T^2 (z_m - z_d)^{2/3}}{T_*^2} = 5.45(1-14.9\zeta)^{-2/3} + 0.00938\zeta^{-1} + 0.000283\zeta^{-2} \quad (\zeta < 0) \tag{8-A1}$$

$$f_{MO}(\zeta) = \frac{C_T^2 (z_m - z_d)^{2/3}}{T_*^2} = 3.97(1+1.61\zeta^{2/3}) + 0.00901\zeta^{-1} + 0.000165\zeta^{-2} \quad (\zeta > 0) \tag{8-A2}$$

However, the fit to temperature does not represent the humidity scaling well.

Since most of the widely used functions in the literature do not capture this trend (possibly due to a lack of neutral data in these studies), Q_H derived using similarity theory tends to be biased towards larger values under near neutral conditions. Although absolute errors are usually small (a few W m^{-2}) so too is the size of Q_H and the frequency of data between -10 and 10 W m^{-2} is significantly under-represented compared to Q_H obtained from EC directly. For example, where Q_H changes sign the similarity functions (An88, DB93 and TG92 (Thiermann and Grassl, 1992)) result in lower values during stable conditions and higher values during unstable conditions giving a steeper change of stability overall (Figure 8-A1c).

Appreciable differences in the fluxes can arise depending on the similarity function used: An88 and DB93 tend to yield higher fluxes than TG92 by about 10-15% on average, with better agreement under unstable conditions. Although the fitted function performs much better under near neutral conditions for Q_H, the overall agreement is not much better than for An88 or DB93 and the performance under near neutral conditions is worse for Q_E. Given that the observed divergence is thought to be a limitation of the conventional scaling technique, we therefore decided against using the experimental fit to derive the scintillometer fluxes. Instead, An88 scaling is used for both T and q, which closely matches the shape of the observed scaling and does not produce as significant an overestimation as DB93.

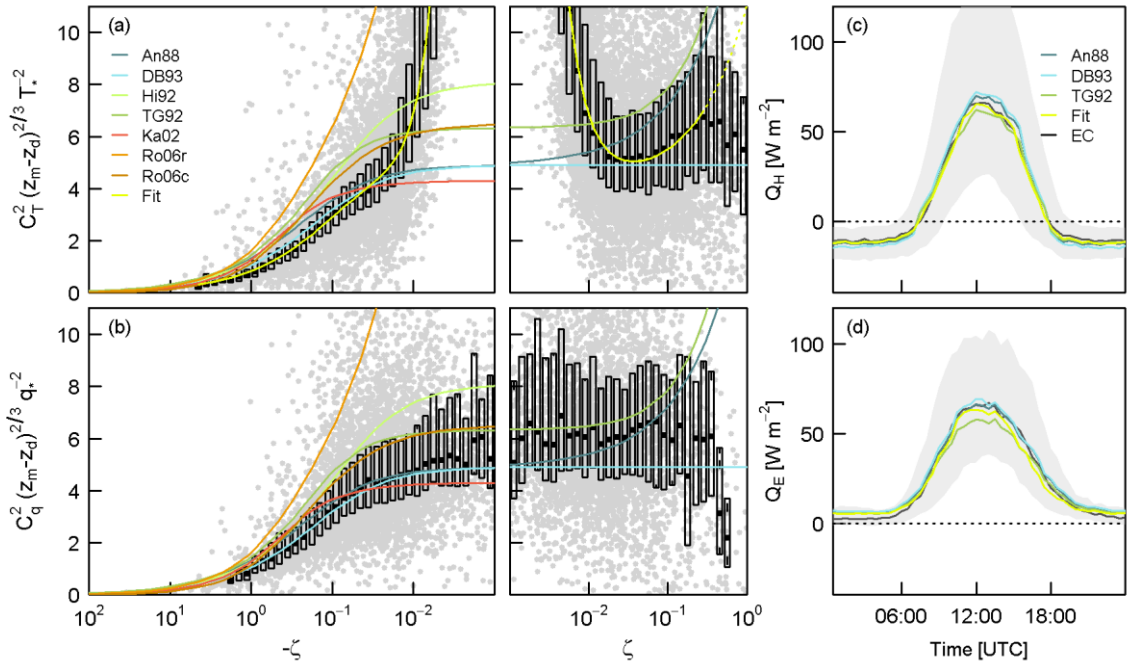

Figure 8-A1 Comparison between EC data and similarity functions from the literature: An88 (Andreas, 1988), DB93 (De Bruin et al., 1993), Hi92 (Hill et al., 1992b), TG92 (Thiermann and Grassl, 1992), Ka02 (Kanda et al., 2002) and Ro06 (Roth et al., 2006) fits to rooftop (r) and canyon (c) datasets. Box plots indicate median and inter-quartile range (IQR) binned by stability. A fit to the Swindon data ($|Q_H|$ > 5 W m^{-2}, $|Q_E|$ > 5 W m^{-2}) is also shown for temperature (a). Median diurnal cycle of (c) Q_H and (d) Q_E for all available data as measured directly by EC (IQR shaded) and as calculated via structure parameters using the similarity functions indicated.

Acknowledgements

We wish to thank the residents of Swindon who kindly gave permission for equipment to be installed on their property. This work was funded by the Natural Environment Research Council, UK.

Chapter 9 Summary and conclusions

The primary objective of this research was to investigate the exchange of energy and mass between the suburban land surface and the atmosphere above. Central to this objective are evaporative processes, as they link the energy balance and water cycle. To date, observations of the latent heat flux in urban areas have been mainly limited to short-term studies during summer. Therefore, the first aspect of this research was to undertake the necessary measurements which would extend observations and understanding to all seasons. Energy, water and carbon dioxide fluxes were measured using the eddy covariance technique for more than 20 months. Additionally, over 2 years of continuous meteorological data were collected. Data were gathered to estimate the contribution of anthropogenic activities to the total energy available and to the CO_2 release. Land cover classification and source area analysis further aided interpretation of the data.

Land cover type and properties of the surface have a major influence on turbulent transport processes. Obtaining representative measurements can be challenging, particularly when the surface is heterogeneous and the source area composition can vary widely. Scintillometers provide measurements that are spatially integrated over large areas and for this reason the second aspect of this work concerns the application of scintillometry. Sensible heat fluxes were estimated from two scintillometers on paths of 2.8 km and 5.5 km. A millimetre-wave scintillometer was deployed on the longer of the two paths in order to derive large-area latent heat fluxes for the study area, representative of 5-10 km^2. The temperature-humidity correlation was also measured using the bichromatic technique. As well as exploring the boundaries of experimental work, theoretical developments have also been made.

These results represent (a) the first suburban dataset of its type for the UK and (b) the first observations of large-area evaporation over urban areas. Using the data collected, the influences of land cover, scale, seasonality, energy and water availability and meteorology are considered. Given the pivotal role of evaporation, improving the representation of evaporative processes is of great interest to the meteorological and hydrological community.

The main findings and contributions of the research presented in this thesis are summarised below, grouped by topic rather than by chapter.

Theoretical work on the development of scintillometry

Spectra of the raw scintillometer signal can offer a deeper understanding of the data collected, including an indication of whether there are unwanted contributions from absorption, mounting vibrations or electronic noise, for example. These assessments are usually based on comparisons with the expected shape of the 'ideal' spectrum calculated assuming a uniform wind field. This work demonstrates that deviations from 'ideal' spectra can occur when the wind field is not uniform along the path, such as when the beam height varies with position. Non-uniform wind fields do not preclude the use of scintillometry to measure C_n^2, although they may lead to deviations from the expected spectral shapes such that estimation of C_n^2 from the spectral plateau is not advised. Obtaining an accurate wind speed measurement from scintillometry is more difficult in non-uniform conditions. This work offers insight into scintillometer spectra and gives theoretical and observational examples under a range of conditions. Most typical is a smearing of the spectra when the crosswind is variable in space and/or time.

Revision of the two-wavelength methodology demonstrated that formulating the equations in terms of specific humidity to obtain structure parameters and the latent heat flux offers several advantages over the use of absolute humidity, which is found in earlier published work. The specific humidity is a conserved variable and thus the more correct option for use with similarity theory. Moreover, the absolute humidity formulations are contaminated by temperature fluctuations so that the latent heat flux is misrepresented. The errors can typically be 5-10% but depend on the Bowen ratio. This work presents new structure parameter coefficients and revised equations for correctly estimating the heat fluxes.

Advances in the practical application of scintillometry

Following initial testing at Chilbolton Observatory and subsequently in Swindon, the long-standing noise problem of the CEH-RAL MWS was finally identified and resolved. The data presented in this thesis were collected after the instrument repair, when analysis of spectra and time-series indicated that the MWS was performing well.

For the first time a two-wavelength scintillometer system was deployed over the urban environment. The bichromatic method was used to measure the path-averaged temperature-humidity correlation. A long time-series has been collected and analysed and the performance of the two-wavelength and bichromatic methods was studied. The observed structure parameters of temperature and humidity indicated the same daily variations and seasonal trends as those estimated by eddy covariance. Whilst the results are generally very promising, some limitations of the two-wavelength and bichromatic methods were observed.

As found in previous trials of the bichromatic method (Lüdi et al., 2005; Beyrich et al., 2012), there is high variability associated with individual measurements, which originates from large uncertainties in the measurement of the cross-structure parameter C_{n1n2}. This can lead to frequent occurrences of measured r_{Tq} being outside the physically meaningful range of -1 to +1. The results presented here seem to suggest that performance is worse when crosswind speeds are low, but further experimental work is required to support or reject this claim. There are also times when the C_{n1n2} term is thought to be too large and can result in negative C_q^2, which may result from unwanted contributions of absorption not fully removed by filtering, or other instrumental or atmospheric effects. Nevertheless, on average the measured r_{Tq} is close to the expected behaviour and almost always follows a diurnal cycle (positive during daytime, negative at night). Observations between June and December exhibit clear changes in the diurnal pattern related to day length – the sign of the sensible heat flux (i.e. stability), rather than net radiation, is the important factor. Measured r_{Tq} sometimes indicated dewfall which cannot be detected by the two-wavelength method as, in the absence of other information, r_{Tq} is always assumed to be negative during the night. Whilst the bichromatic method can be valuable in providing additional information to interpret results, the large associated uncertainties led to the decision to use the more robust two-wavelength structure parameters to calculate the fluxes.

On the whole, the two-wavelength method performed well. Two methodological issues were investigated in light of the experimental results. Firstly, the structure parameter at millimetre wavelengths, C_{n2n2}, passes through a minimum when expressed as a function of the Bowen ratio, which means that two solutions are provided, one at low and one at high Bowen ratios. Secondly, the near-zero C_{n2n2} around this minimum (at $\beta \approx$ 2-3) means the small scintillation signal we attempt to measure is limited by instrumental noise, incomplete removal of absorption fluctuations and any other instrumental or atmospheric effects that may cause fluctuations in the signal, such that the sensitivity of the technique around this region is reduced. The results suggest that the region of reduced sensitivity begins at around $\beta \approx 1.3$ and is thought to extend over a wider range of β than suggested by purely theory-based estimations due to additional effects associated with observations such as absorption. Although there is considerable work to be done on furthering the understanding of these techniques, this study demonstrates that two-wavelength scintillometry can be used in urban areas, providing the Bowen ratio is not too high. The technique is perhaps more suitable for vegetated suburban locations than city centres. In contrast, the single-wavelength method is better suited to higher Bowen ratio conditions, as the influence of temperature-humidity fluctuations is reduced and errors in neglecting the Bowen ratio correction are minimised.

The accuracy of scintillometric fluxes is known to be limited by similarity theory scaling, and the uncertainties associated with similarity functions are much greater in neutral and stable conditions. Similarity scaling was investigated for Swindon using the eddy covariance data. Although humidity generally follows a similar scaling relation to temperature, there are larger differences under neutral and stable conditions and the humidity scaling is more scattered than for temperature. It appears that the scaling for humidity tends to a larger value than for temperature under neutral and stable conditions, which can be expected to result in an overestimation of the latent heat flux under these conditions when identical T-q scaling has been assumed, as is conventional.

Eddy covariance versus scintillometry

Structure parameters, temperature-humidity correlation and fluxes were calculated from both eddy covariance and scintillometry. A limitation of this project is that the nature of the site precludes a direct evaluation between methods (although this was not the aim of the study). The key advantage of the scintillometer measurements is their scale, as they represent an area of 5-10 km^2 (for the long path). Also, the spatial integration means shorter averaging times are possible (fluxes calculated at a resolution of 10 min) and the results are less susceptible to variation in source area composition. The EC results often indicate varying energy partitioning depending on the prevailing wind and whether the footprint is located over vegetated or more densely built areas. The effects of these land cover contrasts are also evident in the carbon fluxes. The advantages of EC include the measurement of other species (such as CO_2, or other trace gases) and that the measurement is more direct; with scintillometry it is necessary to rely on similarity theory to obtain the surface fluxes. In this study, high rates of evaporation directly after rainfall were captured by the two-wavelength scintillometer system, whereas this remains a challenge for open-path eddy covariance systems.

Insights into the suburban environment

As the first suburban campaign of its kind in the UK, this multi-seasonal, multi-scale dataset contributes (a) observations over a new land cover type to the UK community and (b) observations in a different geographical and climatic region to the urban community. The long duration and high continuity of this dataset deepen our understanding of surface-atmosphere interactions outside of the main summer field season and highlight the need for more long-term observations to assess seasonal and inter-annual variability.

Estimation of the anthropogenic heat flux suggests a small contribution to the available energy (6-10 W m^{-2}) in line with estimates for other sites of similar density and climate. The

magnitude of this additional heat release is not sufficient to maintain a positive sensible heat flux all year round. In winter Q_H is negative for much of the daytime, only rising above zero for a few hours around midday when the energy input from Q^* is maximal. Energy is instead partitioned into evaporation due to the ready supply of moisture.

Marked contrasts between the influences of the natural environment and human activity are evident in the carbon fluxes across daily and annual cycles. Uptake by vegetation is a strong signal in summer whilst in winter a double-peaked diurnal pattern results from anthropogenic carbon release. Carbon emissions modelled from domestic energy (gas) use, vehicle use and human metabolism matched the wintertime observations fairly well. Consistent differences between weekdays and weekends were observed. Although photosynthetic uptake exceeded carbon emissions during the middle of the day in summer, daily (24 h) totals were almost always positive, i.e. indicating net daily emission. To date, urban measurements of carbon dioxide fluxes in the UK have focused on city centres (Nemitz et al., 2002; Sparks and Toumi, 2010; Helfter et al., 2011). The Swindon results represent an important comparison dataset; although this suburban site is still a significant annual source of CO_2 at around 1.6 kg C m^{-2} y^{-1}, this contrasts with the magnitude of the city-based emissions (~10 kg C m^{-2} y^{-1}). Swindon's increased vegetation fraction helps to offset the emissions from a smaller population density with lower energy use, and these results illustrate the extent to which vegetation can help to reduce the net input of CO_2 into the atmosphere.

The net storage heat flux estimated using (a) the OHM parameterisation (Grimmond et al., 1991) and (b) the residual of the energy balance as an upper limit, confirmed the significance of this term in the urban energy balance and the difficulties in its accurate quantification. Wintertime presents particular challenges and there is evidence to suggest the OHM coefficients need adjustment for seasonality.

The partitioning of energy between sensible and latent heat fluxes changes significantly with season. During summer, results were broadly in agreement with other studies at sites with similar vegetation fractions. Energy was found to be partitioned approximately equally into sensible and latent heat ($\beta \approx 1$), with sensible heat favoured when water is limited several days after rainfall. The latent heat fluxes are higher when frequent precipitation maintains surface moisture availability, directly after rainfall, and for highly vegetated areas.

Evaporation rates are highest in summer when vegetation is fully leafed-out, whereas the sensible heat flux peaks earlier in the year in late spring. From late spring through to winter there is a trend of decreasing monthly Bowen ratio. Leaf-out increases transpiration which remains high throughout summer whilst the sensible heat flux decreases. As the energy

supplied by net radiation decreases in autumn through to winter, evaporation continues, albeit at lower rates, and the sensible heat flux rapidly decreases due to the limited energy available. The latent heat flux remains positive all year round and is partly maintained by $Q_H < 0$ in winter. At the EC site, monthly midday Bowen ratios ranged from > 2 in spring to ~0.5 in winter.

Despite differences in water availability between 2011 and 2012, the general pattern of the seasonal trends is clearly replicated across both years. However, the Bowen ratio was considerably lower in 2012 when rainfall was well above average, and significant variation is seen between the same months in different years. Both summers were wet and fairly cloudy so vegetation was rarely, if at all, water-stressed, although fluxes of CO_2 and water vapour suggested stomatal closure in summer and autumn under sunny warm conditions.

Inter-annual variability in the energy partitioning was more evident in spring and autumn, related to weather patterns, water availability and associated annual differences in vegetative activity. The driest seasons were spring of both years and the effect on the energy partitioning was particularly evident in March 2012, when β was seen to increase rapidly as the surface dried out over the timescale of a few days. The lowest evaporation rates were observed when the EC source area comprised mostly impervious surfaces and little vegetation.

The amount of vegetation across the whole study area can explain considerably higher evaporation rates determined by the two-wavelength scintillometer system. It is likely that these rates were further enhanced by a nature reserve located near the centre of the BLS-MWS path. Compared to the EC footprint, the BLS-MWS footprint also contains more trees able to access deeper supplies of water. Average daily evaporation was 1-3 mm day^{-1} compared to 0.5-2 mm day^{-1} at the EC site. When vegetation is dormant the surface cover is less suitable as an indication of Q_E and the energy partitioning for the BLS-MWS and EC source areas become more similar. These results thus support the reasoning behind an 'active vegetation index' proposed by Loridan and Grimmond (2012) which accounts for the state as well as the spatial extent of vegetation when describing land cover.

The energy partitioning showed little day-to-day variation at the large-scale, whereas considerable day-to-day variability was observed in the EC data as the source area composition varied and impervious surfaces dried out. The larger scintillometer footprint reduces differences in land cover composition between samples and is less subject to wind direction bias of the source area than are local-scale EC measurements, but does not eliminate them entirely. As average values can be influenced by the wind direction distribution affecting source area composition, footprint climatologies may be useful in describing and interpreting

the results. Variability of local-scale observations due to the changing source area is not accounted for in many models, either for input data or evaluation of the output. The differences in the behaviour of the energy partitioning between the scintillometer and EC observations highlights the need for more large-area observations to represent the land surface at larger scales.

Defining the temporal scales of interest is critical in determining which processes are relevant to the surface-atmosphere interactions. At sub-daily timescales, changes in cloud cover directly impact the energy fluxes at all scales. Sudden rainfall can lead to large latent heat fluxes at the expense of the sensible heat flux, particularly when the rain is of short duration and falls on hot surfaces. Negative sensible heat fluxes were observed on some occasions following rainfall. The net radiation drives the diurnal pattern of meteorological variables, the turbulent fluxes and associated changes in stability, and the temperature-humidity correlation. When the energy is limited, such as during winter, it is used in evaporation rather than heating the atmosphere and as a result Q_H and r_{Tq} are positive for a smaller proportion of the day (Q^* > 0). This behaviour also has implications for the averaging periods used to make comparisons between sites, e.g. during winter the average Bowen ratio for, say, ±2 h around midday can be significantly different to the midday value itself. For periods of several days to a few weeks, radiation patterns are important in determining the size of the fluxes from day to day, and time since rainfall and depletion of near-surface soil moisture affect the energy partitioning particularly when the vegetation fraction is small. Month to month variation is dominated by seasonal controls, primarily vegetation and the annual cycle of solar radiation. Inter-annual variability results from variations in the weather about climatological means, such as rainfall, sunshine hours and temperatures affecting vegetation and soil moisture levels.

For summer months the proportion of net radiation partitioned into the sensible heat flux was shown to decrease with the vegetation fraction of the source area in a broadly consistent way to other local-scale studies in the literature. Major factors influencing the sensible heat flux appear to be the amount of energy supplied by the net radiation and whether incoming radiation is diffuse or direct. The partitioning of energy into turbulent sensible heat and stored heat displays a clear hysteresis pattern across the measurement scales, particularly under clear-sky conditions. Hour-to-hour changes are usually closely matched between the scintillometers and EC; differences occur when the net radiation varies spatially.

The temperature-humidity correlation coefficient measured using EC and the bichromatic method was generally fairly close to 1 during daytime (0.6-0.9) and smaller and negative at night (-0.3 to -0.5). Results for this urban setting were therefore not significantly different from

studies over other surfaces. During winter and under more neutral and stable conditions the behaviour of temperature and humidity was less similar.

Dewfall ($Q_E < 0$) was observed at the EC station and also implied by the bichromatic measurements of r_{Tq} (nocturnal $r_{Tq} > 0$ was assumed to indicate $Q_H < 0$, $Q_E < 0$). Urban dewfall has been little studied (Richards, 2004), yet for UK sites this nocturnal moisture supply may be more relevant than irrigation (in contrast to the North American studies, for example).

The surface conductance, g_s, was estimated by inverting the Penman-Monteith equation and using the observed fluxes. The diurnal cycle was found to be asymmetrical, particularly in non-winter months. This mainly originates from the changing relation between Q_E and the vapour pressure deficit over the course of the day. Typical peak daytime values are 7-10 mm s^{-1}, lower in dry conditions and higher when there is a ready supply of moisture. Nocturnal values are smaller than daytime and largest when wind speeds and water availability are high. Following rainfall wet surfaces lead to large values and erratic changes in g_s. Dewfall results in negative values of g_s, followed by an early morning peak as it subsequently evaporates. These 'measured' surface conductances provide valuable information for model parameterisation and development.

Recommendations for further work

Urban micrometeorology

- Whilst the Swindon campaign extends our knowledge and understanding to a wider range of conditions, it also makes a strong case for more long-term urban datasets. Observations should also incorporate measurements at multiple-scales using complementary approaches. Multiple eddy covariance stations can provide valuable information on the spatial variability at smaller scales, whilst large aperture scintillometers can provide representative measurements across a larger area. Deployment of millimetre-wave scintillometers may be most successful in regions with relatively low Bowen ratios. Multi-scale field campaigns, such as those in Basel (Rotach et al., 2005) or Toulouse (Masson et al., 2008) will be crucial in the development of algorithms for up-scaling fluxes.
- The storage heat flux remains a limiting factor in quantifying the urban energy balance. There is a need for experimental work directed towards quantifying this flux under a wider range of conditions, such as when surfaces are wet or dry and when incoming

radiation is direct or diffuse. Future studies must address the seasonality of this important term in the energy balance and aim to evaluate and improve model estimates.

- The Swindon dataset offers the possibility of evaluating the performance of energy and/or water balance models. This offers considerable new potential for model development and for increasing the applicability to a wider range of sites and conditions, especially where parameterisations may have relied on available summertime data from different climates.
- One of the main findings of the experimental work is that the eddy covariance fluxes tend to have a much more variable energy partitioning compared to the scintillometer fluxes. Modelling may offer insight into whether this is mainly due to spatial averaging or the proportion or type of vegetation in the source area. Model results could be generated for each wind sector, effectively aiming to replicate the measurements that would have been obtained for a range of source area characteristics, including for the actual observed wind direction. Questions to address include to what extent the variation in EC data can be explained by land cover, how this compares to the atmospheric controls and estimation of monthly or annual totals free from bias due to the wind direction distribution.

Scintillometry

- Testing of the two-wavelength and bichromatic techniques is fundamental for future applications of these methods. The region of reduced sensitivity at moderate Bowen ratios must be better understood, either to restrict use of millimetre-wave scintillometry to environments with a consistently low Bowen ratio (and be clear where the threshold lies), or to investigate possible improvements to the system design in order to overcome this issue. Although considerable variability should be expected from the bichromatic method, deeper understanding of the performance under different conditions (e.g. with crosswind) could facilitate quality control and offer insight into suitable methods to reduce the cross-term variability. The relative importance of absorption seems a likely factor limiting measurement performance particularly when the expected scintillation signal is small. More sophisticated filtering of the data (e.g. wind speed dependent cut-offs) may yield improved measurement accuracy. Multiple aperture instruments or recording the phase as well as intensity of the scintillometer signal offer options for more advanced treatment of absorption fluctuations.

- Saturation of the infrared scintillometer could warrant a correction for the cross-correlation, or at least knowledge of the impact. Deployment of a millimetre-wave scintillometer simultaneously with a large aperture (infrared) scintillometer and an extra-large aperture (infrared) scintillometer may offer new insights into several issues.
- Similarity theory adds considerable uncertainties to scintillometric flux estimates. Despite the far-reaching applications of MOST, the relations have been derived based on relatively few data and there is a current lack of consensus on which are the most appropriate functions to use. With improved measurement capabilities and increased demands to understand the atmosphere under a wider range of conditions, further research into these relations would be extremely valuable.
- Sensible and latent heat fluxes were measured at different scales using eddy covariance and scintillometry, although carbon dioxide fluxes were only available from eddy covariance. Extension of the scintillometry technique to greenhouse gases would constitute a major step in measurement capability. Current research investigates composite methods to estimate fluxes of trace gases (Poggio et al., 2000) and water vapour and CO_2 at the field scale (Van Kesteren et al., 2012).

Land-atmosphere interactions

- The temperature-humidity correlation is still relatively poorly understood. Further insights could be gained from understanding the behaviour with stability for example. Although a difficult quantity to measure, the bichromatic scintillometry method offers this possibility, and new developments in instrumentation could potentially reduce uncertainties in the measurement of r_{Tq} from eddy covariance.
- To make progress in up-scaling observations requires careful and extensive experimental campaigns at nested scales, such as the LITFASS experiments over heterogeneous farmland (Beyrich and Mengelkamp, 2006; Beyrich et al., 2012). Datasets from many sources and representative of different scales are required, e.g. extra-large, large, and small aperture scintillometers, eddy covariance at different heights and locations, airborne measurements, satellite data and infrared imagery, and these must be combined with modelling studies to further understand the interactions between patches of different land cover and surface properties.

Appendix A Effects of non-uniform crosswind fields on scintillometry measurements[1]

A1. Introduction

Sensing of the refractive index structure parameter, C_n^2, forms the basis of micrometeorological scintillometry. From measurements of the refractive index structure parameter the temperature and humidity structure parameters of the atmospheric boundary layer can be estimated (Kohsiek, 1982); these in turn can be used to derive the surface fluxes of sensible and latent heat by applying Monin-Obukhov similarity theory (MOST) (Hill et al., 1992b). Scintillometers have an electromagnetic transmitter and receiver separated by distances of a few hundred metres to several kilometres with the propagation path some metres above the land surface. In addition, it is possible to derive a measurement of the horizontal wind speed perpendicular to the beam direction (the crosswind) from the drift of the turbulence pattern through the instrument path (Lawrence et al., 1972; Wang et al., 1981).

Scintillometry offers the advantage of providing spatially integrated measurements at a scale comparable to the grid boxes of mesoscale weather models and resolution of satellite data. It is now being deployed in a greater variety and complexity of locations, whereas initial work sought extensive, flat and homogenous areas where MOST assumptions were clearly satisfied and the source area comprised only one land class, for example extensive level farmland at Flatville, Illinois (Hill et al., 1990) or the flat, dry plain of La Crau, Southern France (De Bruin et al., 1993). The Flevoland experiment in The Netherlands in 1998 (Meijninger et al., 2002a), as well as the LITFASS campaigns in 1998, 2003 and 2009, took place over a variety of different crop types and although fairly flat the land surface is described as heterogeneous (Meijninger et al., 2006). The study of Poggio et al. (2000) in the Mesolcina Valley in the Alps had the aim of testing scintillometry over complex terrain. Similarly, Evans (2009) and Evans and De Bruin (2011) analyse scintillometry data collected over topographically variable chalk downland in Southern England.

Scintillometry allows measurements to be made with minimal interference from instrument support structures. The transmitter and receiver units may be mounted on existing buildings,

[1] Ward, H.C., Evans, J.G. and Grimmond, C.S.B., 2011. Effects of Non-Uniform Crosswind Fields on Scintillometry Measurements. Bound.-Layer Meteor., 141(1): 143-163.

communications masts or landscape features, often resulting in a slant path setup where the beam is not parallel to the land surface below. This is a critical advantage in urban areas where scintillometry has been successfully used to measure the heat fluxes, initially in Tokyo (Kanda et al., 2002), Marseille (Lagouarde et al., 2006) and Basel (Roth et al., 2006).

Even over ideal, horizontal terrain, if a slanted beam is used then the wind speed at the level of the beam would be expected to change as a function of position along the path (i.e. with height). Thus with a slant path, a spatially varying crosswind along the path may occur without violation of MOST assumptions. With varying topography of the underlying landscape, the wind speed along the path will be affected by the shape of the surface below. Depressions or hills alter the flow speed, as the air spreads out and slows down to fill a wider volume or accelerates as it is squeezed through a smaller layer. Of particular importance in urban environments are the zero-plane displacement and aerodynamic roughness length, which influence the local wind speed and are determined by the underlying properties of the surface: the size, shape, density and rigidity of the obstacles (Grimmond and Oke, 1999a). As well as spatial variations, fluctuations in time of both wind speed and direction are present over all surfaces. Here we focus on the expected behaviour of scintillometry measurements under non-uniform crosswind conditions, demonstrated through numerical analyses using scintillation theory. The applicability of MOST, a separate subject, is not discussed here.

The motivation for this work is to provide an improved understanding and prediction of spectral behaviour in order to give increased confidence in data and to enable better informed decisions about the data quality. With knowledge of the expected effects of a varying crosswind, spectral features can be better explained and an appropriate method of analysis chosen.

To date there is minimal discussion of the influence of varying crosswinds on scintillometric spectra in the literature. Tatarski (1961) mentions that experimental plots differ from the uniform crosswind spectrum, attributing this to the wind variability along the path. Here we look at both spatial and temporal variation of crosswind. Otto et al. (1996) generate theoretical spectra allowing for wind speed and direction changes over a 40 min period but their experimental data are not explained by this, suggesting another (perhaps instrumental or stability) problem. We address wind speeds perpendicular to the beam direction. Potvin et al. (2005) introduce a longitudinal timescale and length scale to model the effects of along-path winds, but in general along-path wind has much less impact on scintillometry measurements (Tatarski, 1961).

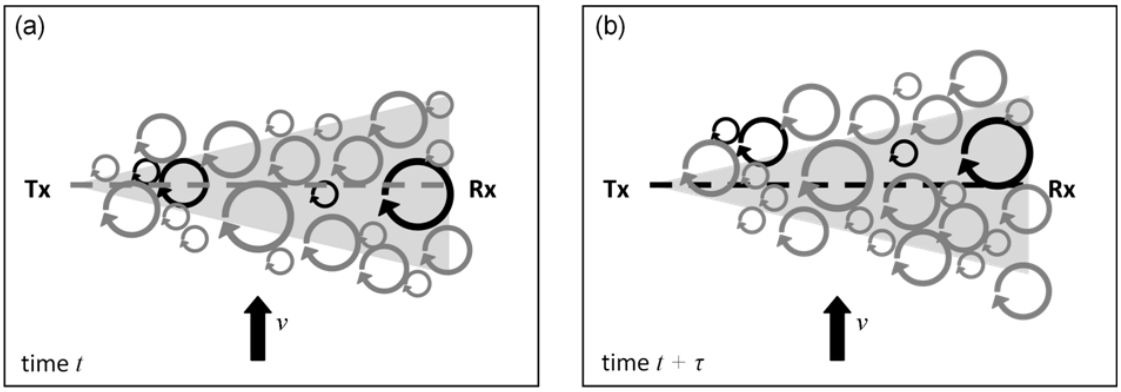

Figure A-1: Illustration of a frozen turbulence pattern being blown through the scintillometer beam. The arrangement of eddies is the same between (a) and (b), as highlighted in black. However the beam passes through a different portion of the pattern at each time and so the refraction pattern changes between time t and $t + \tau$. Tx is the transmitter; Rx the receiver.

A2. Theory

The scintillometer transmitter is a source of electromagnetic radiation of wavelength λ, which propagates as a spherically diverging beam towards the receiver, where the intensity of the radiation is measured. The intensity of the received signal will vary with time due to the changing refractive properties of the medium between the transmitter and receiver – i.e. the turbulent atmosphere made up of eddies of a range of sizes. The size of an eddy (l), is used to define the eddy wavenumber as $K = 2\pi/l$ (all length scales are in units of metres). With zero crosswind, there is no net motion of the turbulence pattern through the beam and the observed intensity fluctuations would be caused by the decay of eddy size: energy is transferred to smaller scales as the larger structures break up into smaller ones in the inertial subrange.

The crosswind moves the turbulence pattern through the scintillometer beam so that intensity fluctuations in the received signal are due to a combination of eddy decay and the transit of different sized eddies through the beam. Over short timescales with appreciable wind speeds, the large scale motion dominates and the eddy pattern can be approximated as being frozen in time (Taylor's frozen turbulence hypothesis (Stull, 1988)). The intensity fluctuations are then due to eddies of different but constant sizes being blown through the beam (Figure A-1). In this investigation Taylor's frozen turbulence hypothesis is assumed to hold. Poggio et al. (2000) discuss the consequences of violation of Taylor's hypothesis on measurements over complex terrain.

Intensity readings can be measured as a time series from a single receiver, with samples separated by a lag time τ, or simultaneous samples can be made by two receivers separated by

a horizontal distance ρ. The intensity difference would be the same in each case if there was a horizontal wind blowing across the path of magnitude $v = \rho/\tau$.

The covariance of the logarithm of the amplitude between two points (C_χ), separated by a distance, ρ, and lag time, τ, is given by (Lawrence et al., 1972):

$$C_\chi(\rho,\tau) = 4\pi^2 k^2 \int_0^L dx \int_0^\infty dK K \Phi_n(K) J_0(K(\rho\frac{x}{L} - v(x)\tau))\sin^2(\frac{K^2 x(L-x)}{2kL}) \qquad \text{(A-1)}$$

where k is the wavenumber of the radiation ($k = 2\pi/\lambda$); x is the position along the path ranging from 0 at the transmitter to L, the path length (in metres), at the receiver; J_0 is a Bessel function of the first kind. Φ_n is the three dimensional Kolmogorov spectrum (Monin and Yaglom, 1971): $\Phi_n(K) = 0.033 C_n^2 K^{-11/3}$, describing the (homogeneous and isotropic) turbulence pattern of the atmosphere. The crosswind speed (i.e. the wind speed perpendicular to the path), v, is written here explicitly as a function of position along the path.

It should be noted:

- In this paper the equations are for spherical waves – the plane wave case is different, as highlighted by Clifford (1971). The spherical geometry demands an additional magnification factor because the divergence of the beam means an eddy of size l at a position x along the path appears bigger by a factor L/x at the receiver and the eddy appears to move faster by the same factor.

- Only the real part of the refractive index fluctuations is considered here; the imaginary part corresponding to phase fluctuations caused by atmospheric absorption (e.g. by water vapour) has been ignored. See Medeiros Filho et al. (1983) and Nieveen et al. (1998) for details.

- In Equation A-1 the source of radiation is taken to be a point source, as is the case for small aperture scintillometers (SAS). For large aperture scintillometers (LAS) an extra term must be included to average over the size of the aperture (Equation A-6). This changes the path weighting function (Figure A-2).

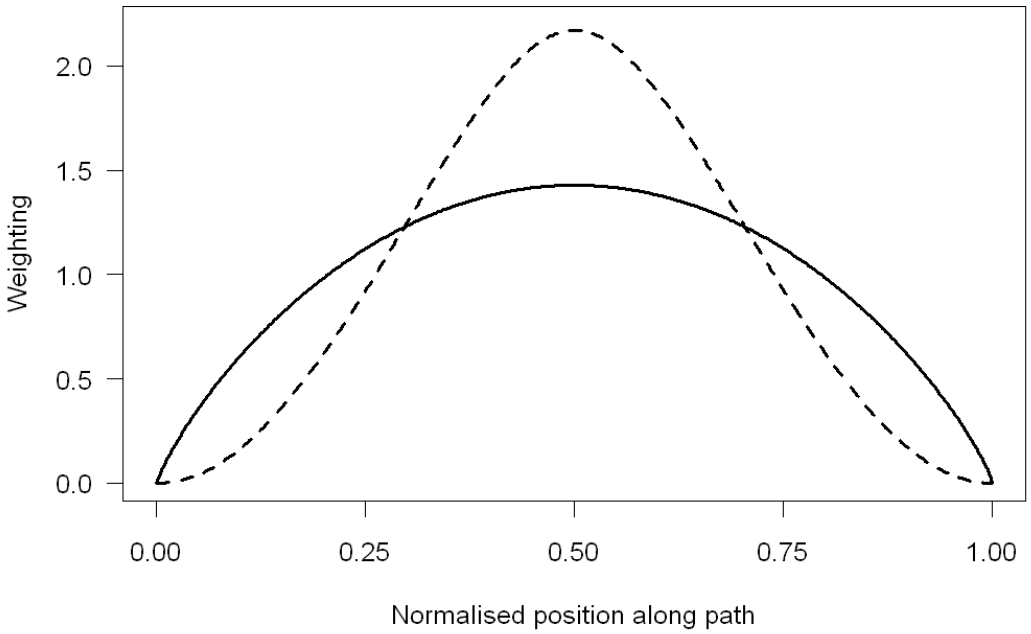

Figure A-2: Path weighting functions (Hill and Ochs 1978) for the Millimetre-Wave Scintillometer (MWS) (solid line) and Large Aperture Scintillometer (LAS) (dashed line).

For a single receiver (ρ = 0) and following (Clifford, 1971) the time-lagged autocorrelation (R_χ) for a diverging beam SAS can be written:

$$R_\chi(\tau) = 4\pi^2 k^2 \int_0^L dx \int_0^\infty dK K \Phi_n(K)\, J_0(Kv(x)\tau) \sin^2\left(\frac{K^2 x(L-x)}{2kL}\right) \qquad \text{(A-2)}$$

Next, as prescribed by Tatarski (1961), we take the Fourier transform of the time-lagged autocorrelation to give the temporal power spectrum of the amplitude (W_χ) (Clifford, 1971):

$$W_\chi(f) = 16\pi^2 k^2 \int_0^\infty d\tau \int_0^L dx \int_0^\infty dK K \Phi_n(K)\, J_0(Kv(x)\tau) \cos(2\pi f \tau) \sin^2\left(\frac{K^2 x(L-x)}{2kL}\right) \qquad \text{(A-3)}$$

where f is the frequency of the intensity fluctuations. Evaluating the time integral gives:

$$W_\chi(f) = 16\pi^2 k^2 \int_0^L dx \int_{\frac{2\pi f}{v(x)}}^\infty dK K \Phi_n(K) \frac{1}{\sqrt{(Kv(x))^2 - (2\pi f)^2}} \sin^2\left(\frac{K^2 x(L-x)}{2kL}\right). \qquad \text{(A-4)}$$

Clifford (1971), who first derived this result for spherical waves, assumed a uniform crosswind over the length of the path. Integrating the power spectral density (PSD), $W_\chi(f)$, over all frequencies (i.e. the area under the power spectrum) gives the variance of the log amplitude, that is $\sigma_\chi^2 = \int W_\chi(f)\, df$. For a uniform crosswind, the standard scintillometer equations are obtained. For a SAS:

$$\sigma_\chi^2 = 0.124 k^{7/6} L^{11/6} C_n^2 . \qquad \text{(A-5)}$$

For the LAS an extra term must be included to average over the size of the aperture, so Equation A-4 becomes (Nieveen et al., 1998):

$$W_\chi(f) = 16\pi^2 k^2 \int_0^L dx \int_{\frac{2\pi f}{v(x)}}^{\infty} dK K \Phi_n(K) \frac{1}{\sqrt{(Kv(x))^2 - (2\pi f)^2}} \sin^2\left(\frac{K^2 x(L-x)}{2kL}\right)$$

$$\times \left[\frac{2J_1(0.5KDx/L)}{0.5KDx/L}\right]^2 \left[\frac{2J_1(0.5KD(1-x/L))}{0.5KD(1-x/L)}\right]^2 \qquad \text{(A-6)}$$

where D is the aperture diameter and J_1 is a Bessel function. The corresponding result for the LAS is (Wang et al., 1978):

$$\sigma_\chi^2 = 0.223 D^{-7/3} L^3 C_n^2 . \qquad \text{(A-7)}$$

Equations A-5 and A-7 can also be obtained through integration of Equation A-1 (and the LAS equivalent) directly, with ρ = 0 and τ = 0, meaning the Bessel function term is equal to one, and

$$\sigma_\chi^2 = R_\chi(0) = 4\pi^2 k^2 \int_0^L dx \int_0^\infty dK K \Phi_n(K) \sin^2\left(\frac{K^2 x(L-x)}{2kL}\right) \qquad \text{(A-8)}$$

which gives Equation A-5 on integration.

The instruments measure the intensity of the received radiation, the variance of the logarithm of which gives the intensity fluctuations (σ_{lnI}). This can be simply related to the variance of the log amplitude through the fact that intensity is the square of the amplitude, hence $\sigma_\chi^2 = 0.25\sigma_{lnI}$.

The temporal power spectrum of the scintillometer measurement is obtained on plotting the PSD, $W_\chi(f)$ (Equations A-4 and A-6), against f. The PSD multiplied by the frequency at each point in the power spectrum gives the frequency spectrum: $f\ W_\chi(f)$ against f. This shows the contribution to σ_χ^2 that can be attributed to different frequencies of refractive index fluctuations. At constant wind speed this is the contribution of different eddy sizes. By working in the frequency domain the dependence on wind speed is introduced; Equations A-4 and A-6 allow the effects of non-uniform crosswinds to be explored. By writing $v = v(x)$ the spatial variability can be studied for a given point in time; the temporal variability is modelled by calculating the spectrum for each subinterval in time with its particular crosswind value and then averaging these spectra over the total time considered (Otto et al., 1996).

As an alternative method to using measured σ_χ^2 values to calculate C_n^2, spectra can be plotted and the area under the curve used to find σ_χ^2 and hence C_n^2. The total area under the curve gives σ_χ^2, or integration up to the corner frequency (see Section A4.1) gives a value that is a fixed proportion of σ_χ^2. Another option is to use the low frequency limit for the level of the power spectrum plateau (Clifford, 1971). This method offers the advantage of being able to exclude additional signal variance due to vibrations of the mounting system (as opposed to atmospheric scintillation) and offers a visual quality control by comparison with theoretical spectra (Von Randow et al., 2008). Previously published comparison spectra assume a constant crosswind; here we verify whether these methods are still applicable when the crosswind is non-uniform.

A3. Methods

Using the presented theory (Section A2) we investigate a range of wind conditions: firstly, spatially varying and secondly, temporally varying crosswind scenarios, evaluating the predicted power and frequency spectra in each case. Calculation of the theoretical spectra was performed in Mathcad (Mathcad 14.0, Parametric Technology Corporation, Massachusetts, USA). Table A-1 lists the input parameters used. These are based on a millimetre-wave scintillometer (MWS – a SAS operating at 94 GHz built for the Centre for Ecology and Hydrology by Rutherford Appleton Laboratory, UK, see Evans (2009) for details) deployed at Sheepdrove Organic Farm, Lambourn, Berkshire, UK. The LAS values correspond to commercially available instruments. Running the simulations for this setup facilitates comparison with the experimental spectra presented in Section A4.4.

Input parameter	k_{MWS}	C_n^2	L	k_{LAS}	D
Value	1970 m^{-1}	10^{-14} $m^{-2/3}$	2430 m	7140000 m^{-1}	0.145 m

Table A-1: Values of the input parameters used in the calculations. Variables are defined in the text; D is the aperture diameter of the LAS 150 instrument (Kipp and Zonen 2005).

Initially simulations were run for several values of a constant uniform wind speed and the resulting spectra analysed. For each program run, a sequence of numbers representing the frequency (between 0.001 and 1000 Hz) was generated and $W_\chi(f)$ (Equation A-4) evaluated at each of these. Then a non-uniform wind speed was introduced – the crosswind was allowed to vary spatially with x, and the resultant spectra plotted. A range of wind path profiles was tested and examples are shown in Section A4.2. Section A4.3 focuses on the temporal variability. This was modelled by averaging spectra for different crosswind conditions over several subintervals.

Comparison with experimental data is made in Section A4.4. The data were collected at Sheepdrove during summer 2006, with the MWS sampled at 80 Hz at an average beam height of approximately 32 m. Wind speed and direction were sampled at 20 Hz by a fast response sonic anemometer (model R3, Gill Instruments Ltd., Lymington, UK) and averaged over ten second intervals, at a height of 4.85 m at the nearby Melville's Trees site, south of the centre of the path. Evans (2009) provides a thorough site description. Unfortunately no raw LAS data were collected, nor any spatial information about the crosswind distribution, as only one nearby wind measurement was available. Therefore the comparison with experimental data is made based on the temporal variability of crosswind. Due to the complexity of the site (a valley with some heterogeneity provided by different crop types) there will be some spatial variation of the wind field above the surface. However, the considerable height of the beam above the valley floor means that these spatial differences are likely to be less significant than the temporal changes along the beam, particularly when the effect of the path weighting is considered.

For each 5 min observed MWS spectrum, two theoretical spectra were computed using the measured crosswind. Wind speed and direction data at ten second intervals were used to find the crosswind speeds, and these scaled by a factor of two to account for the height difference. Then spectra were generated for each ten second subinterval and these averaged over the 5 min to give a theoretical spectrum that includes the effect of the observed varying crosswind. Additionally a single theoretical spectrum was generated using the mean crosswind over the whole 5 min. Both theoretical spectra were scaled to the experimental curve using the 5 min C_n^2 values from the MWS.

A constant value of C_n^2 was assumed for each 5 min dataset and over the whole beam for the majority of the investigation; exceptions are discussed in Section A4.5. In the results we focus mainly on the MWS but similar effects for the LAS were predicted by the simulations.

A4. Results

To provide a foundation for understanding the results, we first consider some details of the scintillometer measurement. The integrand of Equation A-4 can be split into three parts – the refractivity spectrum (see Section A2), the crosswind dependence and the filter function or path weighting function. The square root term has the only dependence on crosswind and dictates the position of the corner frequency. The lower limit on the integration over K prevents this term from becoming imaginary. The peak of the spectrum is produced at frequencies close to $Kv/2\pi$ as this term gets very large.

The sine squared function is the basis of the path weighting function for the MWS (Figure A-2). This term selects the most effective eddy sizes at each position along the path (since this varies with x (Van Kesteren, 2008; Evans, 2009)) and enhances their contribution accordingly – i.e. identically sized eddies will have differing effects on the received intensity signal if they are located at different distances from the receiver. Again, for the LAS the Bessel functions must be included (Equation A-6).

Figure A-3 shows the combination of the wavenumber, refractivity spectrum and filter function, with the crosswind dependence removed (i.e. $K\ \Phi_n(K)\ \sin^2(K^2x(L-x)/2kL)$). The aperture averaging term is included for the LAS (Figure A-4). These plots show the sensitivities of the scintillometers to different wavenumbers (x-axis) with position along the path (y-axis). Displaying the information in this way provides a more complete visual summary of the scintillometer measurement and highlights some features that have not been explicitly shown before. Generally large eddies (low wavenumbers) near the centre of the path are the most important, but it is interesting to see the structure emerge and the repeating pattern of certain eddy sizes that are more significant than others, particularly for the MWS. The origin of the path weighting functions can be seen on comparison between these plots: the ends of the path are much more important for the MWS than the LAS. Whilst the MWS has an oscillating pattern of more and less effective wavenumbers, the LAS only has a small contribution from higher wavenumbers away from the centre of the path.

Figure A-3a shows the path weighting function for an MWS (solid line). This is the sum over all wavenumbers, between the inner and outer scales of turbulence, estimated here as l_0 = 0.01 m and L_0 = 15 m respectively. For a definition of these values see e.g. Meijninger (2003). The dashed lines show how the contributions from various eddies sizes differ. For example, for K = 4-5 m^{-1} the centre of the path is less important than the edges. From Figure A-3b we see that the most effective eddy size depends on the position along the path (as in e.g. Meijninger (2003) or Van Kesteren (2008)). Close to the centre and for the majority of the path, wavenumbers of K = 2-3 m^{-1} are the most significant – the most effective eddy size is the size of the first Fresnel zone, $F = (\lambda L)^{1/2}$. Figure A-3c combines this familiar result with the path weighting function to provide a continuous illustration of the instrument sensitivity. At constant wind speed the contribution of different eddy sizes defines the shape of the spectrum.

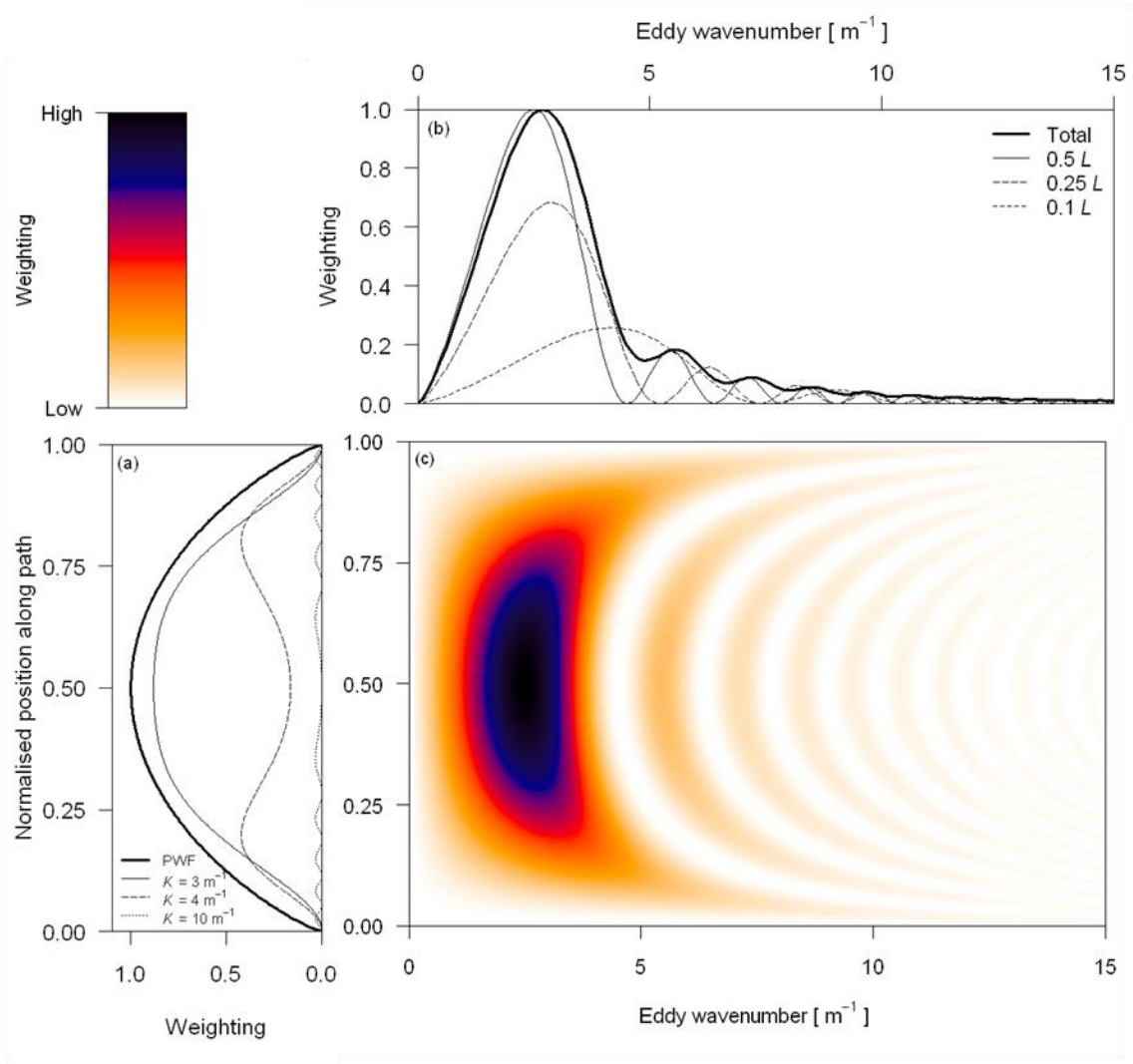

Figure A-3 MWS eddy sensitivity as a function of (a) position along the path of length L, (b) wavenumber and (c) both together. The weighting scale is arbitrary and has been normalized to give a maximum value of 1 (black). The total path weighting function (PWF) is shown in (a).

For the LAS, fluctuations smaller than the aperture size are averaged out over the area of the aperture, resulting in the LAS having reduced sensitivity to small eddies (Figure A-4). The most effective eddy size for a LAS is the same as the aperture diameter (i.e. D). The differing wavelengths of the instruments makes the MWS (a SAS) sensitive to larger eddies than the LAS (Table A-1). The relevant length scales in each case are F for the MWS and D for the LAS – note that these also scale the corner frequencies of the spectra, which are proportional to v/F for the MWS (of the order of 1 Hz) and v/D (about 10 Hz) for the LAS, when the crosswind is uniform. These observations underlie the spectral shapes that are discussed here. Results are presented for the MWS. Generally the behaviour of the LAS was found to be similar.

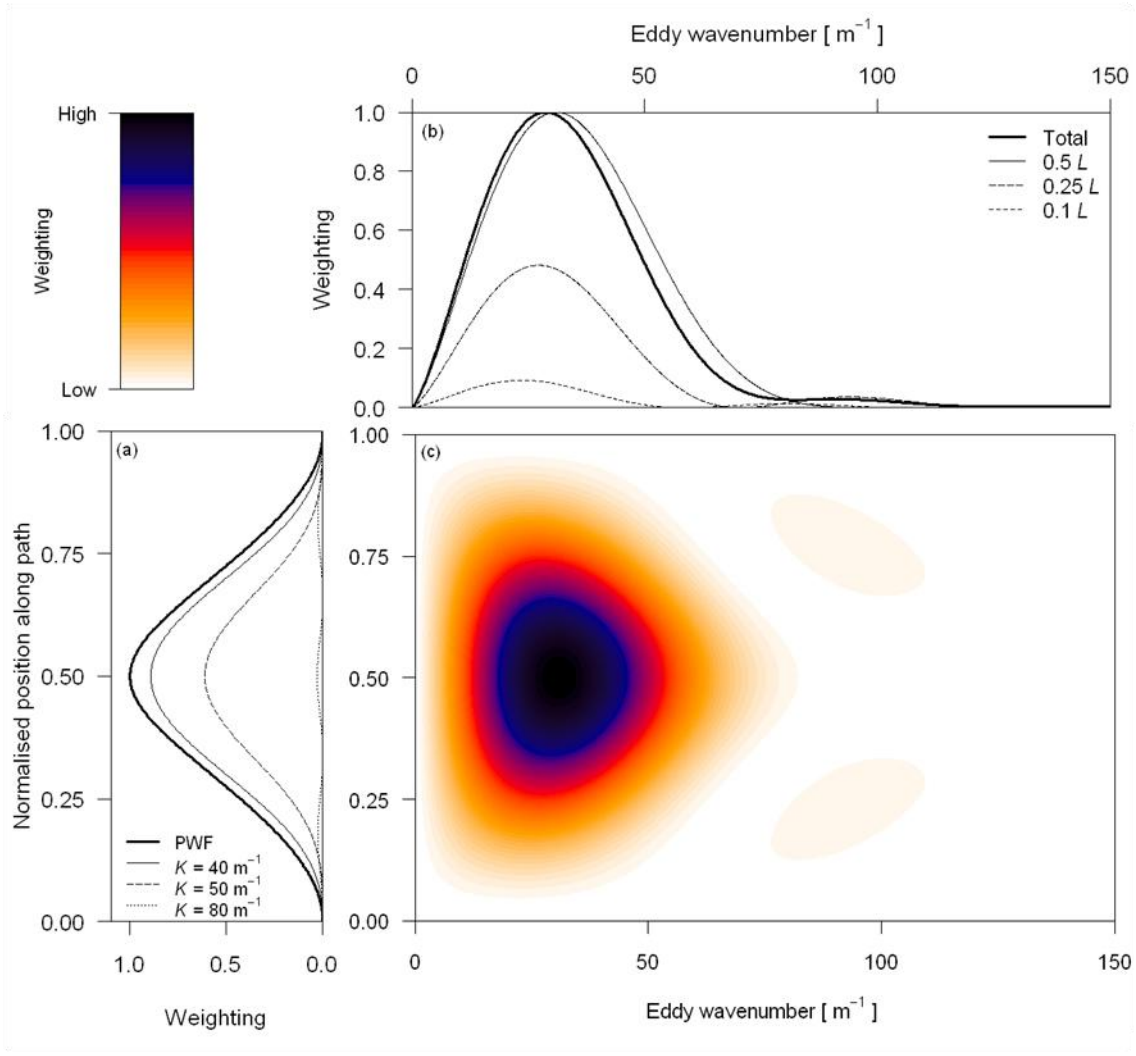

Figure A-4 Same as Figure A-3 but for a LAS.

A4.1. Uniform crosswind simulations

Scenario 1.1: Constant crosswind in space and time

Power spectra and their corresponding frequency spectra for uniform crosswind speeds are presented in Figure A-5 (also Hartogensis (2006), Van Kesteren (2008), Evans (2009)). The corner of the power spectrum and the peak of the frequency spectrum occur at the same frequency, the corner frequency, which is directly proportional to v, when the crosswind is constant. Thus it is possible to make an estimate of v from the frequency spectrum – this is known as the fast Fourier transform technique (Poggio et al., 2000). From the literature it appears there is no single agreed upon definition of the exact position of the corner (Clifford, 1971; Medeiros Filho et al., 1983; Wheelon, 2006). In this study the corner frequency $f_c = v(\lambda L)^{-1/2}$ is marked in Figure A-5; $0.615v/D$ was used for the LAS. Although the position of

the peak moves with crosswind speed, for a uniform crosswind the shape of the frequency spectrum remains the same and the variance of the log amplitude fluctuations do not change.

Figure A-5 illustrates some important spectral characteristics:

- The power spectrum has a plateau for frequencies below the corner frequency (the plateau level is proportional to v^{-1}) and above this decreases with increasing frequency with a slope of -8/3 (MWS) or -12/3 (LAS) (Clifford, 1971). Rao et al. (1999) discuss deviations from the predicted slope that can be attributed to inner scale effects. Since the straightforward Kolmogorov spectrum has been assumed (with no accounting for the Hill bump) this is not covered here. When a modified turbulence spectrum, as given in Frehlich (1992), was used, no significant differences were found, except at very low wind speeds where the spectrum is shifted to low enough frequencies that inner scale effects start to become important.
- A larger crosswind speed moves the corner to higher frequencies and lowers the plateau of the power spectrum to keep the area underneath constant. The whole frequency spectrum is shifted to higher frequencies; the shape and area under the curve remain the same, which means that the wind speed does not affect the amplitude (or intensity) fluctuations observed by the scintillometer. However the level of the plateau and the position of the corner frequency depend on v.
- Some inertial subrange structure is visible in the frequency spectra, such as the ripples at higher frequencies. For the MWS these get closer together with increasing frequency and are a result of the changing eddy sensitivity (Figure A-3, see also Figure A-7b). As a result of the aperture averaging term, the LAS has a reduced contribution at higher frequencies (Figure A-4).

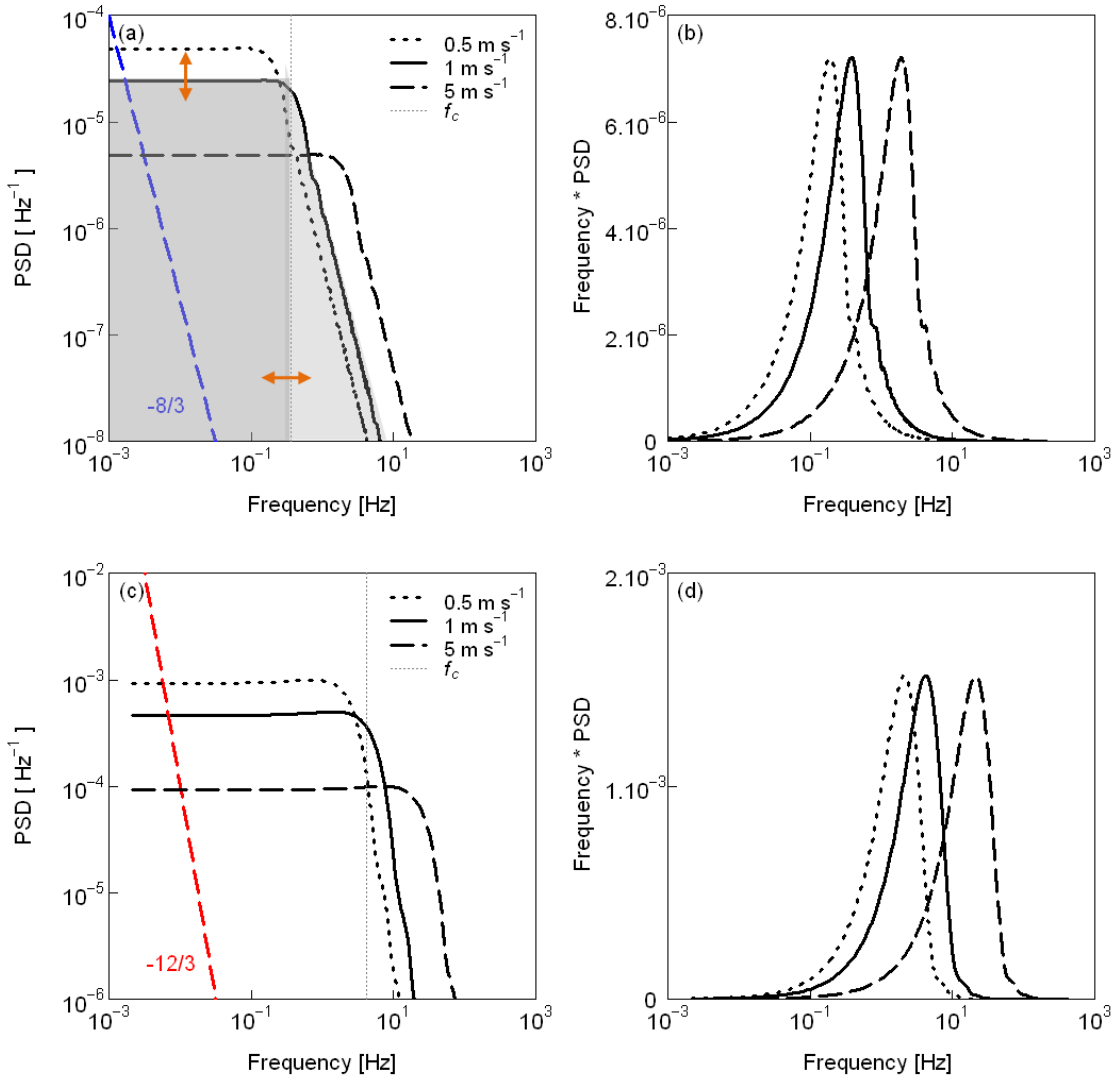

Figure A-5: Power spectra for (a) the MWS and (c) the LAS and the corresponding frequency spectra (b, d) for a range of wind speeds. The positions of the corner frequencies (f_c) have been marked by vertical lines, given by $v(k/L)^{1/2}$ for the MWS and $0.615v/D$ for the LAS for v = 1 m s^{-1}. The LAS spectral shapes are broadly similar to the MWS but the power spectral density falls off as -12/3 at high frequencies. The level of the power spectrum plateau and the position of the corner change with crosswind (arrows in (a)) but the total area underneath the spectrum and the area up to the corner frequency (shaded areas) do not change when the crosswind is uniform.

A4.2. Spatially non-uniform crosswind simulations

Scenario 2.1: Different crosswind for each half of the path

Keeping in mind the findings of the preceding section, the path was split into two halves, with a different crosswind speed in each half (the wind speed was a step function of path length). As shown in Figure A-6, the resulting spectrum (from Equation A-4) is simply the addition of the two individual spectra, for each half of the path, and hence now two corner frequencies are seen. Note that the spectrum differs from the sum of two paths each of length

$L/2$, as the path length dependency of the corner frequency changes the position of the peak. The total area underneath the spectrum is the same as for the uniform crosswind case.

The peaks of the combined spectra do not lie directly beneath the peaks of the uniform crosswind spectra: f_c for each corner is shifted slightly with respect to the individual spectra. It is important to note this effect: even for this relatively simple scenario the reverse retrieval of information from the spectrum becomes much more complex. The corner frequencies of the resultant spectrum correspond to the same sized eddies in each case (the most effective eddy size) but the different wind speed in each half of the path means that the peaks appear at different frequencies due to the square root term in the integrand of Equation A-4. Figure A-6 shows the spectra predicted from theory when the crosswind is non-uniform along the path. Such theoretical plots have not been previously published and spectra of real data have been seen that appear to have similar features (Van Kesteren, 2008).

It should be emphasised that the different spectral shape is most evident at low wind speeds (due to the log scale) and also when there is an appreciable difference between each half of the path (compare 1 and 5 m s^{-1} with 2 and 4 m s^{-1} in Figure A-6). However, even the combination of 2 and 4 m s^{-1} gives the frequency spectrum a distinct shoulder that is not seen for single crosswind speeds. At lower wind speeds, the absolute difference between the speeds for each half of the path can be even smaller and still produce shoulders or distinct peaks as the log scale spreads out.

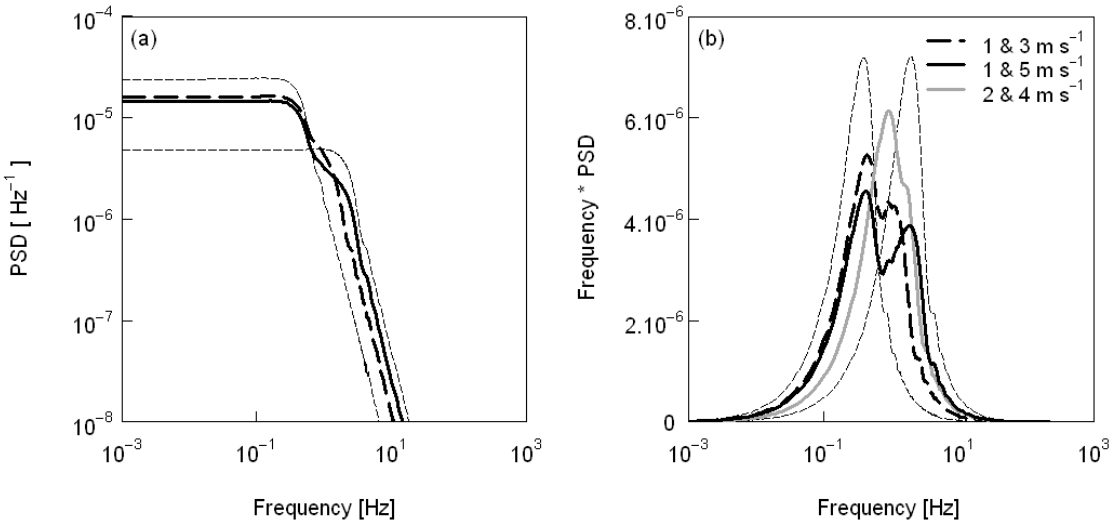

Figure A-6: (a) Power and (b) frequency spectra for a non-uniform crosswind field for the MWS. The legend gives the wind speed for the first and second halves of the path respectively. The thin dashed lines show the spectra for a uniform crosswind for the entire path; 1 m s^{-1} and 5 m s^{-1}. In (b) note that the peaks of the combined spectra do not lie directly beneath the peaks of the uniform crosswind spectra but are displaced slightly.

Scenario 2.2: Middle section of the path

To investigate the relative importance of the middle of the path, a constant wind speed was set for the whole path, except the middle sixth, as this is the most sensitive portion (Figure A-2). The resulting spectra are shown in Figure A-7, with a distinct shoulder produced by the differing crosswind close to the centre of the path. A similar setup could be envisaged in observational data where airflow around a particular body differs from the mean background wind. Examples could include a clump of trees, hill, building or a mast erected close to the centre of the path to make accompanying meteorological measurements.

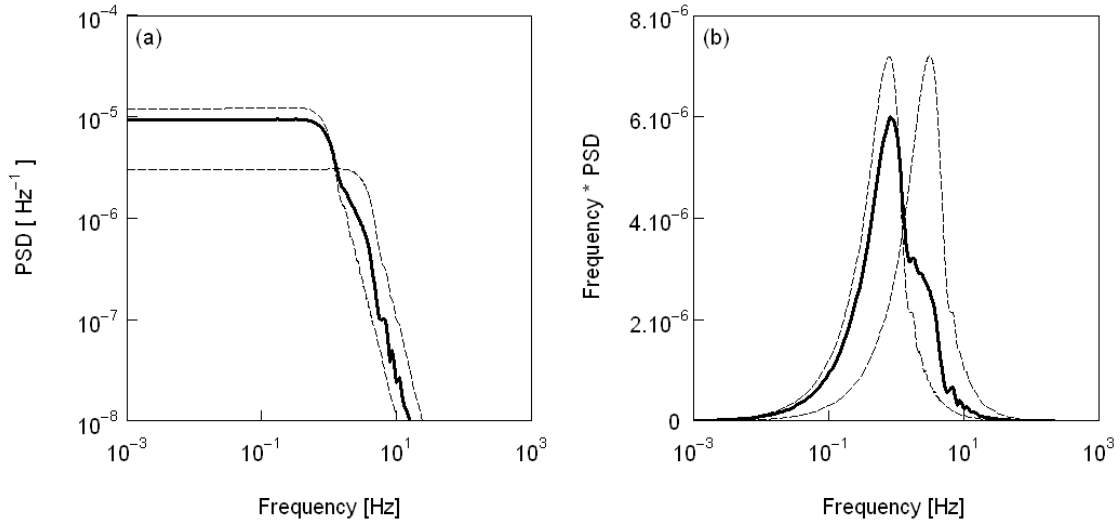

Figure A-7: MWS (a) power and (b) frequency spectra for a constant wind speed of 2 m s^{-1} except for the middle sixth of the path which is at 8 m s^{-1}. The dashed lines show the spectra for a uniform crosswind for the entire path; 2 m s^{-1} and 8 m s^{-1}.

Scenario 2.3: Smoothly varying crosswind

A smoothly varying wind speed reaching a peak in the centre of the path (as might be seen over a gentle valley) was chosen: $v = 5 \sin(\pi x/L)$. Figure A-8 shows the crosswind distribution and the frequency spectrum obtained. The high frequency structural features are clearly enhanced in this case, with the second bump brought out as a distinct peak. In a similar manner to Figure A-6 the eddy sensitivity is unchanged – it is just that the eddies appear to be at a different frequency because of the changing wind speed. This is an important point – that there is no bias in eddy-size sensitivity due to the crosswind. Note that the spectrum is different to that calculated for a constant value of 5 m s^{-1} or the mean wind speed, so that a measurement of the wind speed derived from the position of the peak gives a different value to the wind speed at the centre of the path or the mean wind speed.

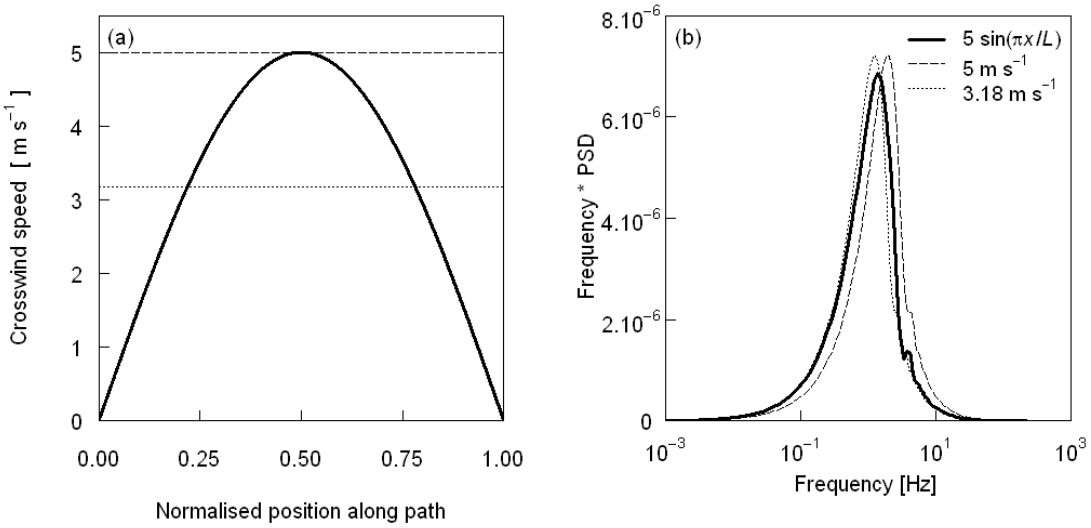

Figure A-8: (a) Crosswind speed distribution and (b) MWS frequency spectrum for $v = 5\ sin(\pi x/L)$. The results for a constant crosswind value of 5 m s^{-1} and 3.18 m s^{-1} (the mean value of $5sin(\pi x/L)$) are also shown.

Scenario 2.4: Linearly varying crosswind

In contrast, a linearly varying crosswind gives a completely smooth spectrum for the MWS, with no subsidiary peaks (Figure A-9). Here the crosswind is such that the superposition of all locations along the path results in the subsidiary peaks being smoothed out. Although not shown here, note that the LAS behaves differently, with the bump in the LAS spectrum being enhanced for linearly varying crosswind speeds.

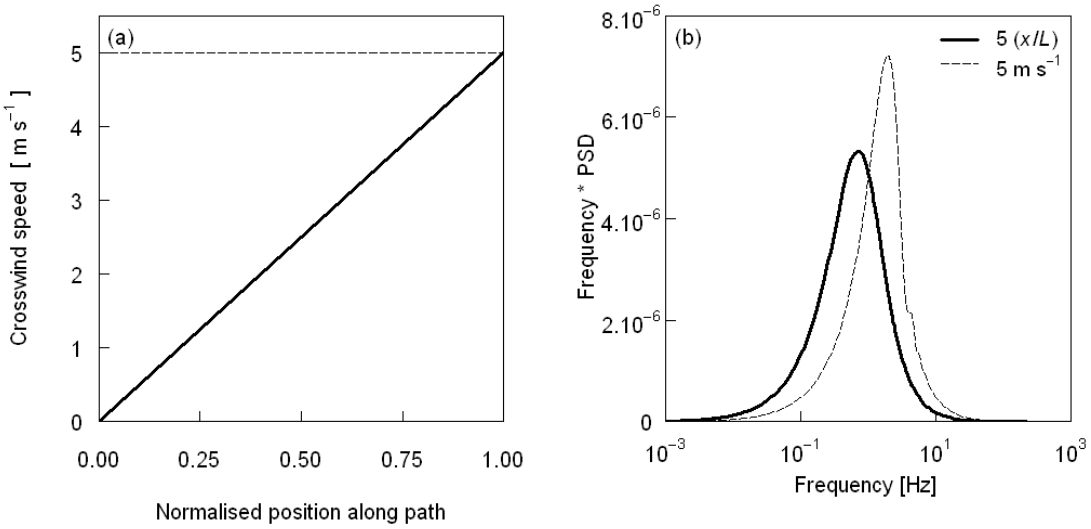

Figure A-9: (a) Crosswind speed distribution and (b) MWS frequency spectrum for $v = 5x/L$ showing the smoothing and spreading of the spectrum. A constant crosswind speed of 5 m s^{-1} is included for comparison.

A4.3. Temporally non-uniform crosswind simulations

Scenario 3.1: Different crosswind for each half of the averaging period

The time period is divided into two equal subintervals, each with a different crosswind. Since the subintervals are equal, the contribution of each to the combined spectrum is the same and the results are as for Figure A-6 where the path has been split spatially into two equally weighted portions (0 - $L/2$ and $L/2$ - L). Two peaks are seen, and the corner frequencies of the combined spectrum differ from those of the respective single crosswind cases.

Scenario 3.2: Crosswind normally distributed

The effects of a crosswind varying randomly in time about a mean value are shown in Figure A-10. These simulations each have the same standard deviation of crosswind speed (1 m s^{-1}) and spectra are shown for a mean crosswind of 1 m s^{-1} and 5 m s^{-1}. Due to the logarithmic scale of the x-axis, fluctuations at lower wind speeds have a more noticeable effect on the spectrum. Compared to the single crosswind case, fluctuations cause the spectra to be smeared out with a less well-defined corner or peak frequency and this is more severe at low wind speeds. The shape of the spectrum varies depending on the particular values of crosswind within the distribution, as illustrated by three curves with a mean crosswind of 1 m s^{-1} – the thick line corresponds to the crosswind variation in Figure A-10a.

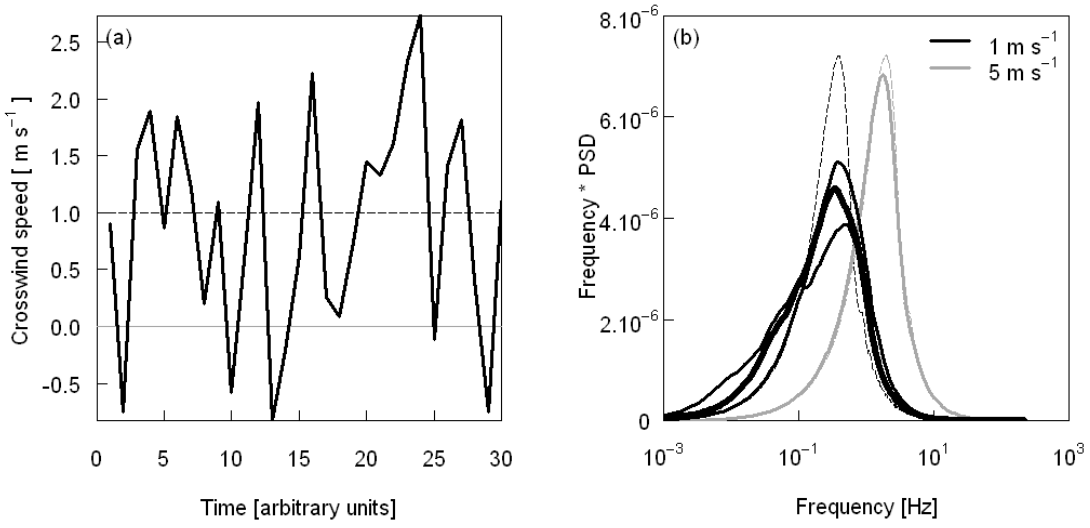

Figure A-10: (a) Random distribution of 30 crosswind values with a mean and standard deviation of 1 m s^{-1} and (b) possible frequency spectra. The thick black line in (b) shows the MWS frequency spectrum corresponding to the crosswind distribution in (a). The frequency spectrum for a mean of 5 m s^{-1} and standard deviation of 1 m s^{-1} is also shown (grey). Dashed lines show the single crosswind case of 1 m s^{-1} (black) and 5 m s^{-1} (grey).

A4.4. Observational data

The spatial (Section A4.2) and temporal (Section A4.3) crosswind variation results are now used to explain observational data. The following scenarios have been selected to illustrate the suitability of assuming a theoretical spectrum based on a single, uniform crosswind under different conditions, and demonstrate that deviations from this 'ideal' shape can be explained by variations in crosswind. In each scenario, one theoretical spectrum is calculated for the mean crosswind (curve 1) and another as the mean of all the ten second crosswind spectra for the 5 min period (curve 2), i.e. temporal variability is used here.

Scenario 4.1: Fairly constant crosswind speed, wind direction perpendicular to path (ideal conditions)

Figure A-11 shows the ideal case, where the crosswind is fairly constant and not too low (mean 1.9 m s^{-1}; standard deviation 0.3 m s^{-1}), the wind direction has an appreciable component perpendicular to the scintillometer beam and there is little difference between the curves 1 and 2. The observed MWS spectra match the theoretical curves well, with a distinct corner frequency corresponding to the mean wind speed. It is thought that the increased contributions above 10 Hz visible in the observed data are due to instrument noise (Van Kesteren, 2008; Evans, 2009).

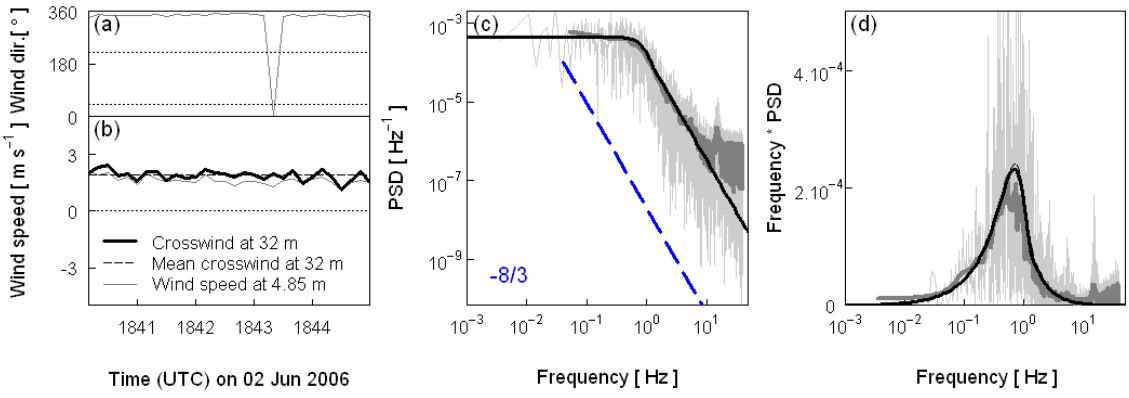

Figure A-11: (a) Measured wind direction (at 4.85 m) and (b) wind speed for a 5 min period, combined and scaled to give the crosswind speed at 32 m. Note that (b) shows the crosswind speed (at 32 m) and wind speed (at 4.85 m) on the same axis. Dotted lines mark the wind directions perpendicular to the beam (a) and show the zero line in (b). Observed (c) power and (d) frequency spectra from the MWS (smoothed and unsmoothed) with the theoretical spectra based on the mean (dashed black line, curve 1) and temporal distribution (solid black line, curve 2) of crosswind. The theoretical spectra have been scaled to the same C_n^2 as the experimental data. In (c) the -8/3 predicted frequency roll-off is shown.

Scenario 4.2: Varying crosswind speed

In Figure A-12, the observed power spectrum is considerably more smeared than the single crosswind model, with no distinct corner. The low-frequency plateau is not clear from the

observational data. Similarly the frequency spectrum is flatter and wider than the single crosswind model, particularly showing an increased contribution to the variance at low frequencies. The theoretical spectra that account for the large variation in crosswind (mean 2.1 m s^{-1}; standard deviation 1.9 m s^{-1}) match the observed spectra well. The single crosswind model does not capture the influence at low frequencies caused by to the close-to-zero crosswind between 0957 and 0958 UTC (Figure A-12a).

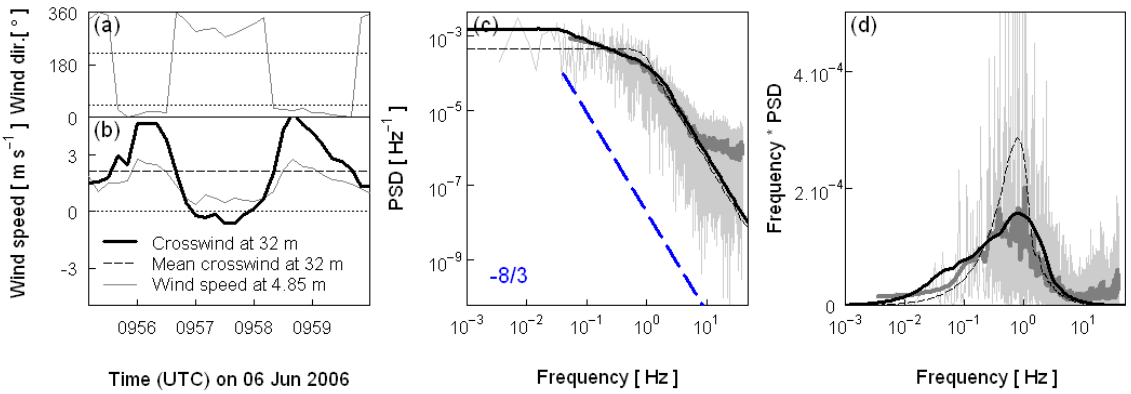

Figure A-12: Same as Figure A-11 but for highly variable crosswind.

Scenario 4.3: Low crosswind speed (wind along path)

Again this smearing of the spectra is seen in Figure A-13, where the wind direction is close to along the path, so that the crosswind component is small and the variations have a clear effect on the spectrum. The power spectrum (Figure A-13c) in particular looks to differ from theory, with a rounded slope in place of the expected -8/3 roll-off. The computed theoretical curve, accounting for the distribution of wind speeds, goes some way to explaining this deviation. This effect would be enhanced for periods of lower C_n^2, when measurements would be closer to the noise floor of the scintillometer, such that fewer decades of inertial subrange roll-off are measured, or the inertial subrange could be obscured completely, as the smearing of the corner runs straight into the noise. Rounding of the corner can be seen in the LITFASS-03 data for both an MWS and LAS (Meijninger et al., 2006). The rounding is more pronounced at lower wind speeds, particularly for the LAS.

With such low crosswinds (mean 0.6 m s^{-1}) the limits of Taylor's hypothesis are approached as the turbulent pattern is blown very slowly through the beam, breaking down as it is transported. Also the theoretical spectra appear at lower frequencies than the observations, which could indicate that perhaps these spectral models should not be extended down to such low wind speeds, without inclusion of other atmospheric effects. Inaccurate scaling between

the wind measurement height and beam height (as this will vary with stability) could also be responsible, as well as limited spatial representativity.

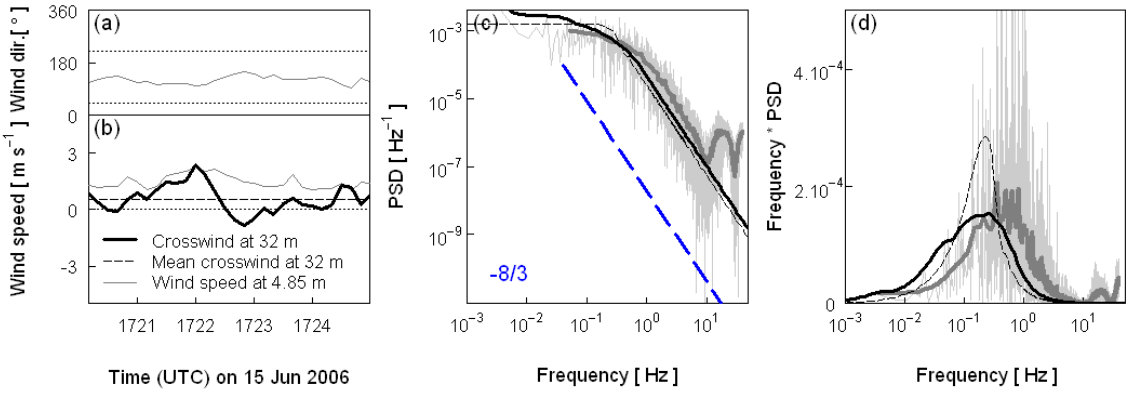

Figure A-13: Same as Figure A-11 but for wind blowing parallel to the path.

Scenario 4.4: Change of wind direction

For the 5 min period in Figure A-14, the wind direction changes from being close to parallel to close to perpendicular to the path, producing a crosswind that increases in magnitude towards the end of the period to become significantly larger than the mean (-4 m s^{-1} compared to a mean of -0.4 m s^{-1}). The theoretical curves accounting for the crosswind distribution match the observed spectra well. The additional point to highlight here is the difference between the corner frequencies of the mean and observed spectrum. A wind speed measurement derived from the corner frequency of the observed scintillometry data would yield a value of 1.3 m s^{-1}, significantly larger than 0.4 m s^{-1}.

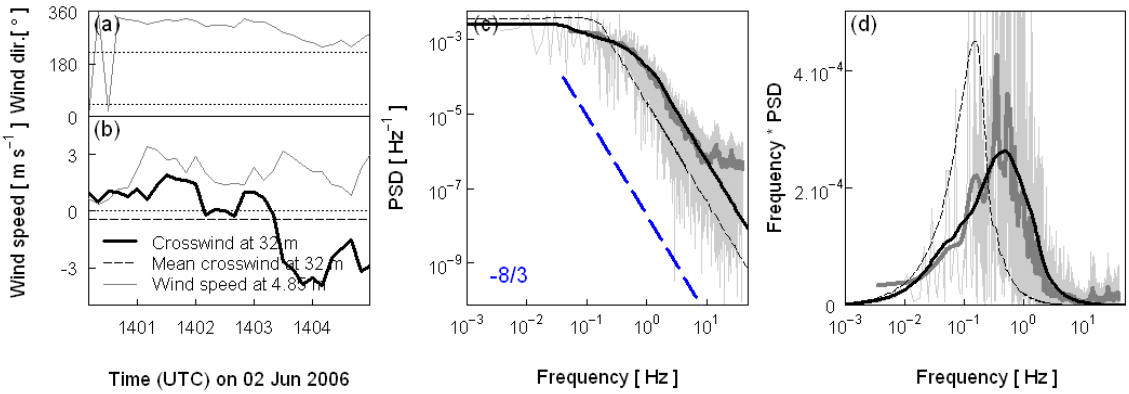

Figure A-14: Same as Figure A-11 but for a change in wind direction from close to parallel to along the path.

A4.5. Varying C_n^2

In the results presented so far C_n^2 has been treated as a constant, in order to look specifically at the effects of wind speed. The scintillometer measures a path-averaged C_n^2, proportional to the area under the spectrum. Spatial or temporal variation of C_n^2 alone does not alter the shape of the spectrum; it is the crosswind variability that gives rise to secondary peaks and smearing. Further simulations showed that if both crosswind and C_n^2 are non-uniform in space and/or time then greater distortions of the spectrum are possible: for each portion of the path or interval in time, the crosswind determines the position along the frequency axis and C_n^2 scales the weighting of that sub-spectrum in the total spectrum.

For scintillometer paths above the blending height and parallel to the land surface, C_n^2 is expected to be uniform along the path. However for slanted paths or over complex terrain, there will be variation along the path length as the beam height changes, since C_n^2 is dependent on measurement height (decreasing as $z^{-4/3}$ for free convection). The literature on the effective height of scintillometer paths deals with this for the estimation of fluxes (Hartogensis et al., 2003; Evans and De Bruin, 2011). The spectral effects become an issue when there is an accompanying variation in wind speed, such that the spectrum gets distorted.

As with wind speed, temporal fluctuations in C_n^2 will occur for all setups. In this study (Section A4.4), the theoretical spectra have been normalized to the observational spectra using the 5 min value of C_n^2. Assuming a constant C_n^2 over the 5 min interval was judged more appropriate than calculating individual C_n^2 values for every ten second subinterval (Cheinet et al., 2011). When studying spectra for longer periods the change in C_n^2 with time could be included.

A5. Discussion

It has been shown that non-uniform crosswinds can be responsible for changes to spectra of scintillometer data, causing them to vary significantly from their 'ideal' shape predicted from theory based on a single crosswind speed. Examples presented demonstrate that we can now largely explain non-ideal observed spectra by including the effect of crosswind variation in the computation of predicted spectra.

The relation between log amplitude fluctuations and C_n^2 measurement has been verified to hold under conditions of varying crosswind. Importantly, the C_n^2 sensitivity remains the same and the scintillometer measures the same size eddies independent of the wind speed distribution. Since the area underneath the spectrum remains unchanged, estimation of C_n^2 based on this method is still valid. Integration of the power spectrum up to the corner

frequency should give a quantity independent of the crosswind and proportional to σ_χ^2, but the problem is identifying the position of the corner (i.e. the upper limit of integration) when the wind speed is non-uniform and the shape of the corner changes. The level of the power spectrum plateau is proportional to v^{-1} and so C_n^2cannot be reliably deduced from the plateau when the wind speed varies. Furthermore, significant variation in crosswind makes locating the low-frequency limit difficult as there may not even be a levelling off. Similarly crosswind estimation based on the position of the peak is no longer reliable. The smoothing of the spectrum under variable conditions makes identification of the corner frequency difficult. Thus derivation of the crosswind speed using scintillometric spectra and the fast Fourier transform technique becomes imprecise and almost impossible when there is a varying crosswind speed. A wind speed distribution must be assumed *a priori*, or taken from independent measurements, in order to replicate the observed spectrum from theory; simply assuming a mean wind speed gives different results. Wang et al. (1981) evaluate the success of several techniques to measure the crosswind from scintillometry – some perform better under non-uniform conditions.

The effects of a non-uniform crosswind are more significant at lower speeds and spatially where there is considerable variation over the middle portion of the path. At very low wind speeds other difficulties become more important in practice: there is evidence that scintillometry does not work well (Poggio et al., 2000; Evans, 2009) since as v becomes very small turbulent decay will no longer remain negligible on the timescale of motion through the beam. Also the shifting of the spectrum to lower frequencies means that inner scale effects can come into play (Rao et al., 1999).

Temporal variability is relevant for all sites, whereas spatial variability is more likely to be a consideration over heterogeneous or complex terrain, or where there is a significant change in beam height. Note that a differing wind speed for a single interval in time will have an identical effect no matter when it occurs, whereas spatial variation is subject to the path weighting, so that it is only variations over the central portion of the path that have a noticeable effect. If C_n^2 varies along with the crosswind even larger changes to the spectrum can be expected, and this can also give increasing weight to the ends of the path.

The difference in path weightings means that spatial variation in crosswind causes more distortion of the spectrum at the very centre of the path for the LAS than the MWS, but since the sensitivity of the LAS is concentrated along a smaller portion of the path (Figure A-2) then it seems reasonable that spatial variation over the path as a whole has less effect for the LAS than the MWS. With temporal variation the effects of non-constant crosswind combine in the same way for the LAS and MWS (sub-spectra are averaged). Theoretically then, the effects

of temporal variation are the same, although the steeper roll-off of the LAS power spectrum means it appears easier to pick out the position of the corner.

Allowances must be made for the non-uniformity of the wind field when drawing comparisons with standard theoretical spectra, as these usually assume a constant wind speed. It is shown here that spectra for non-uniform wind fields exhibit different features, including secondary peaks and shoulders. Also it is easy to see how the smearing of the corner can create the impression of a roll-off different to the -8/3 expected in the inertial subrange (Figure A-13). Perhaps variable crosswind could explain why some experimental spectra do not appear to have the expected frequency decay (e.g. Irvine et al. (2002), Meijninger et al. (2006)). In this paper we have shown theoretical spectra accounting for the crosswind variation are well-matched to our observations.

Without a network of anemometers it is difficult to quantify the spatial variability of wind data. Here, previously unexplained experimental spectra have been largely explained by the temporal variability of crosswind. The agreement between spectra is often very good, especially considering a single wind speed was used to represent the temporal variation along the whole path, and no spatial variation has been included. Future work could include experimental assessment of the spatial effects (see Section A6).

A6. Conclusions

Observed non-ideal spectra have been explained by extending the application of spectral theory to include spatial and temporal crosswind speed variability. This work has shown that measurement of the structure parameter under such conditions is unaffected (as long as the shape of the spectrum, i.e. the level of the plateau, is not relied upon) and that a crosswind measurement based on the position of the peak of the spectrum is not reliable. More exaggerated spectral features may point additionally to varying C_n^2 along the path, which should be considered when interpreting the scintillometer measurements for these times. If spectra cannot be modelled closely by inclusion of varying crosswind alone, this may suggest that C_n^2 varies strongly along the path, or point to other issues, which may be instrumental (noise, vibration) or atmospheric (rain, stability, inner scale effects, absorption) in origin. However if, as has been shown here, atypical spectra are explained by varying crosswind effects, we can now analyse these data with greater confidence and therefore the range of atmospheric conditions studied can be extended.

Further work could include the absorption spectrum model being added to the predicted spectra, since observed spectra contain both scintillation and absorption effects. The limiting cases of very low wind speeds may present a problem to scintillometer measurements, which

could be due to the breakdown of Taylor's hypothesis. In order to evaluate the effects of spatial variability, the wind speed at the beam height must be measured independently at several positions along the path. This could either be achieved with a series of anemometers (as at Boulder, Colorado (Lawrence et al., 1972)) or using a horizontal lidar wind profiling system.

Acknowledgements

We would like to thank Henk De Bruin for valuable scintillometry discussions and the anonymous reviewers for strengthening this paper. This work was funded by the Natural Environment Research Council, UK.

References

Allen, L., Lindberg, F. and Grimmond, C.S.B., 2011. Global to city scale urban anthropogenic heat flux: model and variability. International Journal of Climatology, 31(13): 1990-2005.

Anandakumar, K., 1999. A study on the partition of net radiation into heat fluxes on a dry asphalt surface. Atmospheric Environment, 33: 3911-3918.

Andreas, E.L., 1988. Estimating C_n^2 over snow and sea ice from meteorological data. J. Opt. Soc. Am. A-Opt. Image Sci. Vis., 5(4): 481-495.

Andreas, E.L., 1989. Two-wavelength method of measuring path-averaged turbulent surface heat fluxes. J. Atmos. Ocean. Technol., 6(2): 280-92.

Andreas, E.L., 1990. Three-wavelength method of measuring path-averaged turbulent heat fluxes. J. Atmos. Ocean. Technol., 7(6): 801-14.

Andreas, E.L., 1991. Using scintillation at two wavelengths to measure path-averaged heat fluxes in free-convection. Bound.-Layer Meteor., 54(1-2): 167-182.

Andreas, E.L., Hill, R.J., Gosz, J.R., Moore, D.I., Otto, W.D. and Sarma, A.D., 1998. Statistics of surface-layer turbulence over terrain with metre-scale heterogeneity. Bound.-Layer Meteor., 86(3): 379-408.

Arnfield, A.J., 2003. Two decades of urban climate research: a review of turbulence, exchanges of energy and water, and the urban heat island. International Journal of Climatology, 23(1): 1-26.

Bakan, S., 1978. Note on the eddy correlation method for CO_2 flux measurements. Bound.-Layer Meteor., 14(4): 597-600.

Balogun, A., Adegoke, J., Vezhapparambu, S., Mauder, M., McFadden, J. and Gallo, K., 2009. Surface energy balance measurements above an exurban residential neighbourhood of Kansas City, Missouri. Bound.-Layer Meteor., 133(3): 299-321.

Balogun, A., Tomlin, A., Wood, C., Barlow, J., Belcher, S., Smalley, R., Lingard, J., Arnold, S., Dobre, A., Robins, A., Martin, D. and Shallcross, D., 2010. In-street wind direction variability in the vicinity of a busy intersection in Central London. Bound.-Layer Meteor., 136(3): 489-513.

Bean, B.R. and Dutton, E.J., 1966. Radio meteorology. Washington : U.S. Govt. Print. Office, 435 pp.

Beniston, M., 2004. The 2003 heat wave in Europe: A shape of things to come? An analysis based on Swiss climatological data and model simulations. Geophysical Research Letters, 31(2): L02202.

Bergeron, O. and Strachan, I.B., 2010. Wintertime radiation and energy budget along an urbanization gradient in Montreal, Canada. International Journal of Climatology, 32(1): 137-152.

Bergeron, O. and Strachan, I.B., 2011. CO_2 sources and sinks in urban and suburban areas of a northern mid-latitude city. Atmospheric Environment, 45(8): 1564-1573.

Best, M.J. and Grimmond, C.S.B., 2013. Analysis of the seasonal cycle within the first international urban land-surface model comparison. Boundary Layer Meteorology, 146(3): 421-446.

Beyrich, F., Bange, J., Hartogensis, O., Raasch, S., Braam, M., van Dinther, D., Gräf, D., van Kesteren, B., van den Kroonenberg, A., Maronga, B., Martin, S. and Moene, A., 2012. Towards a Validation of Scintillometer Measurements: The LITFASS-2009 Experiment. Bound.-Layer Meteor., 144(1): 83-112.

Beyrich, F., De Bruin, H.A.R., Meijninger, W.M.L., Schipper, J.W. and Lohse, H., 2002a. Results from one-year continuous operation of a large aperture scintillometer over a heterogeneous land surface. Bound.-Layer Meteor., 105(1): 85-97.

Beyrich, F., Kouznetsov, R.D., Leps, J.P., Lüdi, A., Meijninger, W.M.L. and Weisensee, U., 2005. Structure parameters for temperature and humidity from simultaneous eddy-covariance and scintillometer measurements. Meteorol. Z., 14(5): 641-649.

Beyrich, F. and Mengelkamp, H.T., 2006. Evaporation over a heterogeneous land surface: EVA_GRIPS and the LITFASS-2003 experiment - an overview. Boundary-Layer Meteorology, 121(1): 5-32.

Beyrich, F., Richter, S.H., Weisensee, U., Herzog, H.J., De Bruin, H.A.R. and Meijninger, W.M.L., 2002b. Fluxes over a heterogeneous land surface: Results and perspectives of the LITFASS program. 15th Symposium on Boundary Layers and Turbulence: 653-654.

Blonquist Jr, J.M., Tanner, B.D. and Bugbee, B., 2009. Evaluation of measurement accuracy and comparison of two new and three traditional net radiometers. Agric. For. Meteorol., 149(10): 1709-1721.

Blyth, E.M., Evans, J.G., Finch, J.W., Bantges, R. and Harding, R.J., 2006. Spatial variability of the English agricultural landscape and its effect on evaporation. Agric. For. Meteorol., 138(1-4): 19-28.

Bosveld, F.C., 1999. The KNMI Garderen experiment: micro-meteorological observations 1988–1989, KNMI.

Braam, M., 2008. Determination of the surface sensible heat flux from the structure parameter of temperature at 60 m height during day-time, KNMI.

Braam, M., Bosveld, F. and Moene, A., 2012. On Monin–Obukhov Scaling in and Above the Atmospheric Surface Layer: The Complexities of Elevated Scintillometer Measurements. Bound.-Layer Meteor., 144(2): 157-177.

Brutsaert, W., 1982. Evaporation into the atmosphere. Theory, history, and applications. Kluwer Academic Publishers, 299 pp.

Camuffo, D. and Bernardi, A., 1982. An observational study of heat fluxes and their relationships with net radiation. Bound.-Layer Meteor., 23(3): 359-368.

Chehbouni, A., Watts, C., Kerr, Y.H., Dedieu, G., Rodriguez, J.C., Santiago, F., Cayrol, P., Boulet, G. and Goodrich, D.C., 2000a. Methods to aggregate turbulent fluxes over heterogeneous surfaces: application to SALSA data set in Mexico. Agric. For. Meteorol., 105(1-3): 133-144.

Chehbouni, A., Watts, C., Lagouarde, J.P., Kerr, Y.H., Rodriguez, J.C., Bonnefond, J.M., Santiago, F., Dedieu, G., Goodrich, D.C. and Unkrich, C., 2000b. Estimation of heat and momentum fluxes over complex terrain using a large aperture scintillometer. Agric. For. Meteorol., 105(1-3): 215-226.

Cheinet, S., Beljaars, A., Weiss-Wrana, K. and Hurtaud, Y., 2011. The Use of Weather Forecasts to Characterise Near-Surface Optical Turbulence. Bound.-Layer Meteor., 138(3): 453-473.

Christen, A., van Gorsel, E. and Vogt, R., 2007. Coherent structures in urban roughness sublayer turbulence. International Journal of Climatology, 27(14): 1955-1968.

Christen, A. and Vogt, R., 2004. Energy and radiation balance of a central European city. International Journal of Climatology, 24(11): 1395-1421.

Clifford, S.F., 1971. Temporal-frequency spectra for a spherical wave propagating through atmospheric turbulence. J. Opt. Soc. Am., 61(10): 1285-1292.

Clifford, S.F., Ochs, G.R. and Lawrence, R.S., 1974. Saturation of optical scintillation by strong turbulence. Journal of the Optical Society of America, 64(2): 148-154.

Collier, C.G., 2006. The impact of urban areas on weather. Q. J. R. Meteorol. Soc., 132(614): 1-25.

Coutts, A.M., Beringer, J. and Tapper, N.J., 2007a. Characteristics influencing the variability of urban CO2 fluxes in Melbourne, Australia. Atmospheric Environment, 41(1): 51-62.

Coutts, A.M., Beringer, J. and Tapper, N.J., 2007b. Impact of increasing urban density on local climate: Spatial and temporal variations in the surface energy balance in Melbourne, Australia. Journal of Applied Meteorology and Climatology, 46(4): 477-493.

Crawford, B., Grimmond, C.S.B. and Christen, A., 2011. Five years of carbon dioxide fluxes measurements in a highly vegetated suburban area. Atmospheric Environment, 45(4): 896-905.

De Bruin, H.A.R., Hartogensis, O.K., Allen, R.G. and Kramer, J.W.J.L., 2005. Regional Advection Perturbations in an Irrigated Desert (RAPID) experiment. Theoretical and Applied Climatology, 80(2): 143-152.

De Bruin, H.A.R., Kohsiek, W. and Van den Hurk, B.J.J.M., 1993. A verification of some methods to determine the fluxes of momentum, sensible heat, and water-vapour using standard-deviation and structure parameter of scalar meteorological quantities. Bound.-Layer Meteor., 63(3): 231-257.

Detto, M., Montaldo, N., Albertson, J.D., Mancini, M. and Katul, G., 2006. Soil moisture and vegetation controls on evapotranspiration in a heterogeneous Mediterranean ecosystem on Sardinia, Italy. Water Resour. Res., 42(8): 16.

Eliasson, I., Knez, I., Westerberg, U., Thorsson, S. and Lindberg, F., 2007. Climate and behaviour in a Nordic city. Landscape and Urban Planning, 82: 72-84.

Eliasson, I., Offerle, B., Grimmond, C.S.B. and Lindqvist, S., 2006. Wind fields and turbulence statistics in an urban street canyon. Atmospheric Environment, 40(1): 1-16.

Evans, J.G., 2009. Long-Path Scintillometry over Complex Terrain to Determine Areal-Averaged Sensible and Latent Heat Fluxes. PhD Thesis Thesis, The University of Reading, 181 pp.

Evans, J.G. and De Bruin, H.A.R., 2011. The Effective Height of a Two-Wavelength Scintillometer System. Bound.-Layer Meteor., 141(1): 165-177.

Evans, J.G., McNeil, D.D., Finch, J.F., Murray, T., Harding, R.J. and Verhoef, A., 2010. Evaporation Measurements at Kilometre Scales Determined Using Two-wavelength Scintillometry, BHS Third International Symposium, Role of Hydrology in Managing Consequences of a Changing Global Environment Newcastle University, Newcastle upon Tyne, United Kingdom

Evans, J.G., McNeil, D.D., Finch, J.W., Murray, T., Harding, R.J., Ward, H.C. and Verhoef, A., 2012. Determination of turbulent heat fluxes using a large aperture scintillometer over undulating mixed agricultural terrain. Agric. For. Meteorol., 166-167: 221-233.

Ezzahar, J., Chehbouni, A., Hoedjes, J., Ramier, D., Boulain, N., Boubkraoui, S., Cappelaere, B., Descroix, L., Mougenot, B. and Timouk, F., 2009. Combining scintillometer measurements and an aggregation scheme to estimate area-averaged latent heat flux during the AMMA experiment. Journal of Hydrology, 375(1-2): 217-226.

Ezzahar, J., Chehbouni, A. and Hoedjes, J.C.B., 2007. On the application of scintillometry over heterogeneous grids. Journal of Hydrology, 334(3-4): 493-501.

Feldhake, C.M., Danielson, R.E. and Butler, J.D., 1983. Turfgrass Evapotranspiration. I. Factors Influencing Rate In Urban Environments. Agron. J., 75(5): 824-830.

Flanagan, L.B., Wever, L.A. and Carlson, P.J., 2002. Seasonal and interannual variation in carbon dioxide exchange and carbon balance in a northern temperate grassland. Global Change Biology, 8(7): 599-615.

Foken, T., 2008a. The energy balance closure problem: An overview. Ecol. Appl., 18(6): 1351-1367.

Foken, T., 2008b. Micrometeorology. Springer, 308 pp.

Foken, T. and Wichura, B., 1996. Tools for quality assessment of surface-based flux measurements. Agric. For. Meteorol., 78: 83-105.

Fortuniak, K., Pawlak, W. and Siedlecki, M., 2013. Integral Turbulence Statistics Over a Central European City Centre. Bound.-Layer Meteor., 146(2): 257-276.

Fowler, A.M. and Hennessy, K.J., 1995. Potential impacts of global warming on the frequency and magnitude of heavy precipitation. Natural Hazards, 11(3): 283-303.

Frank, J.M., Massman, W.J. and Ewers, B.E., 2013. Underestimates of sensible heat flux due to vertical velocity measurement errors in non-orthogonal sonic anemometers. Agric. For. Meteorol., 171: 72-81.

Frehlich, R., 1992. Laser scintillation measurements of the temperature spectrum in the atmospheric surface-layer. Journal of the Atmospheric Sciences, 49(16): 1494-1509.

Frey, C.M., Parlow, E., Vogt, R., Harhash, M. and Abdel Wahab, M.M., 2011. Flux measurements in Cairo. Part 1: in situ measurements and their applicability for comparison with satellite data. International Journal of Climatology, 31(2): 218-231.

Garratt, J.R., 1978. Transfer characteristics for a heterogeneous surface of large aerodynamic roughness. Q. J. R. Meteorol. Soc., 104(440): 491-502.

Garratt, J.R., 1992. The Atmospheric Boundary Layer. Cambridge University Press, 316 pp.

Gockede, M., Rebmann, C. and Foken, T., 2003. A combination of quality assessment tools for eddy covariance measurements with footprint modelling for the characterisation of complex sites, 3rd INTAS Workshop on Flux and Concentration Footprints. Elsevier Science Bv, Juupajoki, Finland, pp. 175-188.

Goldbach, A. and Kuttler, W., 2013. Quantification of turbulent heat fluxes for adaptation strategies within urban planning. International Journal of Climatology, 33: 143-159.

Gouvea, M.L. and Grimmond, C.S.B., 2010. Spatially integrated measurements of sensible heat flux using scintillometry, Ninth Symposium on the Urban Environment, Keystone, Colorado.

Green, A.E., Astill, M.S., McAneney, K.J. and Nieveen, J.P., 2001. Path-averaged surface fluxes determined from infrared and microwave scintillometers. Agric. For. Meteorol., 109(3): 233-247.

Green, A.E., Green, S.R., Astill, M.S. and Caspari, H.W., 2000. Estimating latent heat flux from a vineyard using scintillometry. Terrestrial Atmospheric and Oceanic Sciences, 11(2): 525-542.

Green, A.E. and Hayashi, Y., 1998. Use of the scintillometer technique over a rice paddy. Japanese Journal of Agricultural Meteorology, 54(3): 225-231.

Grimmond, C.S.B., 1992. The suburban energy balance: Methodological considerations and results for a mid-latitude west coast city under winter and spring conditions. International Journal of Climatology, 12(5): 481-497.

Grimmond, C.S.B., 2010. Climate of cities, The Routledge Handbook of Urban Ecology. Routledge, pp. 103-119.

Grimmond, C.S.B., Blackett, M., Best, M., Barlow, J., Baik, J.-J., Belcher, S., Bohnenstengel, S.I., Calmet, I., Chen, F., Dandou, A., Fortuniak, K., Gouvea, M.L., Hamdi, R., Hendry, M., Kondo, H., Krayenhoff, S., Lee, S.-H., Loridan, T., Martilli, A., Masson, V., Miao, S., Oleson, K., Pigeon, G., Porson, A., Salamanca, F., Shashua-Bar, L., Steeneveld, G.-J., Tombrou, M., Voogt, J. and Zhang, N., 2010a. The International Urban Energy Balance Models Comparison Project: First results from Phase 1. Journal of Applied Meteorology and Climatology

Grimmond, C.S.B., Cleugh, H.A. and Oke, T.R., 1991. An objective urban heat storage model and its comparison with other schemes. Atmospheric Environment. Part B. Urban Atmosphere, 25(3): 311-326.

Grimmond, C.S.B., King, T.S., Roth, M. and Oke, T.R., 1998. Aerodynamic roughness of urban areas derived from wind observations. Bound.-Layer Meteor., 89(1): 1-24.

Grimmond, C.S.B. and Oke, T.R., 1991. An evapotranspiration-interception model for urban areas. Water Resour. Res., 27(7): 1739-1755.

Grimmond, C.S.B. and Oke, T.R., 1995. Comparison of Heat Fluxes from Summertime Observations in the Suburbs of Four North American Cities. J. Appl. Meteorol., 34(4): 873-889.

Grimmond, C.S.B. and Oke, T.R., 1999a. Aerodynamic properties of urban areas derived from analysis of surface form. J. Appl. Meteorol., 38(9): 1262-1292.

Grimmond, C.S.B. and Oke, T.R., 1999b. Heat storage in urban areas: Local-scale observations and evaluation of a simple model. Journal of Applied Meteorology and Climatology, 38: 922-940.

Grimmond, C.S.B. and Oke, T.R., 1999c. Rates of evaporation in urban areas. Impacts of Urban Growth on Surface and Ground Waters., 259. International Association of Hydrological Sciences Publication.

Grimmond, C.S.B. and Oke, T.R., 2002. Turbulent heat fluxes in urban areas: Observations and a local-scale urban meteorological parameterization scheme (LUMPS). J. Appl. Meteorol., 41(7): 792-810.

Grimmond, C.S.B., Roth, M., Oke, T.R., Au, Y.C., Best, M., Betts, R., Carmichael, G., Cleugh, H., Dabberdt, W., Emmanuel, R., Freitas, E., Fortuniak, K., Hanna, S., Klein, P., Kalkstein, L.S., Liu, C.H., Nickson, A., Pearlmutter, D., Sailor, D. and Voogt, J., 2010b. Climate and More Sustainable Cities: Climate Information for Improved Planning and Management of Cities (Producers/Capabilities Perspective). Procedia Environmental Sciences, 1(0): 247-274.

Grimmond, C.S.B., Salmond, J.A., Oke, T.R., Offerle, B. and Lemonsu, A., 2004. Flux and turbulence measurements at a densely built-up site in Marseille: Heat, mass (water and carbon dioxide), and momentum. J. Geophys. Res.-Atmos., 109: D24101.

Grimmond, C.S.B., Souch, C. and Hubble, M.D., 1996. Influence of tree cover on summertime surface energy balance fluxes, San Gabriel Valley, Los Angeles. Climate Research, 06(1): 45-57.

Guyot, A., Cohard, J.-M., Anquetin, S., Galle, S. and Lloyd, C.R., 2009. Combined analysis of energy and water balances to estimate latent heat flux of a Sudanian small catchment. Journal of Hydrology, 375: 227-240.

Gwilliam, M., Bourne, C., Swain, C. and Pratt, A., 1998. Sustainable Renewal of Suburban Areas. Joseph Rowntree Foundation, York, 87 pp.

Hamilton, I.G., Davies, M., Steadman, P., Stone, A., Ridley, I. and Evans, S., 2009. The significance of the anthropogenic heat emissions of London's buildings: A comparison against captured shortwave solar radiation. Building and Environment, 44(4): 807-817.

Hartogensis, O.K., 2006. Exploring scintillometry in the stable atmospheric surface layer. PhD Thesis Thesis, Wageningen University, 240 pp.

Hartogensis, O.K. and Moene, A.F., 2011. Results of two Optical and Millimetre-wave Scintillometer Systems during LITFASS-2009, 3rd Scintillometer Workshop, Wageningen, The Netherlands.

Hartogensis, O.K., Watts, C.J., Rodriguez, J.C. and De Bruin, H.A.R., 2003. Derivation of an effective height for scintillometers: La Poza experiment in Northwest Mexico. Journal of Hydrometeorology, 4(5): 915-928.

Hasager, C.B. and Jensen, N.O., 1999. Surface-flux aggregation in heterogeneous terrain. Q. J. R. Meteorol. Soc., 125(558): 2075-2102.

Heath, M.A., Walshe, J.D. and Watson, S.J., 2007. Estimating the potential yield of small building-mounted wind turbines. Wind Energy, 10(3): 271-287.

Helfter, C., Famulari, D., Phillips, G.J., Barlow, J.F., Wood, C.R., Grimmond, C.S.B. and Nemitz, E., 2011. Controls of carbon dioxide concentrations and fluxes above central London. Atmospheric Chemistry and Physics, 11(5): 1913-1928.

Hill, R., Ochs, G. and Wilson, J., 1992a. Measuring surface-layer fluxes of heat and momentum using optical scintillation. Boundary-Layer Meteorol., 58(4): 391-408.

Hill, R.J., 1989. Implications of Monin-Obukhov Similarity Theory for Scalar Quantities. Journal of the Atmospheric Sciences, 46(14): 2236-2244.

Hill, R.J., 1997. Algorithms for obtaining atmospheric surface-layer fluxes from scintillation measurements. J. Atmos. Ocean. Technol., 14(3): 456-467.

Hill, R.J., Bohlander, R.A., Clifford, S.F., McMillan, R.W., Priestly, J.T. and Schoenfeld, W.P., 1988. Turbulence-induced millimeter-wave scintillation compared with micrometeorological measurements. IEEE Transactions on Geoscience and Remote Sensing, 26(3): 330-342.

Hill, R.J., Clifford, S.F., Lataitis, R.J. and Sarma, A.D., 1990. Scintillation of millimeter-wave intensity and phase caused by turbulence and precipitation, Atmospheric Propagation in the UV, Visible, IR and MM-Wave Region and Related Systems Aspects (AGARD-CP-454). Agard, Copenhagen, Denmark, pp. 7/1-7/6.

Hill, R.J., Clifford, S.F. and Lawrence, R.S., 1980. Refractive-index and absorption fluctuations in the infrared caused by temperature, humidity, and pressure fluctuations. J. Opt. Soc. Am., 70(10): 1192-1205.

Hill, R.J. and Ochs, G.R., 1978. Fine calibration of large-aperture optical scintillometers and an optical estimate of inner scale of turbulence. Applied Optics, 17(22): 3608-3612.

Hill, R.J., Ochs, G.R. and Wilson, J.J., 1992b. Measuring surface-layer fluxes of heat and momentum using optical scintillation. Bound.-Layer Meteor., 58(4): 391-408.

Hiller, R., McFadden, J. and Kljun, N., 2011. Interpreting CO2 Fluxes Over a Suburban Lawn: The Influence of Traffic Emissions. Boundary-Layer Meteorol., 138(2): 215-230.

Hoedjes, J.C.B., Chehbouni, A., Ezzahar, J., Escadafal, R. and De Bruin, H.A.R., 2007. Comparison of large aperture scintillometer and eddy covariance measurements: Can thermal infrared data be used to capture footprint-induced differences? Journal of Hydrometeorology, 8(2): 144-159.

Hoedjes, J.C.B., Zuurbier, R.M. and Watts, C.J., 2002. Large aperture scintillometer used over a homogeneous irrigated area, partly affected by regional advection. Bound.-Layer Meteor., 105(1): 99-117.

Högström, U., 1988. Non-dimensional wind and temperature profiles in the atmospheric surface layer: A re-evaluation. Bound.-Layer Meteor., 42(1): 55-78.

Home, R., 2009. Land ownership in the United Kingdom: Trends, preferences and future challenges. Land Use Policy, 26, Supplement 1: S103-S108.

Hsieh, C.I., Katul, G. and Chi, T., 2000. An approximate analytical model for footprint estimation of scalar fluxes in thermally stratified atmospheric flows. Adv. Water Resour., 23(7): 765-772.

Ichinose, T., Shimodozono, K. and Hanaki, K., 1999. Impact of anthropogenic heat on urban climate in Tokyo. Atmospheric Environment, 33(24-25): 3897-3909.

Irvine, M., Lagouarde, J.P., Bonnefond, J.M., Grimmond, C.S.B. and Oke, T., 2002. Spectral analyzes of optical scintillation: refraction and absorption components in an urban zone, Preprint Fourth Symposium on the Urban Environment, AMS, Norfolk, Virginia, USA.

Järvi, L., Grimmond, C.S.B. and Christen, A., 2011. The Surface Urban Energy and Water Balance Scheme (SUEWS): Evaluation in Los Angeles and Vancouver. Journal of Hydrology, 411(3-4): 219-237.

Järvi, L., Nordbo, A., Junninen, H., Riikonen, A., Moilanen, J., Nikinmaa, E. and Vesala, T., 2012. Seasonal and annual variation of carbon dioxide surface fluxes in Helsinki, Finland, in 2006-2010. Atmospheric Chemistry and Physics, 12(18): 8475-8489.

Järvi, L., Rannik, U., Mammarella, I., Sogachev, A., Aalto, P.P., Keronen, P., Siivola, E., Kulmala, M. and Vesala, T., 2009. Annual particle flux observations over a heterogeneous urban area. Atmospheric Chemistry and Physics, 9(20): 7847-7856.

Kaimal, J.C. and Finnigan, J.J., 1994. Atmospheric Boundary Layer Flows: Their structure and management. Oxford University Press, 289 pp.

Kanda, M., Moriwaki, R., Roth, M. and Oke, T., 2002. Area-averaged sensible heat flux and a new method to determine zero-plane displacement length over an urban surface using scintillometry. Bound.-Layer Meteor., 105(1): 177-193.

Katul, G.G., Finnigan, J.J., Poggi, D., Leuning, R. and Belcher, S.E., 2006. The influence of hilly terrain on canopy-atmosphere carbon dioxide exchange. Bound.-Layer Meteor., 118(1): 189-216.

Kawai, T. and Kanda, M., 2010. Urban Energy Balance Obtained from the Comprehensive Outdoor Scale Model Experiment. Part I: Basic Features of the Surface Energy Balance. Journal of Applied Meteorology and Climatology, 49(7): 1341-1359.

Kawai, T., Ridwan, M.K. and Kanda, M., 2009. Evaluation of the Simple Urban Energy Balance Model Using Selected Data from 1-yr Flux Observations at Two Cities. Journal of Applied Meteorology and Climatology, 48(4): 693-715.

Keogh, S., Mills, G. and Fealy, R., 2012. The energy budget of the urban surface: two locations in Dublin. Irish Geography, 45(1): 1-23.

Kleissl, J., Gomez, J., Hong, S.H., Hendrickx, J.M.H., Rahn, T. and Defoor, W.L., 2008. Large aperture scintillometer intercomparison study. Bound.-Layer Meteor., 128(1): 133-150.

Kleissl, J., Hartogensis, O. and Gomez, J., 2010. Test of Scintillometer Saturation Correction Methods Using Field Experimental Data. Bound.-Layer Meteor., 137(3): 493-507.

Kleissl, J., Hong, S.H. and Hendrickx, J.M.H., 2009a. New Mexico scintillometer network supporting remote sensing and hydrologic and meteorological models. Bull. Amer. Meteorol. Soc., 90(2): 207-218.

Kleissl, J., Watts, C.J., Rodriguez, J.C., Naif, S. and Vivoni, E.R., 2009b. Scintillometer Intercomparison Study-Continued. Bound.-Layer Meteor., 130(3): 437-443.

Klysik, K., 1996. Spatial and seasonal distribution of anthropogenic heat emissions in Łódź, Poland. Atmospheric Environment, 30(20): 3397-3404.

Kohsiek, W., 1982. Measuring C_T^2, C_Q^2, and C_{TQ} in the Unstable Surface-Layer, and Relations to the Vertical Fluxes of Heat and Moisture. Bound.-Layer Meteor., 24(1): 89-107.

Kohsiek, W. and Bosveld, F.C., 1987. Heat and moisture fluxes and related structure parameters in the unstable surface layer over short vegetations. KNMI-WR-87-7, Koninklijk Nederlands Meteorologisch Instituut.

Kohsiek, W. and Herben, M.H.A.J., 1983. Evaporation derived from optical and radio-wave scintillation. Appl. Opt., 22(17): 2566-2570.

Kohsiek, W., Meijninger, W.M.L., De Bruin, H.A.R. and Beyrich, F., 2006. Saturation of the Large Aperture Scintillometer. Bound.-Layer Meteor., 121(1): 111-126.

Kotthaus, S. and Grimmond, C.S.B., 2012. Identification of micro-scale anthropogenic CO_2, heat and moisture sources - Processing eddy covariance fluxes for a dense urban environment. Atmospheric Environment, 57: 301-316.

Kotthaus, S. and Grimmond, C.S.B., submitted-a. Energy exchange in a dense urban environment - Part I: temporal variability of long-term observations in central London.

Kotthaus, S. and Grimmond, C.S.B., submitted-b. Energy exchange in a dense urban environment – Part II: impact of spatial heterogeneity of the surface

Kustas, W.P., Anderson, M.C., French, A.N. and Vickers, D., 2006. Using a remote sensing field experiment to investigate flux-footprint relations and flux sampling distributions for tower and aircraft-based observations. Adv. Water Resour., 29(2): 355-368.

Lagouarde, J.P., Irvine, M., Bonnefond, J.M., Grimmond, C.S.B., Long, N., Oke, T.R., Salmond, J.A. and Offerle, B., 2006. Monitoring the sensible heat flux over urban areas using large aperture scintillometry: Case study of Marseille city during the ESCOMPTE experiment. Bound.-Layer Meteor., 118(3): 449-476.

Lawrence, R.S., Ochs, G.R. and Clifford, S.F., 1972. Use of scintillations to measure average wind across a light-beam. Applied Optics, 11(2): 239-243.

Lee, X., Massman, W. and Law, B. (Editors), 2004. Handbook of Micrometeorology: A Guide for Surface Flux Measurement and Analysis. Kluwer Academic Publishers, 250 pp.

Lee, X.H. and Massman, W.J., 2011. A Perspective on Thirty Years of the Webb, Pearman and Leuning Density Corrections. Bound.-Layer Meteor., 139(1): 37-59.

Leijnse, H., Uijlenhoet, R. and Stricker, J.N.M., 2007. Hydrometeorological application of a microwave link: 1. Evaporation. Water Resour. Res., 43(4): W04416.

Lemonsu, A., Grimmond, C.S.B. and Masson, V., 2004. Modeling the surface energy balance of the core of an old Mediterranean city: Marseille. J. Appl. Meteorol., 43(2): 312-327.

Leuning, R., van Gorsel, E., Massman, W.J. and Isaac, P.R., 2012. Reflections on the surface energy imbalance problem. Agric. For. Meteorol., 156(0): 65-74.

Li, D., Bou-Zeid, E. and De Bruin, H.A.R., 2011. Monin-Obukhov Similarity Functions for the Structure Parameters of Temperature and Humidity. Bound.-Layer Meteor.

Lindberg, F. and Grimmond, C.S.B., 2011a. The influence of vegetation and building morphology on shadow patterns and mean radiant temperatures in urban areas: model development and evaluation. Theoretical and Applied Climatology, 105(3-4): 311-323.

Lindberg, F. and Grimmond, C.S.B., 2011b. Nature of vegetation and building morphology characteristics across a city: Influence on shadow patterns and mean radiant temperatures in London. Urban Ecosystems, 14(4): 617-634.

Lindberg, F., Holmer, B. and Thorsson, S., 2008. SOLWEIG 1.0 – Modelling spatial variations of 3D radiant fluxes and mean radiant temperature in complex urban settings. International Journal of Biometeorology, 52(7): 697-713.

Liu, H.Z., Feng, J.W., Järvi, L. and Vesala, T., 2012. Eddy covariance measurements of CO2 and energy fluxes in the city of Beijing. Atmos. Chem. Phys. Discuss., 12(3): 7677-7704.

Liu, S.M., Xu, Z.W., Zhu, Z.L., Jia, Z.Z. and Zhu, M.J., 2013. Measurements of evapotranspiration from eddy-covariance systems and large aperture scintillometers in the Hai River Basin, China. Journal of Hydrology, 487: 24-38.

Loridan, T. and Grimmond, C.S.B., 2012. Characterization of Energy Flux Partitioning in Urban Environments: Links with Surface Seasonal Properties. Journal of Applied Meteorology and Climatology, 51(2): 219-241.

Lüdi, A., Beyrich, F. and Matzler, C., 2005. Determination of the turbulent temperature-humidity correlation from scintillometric measurements. Bound.-Layer Meteor., 117(3): 525-550.

Masson, V., Gomes, L., Pigeon, G., Liousse, C., Pont, V., Lagouarde, J.P., Voogt, J., Salmond, J., Oke, T.R., Hidalgo, J., Legain, D., Garrouste, O., Lac, C., Connan, O., Briottet, X., Lachérade, S. and Tulet, P., 2008. The Canopy and Aerosol Particles Interactions in TOulouse Urban Layer (CAPITOUL) experiment. Meteorology and Atmospheric Physics, 102(3-4): 135-157.

Mauder, M., Foken, T., Clement, R., Elbers, J.A., Eugster, W., Grunwald, T., Heusinkveld, B. and Kolle, O., 2008. Quality control of CarboEurope flux data - Part 2: Inter-comparison of eddy-covariance software. Biogeosciences, 5(2): 451-462.

Mauder, M., Liebethal, C., Göckede, M., Leps, J.-P., Beyrich, F. and Foken, T., 2006. Processing and quality control of flux data during LITFASS-2003. Bound.-Layer Meteor., 121(1): 67-88.

Mayer, H., 1999. Air pollution in cities. Atmospheric Environment, 33(24â€“25): 4029-4037.

McPherson, E.G. and Simpson, J.R., 2003. Potential energy savings in buildings by an urban tree planting programme in California. Urban Forestry & Urban Greening, 2(2): 73-86.

Medeiros Filho, F., Jayasuriya, D., Cole, R. and Helmis, C., 1983. Spectral density of millimeter wave amplitude scintillations in an absorption region. Antennas and Propagation, IEEE Transactions on, 31(4): 672-676.

Meehl, G.A. and Tebaldi, C., 2004. More Intense, More Frequent, and Longer Lasting Heat Waves in the 21st Century. Science, 305(5686): 994-997.

Meijninger, W.M.L., 2003. Surface fluxes over natural landscapes using scintillometry. PhD Thesis, Wageningen University, 170 pp.

Meijninger, W.M.L., Beyrich, F., Lüdi, A., Kohsiek, W. and De Bruin, H.A.R., 2006. Scintillometer-based turbulent fluxes of sensible and latent heat over a heterogeneous land surface - A contribution to LITFASS-2003. Bound.-Layer Meteor., 121(1): 89-110.

Meijninger, W.M.L. and De Bruin, H.A.R., 2000. The sensible heat fluxes over irrigated areas in western Turkey determined with a large aperture scintillometer. Journal of Hydrology, 229(1-2): 42-49.

Meijninger, W.M.L., Green, A.E., Hartogensis, O.K., Kohsiek, W., Hoedjes, J.C.B., Zuurbier, R.M. and De Bruin, H.A.R., 2002a. Determination of area-averaged water vapour fluxes with large aperture and radio wave scintillometers over a heterogeneous surface - Flevoland field experiment. Bound.-Layer Meteor., 105(1): 63-83.

Meijninger, W.M.L., Hartogensis, O.K., Kohsiek, W., Hoedjes, J.C.B., Zuurbier, R.M. and De Bruin, H.A.R., 2002b. Determination of area-averaged sensible heat fluxes with a large aperture scintillometer over a heterogeneous surface - Flevoland field experiment. Bound.-Layer Meteor., 105(1): 37-62.

Mestayer, P., Bagga, I., Calmet, I., Fontanilles, G., Gaudin, D., Lee, J.H., Piquet, T., Rosant, J.-M., Chancibault, K., Lebouc, L., Letellier, L., Mosini, M.-L., Rodriguez, F., Rouaud, J.-M., Sabre, M., Tétard, Y., Brut, A., Selves, J.-L., Solignac, P.-A., Brunet, Y., Dayau, S., Irvine, M., Lagouarde, J.-P., Kassouk, Z., Launeau, P., Connan, O., Defenouillère, P., Goriaux, M., Hébert, D., Letellier, B., Mario, D., Najjar, G., Nerry, F., Quentin, C., Biron, R., Cohard, J.-M., Galvez, J. and Klein, P., 2011. The FluxSAP 2010 hydroclimatological experimental campaign over an heterogeneous urban area, 11th EMS Annual Meeting, Berlin, Germany.

Mitchell, V.G., Cleugh, H.A., Grimmond, C.S.B. and Xu, J., 2008. Linking urban water balance and energy balance models to analyse urban design options. Hydrological Processes, 22(16): 2891-2900.

Moene, A. and Schüttemeyer, D., 2008. The Effect of Surface Heterogeneity on the Temperature–Humidity Correlation and the Relative Transport Efficiency. Bound.-Layer Meteor., 129(1): 99-113.

Moene, A.F., 2003. Effects of water vapour on the structure parameter of the refractive index for near-infrared radiation. Bound.-Layer Meteor., 107(3): 635-653.

Moene, A.F., Meijninger, W.M.L., Hartogensis, O.K., Kohsiek, W. and De Bruin, H.A.R., 2004. A review of the relationships describing the signal of a Large Aperture Scintillometer, Internal report 2004/2, Meteorology and Air Quality Group, Wageningen University, Wageningen, The Netherlands.

Moncrieff, J.B., Massheder, J.M., de Bruin, H., Elbers, J., Friborg, T., Heusinkveld, B., Kabat, P., Scott, S., Soegaard, H. and Verhoef, A., 1997. A system to measure surface fluxes of momentum, sensible heat, water vapour and carbon dioxide. Journal of Hydrology, 188-199: 589-611.

Monin, A.S. and Yaglom, A.M., 1971. Statistical Fluid Mechanics: Mechanics of Turbulence, 1. The MIT Press, Cambridge, Massachusetts, 782 pp.

Monteith, J.L., 1965. Evaporation and environment. Symposia of the Society for Experimental Biology, 19: 205-224.

Moriwaki, R. and Kanda, M., 2004. Seasonal and diurnal fluxes of radiation, heat, water vapor, and carbon dioxide over a suburban area. J. Appl. Meteorol., 43(11): 1700-1710.

Moriwaki, R., Kanda, M., Senoo, H., Hagishima, A. and Kinouchi, T., 2008. Anthropogenic water vapor emissions in Tokyo. Water Resour. Res., 44(11): W11424.

Nemitz, E., Hargreaves, K.J., McDonald, A.G., Dorsey, J.R. and Fowler, D., 2002. Meteorological measurements of the urban heat budget and CO2 emissions on a city scale. Environ. Sci. Technol., 36(14): 3139-3146.

Newton, T., Oke, T.R., Grimmond, C.S.B. and Roth, M., 2007. The suburban energy balance in Miami, Florida. Geografiska Annaler: Series A, Physical Geography, 89(4): 331-347.

Nieveen, J.P., Green, A.E. and Kohsiek, W., 1998. Using a large-aperture scintillometer to measure absorption and refractive index fluctuations. Bound.-Layer Meteor., 87(1): 101-116.

Nordbo, A., Järvi, L., Haapanala, S., Moilanen, J. and Vesala, T., 2013. Intra-City Variation in Urban Morphology and Turbulence Structure in Helsinki, Finland. Bound.-Layer Meteor., 146(3): 469-496.

Offerle, B., Grimmond, C.S.B. and Fortuniak, K., 2005a. Heat storage and anthropogenic heat flux in relation to the energy balance of a central European city centre. International Journal of Climatology, 25(10): 1405-1419.

Offerle, B., Grimmond, C.S.B., Fortuniak, K. and Pawlak, W., 2006. Intraurban differences of surface energy fluxes in a central European city. Journal of Applied Meteorology and Climatology, 45(1): 125-136.

Offerle, B., Jonsson, P., Eliasson, I. and Grimmond, C.S.B., 2005b. Urban Modification of the Surface Energy Balance in the West African Sahel: Ouagadougou, Burkina Faso. Journal of Climate, 18(19): 3983-3995.

Oke, T.R., 1979. Advectively-assisted evapotranspiration from irrigated urban vegetation. Boundary Layer Meteorology, 17: 167-173.

Oke, T.R., 1982. The energetic basis of the urban heat-island. Q. J. R. Meteorol. Soc., 108(455): 1-24.

Oke, T.R., 1987. Boundary Layer Climates. Routledge, Taylor and Francis Group, 435 pp.

Oke, T.R. and Cleugh, H.A., 1987. Urban heat storage derived as energy balance residuals. Bound.-Layer Meteor., 39(3): 233-245.

Oke, T.R., Spronken-Smith, R.A., Jáuregui, E. and Grimmond, C.S.B., 1999. The energy balance of central Mexico City during the dry season. Atmospheric Environment, 33(24-25): 3919-3930.

Otto, W.D., Hill, R.J., Sarma, A.D., Wilson, J.J., Andreas, E.L., Gosz, J.R. and Moore, D.I., 1996. Results of the Millimeter-Wave Instrument Operated at Sevilleta, New Mexico. NOAA-TM-ERL-ETL-262, National Oceanic and Atmospheric Administration, Boulder, Colorado.

Owens, J.C., 1967. Optical refractive index of air: dependence on pressure, temperature and composition. Applied Optics, 6: 51-59.

Papaioannou, G., Papanikolaou, N. and Retalis, D., 1993. Relationships of photosynthetically active radiation and shortwave irradiance. Theoretical and Applied Climatology, 48(1): 23-27.

Pasquill, F., 1974. Atmospheric Diffusion. Wiley, 429 pp.

Pauscher, L., 2010. Scintillometer Measurements above the Urban Area of London, University of Bayreuth, 104 pp.

Pawlak, W., Fortuniak, K. and Siedlecki, M., 2010. Carbon dioxide flux in the centre of Łódź, Poland—analysis of a 2-year eddy covariance measurement data set. International Journal of Climatology, 31(2): 232-243.

Perpiñán, O., 2012. solaR: Solar Radiation and Photovoltaic Systems with R. Journal of Statistical Software, 50(9): 1-32.

Peters, E.B., Hiller, R.V. and McFadden, J.P., 2011. Seasonal contributions of vegetation types to suburban evapotranspiration. J. Geophys. Res., 116(G1): G01003.

Poggio, L.P., Furger, M., Prevot, A.S.H., Graber, W.K. and Andreas, E.L., 2000. Scintillometer wind measurements over complex terrain. J. Atmos. Ocean. Technol., 17(1): 17-26.

Potvin, G., Dion, D. and Forand, J.L., 2005. Wind effects on scintillation decorrelation times. Optical Engineering, 44(1): 1-12.

Priestley, C.H.B. and Taylor, R.J., 1972. On the Assessment of Surface Heat Flux and Evaporation Using Large-Scale Parameters. Monthly Weather Review, 100(2): 81-92.

Ramier, D., Berthier, E. and Andrieu, H., 2004. An urban lysimeter to assess runoff losses on asphalt concrete plates. Physics and Chemistry of the Earth, Parts A/B/C, 29(11–12): 839-847.

Rao, R.Z., Wang, S.P., Liu, X.C. and Gong, Z.B., 1999. Turbulence spectrum effect on wave temporal-frequency spectra for light propagating through the atmosphere. J. Opt. Soc. Am. A-Opt. Image Sci. Vis., 16(11): 2755-2762.

Reid, K.H. and Steyn, D.G., 1997. Diurnal variations of boundary-layer carbon dioxide in a coastal cityâ€"Observations and comparison with model results. Atmospheric Environment, 31(18): 3101-3114.

Richards, K., 2004. Observation and simulation of dew in rural and urban environments. Progress in Physical Geography, 28(1): 76-94.

Richards, K., 2005. Urban and rural dewfall, surface moisture, and associated canopy-level air temperature and humidity measurements for vancouver, canada. Bound.-Layer Meteor., 114(1): 143-163.

Roberts, S.M., Oke, T.R., Grimmond, C.S.B. and Voogt, J.A., 2006. Comparison of Four Methods to Estimate Urban Heat Storage. Journal of Applied Meteorology and Climatology, 45(12): 1766-1781.

Rodriguez, F., Andrieu, H. and Creutin, J.-D., 2003. Surface runoff in urban catchments: morphological identification of unit hydrographs from urban databanks. Journal of Hydrology, 283(1-4): 146-168.

Rotach, M.W., Vogt, R., Bernhofer, C., Batchvarova, E., Christen, A., Clappier, A., Feddersen, B., Gryning, S.E., Martucci, G., Mayer, H., Mitev, V., Oke, T.R., Parlow, E., Richner, H., Roth, M., Roulet, Y.A., Ruffieux, D., Salmond, J.A., Schatzmann, M. and Voogt, J.A., 2005. BUBBLE - an Urban Boundary Layer Meteorology Project. Theoretical and Applied Climatology, 81(3-4): 231-261.

Roth, M., 1993. Turbulent transfer relationships over an urban surface. II: Integral statistics. Q. J. R. Meteorol. Soc., 119(513): 1105-1120.

Roth, M., 2000. Review of atmospheric turbulence over cities. Q. J. R. Meteorol. Soc., 126(564): 941-990.

Roth, M. and Oke, T.R., 1995. Relative efficiencies of turbulent transfer of heat, mass, and momentum over a patchy urban surface. Journal of the Atmospheric Sciences, 52(11): 1863-1874.

Roth, M., Salmond, J.A. and Satyanarayana, A.N.V., 2006. Methodological considerations regarding the measurement of turbulent fluxes in the urban roughness sublayer: The role of scintillometery. Bound.-Layer Meteor., 121(2): 351-375.

Sailor, D.J., 2011. A review of methods for estimating anthropogenic heat and moisture emissions in the urban environment. International Journal of Climatology, 31(2): 189-199.

Sailor, D.J. and Lu, L., 2004. A top-down methodology for developing diurnal and seasonal anthropogenic heating profiles for urban areas. Atmospheric Environment, 38(17): 2737-2748.

Samain, B., Defloor, W. and Pauwels, V.R.N., 2012. Continuous Time Series of Catchment-Averaged Sensible Heat Flux from a Large Aperture Scintillometer: Efficient Estimation of Stability Conditions and Importance of Fluxes under Stable Conditions. Journal of Hydrometeorology, 13(2): 423-442.

Samain, B., Ferket, B.V.A., Defloor, W. and Pauwels, V.R.N., 2011a. Estimation of catchment averaged sensible heat fluxes using a large aperture scintillometer. Water Resour. Res., 47(5): W05536.

Samain, B., Simons, G.W.H., Voogt, M.P., Defloor, W., Bink, N.-J. and Pauwels, V.R.N., 2011b. Consistency between hydrological model, large aperture scintillometer and remote sensing based evapotranspiration estimates for a heterogeneous catchment. Hydrology and Earth System Sciences, 8(6): 10863-10894.

Schmid, H.P., 1994. Source areas for scalars and scalar fluxes. Bound.-Layer Meteor., 67(3): 293-318.

Schmid, H.P., Cleugh, H.A., Grimmond, C.S.B. and Oke, T.R., 1991. Spatial variability of energy fluxes in suburban terrain. Bound.-Layer Meteor., 54(3): 249-276.

Schmid, H.P., Grimmond, C.S.B., Cropley, F., Offerle, B. and Su, H.-B., 2000. Measurements of CO2 and energy fluxes over a mixed hardwood forest in the mid-western United States. Agric. For. Meteorol., 103(4): 357-374.

Schotanus, P., Nieuwstadt, F.T.M. and Bruin, H.A.R., 1983. Temperature measurement with a sonic anemometer and its application to heat and moisture fluxes. Bound.-Layer Meteor., 26(1): 81-93.

Schreider, S.Y., Smith, D.I. and Jakeman, A.J., 2000. Climate Change Impacts on Urban Flooding. Climatic Change, 47(1): 91-115.

Scintec, 2009. Scintec Boundary Layer Scintillometer Hardware Manual, Rottenburg, Germany, pp. 67.

Slatyer, R.O. and McIlroy, I.C., 1961. Practical microclimatology. CSIRO, Melbourne, 310 pp.

Solignac, P.A., Brut, A., Selves, J.L., Beteille, J.P., Gastellu-Etchegorry, J.P., Keravec, P., Beziat, P. and Ceschia, E., 2009. Uncertainty analysis of computational methods for deriving sensible heat flux values from scintillometer measurements. Atmospheric Measurement Techniques, 2(2): 741-753.

Song, T. and Wang, Y., 2012. Carbon dioxide fluxes from an urban area in Beijing. Atmospheric Research, 106: 139-149.

Sparks, N. and Toumi, R., 2010. Remote sampling of a CO_2 point source in an urban setting. Atmospheric Environment, 44(39): 5287-5294.

Spronken-Smith, R.A. and Oke, T.R., 1998. The thermal regime of urban parks in two cities with different summer climates. International Journal of Remote Sensing, 19(11): 2085-2104.

Spronken-Smith, R.A., Oke, T.R. and Lowry, W.P., 2000. Advection and the surface energy balance across an irrigated urban park. International Journal of Climatology, 20(9): 1033-1047.

Steeneveld, G.J., Tolk, L.F., Moene, A.F., Hartogensis, O.K., Peters, W. and Holtslag, A.A.M., 2011. Confronting the WRF and RAMS mesoscale models with innovative observations

in the Netherlands: Evaluating the boundary layer heat budget. Journal of Geophysical Research: Atmospheres, 116(D23): D23114.

Stull, R.B., 1988. An Introduction to Boundary Layer Meteorology. Kluwer Academic Publishers, 666 pp.

Suarez, P., Anderson, W., Mahal, V. and Lakshmanan, T.R., 2005. Impacts of flooding and climate change on urban transportation: A systemwide performance assessment of the Boston Metro Area. Transportation Research Part D: Transport and Environment, 10(3): 231-244.

Tatarski, V.I., 1961. Wave Propagation in a Turbulent Medium. McGraw-Hill, New York, 285 pp.

Theeuwes, N.E., Solcerová, A. and Steeneveld, G.J., 2013. Modeling the influence of open water surfaces on the summertime temperature and thermal comfort in the city. Journal of Geophysical Research: Atmospheres.

Thiermann, V. and Grassl, H., 1992. The measurement of turbulent surface-layer fluxes by use of bichromatic scintillation. Bound.-Layer Meteor., 58(4): 367-389.

Thomas, M.V., Malhi, Y., Fenn, K.M., Fisher, J.B., Morecroft, M.D., Lloyd, C.R., Taylor, M.E. and McNeil, D.D., 2011. Carbon dioxide fluxes over an ancient broadleaved deciduous woodland in southern England. Biogeosciences, 8(6): 1595-1613.

United Nations, 2011. Annual Report 2010.

van Dinther, D.l., Hartogensis, O.K. and Moene, A.F., 2013. Crosswinds from a Single-Aperture Scintillometer Using Spectral Techniques. J. Atmos. Ocean. Technol., 30(1): 3-21.

Van Kesteren, A.J.H., 2008. Sensible and Latent Heat Fluxes with Optical and Millimetre Wave Scintillometers: A Theory Review and the Chilbolton Experiment. Masters Thesis, Wageningen University, Wageningen, 99 pp.

Van Kesteren, B. and Hartogensis, O., 2011. Analysis of the Systematic Errors Found in the Kipp & Zonen Large-Aperture Scintillometer. Bound.-Layer Meteor., 138(3): 493-509.

Van Kesteren, B., Hartogensis, O.K., van Dinther, D., Moene, A.F. and De Bruin, H.A.R., 2012. Measuring H2O and CO2 fluxes at field scales with scintillometry: Part I – Introduction and validation of four methods. Agric. For. Meteorol.

van Ulden, A.P. and Holtslag, A.A.M., 1985. Estimation of atmospheric boundary layer parameters for diffusion applications. Journal of Climate and Applied Meteorology, 24(11): 1196-1207.

Vesala, T., Järvi, L., Launiainen, S., Sogachev, A., Rannik, Ü., Mammarella, I., Siivola, E., Keronen, P., Rinne, J., Riikonen, A.N.U. and Nikinmaa, E., 2008. Surface–atmosphere interactions over complex urban terrain in Helsinki, Finland. Tellus B, 60(2): 188-199.

Von Randow, C., Kruijt, B., Holtslag, A.A.M. and de Oliveira, M.B.L., 2008. Exploring eddy-covariance and large-aperture scintillometer measurements in an Amazonian rain forest. Agric. For. Meteorol., 148(4): 680-690.

Wang, T.I., Ochs, G.R. and Clifford, S.F., 1978. A saturation-resistant optical scintillometer to measure C_n^2. J. Opt. Soc. Am., 68(3): 334-338.

Wang, T.I., Ochs, G.R. and Lawrence, R.S., 1981. Wind measurements by the temporal cross-correlation of the optical scintillations. Applied Optics, 20(23): 4073-4081.

Ward, H.C., Evans, J.G. and Grimmond, C.S.B., 2011. Effects of Non-Uniform Crosswind Fields on Scintillometry Measurements. Bound.-Layer Meteor., 141(1): 143-163.

Ward, H.C., Evans, J.G. and Grimmond, C.S.B., 2013a. Multi-season eddy covariance observations of energy, water and carbon fluxes over a suburban area in Swindon, UK. Atmos. Chem. Phys., 13(9): 4645-4666.

Ward, H.C., Evans, J.G., Hartogensis, O.K., Moene, A.F., De Bruin, H.A.R. and Grimmond, C.S.B., 2013b. A critical revision of the estimation of the latent heat flux from two-wavelength scintillometry. Q. J. R. Meteorol. Soc.

Webb, E.K., Pearman, G.I. and Leuning, R., 1980. Correction of flux measurements for density effects due to heat and water-vapor transfer. Q. J. R. Meteorol. Soc., 106(447): 85-100.

Weber, S. and Kordowski, K., 2010. Comparison of atmospheric turbulence characteristics and turbulent fluxes from two urban sites in Essen, Germany. Theoretical and Applied Climatology, 102(1): 61-74.

Wesely, M.L., 1976. Combined effect of temperature and humidity fluctuations on refractive-index. J. Appl. Meteorol., 15(1): 43-49.

Wheelon, A.D., 2006. Electromagnetic scintillation: weak scattering, 2. Cambridge University Press, Cambridge, 446 pp.

Wilson, K., Goldstein, A., Falge, E., Aubinet, M., Baldocchi, D., Berbigier, P., Bernhofer, C., Ceulemans, R., Dolman, H., Field, C., Grelle, A., Ibrom, A., Law, B.E., Kowalski, A., Meyers, T., Moncrieff, J., Monson, R., Oechel, W., Tenhunen, J., Valentini, R. and Verma, S., 2002. Energy balance closure at FLUXNET sites. Agric. For. Meteorol., 113: 223-243.

Wood, C.R. and Järvi, L., 2012. An overview of urban climate observations in Helsinki, Magazine of the Finnish Air Pollution Prevention Society, pp. 30-33.

Wood, C.R., Pauscher, L., Ward, H.C., Kotthaus, S., Barlow, J.F., Gouvea, M., Lane, S.E. and Grimmond, C.S.B., 2013. Wind observations above an urban river using a new lidar technique, scintillometry and anemometry. Science of The Total Environment, 442(0): 527-533.

Wyngaard, J.C., 1973. On surface-layer turbulence. In: D.A. Haugen (Editor), Workshop on micrometeorology. American Meteorological Society, pp. 101-149.

Wyngaard, J.C. and Clifford, S.F., 1978. Estimating momentum, heat and moisture fluxes from structure parameters. Journal of the Atmospheric Sciences, 35(7): 1204-1211.

Wyngaard, J.C., Izumi, Y. and Collins, J.S.A., 1971. Behavior of the Refractive-Index-Structure Parameter near the Ground. J. Opt. Soc. Am., 61(12): 1646-1650.

Xiao, J., Davis, K.J., Urban, N.M., Keller, K. and Saliendra, N.Z., 2011. Upscaling carbon fluxes from towers to the regional scale: Influence of parameter variability and land cover representation on regional flux estimates. Journal of Geophysical Research: Biogeosciences, 116(G3): G00J06.

Xiao, Q., McPherson, E.G., Simpson, J.R. and Ustin, S.L., 2007. Hydrologic processes at the urban residential scale. Hydrological Processes, 21(16): 2174-2188.

Xie, X.M., Huang, Z. and Wang, J.S., 2005. Impact of building configuration on air quality in street canyon. Atmospheric Environment, 39(25): 4519-4530.

Xu, C.Y. and Chen, D., 2005. Comparison of seven models for estimation of evapotranspiration and groundwater recharge using lysimeter measurement data in Germany. Hydrological Processes, 19(18): 3717-3734.

Zhang, X., Friedl, M.A., Schaaf, C.B., Strahler, A.H. and Schneider, A., 2004. The footprint of urban climates on vegetation phenology. Geophys. Res. Lett., 31(12): L12209.

Zieliński, M., Fortuniak, K. and Pawlak, W., 2012. Turbulent sensible heat flux in Łódź obtained from scintillometer measurements - comparison of free and mix algorithms. Contemporary Trends in Geoscience, 1: 109-117.

Zilitinkevich, S.S., Mammarella, I., Baklanov, A.A. and Joffre, S.M., 2008. The effect of stratification on the aerodynamic roughness length and displacement height. Bound.-Layer Meteor., 129(2): 179-190.